

SGP-TR-203

In-Situ Multifunctional Nanosensors for Fractured Reservoir Characterization

Mohammed Alaskar

August 2013

Financial support was provided through the
Stanford Geothermal Program under
Department of Energy Grant No. DE-FG36-08GO18192,
and by the Department of Energy Resources Engineering,
Stanford University



Stanford Geothermal Program
Interdisciplinary Research in
Engineering and Earth Sciences
STANFORD UNIVERSITY
Stanford, California

Disclaimer: This report was prepared as an account of work sponsored by the Department of Energy's Geothermal Technologies Program. Neither the United States Government nor any agency thereof, nor any of their employees, makes any warranty, express or implied, or assumes any legal liability or responsibility for the accuracy, completeness, or usefulness of any information, apparatus, product, or process disclosed, or represents that its use would not infringe privately owned rights. Reference herein to any specific commercial product, process, or service by trade name, trademark, manufacturer, or otherwise does not necessarily constitute or imply its endorsement, recommendation, or favoring by the United States Government or any agency thereof. The views and opinions of authors expressed herein do not necessarily state or reflect those of the United States Government or any agency thereof

ABSTRACT

The goal of this research was to develop methods for acquiring reservoir temperature data within the formation and to correlate such information to fracture connectivity and geometry. Existing reservoir-characterization tools allow temperature to be measured only at the wellbore. Temperature-sensitive nanosensors will enable in-situ measurements within the reservoir. Such detailed temperature information enhances the ability to infer reservoir and fracture properties and inform reservoir engineering decisions. This thesis provides the details of the experimental work performed in the process of developing temperature nanosensors. Several potential nanosensor candidates were investigated for their temperature-sensitivity. Particle mobility through porous and fractured media was investigated.

In order for temperature nanosensors to map the reservoir temperature distribution and ultimately to characterize the fracture network, they must be transported through typical porous and fractured formation rocks without significant retention within the formation pores and/or fractures. To investigate retention mechanisms, various laboratory-scaled core-flooding and micromodel transport experiments were conducted. The results showed that the size and/or size distribution, shape, and surface charge of the particles were influential parameters governing the transport of particles through porous and fractured media. There was an optimum particle size relative to the pore size distribution of the tested rock, at which the particles experience the least retention. Pore-scale observations showed that polydisperse particle size distribution affected the particle transport adversely. Experiments also indicated that elongated or nonspherical particles exhibited greater retention within the porous medium, primarily because of their shape. Compatibility of the particle surface characteristics (surface charge) with the rock material was found to be crucial for particle transport.

The transport of particles, particularly silica particles, through fractured rock was investigated. Experimental results showed that the recovery of the particles was dependent on the particle size, concentration and flow rate. The controlling transport mechanisms of silica particles were also identified. Results showed that the existence of fractures facilitated the particle transport. Particles were found to flow with the fast-moving streamlines that exist within the fracture. Pore-scale experiments confirmed by visual observation that fractures are favorable conduits for particle transport. Particle tracking showed particles were flowing with velocities comparable to maximum velocity of bulk fluid assuming a parallel-plate fracture model.

The concept of using particles as a fracture caliper mechanism to estimate the fracture aperture was addressed. The feasibility of estimating the fracture aperture by correlating the size of the largest recovered particles to the fracture opening was verified by injecting a wide size distribution of particles through a fracture of predetermined hydraulic aperture. Experimental results showed that the size of the largest recovered particle was similar to the estimated aperture. Visual observations using micromodels were consistent with the results of the core-scale experiments.

Temperature sensing mechanisms of potential candidates were investigated. Temperature-sensitive particles investigated in this study include the irreversible thermochromic, dye-attached silica and tin-bismuth particles. A combined heat and flow test confirmed the temperature-sensitivity of the irreversible thermochromic particles by observing the color change. A detectable change in the fluorescent emission spectrum of the dye-attached silica particles upon heating was observed. A simple sensing mechanism of melting and growth in particle size of tin-bismuth particles was demonstrated.

The processing and detection of silica-encapsulated DNA particles with hydrofluoric acid chemistry was tested. A protocol to release the DNA by dissolving the silica layer without completely destroying the DNA was established. The silica-encapsulated DNA particles were flowed through a porous medium at high temperature. Some dissolution of silica particles was observed, leading to a reduction in their size.

This research study showed that synthesizing particles to respond to a specific reservoir property such as temperature is feasible. Using particles to measure reservoir properties is advantageous because particles can be transported to areas in the reservoir that would not be accessible by other means and therefore provide measurements deep within the formation.

ACKNOWLEDGMENT

Financial support for this research from the U.S. Department of Energy (DOE) is greatly appreciated. I am grateful to Saudi Aramco for the scholarship to pursue my Ph.D. at Stanford, without which the study would not be possible. I am also thankful to Stanford Geothermal Program for the additional financial support.

I sincerely thank my research advisor Prof. Roland Horne for his endless support, guidance, encouragement during my Ph.D. program. Thank you for allowing me to explore areas those are of my interest. I have learned from him not only technically, but on a personal level. You taught me how to look into the scientific problems and conduct research. For that I am very grateful.

I also like to thank the people who helped me through the course of my research. Thank you to Prof. Yi Cui for being supportive during the initial stages of this work by providing ideas of nanosensors, allowing me to use his lab and the help from his research group. Thank you to Dr. Kewen Li who helped me getting started in the geothermal lab. I would like to acknowledge Dr. Karrie Weaver in Stanford ICP-MS/TIMS Facility for her help with the hydrofluoric chemistry. Thank you to Robert Jones in Stanford Nanocharacterization Laboratory for his support in preparing my samples for electron microscopy. Many thanks to the staff of Stanford Nanofabrication Facility for their help during the fabrication of the micromodels used in this study. Special thanks to Cynthia Ross for her help, time and efforts in the design of the micromodel mask. Thank you to Shripa Patel in Protein and Nucleic Acid Facility of Stanford Medicine School for her support in conducting the real-time polymerase chain reaction analysis for DNA amplification. Special acknowledgment goes to my research partners Morgan Ames, Chong Liu and Stephen Connor for their collaboration in this research. Thanks to Dr. Clement Levard from the Department of Geological and Environmental Sciences in Stanford for providing particles to be used in this study. Thanks to Dr. Ronny Pini from

the Benson lab for being supportive and allowing me to use some of his instruments. I would also like to acknowledge the contribution of my colleagues in the Stanford Geothermal Program during the weekly discussion and brainstorm research meeting.

Thanks to the entire department of Energy Resources Engineering at Stanford. Many thanks to all students and friends for being supportive over the course of my Ph.D. studies. I would also like to thank the administrative staff for their immense support, including Sandy Costa, Yolanda Williams, Joanna Sun, Joleen Castro and Kay Wangelin.

I am indebted to my family, my parents and my siblings for their unlimited support and encouragement. I am also very thankful to my wife, Monerah, for her support and patience over the years that I have pursued my Ph.D. I wanted you to know if it was not for that I would have not been able to achieve what I have accomplished, you are very much appreciated. I thank God for my little angels, Fahad and Nasser, for bringing joy and happiness into our lives.

NOMENCLATURE

Variables

η_0 Single-collector contact efficiency

η Actual single-collector removal efficiency

α Attachment efficiency

A_s Porosity-dependent parameter of Happel flow sphere-in-cell model

f Porosity of medium

N_R Particle to collector aspect ratio

N_{Pe} Peclet number

N_{vdW} van der Waals number

N_A Attraction number

N_G Gravity number

d_p Particle diameter m

d_c Collector diameter m

d_g Grain size m

d_{50} Median grain size m

d_m Mean size of solid matrix m

U Fluid approach velocity m/s

A_H Hamaker constant J

k_B Boltzmann constant J/K

T Absolute temperature K

ρ_p Particle density kg/m^3

ρ_f Fluid density kg/m^3

ρ_w Water density kg/m^3

μ Fluid viscosity $kg/m \cdot s$

D Bulk diffusion coefficient m^2/s

L_f Filter medium packed length m

(C/C_o) Relative concentration of effluent to influent

$(C/C_o)_{max}$ Maximum recovered relative concentration

$(C/C_o)_{cum}$ Cumulative relative concentration

Φ_{total} Total interaction energy J

Φ_{el} Electrostatic double layer interaction energy J

Φ_{vdW} van der Waals interaction energy J

$\Phi_{acid-base}$ Acid-base interaction energy J

Φ_{Born} Born repulsive interaction energy J

$\epsilon_r \epsilon_0$ Dielectric permittivity of suspending fluid J/V^2m

$\zeta_1 \zeta_2$ Zeta potentials *V*

r_c Particle radius *m*

h Separation distance *m*

κ Debye constant *1/m*

γ Characteristic wavelength of dielectric *m*

σ Born collision diameter *m*

Pe Peclet number

V_{avg} Average water velocity *m/s*

b Fracture aperture *m*

W Fracture width *m*

θ Fracture orientation angle *degree*

U_s Particle settling velocity *m/s*

L_s Stoke settling length scale *m*

L_D Diffusion length scale *m*

τ Residence time *s*

$d(H)$ Hydrodynamic diameter *m*

U_E Electrophoretic mobility *m/s*

ε Dielectric constant

$f(ka)$ Henry's function

A_{abs} Absorbance

ε_{abs} Molar absorptivity constant

c Concentration

L_{path} Cuvette path length m

I Light intensity passing through the sample

I_o Light intensity before passing the sample

k_{gas} Gas permeability *darcy*

k_w Water permeability *darcy*

k_{eq} Equivalent permeability *darcy*

k_t Total permeability *darcy*

k_m Matrix permeability *darcy*

k_f Fracture permeability *darcy*

k_{kc} Kozeny-Carman permeability *darcy*

q Volumetric flow rate cm^3/s

q_o Outlet volumetric flow rate cm^3/s

q_f Fracture volumetric flow rate cm^3/s

q_1, q_2 Matrix volumetric flow rates cm^3/s

p_i Inlet absolute pressure *atm*

p_o Outlet absolute pressure *atm*

d Diameter of flow medium *m*

r Flow medium radius *m*

L Flow medium length *m*

A Flow medium cross-sectional area *m*²

A_f Fracture cross-sectional area *m*²

A_m Matrix cross-sectional area *m*²

A_t Total cross-sectional area *m*²

\emptyset Porosity of flow media

\emptyset_{sat} Porosity by saturation

\emptyset_{Hg} Porosity by mercury intrusion

V_p Pore volume of flow medium *m*³

V_B Bulk volume of flow medium *m*³

W_{total} Total water weight *kg*

V_{tube} Dead volume of tubes and fittings *m*³

d_{pore} Mean pore size *m*

Δp Differential pressure *atm*

V_{NP} Nanofluid injected volume *m*³

u Darcy velocity m/s

v Pore velocity m/s

v_p Particle velocity m/s

v_m Matrix pore velocity m/s

v_f Fracture pore velocity m/s

z Micromodel depth m

Abbreviations

CML Carboxylate-modified latex particles

PVP Polyvinyl pyrrolidone

TEA Triethanolamine

TEOS Tetraethyl orthosilicate

EGS Enhanced geothermal system

SEM Scanning electron microscopy

DLS Dynamic light scattering

DLVO Derjaguin-Landau-Verwey-Overbeek

XDLVO Extended DLVO

PV pore volume

DNA Deoxyribonucleic acid

T/C Throat to colloid ratio

TABLE OF CONTENTS

ABSTRACT.....	V
ACKNOWLEDGMENT.....	IX
NOMENCLATURE	XI
LIST OF TABLES.....	XXIII
LIST OF FIGURES	XXV
CHAPTER 1	1
INTRODUCTION	1
1.1 Motivation.....	1
1.2 Purpose of study.....	2
1.2.1 Problem statement.....	2
1.2.2 Methodology	4
CHAPTER 2	7
PARTICLE TRANSPORT THEORY	7
2.1 Transport in porous media	7
2.1.1 Filtration theory	8
2.1.2 Interaction energy	11
2.2 Transport in fractured media.....	14
2.2.1 Enhanced transport of particles in fractured rocks	14
2.2.2 Deposition mechanisms of particle in fractured rocks.....	15
2.2.2.1 Physical straining and matrix diffusion	15
2.2.2.2 Gravitational sedimentation	17
2.2.2.3 Particle adsorption	18
2.3 Chapter summary	19
CHAPTER 3	21
PRELIMINARY EXPERIMENTATION WITH INJECTION OF NANOMATERIALS INTO POROUS ROCKS	21

3.1 Background.....	21
3.2 Requirements for nanomaterials	21
3.2.1 Preparation of nanomaterials	22
3.2.1.1 Silica (SiO ₂) nanoparticles.....	22
3.2.1.2 Silver (Ag) nanowires and nanoparticles.....	23
3.2.1.3 Hematite nanorice (Fe ₂ O ₃).....	24
3.2.1.4 Tin-bismuth (Sn-Bi) nanoparticles	25
3.2.2 Characterization of nanoparticles	26
3.2.2.1 Dynamic Light Scattering (DLS).....	26
3.2.2.2 Zeta potential measurement	27
3.2.2.3 Ultraviolet -visible spectrophotometry	28
3.2.2.4 Scanning Electron Microscopy (SEM).....	29
3.3 Characterization of core samples and slim tubes.....	30
3.3.1 Rock cores pore size distribution.....	30
3.3.2 Rock cores permeability measurements.....	32
3.3.3 Slim tube permeability measurements.....	38
3.4 Nanofluid injection experiments.....	42
3.5 Results.....	44
3.5.1 Silver nanowire (AgNW) injection experiment results	45
3.5.2 Silver (Ag) nanosphere characterization and injection experiment results ..	48
3.5.2.1 Ag nanoparticle characterization	49
3.5.2.2 Ag nanoparticle injection experiment results	51
3.5.3 Hematite (Fe ₂ O ₃) nanorice characterization and injection experiment	
results	55
3.5.3.1 Hematite and coated hematite nanorice characterization.....	55
3.5.3.2 Uncoated and PVP coated hematite injection experiment results	59
3.5.4 Tin-bismuth (Sn-Bi) alloy nanoparticle characterization and injection	
experiment results	63

3.5.5 Silica (SiO ₂) nanoparticle characterization and injection experiment results	70
3.5.5.1 Berea, silica (SiO ₂) nanoparticle injection experiment results	72
3.5.5.2 Sand-packed tube silica (SiO ₂) nanoparticle injection experiment results	77
3.5.5.3 Greywacke, silica (SiO ₂) nanoparticles injection experiment results	81
3.6 Chapter summary	86
CHAPTER 4	89
EXPERIMENTAL INVESTIGATION OF PARTICLE TRANSPORT THROUGH FRACTURED MEDIA.....	89
4.1 Background	89
4.2 Characterizations of silica particle suspensions and flow media.....	90
4.2.1 Silica particles	90
4.2.2 Characterization of flow media.....	94
4.2.2.1 Pore size distribution.....	94
4.2.2.2 Fractured rocks and glass fracture model permeability measurements.....	96
4.2.2.2.1 Fractured greywacke permeability measurements	96
4.2.2.2.2 Glass fracture model permeability measurements	99
4.2.2.2.3 Fractured Berea permeability measurements	102
4.3 Particle suspension injection methods	104
4.3.1 Fractured greywacke experimental setup and injection method.....	104
4.3.2 Glass fracture model description and injection method.....	107
4.3.3 Fractured Berea experimental setup and injection method.....	109
4.4 Results and discussion	111
4.4.1 Fractured greywacke core experiment results and discussion	111
4.4.1.1 Impact of particle size and input concentration of on particle recovery.....	112
4.4.1.2 Particle deposition and transport mechanisms.....	119

4.4.1.3 Fracture aperture estimation using particles (Fracture caliper concept).....	121
4.4.2 Fractured Berea core experiment results and discussion	123
4.4.2.1 Influence of particle size, input concentration and fluid velocity on particle recovery.....	123
4.4.2.2 Filtration theory prediction of transport mechanisms within the rock matrix	127
4.4.2.3 Particle removal by physical straining	134
4.4.2.4 Particle deposition and transport mechanisms inside the fracture	137
4.5 Chapter summary	141
CHAPTER 5	143
PORE SCALE OBSERVATION OF PARTICLE TRANSPORT IN FRACTURE-MATRIX SYSTEMS	143
5.1 Background.....	143
5.2 Characterizations of microparticle suspensions.....	144
5.3 Micromodel fabrication and characterization	147
5.3.1 Micromodel characterization	148
5.3.1.1 Micromodel A.....	148
5.3.1.2 Micromodel B	150
5.3.2 Micromodel fabrication	158
5.4 Micromodel experimental setup and injection method.....	160
5.4.1 Silica particle Micromodel A injection method.....	161
5.4.2 CML particle Micromodel B injection method	162
5.5 Results and discussion	164
5.5.1 Silica particle injections into Micromodel A.....	164
5.5.2 CML particle injections into Micromodel B.....	168
5.6 Chapter summary	180
CHAPTER 6	183
POTENTIAL TEMPERATURE-SENSITIVE NANOSENSOR CANDIDATES	183

6.1 Background.....	183
6.2 Tin-bismuth (Sn-Bi) alloy nanoparticle heat test.....	184
6.3 Dye-attached silica nanoparticle heating experiment	190
6.3.1 Synthesis of fluorescent dye-attached silica nanoparticles	190
6.3.2 Dye-attached silica nanoparticle characterization	191
6.3.3 Heating experiment of dye-attached silica nanoparticles	194
6.4 Thermochromic microparticles.....	195
6.4.1 Irreversible thermochromic ink bench heat tests	196
6.4.2 Magenta thermochromic ink combined heat and transport experiment.....	200
6.4.2.1 Magenta thermochromic injection experimental method	200
6.4.2.2 Results and discussion	203
6.5 Silica-encapsulated DNA nanoparticles	207
6.5.1 Silica-DNA particles.....	207
6.5.2 Sample preparation and DNA quantification.....	208
6.5.3 Silica-encapsulated DNA combined heat and transport experiment	210
6.5.3.1 Characterization of porous medium.....	210
6.5.3.2 Experimental setup and injection method.....	210
6.5.3.3 Silica-protected DNA injection results	213
6.6 Chapter summary	214
CHAPTER 7	217
CONCLUSIONS AND RECOMMENDATIONS FOR FUTURE WORK.....	217
7.1 Conclusions.....	217
7.1.1 Potential temperature-sensitive particles	217
7.1.1.1 Irreversible thermochromic particles	217
7.1.1.2 Silica-based temperature-sensitive particles.....	218
7.1.1.3 Tin-bismuth alloy particles	219
7.2 Particle mobility in porous and fractured systems.....	220
7.2 Recommendations for future work	222
APPENDIX A.....	225

MICROMODEL FABRICATION PROGRAM.....	225
APPENDIX B.....	231
PRESSURE TRANSDUCER AND MASS FLOW METER CALIBRATION.....	231
APPENDIX C.....	235
IRREVERSIBLE THERMOCHROMIC DATA.....	235
BIBLIOGRAPHY.....	241

LIST OF TABLES

<i>Number</i>	<i>Page</i>
Table 3.1: Core characterization data ^a	31
Table 3.2: Slim tube characterization data.....	40
Table 3.3: Summary of flow experiments parameters ^a	42
Table 3.4: Summary of Ag nanoparticle properties and analysis data ^a	53
Table 3.5: Summary of coated and uncoated hematite nanorice properties ^a	56
Table 3.6: Summary of Sn-Bi alloy nanoparticle properties and analysis data ^a	67
Table 4.1: Fractured rocks and glass fracture model characterization data ^a	95
Table 4.2: Summary of fractured rocks and glass model flow experiments parameters ^a	105
Table 4.3: Results of fractured greywacke and Berea rock samples ^a	113
Table 4.4: Summary of calculated length scales and Peclet number for blue, green and red silica particles in fractured greywacke core ^a	121
Table 4.5: Summary of attachment, single-collector contact and actual efficiencies calculated for silica particles injection experiments into the fracture Berea core ^a	132
Table 4.6: Summary of calculated length scales and Pe number for 2 and 5 μm silica particles in fractured Berea core ^a	139
Table 4.7: Comparison between observed particle velocity and the average water velocity inside the fracture during silica injection into fractured Berea core ^a	140
Table 5.1: Summary of physical and chemical properties of CML particles ^a	146
Table 5.2: Summary of physical properties of Micromodel A ^a	151
Table 5.3: Summary of physical properties of Micromodel B ^a	151
Table 5.4: Summary of matrix and fracture permeability for micromodel B1 and B2 ^a ..	155
Table 5.5: Summary of water velocities and average resident time in fracture for micromodel B1 and B2 ^a	163

Table 5.6: Particle velocity of selected injection ^a	171
Table 5.7: Summary of calculated length scales and Peclet number for different particles, apertures and channel depths ^{a,b}	177
Table 6.1: Summary of the physical properties of the glass beads packed column ^a	201

LIST OF FIGURES

<i>Number</i>	<i>Page</i>
Figure 3.1: Pore size distribution of Berea and greywacke core samples.	32
Figure 3.2: Schematic of the apparatus for measuring gas permeability.....	33
Figure 3.3: Gas permeability versus the reciprocal of mean pressure of Berea and greywacke core samples. Note that the gas permeability measurement was not performed for Berea IV and thus not shown in this plot.	35
Figure 3.4: Steady-state, single-phase pressure drop versus flow rates for Berea I, II and III and greywacke core samples. Berea IV was not included because gas permeability measurement was not conducted.	35
Figure 3.5: Schematic of apparatus for liquid permeability measurement.	36
Figure 3.6: Steady-state, single-phase pressure drop versus water flow rates for Berea I, II and III core samples.	38
Figure 3.7: Polypropylene slim tubes (A) 30 cm long packed with glass beads, (B) 1000 cm long packed with sand.....	39
Figure 3.8: Gas permeability versus the reciprocal of mean pressure of long slim tube packed with sand used during silica nanoparticle injection.....	41
Figure 3.9: Steady-state, single-phase pressure drop versus gas and water flow rates for the long sand-packed tube.	41
Figure 3.10: Experimental apparatus for nanofluid injection into (a) core samples, (b) 10 m sand packed tube and (c) 30 cm glass bead packed tube.	43
Figure 3.11: Optical density of Ag nanowires influent (red curve) and selected effluent samples. The optical density of the effluent samples presented as flat lines, indicating these samples are free of Ag nanowires.....	46
Figure 3.12: Permeability measurement during the Ag nanowires injection experiment. Permeability dropped during the injection of the nanofluid until it stabilized (plateau) at approximately 45% of initial permeability.	47

Figure 3.13: Gas permeability comparison before and after cutting the slice at the inlet.	47
Figure 3.14: SEM imaging on the front side of the slice at different magnifications post the injection of AgNW into Berea II sandstone. The micrographs show the nanowires meshing and plugging at the pores.....	48
Figure 3.15: SEM image of the silver nanoparticles. (Levard, personal communication)	50
Figure 3.16: Optical density and calibration curve of diluted silver nanofluids of known concentrations. The maximum absorbance (peak) was at wavelength of 408 nm. Note the linearity of the calibration curve, indicating the applicability of Beer-Lambert Law. The calibration equation is showing in the graph. The secondary horizontal axis of optical density is associated with the secondary vertical axis of concentration.	50
Figure 3.17: Silver nanoparticles detected at effluent (a) visually based on color (b) SEM image from the third post injected pore.....	52
Figure 3.18: Production history (return curve) of silver nanoparticles.....	52
Figure 3.19: Total interaction energy between Ag nanoparticles and Berea core. The interaction energy is normalized to the thermal energy (Boltzmann constant and absolute temperature). The total interaction energy plot shows a shallow energy barrier below $6 k_B T$ with considerable attractive interaction at the primary energy minima.	54
Figure 3.20: SEM image of uncoated hematite nanoparticles. Their shape bears remarkable resemblance to grains of rice.	57
Figure 3.21: SEM image of SiO ₂ coated hematite. Coated sample did not retain its spindle-like shape as a result of the 50 nm SiO ₂ coat.	57
Figure 3.22: Optical density and calibration curve of diluted hematite suspension of known concentrations. The maximum absorbance (peak) was at wavelength of 420 nm. The calibration equation is showing in the graph.	

The secondary horizontal axis of optical density is associated with the secondary vertical axis of concentration.....	58
Figure 3.23: SEM imaging from within the pores of Berea sandstone at (a) front side, (b) back side (free of nanorice) of the slice at inlet side.....	59
Figure 3.24: Hematite nanorice aggregation on the surface of glass beads at (a) and (b) inlet and (c) and (d) outlet side of the flow apparatus. Aggregation at the tip of the nanorice can be seen in image c.	61
Figure 3.25: Production history (return) curve of PVP-coated hematite nanorice.	61
Figure 3.26: SEM image showing the polydispersity of the tin-bismuth nanoparticles. The nanoparticles range in size from 0.05 to 0.60 μm	64
Figure 3.27: SEM imaging showing the Sn-Bi nanoparticles at the effluent during (a) injection and (b) backflushing of the Berea sandstone. Only particles smaller than 200 nm were transported through pore spaces, while larger particles were trapped at the inlet of the core and mobilized during backflushing.....	64
Figure 3.28: Permeability measurements during the injection of the Sn-Bi nanoparticles. The permeability value dropped significantly during the injection of the nanofluid, and then increased to plateau. Backflushing increased the permeability slightly.	65
Figure 3.29: A micrograph from within the pore spaces at the inlet side of Berea sandstone used during the tin-bismuth injection. Nanoparticle entrapment is apparent. Sn-Bi nanoparticles covered most of the pore surfaces.....	66
Figure 3.30: SEM images from within the pore spaces of the Berea sandstone. They demonstrate the bridging and plugging phenomena.	66
Figure 3.31: Visual characterization of effluent samples for their Sn-Bi nanoparticles content based on color.	69
Figure 3.32: Micrographs of effluent collected during the injection of Sn-Bi nanoparticle into slim tube packed with glass beads.	69

Figure 3.33: Size distribution by volume percentage of the SiO₂ particles suspensions used during injection into Berea, greywacke sandstones and sand packed tube. Note the Bimodal distribution of the nanofluid suspension injected into greywacke core. The measurements were performed using DLS.71

Figure 3.34: Micrographs of the (a) 0.10 μm and (b) 0.07 to 0.35 μm SiO₂ nanospheres influent.71

Figure 3.35: Total interaction energy between SiO₂ particles and rock surfaces. The interaction energy is normalized to the thermal energy (Boltzmann constant and absolute temperature). Hamaker constant used is 6.0×10⁻²¹ J as per Israelachvili (1992) for SiO₂/SiO₂ nanoparticle in water. The total interaction energy plot shows a shallow energy barrier below as the particle size decreases.72

Figure 3.36: Particle size distribution by volume percentage of effluent sample containing core fines and debris.74

Figure 3.37: SEM image of rock fine relative to injected SiO₂ nanoparticles.....74

Figure 3.38: Production history of the 0.10 μm SiO₂ particles using DLS. Note that this is not concentration or return curve. DLS only identify the existence of particle based on its size. Each data point in this figure is taken from different effluent sample for the same particle size.....76

Figure 3.39: Rock sections for SEM analyses.76

Figure 3.40: Nanoparticles at the middle section of the rock. Nonspherical objects are the natural fines and debris from the rock itself.76

Figure 3.42: Production history of the 0.35 μm SiO₂ particles using DLS. Note that this is not concentration or return curve. Particle recovery was during the second post-injected pore volume. The first data point in the plot was from the effluent sample after which particles were detected. The last data point is from effluent after which particles were not detected.....79

Figure 3.43: Visual characterization of effluent samples for their SiO₂ nanoparticles content based on color.79

Figure 3.44: SEM images of effluent samples a, b and c of Figure 3.43.....	80
Figure 3.45: Core fines and debris in preflush effluent sample prior to SiO ₂ injection. ...	82
Figure 3.46: (a) Effluent sample during injection of nanofluid, (b) close-up image.	83
Figure 3.47: (a) Effluent sample at the fifth post-injected pore volume showing SiO ₂ nanospheres with broken side, (b) close-up image.	84
Figure 3.48: SEM images showing SiO ₂ nanospheres, (a) unusual appearance, (b) distorted particles.	84
Figure 3.49: SEM images of the pore spaces of greywacke core sections at, (a) inlet, (b) middle, (c) and (d) outlet.	85
Figure 4.1: SEM micrographs of (a) blue, (b) green and (c) red fluorescent silica particles. The shape uniformity of the silica particles is evident. The blue and green particles have a uniform size, whereas the red particles have a wide size distribution.	91
Figure 4.2: Emission spectrum of the blue, green and red fluorescent silica particles. The peak emission of the blue, green and red dye is at wavelength 430, 530 and 577 nm, respectively.	91
Figure 4.3: Fluorescent emission and calibration curve of (a) blue, (b) green and (c) red silica microparticle samples of known concentrations. The maximum emission (peak) was at wavelength of 430, 530 and 577 nm for blue, green and red silica suspensions. Note the linearity of the calibration curve, indicating the applicability of Beer-Lambert Law. The calibration equation is showing in each graph. The secondary horizontal axis of optical density is associated with the secondary vertical axis of concentration.	92
Figure 4.4: Total interaction energy between silica particles and surfaces. The interaction energy is normalized to the thermal energy (Boltzmann constant and absolute temperature). Hamaker constant used is 6.0×10^{-21} J as per Israelachvili (1992) for SiO ₂ /SiO ₂ particles in water. The total interaction energy plot shows a strong energy barrier above 1000 <i>kBT</i> for all particle sizes.	93

Figure 4.5: Pore size distribution of fractured Berea sandstone obtained by mercury intrusion method. The core sample has an average pore size of 15.44 μm96

Figure 4.6: A picture of the experimental setup used during the permeability measurement of the fractured greywacke core, (a) showing manometer (pressure), core assembly and balance (flow rate), (b) close-up image showing the core assembly and (c) an image of the fractured greywacke core showing the orientation of the fracture.98

Figure 4.7: Fracture permeability as function of flow rate, with an average fracture permeability of about 79.48 darcy. Note that the angle by which the fracture is orientated is about 40 degrees. The validity of Darcy law under experimental conditions was confirmed through the linearity between flow rate and pressure drop (the secondary horizontal axis of flow rate is associated with the secondary vertical axis of fracture permeability).99

Figure 4.8: Fracture permeability of the glass fracture model, with and without 102 μm shims.101

Figure 4.9: Validity of Darcy law under experimental conditions was confirmed through the linearity between flow rate and pressure drop.101

Figure 4.10: Schematic of the sandstone core plug with the location of the fracture. The fracture extends from the inlet to the outlet. The fracture was created by saw-cutting the core into two pieces at the center.102

Figure 4.11: Total permeability measured at different volumetric flow rates. The validity of Darcy's law is also verified through the linear relationship between pressure drop and volumetric flow rate.104

4.12: A picture of the silica particle injection apparatus showing the manometer and syringe used for pressure measurements and particle suspensions injection, respectively.106

Figure 4.13: Pictures of fracture glass model, showing (a) the bolted frame, top glass and bottom aluminum plates and (b) the fracture location.108

Figure 4.14: Schematic of the fracture apparatus (adopted from Diomampo, 2001).109

Figure 4.15: Schematic of the experimental apparatus employed in the silica particle transport.	110
Figure 4.16: Relative concentrations of (a) green and (b) red silica particles at two different suspension concentrations following their injection through fractured greywacke sandstone. The cumulative relative concentration is also included. For the green particles, data points beyond the sixth pore volume represent backflushing samples. For the red particles, backflushing samples start at the sixth pore volume and third pore volume for the 2C and C suspensions, respectively.....	115
Figure 4.17: Permeability measurement before and during the injection of the blue and green silica particles at different concentrations into fractured greywacke core. The permeability is decreasing as more particles are injected.....	118
Figure 4.18: Micrograph of the interior of Berea sandstone showing natural fracture with two 100 nm SiO ₂ nanoparticles at its entry. Smaller nanoparticles would have entered the fracture providing direct fracture aperture measurement based on recovered particle size.	122
Figure 4.19: Optical images for red fluorescent silica particles of (a) influent, (b) effluent samples. Only particles of about 23 μm flowed through the fracture of predetermined aperture of 30.68 μm.	122
Figure 4.20: Breakthrough curves of blue (2 μm) silica particles transported in fractured Berea sandstone showing (a) the maximum and (b) cumulative relative concentration. Note the steady decrease in the relative concentration for all breakthrough curves, and the gradual increase of the cumulative relative concentration until the end of the injection. The return curves were more sensitive to suspension concentrations than fluid velocity.....	125
Figure 4.21: Breakthrough curves of green (5 μm) silica particles transported in fractured Berea sandstone showing (a) the maximum and (b) cumulative	

relative concentration. Most breakthrough curves exhibited a sharp decrease in relative concentrations, except for the silica suspensions of concentration C injected at 3 and 10 cm³/min. The cumulative relative concentrations reached a plateau at different pore volumes depending on the injection flow rate. The return curves were more sensitive to fluid velocity than suspension concentrations.126

Figure 4.22: Semilog plot of single-collector contact efficiency, with respective contribution of each transport mechanism, calculated for silica particles used in this study. Hamaker constant $A_H=6\times 10^{-21}$ J, T= 21 °C, $\rho_p= 2.2$ g/cm³, $d_c= 150$ μ m, $f= 21\%$, $v= 6.84\times 10^{-5}$ m/s.128

Figure 4.23: A log-log plot of the effect of fluid velocity on the physical transport mechanisms of diffusion, interception and gravitational sedimentation for silica particle of size (a) 2 μ m and (b) 5 μ m. Parameters used here are the same as those used in Figure 4.22.130

Figure 4.24: Permeability measurements during the injection of the 2 μ m silica particles at different suspension concentrations, C, 2C and 4C. Flow rate was 3 cm³/min. The rate of reduction in total permeability was the highest during the injection of silica suspension with highest mass concentration. ..137

Figure 5.1: Example micrographs of (a) 6 μ m and (b) 10 μ m latex particles. Image (a) shows particles 2 to 3 times larger in diameter than nominal size, whereas image (b) confirms a uniform size of the 10 μ m particles. Micrographs of the 2 and 4.5 μ m particles are not shown; however, they exhibited the similar characteristics to the 10 μ m (uniform shape and size).146

Figure 5.2: XDLVO interaction energy between latex particles and silicon micromodel. The interaction energy is normalized to the thermal energy ($k_B T$). Here Hamaker constant for latex-water-quartz is 4.04×10^{-21} J (Israelachvili, 1992), T is 293K.147

Figure 5.3: Sandstone thin section (a) SEM, and (b) digitally manipulated images used in the design of Micromodel A (Rangel-Germán, 2002).149

Figure 5.4: Schematic of Micromodel A showing the repeated pattern and fracture channels (Rangel-Germán, 2002). Note that inlet and outlet port location were modified from the original design.....	149
Figure 5.5: Water permeability of Micromodel A measured at various volumetric flow rates showed an average value of approximately 1.09 darcy. This is in agreement with measurement performed by Inwood (2008). The linearity between the flow rates and pressure drop indicated the validity of Darcy Law.....	150
Figure 5.6: (a) SEM image of the porous medium, (b) a close-up image showing the heterogeneity and surface roughness of the grains, (c) schematic of Micromodel B showing the flow regions, fracture channels (in red) and (d) an image of the fracture surrounded by porous medium.	152
Figure 5.7: Grain size distribution based on the relative grain area and number of grains, obtained by image analysis. The relative grain area distribution indicated that the average grain size was about 60.9 μm	154
Figure 5.8: Pore size distribution of the pore network obtained by mercury intrusion, indicating an average pore diameter of about 9.53 μm	154
Figure 5.9: Matrix permeability of Micromodel B1 and pressure drop at various volumetric flow rates. The average matrix permeability was about 0.3 darcy. The pressure drop with relation to volumetric flow rate was relatively linear, indicating applicability of Darcy’s law at experimental flow conditions.....	156
Figure 5.10: Schematic of block of fractured rock showing the micromodel orientation with respect to the fracture.	157
Figure 5.11: Total and matrix permeability measured at various volumetric flow rates for Micromodels B1 and B2, assuming a parallel plate fracture (cubic law) and flow in tube (Poiseuille’s law). Note that the total and matrix permeability of Micromodel B2 did not change much when treating the	

fracture as parallel plate or tube. All these measurements were conducted in flow region 4, with fracture aperture of 25 μm	158
Figure 5.12: Schematic of the experimental apparatus employed in the particle transport through micromodels.	161
Figure 5.13: Image (a) showing particle-particle interaction (aggregation), particle attachment to grain surface and straining. Images (b) and (c) are showing straining during the injection of suspension concentration 0.49 and 1.92 mg/ml, respectively. Particle straining at the fracture-matrix interface is prominent with increasing suspension concentration.	166
Figure 5.14: A log-log plot showing the effect of grain size on the physical transport mechanisms of diffusion, interception and gravitational sedimentation for silica of particle size 2 μm in Micromodel A. Hamaker constant $A_H=6\times 10^{-21}$ J, $T= 21$ $^{\circ}\text{C}$, $\rho_p= 2.2$ g/cm^3 , $f= 21\%$, $v= 2.84\times 10^{-5}$ m/s.	167
Figure 5.15: Two-dimensional velocity field for section of Micromodel B. Blue color indicates slow fluid velocity, red color indicates higher velocity.....	169
Figure 5.16: Optical images obtained at the inlet pore spaces during the transport of particle size (a) 2, (b) 4.5, (c) 6 and (d) 10 μm through Micromodel B1. These images were captured at the same location at the end of the flow experiments, showing the overwhelming straining as particle size increases. Images taken at magnification of 100X.	173
Figure 5.17: Optical imaging of the 6 μm particles straining during their transport into (a) Micromodel B1 (aperture 25 μm) and (b) Micromodel B2 (aperture 25 μm), showing the influence of the physical dimensions (or depth) of flow conduit on particle transport.	174
Figure 5.18: Optical images captured at the end of the 2 μm particle experiments at (a) 5×10^{-5} and (b) 5×10^{-4} cm^3/min injection rates. This confirmed that the particle deposition mechanism was flow dependent.....	174

Figure 5.19: Optical image at the 25 μm aperture fracture during the injection of 2 μm particles at low flow rate (Micromodel B1), showing particle entering the matrix and depositing at the sides of the fracture.	176
Figure 5.20: An optical image showing an example of particle interception by a grain at the fracture-matrix interface.....	176
Figure 5.21: Optical images at the end of injection showing particle size of 10 and 6 μm plugging the (a) 25 μm aperture in micromodel B1 and (b) 15 μm aperture in micromodel B2, respectively. Images taken at magnification of 100X. This finding illustrated the effect of both fracture dimensions on particle transport.	179
Figure 5.22: An optical image showing the plugging of the 25 μm fracture (Micromodel B1) by particles of the polydisperse (Mix 2) sample. This image also shows particles flowing through the surrounding grains and plugging small pore throats.....	179
Figure 6.1: Phase diagram of tin-bismuth. Reproduced from National Institute of Standards and Technology (NIST).	185
Figure 6.2: Experimental apparatus for tin-bismuth heating experiment. Experimental setup and heating experiments were carried out by Morgan Ames.	185
Figure 6.3: Comparison of particle size distribution of original and heated tin-bismuth sample. There is an increase in the average size of about 0.080 μm after heating. The secondary peak is indicative of large aggregate caused by particle fusion upon melting.	187
Figure 6.5: Micrographs of tin-bismuth nanoparticles (a) before and (b) after heating. The sample was heated to 210°C. The melting and fusion of particles were evident.....	187
Figure 6.6: Optical images of the tin-bismuth alloy (a) before and (b) after heating (250°C for 2 hours) showing the growth of the individual particle size.....	188

Figure 6.7: SEM images of the tin-bismuth alloy particles after heating at 250°C for 2 hours. The micrographs shows that the alloy particles were not flattened due to heat, but still hold their spherical shape.....189

Figure 6.8: Schematic representation of silica nanoparticle surface modification and dye attachment. Adopted from Saleh, et al. (2010).192

Figure 6.9: Fluorescent microscopy image of dye-attached silica nanoparticles on quartz substrate. The whole substrate was bright (compared to black). Brighter areas indicated that there were more fluorescent molecules at these locations.....192

Figure 6.10: Fluorescence spectrum of (a) Oregon 488 dye molecule solution and (b) bare silica (no dye attachment) nanoparticles as control, dye-attached silica nanoparticles in water and dye-attached silica nanoparticles on quartz substrate. All samples were excited at wavelength of 400 nm. The dye-attached samples showed two peaks at 425 and 530 nm, compared to the free dye (Oregon 488) which has one peak at 530 nm.....193

Figure 6.11: Fluorescence spectrum of the dye-attached silica nanoparticle before (red) and after (black) heating at 200°C for 15min. The samples were excited at wavelength of 360 nm. The change in the fluorescent spectrum can be readily distinguished as an indication to a temperature exposure.....194

Figure 6.12: A picture of the coiled tube used during the bench heat test of the irreversible thermochromic ink. The coiled tube is submerged in oil bath heated to desired temperature.197

Figure 6.13: Snapshots of (a) black and (b) magenta irreversible thermochromic ink samples heated for 3 minutes at different temperatures below and above reaction temperature. The density or intensity of the sample color is increasing with increasing temperature. The color is fully developed at about 35°C and 10°C above the rated temperature of the black and magenta concentrate samples, respectively.198

Figure 6.14: Color density as function of temperature of various irreversible thermochromic inks heated for 3 minutes. This test was performed by the manufacturer (Adopted from the product color comparison chart).	198
Figure 6.15: Electron micrographs of the black thermochromic concentrate (a) before and (b) after heating. By comparison, it can be clearly seen that the particles change their structures to form spherical particles.	200
Figure 6.16: (a) Experimental apparatus used during the combined heat and transport experiment, and (b) condenser column packed with glass beads.	202
Figure 6.17: A snapshot of the thermochromic sample entering the heated zone of the glass beads column. The sample has changed its color immediately from off-white to magenta as a result of temperature. The change in color confirmed that the column temperature is at least 60°C.	204
Figure 6.18: Snapshots of the thermochromic slug during its flow under heat through the glass bead column.	205
Figure 6.19: Optical images of the (a) unheated and (b) heated thermochromic sample. The particles change shape from crystalline to spherical solids.	206
Figure 6.20: Amplification plot of standards and nucleic acid samples.	211
Figure 6.21: Standard curve of standards and samples showing the relation between the cycle threshold and concentration (picogram per microliter).	211
Figure 6.22: Schematic of the experimental apparatus for testing the silica-encapsulated DNA particles.	212
Figure 6.23: Electron micrograph of (a) influent, (b) and (c) effluent sample during particle injection at 150°C showing reduction in particle size and particle aggregation, respectively, (d) effluent sample collected during injection at room temperature where neither the particle size nor aggregation of particles were observed.	214
Figure B.1: Schematic of the pressure transducer calibration process diagram.	232
Figure B.2: Schematic of the experimental setup used during the mass flow meter calibrations.	234

CHAPTER 1

INTRODUCTION

1.1 Motivation

The global energy demand is predicted to grow by 50% over the next two decades (Energy Information Administration, 2006). Meeting such demand is a huge challenge for energy suppliers around the world. For instance, the average worldwide recovery of oil is about 35% of proven reserves. Increasing oil recovery by 10 to 15 % would double the current proven reserves of about 1.2 trillion barrels; as these reserves are not recoverable economically with current technologies. Therefore, efforts must be intensified to increase the amount of energy that can be extracted from the ground, not only by developing enhanced oil recovery technologies but also by increasing the efficiency of other alternative energy sources such as geothermal energy.

The majority of geothermal energy is generated from conventional hydrothermal systems, where heat, fluid and rock permeability occur naturally. Enhanced Geothermal Systems (EGS), on the other hand, only require naturally occurring heat. The rock permeability is created by hydraulic fracturing and working fluid is pumped through the reservoir. Because heat increases with depth, EGS appears to be feasible virtually anywhere in the world provided it is economically viable to drill to greater depths. Within the next 50 years, the installed capacity of EGS in the United States could yield 100 GWe (Tester et al., 2006).

In both geothermal and oil environments, reservoir description including fracture characterization plays an important role in new field development and existing asset management. Numerous studies have been dedicated to obtaining reservoir information from thousands of feet below the earth's surface. Despite advances in seismic, tracer

CHAPTER 1. INTRODUCTION

testing and other imaging and sensing technologies, reservoirs (particularly fracture networks) are still poorly known.

The flow through natural and engineered geothermal reservoirs as well as through carbonate rock formations is largely fracture-dominated. This has spurred a wide interest among researchers in developing new methods to characterize the fracture networks within a reservoir. Acquiring specific data about the reservoir parameters of pressure and temperature, near the wellbore and far out in the formation, and correlating such information to fracture connectivity and geometry were the subjects of this research.

1.2 Purpose of study

The purpose of this study was to develop a new method to predict reservoir parameters and to characterize fracture networks in geothermal and carbonate reservoirs using nanosensors. In-situ multifunction nanosensors and the fundamental theory used to predict reservoir parameters based on their measurements were investigated.

1.2.1 Problem statement

In the development of enhanced geothermal systems, the characterization of the size, shape and conductivity of fractures is crucial. Unlike conventional geothermal systems, enhanced geothermal systems do not require natural convective hydrothermal resources, but rather can be created in a hot, dry and impermeable volume of rock. Hydraulic stimulation of fractures is the primary means of creating functional geothermal reservoirs at such sites to allow economical heat recovery. The energy extraction rate is significantly dependent on the creation of fractured area within the targeted hot rock volume. Mapping fractured area is of equal importance. However, existing fracture characterization tools and analysis approaches are inadequate, especially at higher temperature and greater depth. Pressure and temperature are measured only at the wellbore, and it is not possible to determine the conditions out in the reservoir. There are no effective means to measure such properties far in the rock formations. Thus, the objectives of this research was to provide a new tool (nanosensors) and to develop

CHAPTER 1. INTRODUCTION

reservoir engineering approaches to estimate reservoir parameters and characterize fracture networks based on the measurements from these tools. Natural and enhanced geothermal reservoirs as well as carbonate rock such as the Arab-D formation of Ghawar field (Cantrell and Hagerty, 1999), the world's largest oil reservoir, are the primary applications intended in this study.

Temperature-sensitive nanomaterials have already been used in the biomedical industry for drug delivery to particular types of body cell that differ in temperature from normal cells (Sutton et al., 2007). Nanoparticle drug carriers are made to target disease-specific locations and release the drug at controlled rates (Kreuter, 1994; Moghimi et al., 2001; Panyam and Labhasetwar, 2003; Panyam et al., 2003). Thermally-activated nanoparticles in biomedical applications were designed to respond to temperatures slightly above 37°C (Chilkoti et al., 2002). Although this temperature is much lower than that in subsurface reservoirs, this concept shows promise. Thus, synthesizing temperature-sensitive nanomaterials that are applicable for geothermal and oil reservoirs may be feasible. Several investigators have proposed functionalized nanoparticles to measure reservoir properties. Rose et al. (2011) proposed surface-modified quantum dots to measure the fracture surface area at the interwell spacing in enhanced geothermal systems. Redden et al. (2010) suggested the use of encapsulated nanoreactors to infer the temperature history in geothermal reservoir applications. Saggaf (2008) envisioned futuristic multifunctional nanorobots (called resbots) to measure and store information about pressure, temperature and fluid type.

This study investigated a number of temperature-sensitive nanoparticle candidates that have a reaction temperature within a temperature range appropriate to geothermal reservoirs. This study focused on investigating their temperature sensitivity and mobility through porous and fractured systems.

1.2.2 Methodology

It is envisioned that nanoparticles of different sizes, shapes and materials can accompany the fluids injected at one well and can be recovered from another well within the same reservoir. The nanoparticles that made their way to the producing well would be analyzed and correlated with the fracture properties. The recovered particle size distribution can be related to the size distribution of the fractures.

Tailored nanomaterials may have the ability to record parameters such as pressure and temperature and register fluid type encountered within the reservoir. These data could be utilized to estimate in-situ reservoir parameters, evaluate new reservoir development plans and determine ways to operate fractured reservoirs more efficiently. Temperature-sensitive nanotracers can be used to assess new geothermal developments by observing their behavior at different temperatures. Temperature-sensitive nanotracers could also be used to provide information on how much heat is removed and how quickly the heat is replenished.

Making functional nanosensors involves novel material syntheses and deep understanding of their transport mechanisms at macro- and microscale. In this study, we conducted experiments to investigate the heat sensitivity of potential temperature-sensitive particles and their transport through porous and/or fractured systems. The roles of several transport mechanisms were assessed by a series of flow experiments using inert particles (nonfunctional particles) of different shapes, sizes and surface characteristics. Slim tubes packed with sand or glass beads, porous cores, fractured cores and micromodels of fractured systems were used.

This thesis consists of two main parts, as well as a chapter summarizing the results and future work. The first part provides the details of the investigation into the transport of passive particles in porous and fractured media as well as in micromodels. The second part is dedicated to the investigation of the heating and transport of temperature-sensitive

CHAPTER 1. INTRODUCTION

particles; namely, tin-bismuth alloy particles, thermochromic polymer particles, dye-attached and DNA encapsulated silica particles.

The first chapter provides an introduction and motivation of this research. The second chapter summarizes previous work with regard to particle transport theory in porous and fractured media.

The third chapter describes the details of particle transport experiments through various porous media, including consolidated rocks and sand columns, using inert particles. The objective of this set of experiments was to verify the feasibility of the transport of particles of specific materials that could potentially be used as a temperature sensor.

The fourth chapter discusses the experiments with regard to particle transport in fractured cores. The chapter focuses in effect of the physical parameters on particle transport.

The fifth chapter is focuses on pore-scale observations of particle transport in fracture media using micromodels. The chapter provides visual observation of particle transport mechanisms through fractures.

The sixth chapter shows the preliminary results of heat and/or simultaneous heat and flow conducted using some temperature-sensitive potential candidates that are considered during this study.

The seventh chapter presents the conclusions and outlines recommendations for future work.

CHAPTER 2

PARTICLE TRANSPORT THEORY

The objective of this research was to develop functional nanosensors to measure reservoir temperature at the interwell spacing, and use this measurement to infer other reservoir and/or fracture properties. For successful deployment of temperature nanosensors, they have to be transported through pores and fractures without significant retention. This chapter will summarize prior studies in this subject, as well as provide a review of some of the underlying theory.

2.1 Transport in porous media

The physical and chemical transport processes that determine the fate of particles flowing through saturated and unsaturated porous media have been studied extensively in colloid science. The processes affecting particle transport are the same as those that influence solute transport, i.e., advection, diffusion, dispersion, and adsorption (Bradford et al., 2002). Particle motion along fluid streamlines is advection. Due to heterogeneity of the fluid velocity field and tortuosity of paths within porous media, particle dispersion can occur, which may lead to earlier breakthrough for particles than for solutes. Investigators suggested that particle dispersion is caused partly by size exclusion or straining (Bales et al., 1989; Harter et al., 2000; Dong et al., 2002; Sirivithayapakorn and Keller, 2003). Straining is the trapping of particles of diameter larger than or equal to the pore throats to be entered. Because larger particles are excluded from smaller pore throats, they will travel through fewer pathways which in turn will reduce their travel time. Also, large particles tend to travel along higher velocity streamlines (excluded from lower velocity regions near pore walls), thus increasing particle velocity compared to conservative tracers (Auset and Keller, 2004). Interaction among particles (Brownian motion) will

result in diffusion of particles, with large particles experiencing less diffusion than small ones (Keller and Auset, 2007). Adsorption processes, which are commonly referred to as attachment through interactions (chemisorbed or physisorbed) leading to a filtration effect, are assumed to be the main processes that limit particle transport. Particle attachment is the removal of particles from solution by collision with and deposition onto a pore or fracture surface (Bradford et al., 2002). Particle removal by physical mechanisms includes Brownian diffusion, interception, and gravitational sedimentation. Interception occurs when a particle moving along a streamline comes in contact with a collector (grain) due to its finite size. Particles with densities greater than that of the suspension fluid may experience settling or gravitational deposition onto the collector surface. Diffusion of particles into porous media can result in more contact with the grains (Tufenkji and Elimelech, 2004). Bradford et al. (2002) suggested that smaller particles are removed primarily by diffusive transport, while larger ones are removed by interception and sedimentation.

2.1.1 Filtration theory

Filtration theory has been used to describe the transport of particles in porous media by predicting the single-collector contact efficiency (η_0), which is defined as the ratio of the number of collisions between particles and a filter medium grain to the total number of potential collisions in the projected cross-sectional area of the medium grain. The single-collector contact efficiency represents the sum of contributions of the individual physical transport mechanisms, i.e., diffusion, interception and gravitational sedimentation (Auset and Keller, 2006). The classical water filtration model was first presented by Yao et al. (1971) and modified by other authors (e.g., Rajagopalan and Tien, 1976; Rajagopalan et al., 1982). However, the model does not consider the influence of hydrodynamic (viscous) interactions and the universal van der Waals attractive forces. Colloid filtration was predicted accurately by solving the convective-diffusion equation numerically (Elimelech et al., 1995; Prieve and Ruckenstein, 1976), revealing the importance of the hydrodynamic interactions on colloid filtration. Tufenkji and Elimelech (2004) have proposed a new correlation equation (Equation 2.1) based on a numerical solution of the

governing convective-diffusion equation that incorporates the effect of hydrodynamic interactions and van der Waals attractive forces.

$$\begin{aligned} \eta_0 = & 2.4A_s^{1/3}N_R^{-0.081}N_{Pe}^{-0.715}N_{vdW}^{0.052} + 0.55A_sN_R^{1.675}N_A^{0.125} \\ & + 0.22N_R^{-0.24}N_G^{1.11}N_{vdW}^{0.053} \end{aligned} \quad (2.1)$$

The three terms correspond to diffusion, interception and gravitational sedimentation, respectively. The dimensionless parameters are defined as:

$$\begin{aligned} N_R &= \frac{d_p}{d_c} & N_{Pe} &= \frac{Ud_c}{D} & N_{vdW} &= \frac{A}{kT} \\ N_A &= \frac{A}{12\pi\mu(d_p/2)^2U} & N_G &= \frac{2(d_p/2)^2(\rho_p - \rho_f)g}{9\mu U} \\ A_s &= \frac{2(1 - \gamma^5)}{2 - 3\gamma + 3\gamma^5 - 2\gamma^6} & \text{where } \gamma &= (1 - f)^{1/3} \end{aligned}$$

where N_R is the aspect ratio, N_{Pe} is the Peclet number characterizing the ratio of convective to diffusive transport, N_{vdW} is the van der Waals number characterizing the ratio of van der Waals interaction energy to colloid thermal energy, N_A is the attraction number which represents the combined influence of van der Waals attraction forces and fluid velocity on particle deposition rate due to interception and N_G is the gravity number which is the ratio of the Stokes particle settling velocity to the fluid velocity. A_s is a porosity-dependent parameter of Happel flow sphere-in-cell model and f is the porosity (Happel, 1958). The parameters in these dimensionless numbers are as follows: d_p and d_c are the particle and collector diameters in meters, respectively, U is the fluid approach velocity in meters per second, A is Hamaker constant in Joules, k_B is the Boltzmann constant in Joules per degree Kelvin, T is absolute temperature in degrees Kelvin, ρ_p and ρ_f are particle and fluid densities in kilograms per cubic meter, respectively, μ is the absolute fluid viscosity in kilograms per meter-second and g is gravitational acceleration in meters per square second. D is the particle bulk diffusion coefficient, which can be estimated from the Stokes-Einstein equation (Russel et al., 1989), given as

$$D = \frac{k_B T}{3\pi\mu d_p} \quad (2.2)$$

Under practical conditions, the single-collector contact efficiency (η_0) is overestimated. The actual single-collector removal efficiency (η) is frequently expressed as a product of an empirical attachment efficiency (α), or sticking efficiency, and the single-collector contact efficiency:

$$\eta = \alpha\eta_0 \quad (2.3)$$

The attachment efficiency (α) is defined as the probability that successful collisions between particles and collector grains will result in attachment (Auset and Keller, 2006). The attachment efficiency is usually determined using experimental data for given physiochemical conditions (i.e. normalized concentration of the breakthrough curve) (Elimelech et al., 1995). The attachment efficiency is expressed as (Tufenkji and Elimelech, 2004):

$$\alpha = -\frac{2}{3} \frac{d_c}{(1-f)L_f\eta_0} \ln(C/C_0) \quad (2.4)$$

where L_f is the filter medium packed length and C/C_0 is the ratio of effluent (outlet) concentration to the influent (inlet) concentration.

Experimental data of the transport of colloids are not always in agreement with filtration theory. Discrepancies have been attributed to soil surface roughness (Kretzschmar et al., 1997; Redman et al., 2001), charge heterogeneity (Johnson and Elimelech, 1995), and underestimation of attachment coefficients due to the existence of repulsive forces between particles and porous medium (Ryan and Elimelech, 1996). Bradford et al. (2002) attributed such discrepancies to the fact that filtration theory does not account for straining. The degree to which particles are excluded by straining is function of porous medium characteristics and particle size and/or concentration. Complete straining occurs when particles are excluded from all pore throats (McDowell-Boyer et al., 1986), resulting in a filter cake that may reduce the porous medium permeability (Willis and Tosun, 1980). Incomplete straining, on the other hand, occurs when particles are rejected

from pore throats smaller than the critical size, resulting in permeability reduction that is less pronounced (Bradford et al., 2002).

Some studies have been conducted to investigate the relation between the size of particle and pore size distribution and its influence on particle straining. Sakthivadivel (1966 and 1969) proposed that particles larger than 5% of the median grain diameter were subjected to exclusion by straining. Matthess and Pekdeger (1985) extended this rule to include porous media consisting of a distribution of grain sizes. Their theoretical criteria suggested that particle to median grain size ratio should be greater than 18% for straining to occur in uniform sand. Experimental data by Harvey et al. (1993), however, was not in agreement with the criterion suggested by Matthess and Pekdeger (1985). Herzig et al. (1970) suggested that straining is important when the particle to grain diameter ratio exceeds 0.2. Xu et al. (2006) studied the effect of straining on the mobility of particles within groundwater aquifers and granular filters. They suggested that accurate description of particle mobility requires considering the effects of straining when the ratio of particle diameter to the median grain size (d_p/d_{50}) exceeds 0.008. Other researchers (e.g., Auset and Keller, 2006) studied the mechanisms of particle removal, including straining, by examining the relative particle size (i.e. throat to particle ratio T/C) using polystyrene beads (3-7 μm in diameter and particle density of 1.05 g/cm^3). They reported that straining was the primary attachment mechanism for T/C less than 1.8. For T/C greater than 2.5, only interception was observed for particles larger than or equal to 3 μm . For T/C ratios in between above values, straining and interception were the removal mechanism. Note that removal mechanism by gravity was not considered because the density of the polystyrene was similar to that of suspension fluid (i.e. water).

2.1.2 Interaction energy

The potential of particle attachment to a Solid-Water-Interface (SWI) and stability of particle suspensions can be assessed by determining the interaction energy (Elimelech et al., 1995). Interactions between particles and the surface of a porous medium are usually evaluated using the classical Derjaguin-Landau-Verwey-Overbeek (DLVO) theory

(Derjaguin and Landau, 1941; Verwey and Overbeek, 1948). According to this theory, the total interaction energy is the sum of van der Waals and electrostatic double layer interactions:

$$\Phi_{total}(h) = \Phi_{el}(h) + \Phi_{vdw}(h) \quad (2.5)$$

Other forces that are significant for surfaces in aqueous environments are included in the extended DLVO (XDLVO) approach (Van Oss, 1993; Brant and Childress, 2002). These forces are the acid-base and repulsive Born interactions. The total interaction energy based on the XDLVO approach is expressed as:

$$\Phi_{total}(h) = \Phi_{el}(h) + \Phi_{vdw}(h) + \Phi_{acid-base}(h) + \Phi_{Born}(h) \quad (2.6)$$

The electrostatic double layer interaction approximations available in the literature were derived from the Poisson-Boltzmann equation for charged bodies in ionic solutions. The electrostatic double layer interaction energy (which decays with the separation distance) can be approximated using the constant surface potential interaction expression derived by Hogg et al. (1966) for sphere-sphere interaction as:

$$\Phi_{el}(h) = \pi \varepsilon_r \varepsilon_0 \frac{r_{c1} r_{c2}}{(r_{c1} + r_{c2})} \left[2 \zeta_1 \zeta_2 \ln \left(\frac{1 + e^{-\kappa h}}{1 - e^{-\kappa h}} \right) + (\zeta_1^2 + \zeta_2^2) \ln(1 - e^{-2\kappa h}) \right] \quad (2.7)$$

where $\varepsilon_r \varepsilon_0$ is the dielectric permittivity of the suspending fluid J/V²-m, r_{c1} is the particle radius in meters, r_{c2} is the radius of a second particle in meters, κ is the Debye constant in 1/m and is given as $1/\kappa = 3.05 \times 10^{-10} I^{0.5}$ (I is the ionic strength, pure water $I \approx 10^{-6}$), and $\zeta_1 \zeta_2$ are surface potentials of interacting surfaces in Volts (usually replaced by zeta potentials) and h is the separation distance in meters. The particle-surface system is usually treated as a sphere-plate interaction, and thus Equation (2.6) is modified by taking the limit as r_{c2} goes to infinity that results in the replacement of the quantity $(r_{c1} r_{c2}) / (r_{c1} + r_{c2})$ by r_{c1} (Bradford and Torkzaban, 2008).

The van der Waals interactions are usually attractive and decay according to the square of the distance separating two charged bodies. Derjaguin's approximation of the van der Waals interaction energy for sphere-sphere interactions can be expressed as given by Gregory (1981) as:

$$\Phi_{vdw}(h) = -\frac{A_H}{6h} \frac{r_{c1}r_{c2}}{(r_{c1} + r_{c2})} \left(1 + \frac{14h}{\lambda}\right)^{-1} \quad (2.8)$$

where h is the surface to surface separation distance in meters, λ is the characteristic wavelength of the dielectric, usually assumed to be equal to 100 nm (Gregory, 1981), A is Hamaker constant in joules. Similarly, if the system is treated as sphere-plate interaction, the quantity $(r_{c1}r_{c2})/(r_{c1} + r_{c2})$ is replaced by r_{c1} .

The hydrate layer and structural forces ($\Phi_{acid-base}$) are assumed to be negligible and therefore were not included in the calculation of the total interaction energy. As the electron shells begin to overlap between atoms, strong repulsive forces exist between these atoms (Φ_{Born}). The Born repulsive interactions are short-range forces that act over a distance of several nanometers. An expression for Born repulsive interaction energy between a sphere and flat-plant was derived by Ruckenstein and Prieve (1976) to obtain:

$$\Phi_{Born}(h) = \frac{A_H\sigma^6}{7560} \left(\frac{8r_c + h}{(2r_c + h)^7} + \frac{6r_c - h}{h^7} \right) \quad (2.9)$$

Where σ is Born collision diameter that often assumed to have a value of 0.5 nm (Hahn et al., 2004), A_H is Hamamer constant in J/K, h is the separation distance in meters and r_c is the particle radius in meters.

The total interaction energy, when plotted as function separation distance, demonstrates the magnitude and type of interactions (repulsive or attractive). Knowledge of interaction energy is of a particular interest when studying the transport of particles because it provides insight regarding what conditions are favorable for aggregation, attachment, and detachment of particles.

2.2 Transport in fractured media

Particle transport and retention in fractured media differ greatly from that in porous media due to differences in the geometry of the transport conduits (Knapp et al., 2000). Large flow paths facilitate deeper infiltration of particles in fractured rocks compared to porous media (Weisbrod et al., 2002). Investigating particle behavior in discrete fractures is useful for understanding the controlling transport mechanisms. Mechanisms effecting particle transport in fractured media include advection, dispersion, adsorption, desorption, physical straining and air-water interface capturing (Wei et al., 2012). Several experimental investigations of particle transport in fracture materials focused on particle transport in volcanic rocks (Champ and Schroeter, 1988; Bales et al., 1989; Reimus, 1995; Vilks and Bachinski, 1996; Vilks et al., 1997), in artificial fractures (Smith et al., 1985; McKay et al., 1993b; McKay et al., 1995; Hinsby et al., 1996; Harton, 1996) or in fractured clays (Cumbie and McKay, 1999).

2.2.1 Enhanced transport of particles in fractured rocks

Vilks and Bachinski (1996) investigated the influence of particle size, velocity and direction of water flow and flow path on the transport of particles in a fractured granite block. They concluded that particle transport was sensitive to flow path and direction, and that the recovery rates were dependent on flow velocity relative to a critical velocity below which significant particle retention was observed. It has been widely observed that particles transport faster than conservative solutes in fractured media (e.g., Champ and Schroeter, 1988; Reimus, 1995; Knapp et al., 2000; Zvikelsky and Weisbrod, 2006; Zvikelsky et al., 2008; Tang and Weisbrod, 2009 and 2010). Fractures are favorable flow conduits for particles because fractures represent large flow paths with high velocities relative to the surrounding matrix, the absence of diffusion between fracture and matrix of low permeability and/or small pore throat size and the fact that particles of the same charge as the flow medium will most likely flow following central streamlines reducing collision with matrix grains and hence lower the probability of attachment (Zvikelsky and Weisbrod, 2006). Bales et al. (1989) observed that the transport of bacteriophages in

fractured porous tuff was three times faster than conservative solute tracer. McCarthy et al. (2002) studied the transport of fluorescent polystyrene particles in fractured shale saprolite. They reported that the particles arrived much sooner than bromide tracer by a factor of five. Investigators commonly attribute the enhanced transport of particles in fractured media to size and charge exclusion effects and Taylor dispersion (Becker et al., 1999; Zvikelsky and Weisbrod, 2006; Wei et al., 2012). Because of the large size of particles compared to pore throat size, particles are excluded from low flow regions of the rock matrix following fluid streamlines in fracture (Smith and Degueudre, 1993; Grindrod and Lee, 1997; Becker et al., 1999). Bradford et al. (2002 and 2003) in their study of particle transport in a sand column reported that size exclusion at inlet grains created dead ends, forcing subsequent particles through a larger continuous pore network. The charge exclusion comes into effect when both particles and solid surfaces are of like charge. As particles approach solid surface or grain, an electrostatic repulsive barrier forces the particles away from grain wall into moving streamlines within the fracture and thus faster breakthrough of particles. When particle size increases, Taylor dispersion could significantly enhance the transport of particles. Reimus (1995) attributed the rapid breakthrough of particles compared to solute tracers in fractured tuff core to lack of molecular diffusion, which would prevent particles from migrating out of high velocity streamline in the fracture.

2.2.2 Deposition mechanisms of particle in fractured rocks

Mechanisms of particle deposition in fractured rocks are not as completely understood as is the case in porous media. Physical straining, matrix diffusion, gravitational sedimentation and adsorption are considered the main particle retention mechanisms in saturated fractured rocks (Wei et al., 2012).

2.2.2.1 Physical straining and matrix diffusion

Physical straining of particles is directly related to the particle size and shape relative to the size and geometry of the flow conduit (pore throats or fracture) (Swanton, 1995). Straining could occur within the fracture at areas of small apertures. Particles flowing

through a fracture may also be trapped physically in the rock matrix, given that particles can access rock matrix and their size is larger than surrounding pore throats. This would result in dead ends preventing subsequent particles from further penetration (Cumbie and McKay, 1999), and/or forcing them through larger continuous pores or fractures (Bradford et al., 2002 and 2003). Conversely, if particle size is smaller than surrounding pores, particles may enter into the rock matrix which would increase the probability of particle collision with matrix grains and thus further particle filtration (James and Chrysikopoulos, 1999; Oswald and Ibaraki, 2001; Alonso et al., 2007). It should be mentioned that matrix diffusion is proportional to rock matrix porosity, and inversely proportional to fluid velocity and particle size.

Particles at the microscale are expected to travel along higher velocity streamlines (excluded from lower velocity regions near pore walls or fracture surfaces). Interaction among particles (Brownian motion) will result in diffusion of particles, with large particles experiencing less diffusion (Equation 2.2) than smaller ones (Keller and Auset, 2007). Particle motion along fluid streamlines is advection. The significance of diffusion and advection on particle transport can be evaluated by examining Peclet (Pe) number for each particle size under a specific flow conditions (i.e. fluid velocity) (Zvikelsky and Weisbrod, 2006). Detwiler et al. (2000) defined the Peclet number in a parallel plate aperture as:

$$Pe = \frac{V_{avg}b}{D} \quad (2.10)$$

where V_{avg} is the average water velocity inside the fracture in m/s, b is the fracture aperture in meters. Advection would be the dominating transport mechanism if Pe is greater than 1.0.

Some studies have managed to define an optimum particle size for transport through the fractured system under investigation. Reimus (1995) studied the transport of synthetic particles in saturated fractured tuff. The study predicted an optimum particle size, greater than which would lead to particle retention due to gravitational settling or straining in

small aperture regions of the fracture. Attenuation of particles smaller than the optimum size was attributed to the rapid diffusion within the fracture, hence more collisions with and attachment to the fracture walls. In a fractured granite block, Becker et al. (1999) found that 0.36 μm particles exhibited higher recovery compared to 0.83 μm particles. In a study with latex particles in fractured shale saprolite, Cumbie and McKay (1999) reported a greater recovery for 0.5 μm particles relative to 0.05, 0.1 and 1.0 μm particles. McCarthy et al., (2002) observed a higher recovery of particles with a size of 0.5 μm than particles in the size range of 0.1 to 2.1 μm for the same fractured material. Zvikelsky and Weisbrod (2006) studied the impact of particle size on transport of latex particles in saturated, naturally discrete fractured chalk cores. They observed greater recovery rates and relative concentration (C/C_o) of particles of 0.2 μm than 0.02 μm and 1.0 μm . Field experiments, on the other hand, of particle transport (including McKay et al., 1993a, 2000; Vilks et al., 1997; Becker et al., 1999, 2003; Weisbrod et al., 2002; Mori et al., 2003; Becker and Shapiro, 2003) found inconsistent optimum size for particle recovery. Most studies attributed the low particle recovery to diffusion because of long travel time and low water velocity.

2.2.2.2 Gravitational sedimentation

Gravitational sedimentation is recognized to be a significant filtration mechanism of particles in fractures, especially for dense particles. Gravity forces and associated settling velocity will cause the particle to move across streamlines until it reaches solid surface and deposits on it, if the conditions are favorable for attachment. Similar to particle transport by diffusion, gravitational sedimentation is a function of fluid velocity. Settled particles may be remobilized by increasing flow rates (Wei et al., 2012). Reimus (1995) described fluid advection, gravitational settling and, to lesser extent, matrix diffusion, to be the governing mechanisms of particle transport in fractures. Zvikelsky et al. (2008) studied the transport of clay, with much higher density compared to model particles, in fractured chalk. They observed that clay particles experienced higher attenuation and slower breakthrough times as compared with those of particles, mainly due to gravity settling.

The relative effect of diffusion and gravity settling (which are highly dependent on particle size) on flowing particle of different sizes through a fracture can be assessed using their characteristic transport length scales over resident time as per the model suggested by Becker et al. (1999). The Stoke rate of settling is proportional to the square of the particle diameter, while Brownian diffusion (Equation 2.2) is inversely proportional to its size. The length scale of Stoke settling (L_s) of spherical particle (Happel and Brenner, 1965) is expressed as:

$$U_s = \left(\frac{1}{18\mu} \right) (\rho_p - \rho_f) g d_p^2 \quad (2.11)$$

$$L_s = U_s \tau \quad (2.12)$$

and the length scale of diffusion (L_D):

$$L_D = \sqrt{2D\tau} \quad (2.13)$$

where U_s is the settling velocity of spherical particle in m/s under creeping flow conditions ($Re \ll 1$), d_p is the particle diameter in meters, g is the gravitational acceleration in m/s^2 , ρ_p and ρ_f are the density of the particle and fluid in kg/m^3 , respectively, μ is fluid dynamic viscosity in Pa.s, τ is resident time, k_B is the Boltzmann constant in J/K, T is water temperature in K and D is Brownian diffusion that can be calculated from Equation (2.2). According to this model, gravity settling would have a dominant effect over diffusion if L_s/L_D ratio is greater than 1.0, given that the lower surface of the fracture is accessible by the particles (i.e. $L_s/0.5b$ is greater than 1.0).

2.2.2.3 Particle adsorption

In filtration, adsorption is when a particle is attached to the solid-liquid interface. When particles approach a fracture surface, electrostatic interactions come into play. Reimus (1995) suggested that, in the region near the rock surface (at separation distance much less than the particle radius), electrostatic forces (effectively, surface charge) could have a negative effect on the transport of particles. Local charge heterogeneity, attractive van der Waals forces, surface roughness of fracture wall and solution chemistry could result

CHAPTER 2. PARTICLE TRANSPORT THEORY

in particle adsorption onto the fracture wall (Chinju et al., 2001; Vilks et al., 2008; Vilks and Miller, 2009; Alonso et al., 2009). Decreasing the pH and increasing the ion strength of solution will result in a lower surface charge and reduction in the repulsive energy barrier, respectively, on the particle and fracture surface (Kretzschmar et al., 1999). Therefore, under such favorable attachment conditions, if particles were brought to fracture surfaces by, for example, viscous drag, diffusion or dispersion, a contact with fracture surface is initiated and particles may be further attached. The adsorption mechanism of particles to fracture surface is still poorly understood (Wei et al., 2012). Many investigators (e.g., Kretzschmar et al., 1999; Hoek and Agarwal, 2006; Bayouhdh et al., 2009; Mondal and Sleep, 2012) have adapted the classical DLVO theory (which was originally developed for porous media) to describe particle adsorption in fractured rocks. In this work, approximation of the total interaction energy, based on XDLVO theory, was used to identify the type and magnitude of acting forces between particles and fractured systems. The details can be found in Section 2.1.1.2.

2.3 Chapter summary

This chapter provided a review of previous studies and fundamental theory of particle transport in porous and fractured media. A useful temperature sensor must be transported through distances of interwell spacing, and therefore particle mobility was investigated.

In porous media, filtration theory was often used to predict particle attachment. Previous studies had shown that the filtration theory failed to provide complete estimation of particle attachment due to the existence of repulsive forces between particles and porous medium and the fact that the theory does not account for straining. Investigators attempted to provide metrics that relate the size of the particle to pore size, to predict when straining may occur. In this study, the extended DLVO theory (XDLVO) was used to estimate the forces between particles and surfaces. Published metrics were also applied to evaluate straining.

CHAPTER 2. PARTICLE TRANSPORT THEORY

Because fracture-dominated reservoirs are the main application intended for the temperature-sensitive particles, the transport mechanisms of particles through fractured media were reviewed. Straining, matrix diffusion, gravitational sedimentation and adsorption were considered the main particle transport mechanisms. Gravitational sedimentation was identified as a significant transport mechanism for particles in fractures, particularly for dense particles such as silica particles. Investigated temperature nanosensors in this study include silica-based particles.

It was widely observed that fractures enhance the transport of particles through fractures because fractures represent large flow paths with high velocities relative to surrounding pore network. This observation was usually based on the interpretation of breakthrough curves. In this study, the mobility of silica particles through fractured rocks was carried out. Direct observation on the influence of fracture on particle transport was also address through the use of micromodels using latex particles.

CHAPTER 3

PRELIMINARY EXPERIMENTATION WITH INJECTION OF NANOMATERIALS INTO POROUS ROCKS

3.1 Background

In order to investigate the feasibility of utilizing nanosensors to illuminate reservoir properties in general and fracture network properties in particular, it was essential to verify their transport through typical formation rock samples. Initial testing with nanoparticles was also required to develop the understanding of their optimum injection procedures, sampling strategies and characterization techniques. Accordingly, various laboratory-scaled core-flooding experiments with inert nanoparticle suspensions were conducted. Specifically, nanoparticle suspensions were injected into Berea and greywacke cores as well as slim tubes packed with sand or glass beads.

The following sections will provide the details of the nanomaterial selection and characterization methods, experimental apparatus, rock cores and slim tube characterization and results.

3.2 Requirements for nanomaterials

Nanoparticles used in this study and ultimately in the reservoir must be safe to handle and environmentally benign. The particles should be stable, remain in suspension and disperse in solution. Moreover, the affinity of such particles to the reservoir formation should be verified, and the particles must not interact with the rock matrix (Kanj et al. 2009).

3.2.1 Preparation of nanomaterials

Silica particles, silver (Ag) nanowires, Ag nanoparticles, tin-bismuth (Sn-Bi) alloy nanoparticles, iron oxide (Fe_2O_3) nanoparticles (commonly known as hematite nanorice), and polyvinyl pyrrolidone (PVP) coated Fe_2O_3 nanoparticles were used for initial experimentation. The following sections discuss the synthesis of particles used in this study. These discussions on synthesis are not meant to be exhaustive; the reader is instead referred to original work for further details.

3.2.1.1 Silica (SiO_2) nanoparticles

As two of the candidates for a temperature-sensitive nanosensor, this study investigated the use of silica nanoparticles with dyes attached using a temperature-sensitive covalent linkage (Section 6.3) and silica-encapsulated DNA (Section 6.5), and so the mobility of silica particles in reservoir rocks was a target for investigation.

The processes for the preparation of monodisperse silica particles followed the study done by Bogush et al. (1988). The nanoparticle preparation was accomplished by the hydrolysis of tetraethyl orthosilicate (TEOS) in aqueous ethanol solutions containing ammonia. Initially, particle sizes in the range of 0.05-0.35 μm were targeted.

The correlation resulting from Bogush et al. (1988) was used as an engineering tool in the determination of single-sized particles. The expression was fitted to the experimental observations and written as:

$$d = A[H_2O]^2 \exp(-B[H_2O]^{1/2}) \quad (3.1)$$

with

$$A = A[TEOS]^{1/2} (82 - 151[NH_3] + 1200[NH_3]^2 - 366[NH_3]^3) \quad (3.2)$$

and
$$B = 1.05 + 0.523[NH_3] - 0.128[NH_3]^2 \quad (3.3)$$

where d is the average diameter in nanometers and the concentrations of the reagents are in the units of mol/l. Bogush et al. (1988) reported that most of the particle diameters obtained from the correlation were within 20% of those obtained experimentally.

3.2.1.2 Silver (Ag) nanowires and nanoparticles

Ag nanoparticles can be made in different shapes, allowing for investigation of shape-related constraints to nanoparticle flow within porous media. In fact, our initial ideas of temperature-sensitive nanoparticles revolved around particles that can change shape as their characteristic of temperature measurement. For example, a rod-like nanoparticle can transform to a sphere once exposed to a certain temperature; hence, the motivation for studying the flow of rod-like particles. The Ag nanowires used in this study had diameters in the range of 0.05 to 0.10 μm , and lengths in the range of 5 to 10 μm . The conditions for preparing uniform Ag nanowires followed, for the most part, the study by Sun et al. (2002). The formation of Ag nanowires was accomplished by reducing silver nitrate (AgNO_3) with ethylene glycol in the presence of Ag seeds. Polyvinyl pyrrolidone (PVP) was then added to direct the growth of Ag into uniform nanowires. The longitudinal and lateral dimensions of the Ag nanowires were controlled by changing the reaction conditions. Sun et al. (2002) reported that increasing the reaction temperature resulted in the formation of shorter nanowires. This synthetic method provided uniform nanowires with high yield (mass production) at relatively low temperature. The spherical Ag nanoparticles synthesis is a protocol adapted from Kim et al. (2006).

The morphological evolution involved in the growth process of the silver nanowires was explored extensively by Sun et al. (2002). They showed the typical absorbance spectra of the silver nanowires (Figure 3c in Sun et al., 2002) at different reaction times of relatively long silver nanowires. The increase in intensity of the two surface plasmon resonance (SPR) peaks at 350 and 380 nm (from curve k to m) was indicative of the further elongation of the silver nanowires and the increase in the number of formed nanowires as the reaction completed at 60 minutes. So the concentration of the nanowires in the sample was in direct relation to the absorbance levels and can be calculated from Beer-Lambert Law as explained in Section 3.2.2.2. For instance, the absorbance levels at 350 and 380 nm peaks had increased by roughly two fold as the reaction continued (curves k to m of Figure 3c in Sun et al., 2002).

3.2.1.3 Hematite nanorice (Fe_2O_3)

Hematite was chosen for a number of reasons. First, it furthered the investigation of the feasibility of transporting nonspherical nanoparticles through porous media. Second, the particles can be made using a relatively simple synthesis. The surface chemistry and surface charge of these nanoparticles can be modified, and there are known processes for coating hematite nanorice with other materials, which makes it a valuable candidate for functional nanotracers. Hematite is also stable at reservoir conditions and can be detected by its optical and magnetic signals. Finally, because of its unique geometry, nanorice can be distinguished visually from natural minerals that may be present in the geofluid using scanning electron imaging. Monodisperse hematite nanorice particles were synthesized using forced hydrolysis of solutions of ferric chloride, as suggested by Ozaki (1984). This hydrothermal synthesis was carried out by preparing 100 ml of aqueous solution of 2.0×10^{-2} M iron chloride and 4.0×10^{-4} M monopotassium phosphate and holding it at 100°C for 72 hours (Wang et al. 2006). The precipitated nanoparticles were centrifuged and washed several times, then dispersed in 100 ml of water. These nanoparticles were found to be approximately 500 nm in length and 100 nm in diameter, with a 5:1 aspect ratio.

After early results (Section 3.5.3) indicated a difficulty in getting the iron oxide particles to pass through the core, it was postulated that their elongated shape caused them to have nonuniform surface potential that resulted in clustering of the particles. Because this would be a general property of rod-shaped particles, an investigation of this issue was initiated, by coating the hematite nanoparticles with different materials to alter their surface charges.

Hematite nanoparticles were coated with silica and the surfactants triethanolamine (TEA) and polyvinyl pyrrolidone (PVP) in order to modify their surface properties and determine if transport is limited by geometry or surface properties. Silica was particularly attractive as a coating because it had already been injected into a core and recovered successfully. To perform this coating, 0.3 ml of hematite nanofluid suspended in water

CHAPTER 3. PRELIMINARY EXPERIMENTATION WITH INJECTION OF NANOMATERIALS INTO POROUS ROCKS

was diluted with 4 ml of water and 20 ml of ethanol, a slight variation of the process suggested by Lu (2002). 0.5 ml of 30 wt % ammonia solution and tetraethyl orthosilicate (TEOS) were added while the solution was stirred magnetically, and the reaction continued for 3 hours at room temperature. The coated nanorice were separated from the reaction medium by centrifugation and suspended in water. To coat the iron oxide nanoparticles with PVP, a 0.1 M solution of PVP in ethanol was prepared. Iron oxide nanofluid was then added, sonicated for 1 hour, and soaked overnight. The coated particles were cleaned by centrifugation three times at 6.5 krpm to remove excess surfactant. The TEA coating was identical, except a 0.1 M solution of TEA in water was used instead.

3.2.1.4 Tin-bismuth (Sn-Bi) nanoparticles

The Sn-Bi alloy nanoparticles were synthesized by Morgan Ames. This section (Section 3.2.1.4) was written originally by Morgan Ames and adopted from our joint paper Alaskar et al. (2012). The Sn-Bi alloy nanoparticles were selected for their potential to be used as temperature sensors because of their temperature sensitivity. One promising idea is a core-shell particle with an inert, magnetic core and a shell that undergoes decomposition or phase change. One of the reasons hematite was investigated is because of its behavior under an applied magnetic field. This would make it an ideal material for the inert core, while the shell could be a metal alloy with a low melting point, such as Sn-Bi alloy. Sn-Bi alloys could be used as sensors in the temperature range between the eutectic melting point of the alloy (139°C) and the pure melting points of Bi and Sn (271°C and 232°C, respectively). To synthesize the Sn-Bi alloy nanoparticles, Sn and Bi were melted together at the eutectic composition (approximately 60 wt% Bi and approximately 40 wt% Sn). After it was cooled to room temperature, 100 mg of the alloy was sonicated in 10 ml of mineral oil, a slight variation of the sonochemical method suggested by Chen et al. (2005). An ultrasonic processor with a 0.5 in. replaceable tip was used. The sonicator was operated at 100 W (20% power), with a pulse setting of 1 second on, 10 seconds off. The sonicator is capable of operating at 500 W, but was not operated as such because of concerns that the organic solvent would break the

CHAPTER 3. PRELIMINARY EXPERIMENTATION WITH INJECTION OF NANOMATERIALS INTO POROUS ROCKS

replaceable tip. The mixture was cooled to room temperature and centrifuged. The alloy particles were washed several times with ethanol and suspended in a solution of 100 mM PVP in ethanol.

3.2.2 Characterization of nanoparticles

In general, the quantity of the nanotracer produced at the sampling (exit point) should be sufficient to be recognizable and at concentrations at least factor of three above the lower detection limit of the devices used to analyze the effluent. Characterization of the nanofluid prior to and after injection was carried out by various techniques. Dynamic Light Scattering (DLS) and Ultraviolet-visible Spectroscopy (UV-visible Spectroscopy) were used to detect the nanoparticles. Scanning Electron Microscopy (SEM) was also utilized to confirm the findings.

Characterization of the rock pore spaces following the injection was carried out to study the nanoparticle dissemination inside the rock sample. The objective was to understand the particle size distribution and the way in which the nanoparticles arranged themselves within the porous medium (Kanj et al., 2009). A brief description of the characterization methods is incorporated in the following sections.

3.2.2.1 Dynamic Light Scattering (DLS)

DLS is a technique used to measure sizes of particles suspended in liquid. The technique measures the random motion of suspended particles resulting from the bombardment by surrounding solvent molecules. This movement is known as Brownian motion. When particles are illuminated with a laser, the scattered light intensity varies depending on the size of the particles (the smaller the particle, the further the distance it moves because of solvent molecule bombardment) hence their Brownian motion (Schmitz, 1990). These changes in light intensity are related to particles size using the Stokes-Einstein relationship given as:

$$d(H) = \frac{k_B T}{3\pi\mu D} \quad (3.4)$$

CHAPTER 3. PRELIMINARY EXPERIMENTATION WITH INJECTION OF NANOMATERIALS INTO POROUS ROCKS

where $d(H)$ is hydrodynamic diameter, D is translational diffusion coefficient, k_B is Boltzmann's constant, T is absolute temperature and μ is viscosity.

It should be mentioned that the particle size measured by DLS is the hydrodynamic diameter (how particles diffuse in a fluid). DLS assumes that the particles being measured have the same translational diffusion coefficient as spheres. Because the translational diffusion coefficient depends on various factors beside the particle core such as surface structure, concentration and the ion type of the medium, the reported size could be larger than the actual particle size (Schmitz, 1990). Therefore, SEM imaging was used here to confirm the DLS measurements.

DLS was utilized to determine the particle size distribution of the injected nanofluid and the effluent samples. These measurements were performed using the Zetasizer Nano ZS device manufactured by Malvern instruments. This device can detect particles as small as 0.6 nm. The Zetasizer is also capable of measuring the zeta potential of particles.

3.2.2.2 Zeta potential measurement

Charged particles are surrounded by ions that exist in two regions; inner (Stern layer) and outer (Diffuse layer) regions. The ions are strongly bounded to the particle at inner region, whereas ions in the outer region are less firmly attached. The particles and ions within the diffuse layer form a notional boundary called hydrodynamic shear surface or slipping plane. When particles move, ions within this boundary move with them. Ions outside this boundary do not move with the particle. The potential across the boundary is the zeta potential. The higher the zeta potential, the more stable and disperse the particle. Generally, particle suspensions with net charge higher than either +30 mV or -30 mV are considered stable.

The zeta potential is measured by determining the particle electrophoretic mobility and the application of Henry equation. The electrophoretic mobility is the velocity of a particle in an electric field. The velocity of the particle is measured using Laser Doppler Velocimetry (LDV). Henry equation is given as:

$$U_E = \frac{2\varepsilon\zeta f(ka)}{3\mu} \quad (3.5)$$

where U_E is the electrophoretic mobility, ε is the dielectric constant, ζ is the zeta potential, μ is the viscosity and $f(ka)$ is Henry's function which is usually taken as either 1.5 or 1.0, Smoluchowski and Huckel approximation, respectively. The zeta potential measurements were performed using the Zetasizer Nano ZS by Malvern.

3.2.2.3 Ultraviolet -visible spectrophotometry

UV-visible spectrophotometry involves the spectroscopy of photons in the UV-visible region, which means that it deals with light in the visible, near-ultraviolet and near-infrared ranges. The spectrophotometer is an instrument used to measure the light intensity as a function of wavelength of light. The Beer-Lambert law is used to quantify the concentrations of absorbing species in solution (Wittung et al., 1994). The law states that the absorbance of a solution is directly proportional to the path length through the sample and the concentration of absorbing species in solution. The Beer-Lambert law is given by:

$$A_{abs} = -\log_{10} \left(\frac{I}{I_0} \right) = \varepsilon_{abs} c L_{path} \quad (3.6)$$

where A_{abs} is the measured absorbance, I is the intensity of light passing through the sample, I_0 is the intensity of light before it passes through the sample, L_{path} is path length through the sample, c is the concentration of absorbing species and ε_{abs} is the molar absorptivity constant which is specific for each species and wavelength at particular temperature and pressure.

Therefore, measuring the absorbance of the substances in solution and knowing the path length of the sample along with the absorptivity constant, the concentration of the substance can be calculated. However, the absorptivity constant is not readily available for materials and/or at desirable conditions of temperature and pressure. Due to the difficulty in obtaining the absorptivity constant, it is common to determine the concentrations by constructing a calibration curve. By doing so, it is not necessary to rely

CHAPTER 3. PRELIMINARY EXPERIMENTATION WITH INJECTION OF NANOMATERIALS INTO POROUS ROCKS

on a value of the absorptivity or the reliability of Beer's Law. This is accomplished by making a few dilutions, each with accurately known concentration. It is important to ensure that those concentrations bracket the unknown concentrations under investigation. For each dilution, the absorbance is measured and plotted against the sample concentration. This is the calibration curve. Note that the Beer-Lambert law assumes a linear relationship between absorbance and concentration. It is worth mentioning that the Beer-Lambert law implies that there is an equal effect of the changes in concentration and path length. For example, dilution of the sample by a factor of 12 has the same effect on absorbance as reducing the path length from 12 to 1 millimeter.

The UV-visible absorbance spectra were measured at room temperature using a Shimadzu UV-1700 double beam spectrophotometer with a 12 mm square polystyrene cuvette. All samples had been sonicated prior to analysis to disperse the particles.

3.2.2.4 Scanning Electron Microscopy (SEM)

Microscopy-based techniques provide a tool for the characterization of particle size, size distribution and morphology. A major advantage of microscopy-based techniques is the capability to identify the particle shape (Jillavenkatesa et al., 2001). This is particularly important in nanofluid injection experiments because it enables us to distinguish the injected nanoparticles from preexisting objects such as rock fines and debris. Scanning Electron Microscopy (SEM) generates images of a sample surface by scanning it with a high energy beam of electrons. Signals produced from the interaction between electrons and the sample surface can provide detailed information about the sample topography. Generated signals include secondary electrons, backscattered electrons, diffracted backscattered electrons, photons, visible light and heat (Egerton, 2005). Among those signals, secondary and backscattered electrons are used for sample imaging. The sample morphology and topography are best imaged using secondary electron. SEM enables the evaluation of the details at higher magnifications and resolutions and that makes it suitable for particle measurements in the submicron sizes (Clarke, 2002).

CHAPTER 3. PRELIMINARY EXPERIMENTATION WITH INJECTION OF NANOMATERIALS INTO POROUS ROCKS

The measurements were performed using a Philips FEI XL30 Sirion SEM instrument with Field Emission Gun source at the Stanford Nano Characterization Laboratory. As mentioned earlier, SEM imaging is useful to confirm the DLS measurements which are simpler and cheaper but do not distinguish between the particles other than by size. Moreover, SEM was used to study the location of nanoparticles inside the rock matrix and how they arrange themselves in the pore spaces.

3.3 Characterization of core samples and slim tubes

Prior to nanofluid injection, standard experiments to characterize the rock cores and slim tubes were performed, including the pore size distribution, porosity and permeability measurements. Preliminary testing of nanofluid injection was carried out using five different cores; Berea I, Berea II, Berea III, Berea IV and greywacke. Core sample dimensions, porosity, permeability, pore size distribution and pore volume calculations are summarized in Table 3.1. Silica nanoparticles, silver nanowires, hematite nanorice and tin-bismuth nanoparticles were transported through Berea I, Berea II, Berea III and Berea IV, respectively. The silver nanoparticles were injected into Berea II (the same core sample used during the injection of silver nanowires after removing a slice of that core where the nanowires were trapped). The greywacke core sample was used during the injection of silica nanoparticles. Slim tubes properties are summarized in Table 3.2 in Section 3.3.3.

3.3.1 Rock cores pore size distribution

The pore size distribution of the core samples was measured by the mercury (Hg) intrusion method. The intrusion of mercury was performed using the AutoPore IV 9500 Mercury Porosimeter manufactured by Micromeritics. This porosimeter covers a pressure range up to 33,000 pound per square inch (psi) and pore diameter range from approximately 360 to 0.005 micrometers. The device has two low-pressure ports and one high-pressure chamber.

CHAPTER 3. PRELIMINARY EXPERIMENTATION WITH INJECTION OF NANOMATERIALS INTO POROUS ROCKS

Table 3.1: Core characterization data^a

Property	Berea I	Berea II	Berea III ^b	Berea IV	Greywacke
	SiO ₂	AgNW, Ag	Fe ₂ O ₃	Sn-Bi	SiO ₂
d (cm)	3.8	3.8	3.8	3.8	3.8
L (cm)	6.0	5.8	4.9	5.1	5.6
Φ_{Hg} (%)	19.4	19.0	N/A	N/A	6.1
Φ_{sat} (%)	18.4	18.2	17.1	17.5	4.0
k_{gas} (md)	174	131	152	N/A	8.0×10^{-4}
k_{eq} (md)	85.8	84.9	72.2	N/A	0.8×10^{-4}
k_w (md)	61.1	93.3	60.7	125.3	1.5×10^{-4}
d_{pore} (μm)	8.8	8.8	8.8	8.8	0.05
PV (cm ³)	12.5	12.0	9.1	10.0	2.40

^a d and L are core diameter and length, respectively, Φ_{Hg} and Φ_{sat} are porosity by mercury intrusion and resaturation, respectively, k_{gas} , k_{eq} and k_w are the gas, liquid equivalent and water permeability, respectively, d_{pore} is mean pore size, PV is pore volume and N/A indicates that measurement was not performed.

^bNote that Berea II core was used during the injection of silver nanowires and nanospheres. All properties are the same except that the core was shortened (5.8 to 4.1 cm) during the silver injection that changed the PV from 12.0 to 8.0 cm³.

Prior to analysis, the sample must be weighed and all relevant sample information entered. Pressure points, at which data were collected, were then specified. Following that, the samples were loaded into a penetrometer and were ready for measurements. The analysis was conducted in two stages, low-pressure and high-pressure. Firstly, the penetrometer was loaded in the low-pressure port to evacuate all gases and then backfilled with mercury. The data were collected at pressures up to 30 psi. Secondly, the penetrometer was removed and installed in the high-pressure chamber. The analysis was resumed and data were collected up to pressure as high as 33,000 psi.

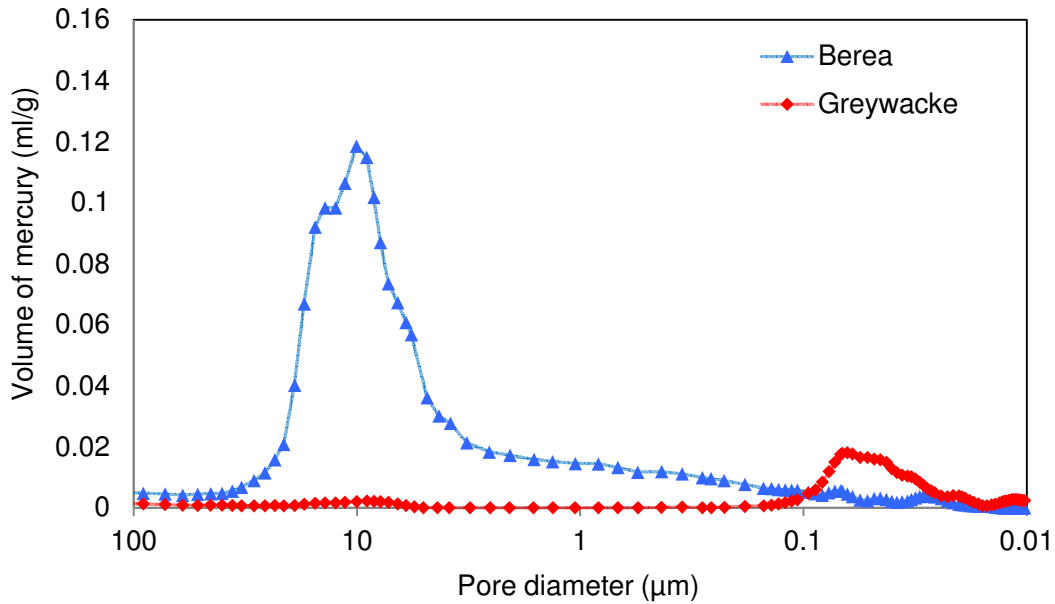


Figure 3.1: Pore size distribution of Berea and greywacke core samples.

The principal idea behind the pore volume measurements was as follows. The pore volume data were generated through the calculation of the volume of mercury left in the penetrometer stem as pressure was applied. As pressure increased, mercury from the penetrometer stem was forced to enter the pores. Smaller pores require higher pressure to overcome capillarity. Mercury was the nonwetting phase, and its surface tension, contact angle and radius of curvature were used to obtain the pore diameter at a given pressure (Micromeritics, 2008).

Measurements conducted on the Berea and greywacke rocks showed the cores to have pore sizes as large as 50 and 0.15 μm , respectively. The pore size distributions of both core samples are depicted in Figure 3.1.

3.3.2 Rock cores permeability measurements

Permeability is defined as the ability to transmit fluids through a porous medium. Initially, the gas permeability was determined for all core samples. The Klinkenberg effect (gas slippage) was considered to evaluate the equivalent liquid permeability. Then,

CHAPTER 3. PRELIMINARY EXPERIMENTATION WITH INJECTION OF NANOMATERIALS INTO POROUS ROCKS

the liquid permeability for the same core samples was measured. Figure 3.2 is a schematic of the apparatus used in the measurement of gas permeability. The gas flowed in this experiment was nitrogen (N_2). The pressures at the upstream (inlet) and downstream (outlet) of the core were measured using differential pressure transducers manufactured by Celesco Company. These transducers (Model DP30) have a linearity of 0.5% and a repeatability of 0.5% full scale. Both differential pressure transducers were calibrated using a standard pressure gauge with an accuracy of 0.1 psi. The flow rate of nitrogen gas was measured using a mass flow meter manufactured by Matheson (Model 8272-0423). The meter has the capability to measure flow rates from 0 to 2000 cm^3/min . At low gas flow rates (from 0 to 200 cm^3/min), another mass flow meter (Model 8172-0422) manufactured by the same company was used. The mass flow meters were calibrated using a stop-watch and graduated cylinder (as the standard method of measuring the flow rate). Prior to permeability measurement, each core was first dried in a furnace at $75^\circ C$ under vacuum pressure of 0.09 MPa for 24 hours. After weighing the core sample, it was placed inside the core-holder under a confining pressure of 30 atm.

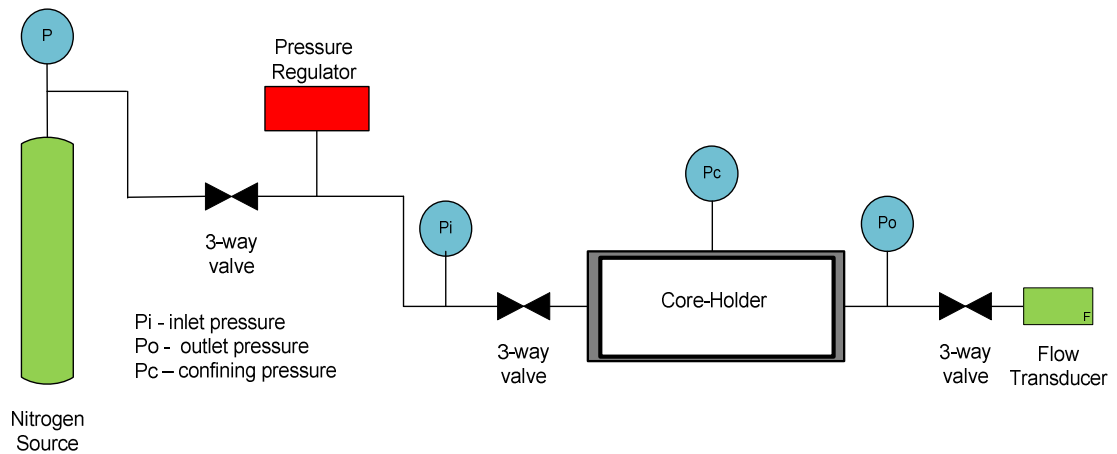


Figure 3.2: Schematic of the apparatus for measuring gas permeability.

CHAPTER 3. PRELIMINARY EXPERIMENTATION WITH INJECTION OF NANOMATERIALS INTO POROUS ROCKS

The gas permeability measurement was then started by introducing nitrogen at different flow rates and inlet pressures. The gas permeability was calculated by applying Darcy's law for horizontal flow compressible fluid which is given as:

$$k_{gas} = \frac{2q_o p_o \mu L}{A(p_i^2 - p_o^2)} \quad (3.6)$$

where μ is the viscosity in centipoises, q_o is outlet volumetric flow rate in cm^3/s , A is the core cross-sectional area in cm^2 , L is the core length in cm and p_i and p_o are inlet and outlet absolute pressures in atmospheric unit, respectively.

The gas permeability of Berea and greywacke cores as a function of the reciprocal of mean pressure is depicted in Figure 3.3. Note that the gas permeability measurement was not performed for Berea IV core, so it is not shown in Figure 3.3. According to the Klinkenberg effect, extrapolating the straight line to infinite mean pressure (or zero reciprocal of mean pressure) intersects the permeability axis at a point designated as the equivalent liquid permeability (Amyx et al., 1960). All gas and equivalent liquid permeability values are summarized in Table 3.1.

The validity of Darcy's law (Equation 3.6) for single-phase flow was examined by plotting the equivalent pressure drop $(p_i^2 - p_o^2)/2p_o$ as function of gas flow rate in the porous medium. Figure 3.4 demonstrates the linear relationship between the pressure drop and gas flow rates for Berea I, II, III and greywacke core samples, which indicated that inertia contribution of gas flow is negligible. Note that the gas permeability measurement of Berea IV was not performed, thus it was not included in Figure 3.4.

CHAPTER 3. PRELIMINARY EXPERIMENTATION WITH INJECTION OF NANOMATERIALS INTO POROUS ROCKS

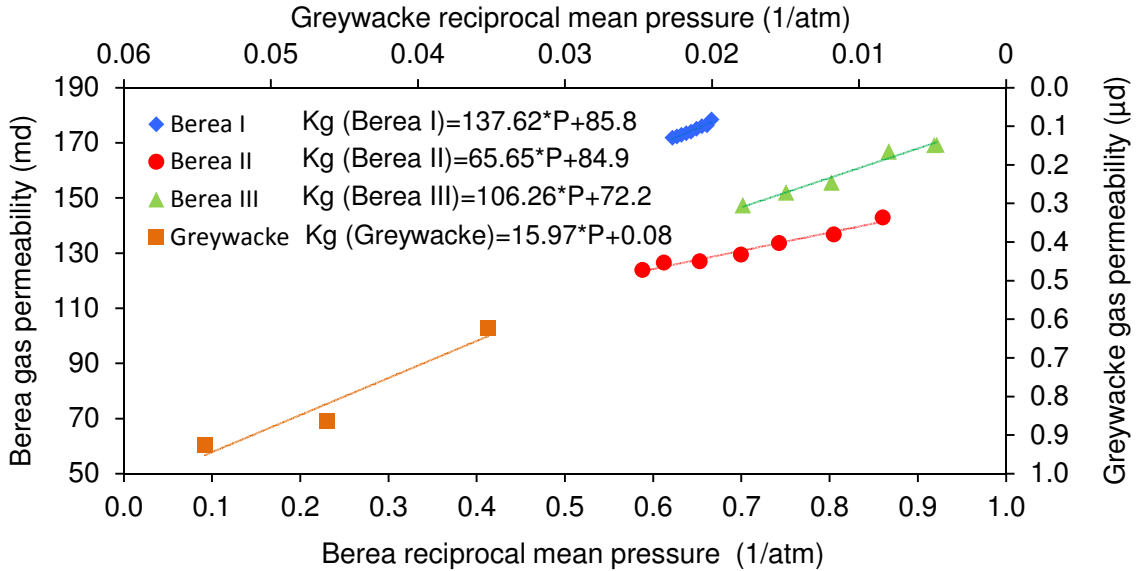


Figure 3.3: Gas permeability versus the reciprocal of mean pressure of Berea and greywacke core samples. Note that the gas permeability measurement was not performed for Berea IV and thus not shown in this plot.

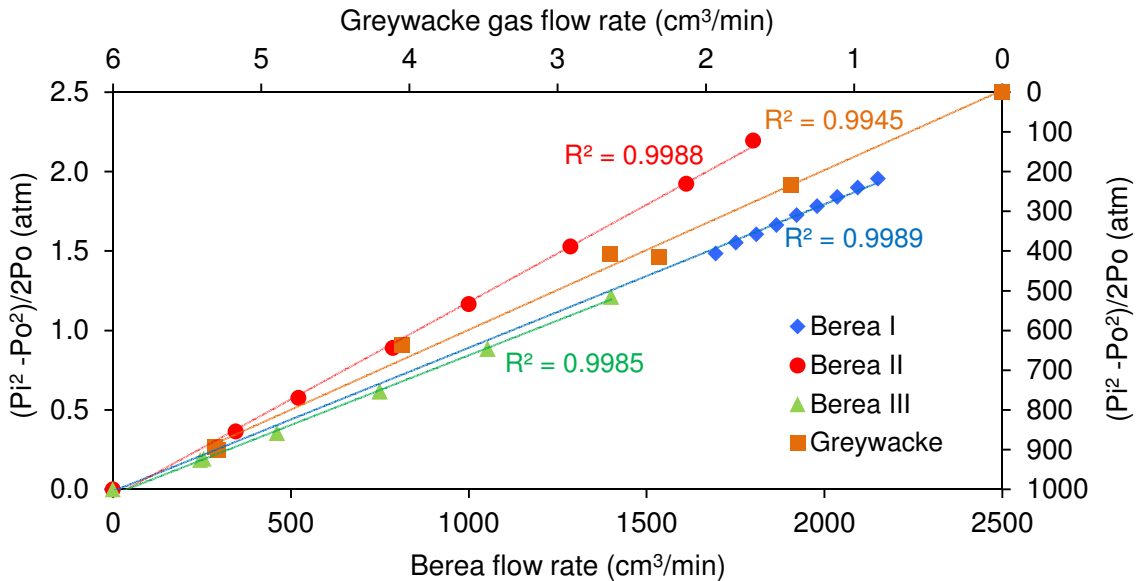


Figure 3.4: Steady-state, single-phase pressure drop versus flow rates for Berea I, II and III and greywacke core samples. Berea IV was not included because gas permeability measurement was not conducted.

CHAPTER 3. PRELIMINARY EXPERIMENTATION WITH INJECTION OF NANOMATERIALS INTO POROUS ROCKS

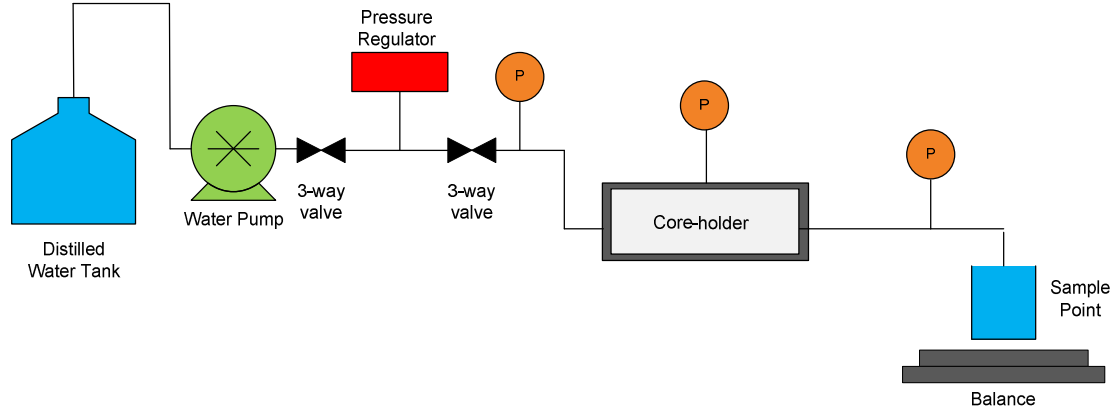


Figure 3.5: Schematic of apparatus for liquid permeability measurement.

The liquid permeability was measured for the same core samples. A schematic of the apparatus used in the measurement of liquid permeability is shown in Figure 3.5. The core samples were first saturated with pure water inside the core-holder. The cores and related system were evacuated using Welch Vacuum Pump (Model No. 8915A) for 4 hours at a vacuum pressure below 100 millitorr to remove moisture. Pure water was introduced to saturate completely the sample and connecting tubes. The total amount of water entered the system was determined by measuring the weight of water container before and after saturation using a balance. The pore volume, and hence porosity, was calculated by subtracting the volume of tubes and fitting from the total volume. The porosity calculation is as follows:

$$\phi = \frac{V_p}{V_B} \cdot 100 \quad (3.7)$$

$$V_p = \frac{W_{total}}{\rho_w} - V_{tube} \quad (3.8)$$

$$V_B = \frac{\pi}{4} dL \quad (3.9)$$

where ϕ is the porosity in percentage, V_p and V_B are pore and bulk volumes in cm^3 , respectively. W_{total} is the total weight of water that entered the system during the saturation process in gram. ρ_w is the water density at test temperature in g/cm^3 . V_{tube} is

CHAPTER 3. PRELIMINARY EXPERIMENTATION WITH INJECTION OF NANOMATERIALS INTO POROUS ROCKS

the dead volume of tubes and connecting fittings in cm^3 (calculated using the length and diameter of tubes and fittings). d and L are the diameter and length of the core in cm, respectively.

Following the core saturation, an automated constant-rate pump (Dynamax, Model SD-200) manufactured by Rainin Instrument Company was used to inject the pure water. The minimum pumping rate of the pump is $0.05 \text{ cm}^3/\text{min}$ with an accuracy of $0.01 \text{ cm}^3/\text{min}$. The flow rates of the water pump were calibrated before the experiment using a stopwatch and a Mettler balance (Model PE 300). The accuracy of the balance is 0.01 g and the range is from 0 to 300 g. The liquid permeability results are found in Table 3.1. Darcy's law for horizontal flow was utilized to compute the permeability. Darcy's law for horizontal flow of incompressible fluid is given as:

$$k_w = \frac{q\mu L}{A\Delta p} \quad (3.10)$$

where q is the volumetric flow rate in cm^3/s , μ is the viscosity in centipoises, L and A are the length and the cross-sectional area of the core in cm and cm^2 , respectively. Δp is the differential pressure across the core sample in atmospheres.

Similar to the gas flow, a linear relationship was also observed between the water flow rates and pressure drop Δp in Equation 3.10. This is demonstrated in Figure 3.6 for Berea I, II and III rock samples. Because only a single flow rate was used during the liquid permeability measurements of greywacke core, the linearity between pressure drop and flow rate was not examined.

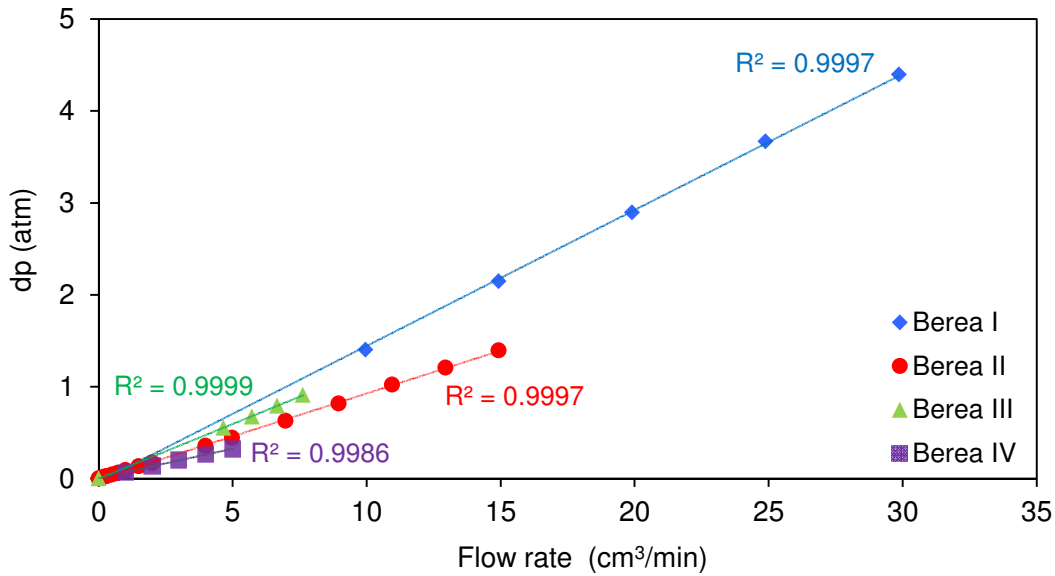


Figure 3.6: Steady-state, single-phase pressure drop versus water flow rates for Berea I, II and III core samples.

3.3.3 Slim tube permeability measurements

This section describes the measurements of the porosity, permeability and pore volume of slim tubes packed with glass beads or sand. To investigate the mobility of nanoparticles in the absence of the rock materials (such as clays), hematite and tin-bismuth nanoparticles were injected into two separate slim tubes packed with glass beads. The 30 cm long and 0.4318 cm inner diameter polypropylene tubes were packed with glass beads (Glasperlen 1 mm in diameter from B. Braun Biotech International) and fitted with screens and valves at each end. A polypropylene slim tube is pictured in Figure 3.7A. The proof of concept of passing nanoparticles through porous media had been established for a small core but not for longer paths approaching those encountered in a subsurface reservoir. The transport and recovery of nanoparticles through a longer flow path was investigated by passing the silica nanoparticles through a 1000 cm long and 0.4318 cm inner diameter slim tube packed with sand. The polypropylene tube was packed with sand of 1 mm maximum diameter and fitted with filter paper, screens, and valves at each end. This longer slim tube can be seen in Figure 3.7B.

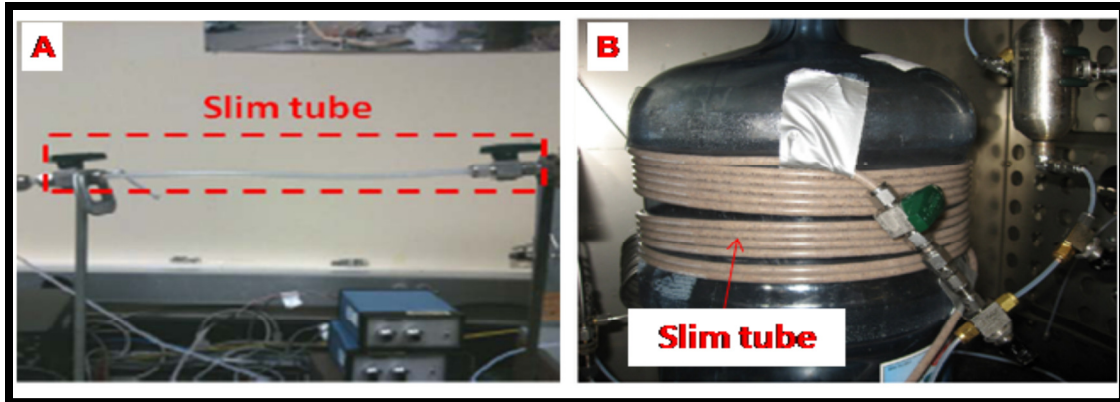


Figure 3.7: Polypropylene slim tubes (A) 30 cm long packed with glass beads, (B) 1000 cm long packed with sand.

A summary of slim tube dimensions, porosity, permeability and pore volume calculations can be found in Table 3.2. The pore volume, porosity and permeability measurement procedures were very similar to those outlined in Section 3.3.2 for rock core samples. When required, the diaphragm of the pressure transducers was replaced based on the pressure range used during the experiment. All other equipment was the same as those used during rock cores characterization experiments (i.e. water pump, balance etc...). The gas permeability was measured only for the long sand-packed tube, but not the short glass bead packed tubes. Darcy's law of horizontal flow for compressible flow (Equation 3.6) was applied and Klinkenberg effect was demonstrated (Figure 3.8).

The sand-packed tube was saturated initially by evacuating the system for at least 4 hours under vacuum below 100 millitorr. The weight of the water, of known density, displaced inside the system was measured using a balance. The pore volume of the tube was then determined by discounting the dead volume of connecting lines from the total volume of displaced water, and thus the porosity was calculated. The water permeability of the sand and glass bead packed tubes was measured. Darcy's law of incompressible fluid for horizontal flow (Equation 3.10) was used to calculate the water permeability. The validity of this equation in this measurement was confirmed by the linear relationship between the pressure drop and the water flow rates (Figure 3.9). This was only verified for the sand-packed tube.

CHAPTER 3. PRELIMINARY EXPERIMENTATION WITH INJECTION OF NANOMATERIALS INTO POROUS ROCKS

Table 3.2: Slim tube characterization data

<i>Property</i>	<i>Tube I</i>	<i>Tube II</i>	<i>Tube III</i>
	<i>SiO₂</i>	<i>Fe₂O₃</i>	<i>Sn-Bi</i>
<i>d (cm)</i>	0.4318	0.4318	0.4318
<i>l (cm)</i>	1000	30	30
<i>Φ_{sat} (%)</i>	24.2	48	58
<i>k_{gas} (md)</i>	50.2	N/A	N/A
<i>k_{eq} (md)</i>	40.1	N/A	N/A
<i>k_w (md)</i>	49.9	19	18.1
<i>PV (cm³)</i>	35.5	2.6	2.6

^a*d* and *l* are tube diameter and length, respectively, *Φ_{sat}* is porosity by resaturation method, *k_{gas}*, *k_{eq}* and *k_w* are the gas, liquid equivalent and water permeability, respectively, *PV* is pore volume and N/A indicates that measurement was not performed.

CHAPTER 3. PRELIMINARY EXPERIMENTATION WITH INJECTION OF NANOMATERIALS INTO POROUS ROCKS

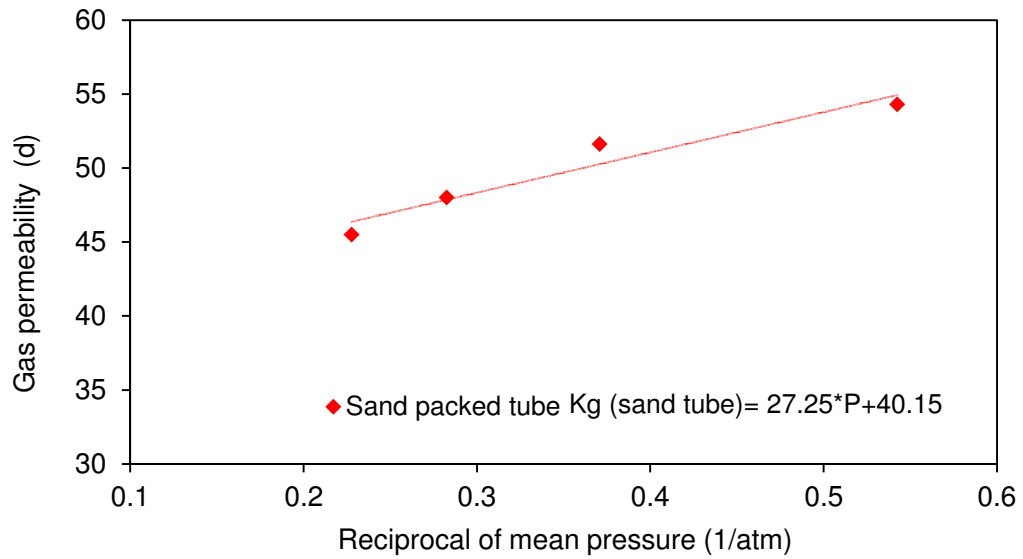


Figure 3.8: Gas permeability versus the reciprocal of mean pressure of long slim tube packed with sand used during silica nanoparticle injection.

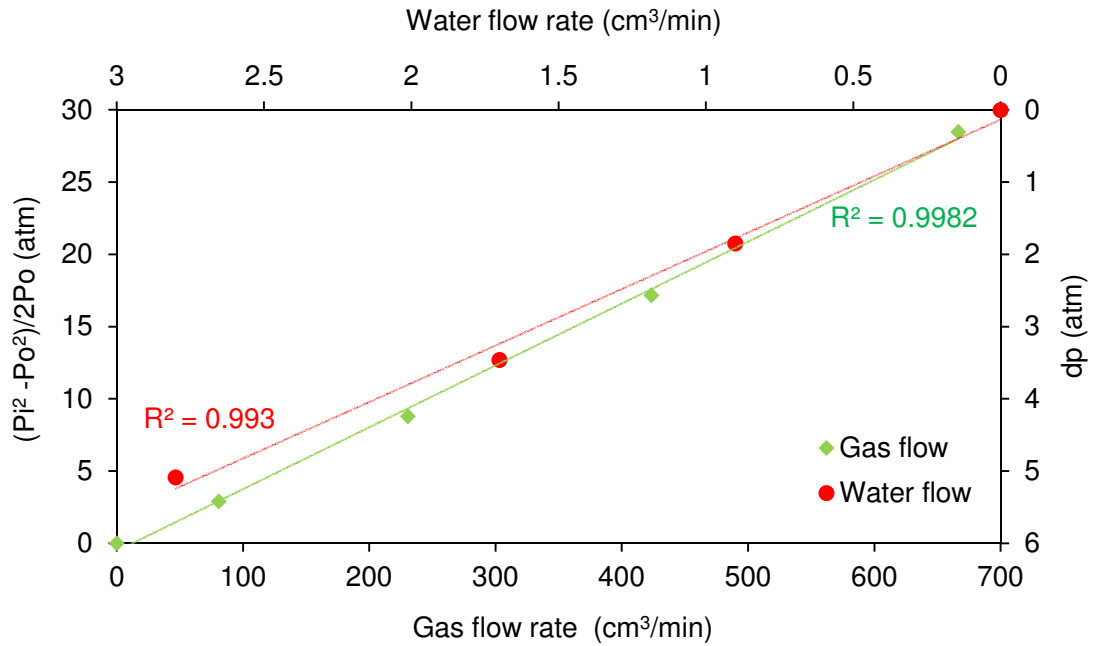


Figure 3.9: Steady-state, single-phase pressure drop versus gas and water flow rates for the long sand-packed tube.

3.4 Nanofluid injection experiments

Preliminary testing with the injection of various nanofluid suspensions was carried out to investigate the viability of transporting nanomaterials of different shapes and sizes through a porous medium. Berea and greywacke sandstones, sand or glass beads packed tubes, were used in the nanofluid injection experiments. The injection process and sampling strategies in all experiments were similar, however, they differed in some aspects such as total pore volume injected, flow rates and sampling frequency. A summary of the injection experiment flow parameters can be seen in Table 3.3.

Table 3.3: Summary of flow experiments parameters^a

Nanoparticle	Flow medium	q (cm^3/min)	u (cm/min)	v (cm/min)	V_{NP} (cm^3)	Post PV (cm^3)
	<i>Berea I</i>	1.0	0.08	0.48	2PV	4.88
SiO_2	<i>Tube I</i>	1.8	12.29	50.78	0.2PV	19.40
	<i>Greywacke</i>	6.98×10^{-4}	6.47×10^{-5}	1.60×10^{-3}	2PV	8.30
$AgNW$	<i>Berea II</i>	1.0	0.08	0.48	2PV	30.08
Ag	<i>Berea III</i>	1.0	0.08	0.52	0.25PV	3.81
	<i>Berea III^b</i>	2.0	0.18	0.01	0.4PV	3.29
Fe_2O_3	<i>Tube II</i>	0.1	0.68	1.42	0.4PV	4.60
	<i>Berea IV</i>	1.0	0.09	0.50	0.3PV	12.82
$Sn-Bi$	<i>Tube III</i>	0.5	3.41	5.88	1PV	7.11

^aHere q is the volumetric flow rate, u is Darcy velocity, v is the pore velocity, V_{NP} is the injected nanofluid volume and post PV is the volume of water injected following the injection of nanofluid. PV denotes pore volume.

CHAPTER 3. PRELIMINARY EXPERIMENTATION WITH INJECTION OF NANOMATERIALS INTO POROUS ROCKS

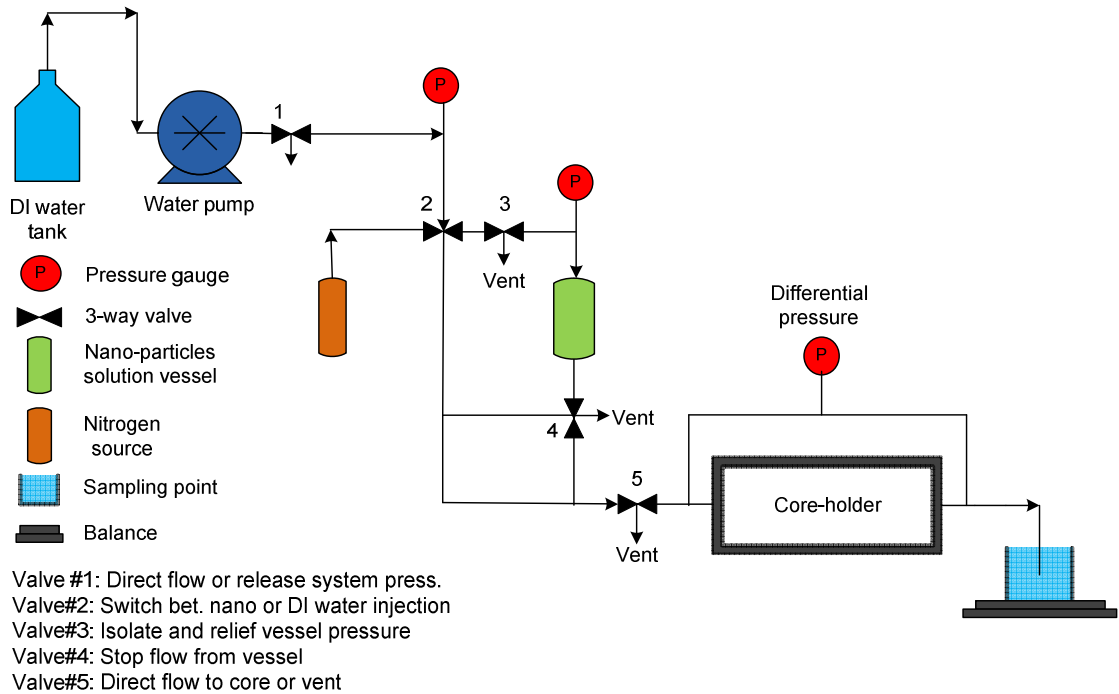


Figure 3.10: Experimental apparatus for nanofluid injection into (a) core samples, (b) 10 m sand packed tube and (c) 30 cm glass bead packed tube.

A schematic of the experimental apparatus is shown in Figure 3.10. Note that equipment used during the nanofluid injection experiments was the same as those used during permeability experiments. Nanofluid solution was contained in a pressure vessel downstream of the water pump. The nanofluid was injected into the core with the aid of nitrogen pressure. A water pump was used during the post injection of deionized water. The rock cores were inserted into the core-holder to hold them in place during injection. As needed, the core-holder was replaced by sand or glass bead packed tubes. The configuration also allowed for injection of particle-free water, without interrupting the flow.

Prior to the injection of the nanofluids, the cores were preflushed with pure water to displace rock fines and debris. The nanofluid injection sequence was similar to the process suggested by Kanj et al. (2009). The sequence involved the injection of a fraction of a pore volume of nanofluid followed by a continuous injection of deionized water. All

CHAPTER 3. PRELIMINARY EXPERIMENTATION WITH INJECTION OF NANOMATERIALS INTO POROUS ROCKS

nanofluid suspensions were thoroughly sonicated prior to injection using Branson 2510 Sonicator. The pore volume was determined as outlined in Section 3.3.2. Depending on the experiment, several pore volumes of deionized water were injected while the effluent samples were collected. The total time of the experiment, flow rates and frequency of sampling were also experiment dependent. For instance, the total time of the greywacke injection experiment was approximately 20 days. The injection was at the rate of one cm^3/day at differential pressure of about 700 psig. The injection pressure was kept at that level due to the limitation of the maximum allowable confining pressure of the core-holder (i.e. 1000 psig).

Sampling immediately following the injection was very frequent. As time progressed, the sampling frequency was reduced. There was no harm in taking samples more frequently than necessary as time required to collect the samples was not an issue. Not all these samples needed to be analyzed. If the infrequent samples had not indicated the trend of the returning nanoparticles, more details could still be obtained by analyzing the samples in between. If the samples had not been taken frequently enough, there would be no way to recover the results without repeating the experiment.

3.5 Results

This section provides the results of the nanofluid injection experiments conducted on Berea, greywacke core samples and slim tubes with different nanofluid suspensions. We investigated the effect of the particle size and/or size distribution, shape, and surface charge on their transport through various porous media. Hypotheses made in relation to the specific experiment objective were also verified as applicable. The effect of the shape of the particles was explored through the injection of Ag nanowires. The results were supported by injecting the same material of identical surface characteristics but with different shape (i.e., spherical Ag nanoparticles). The surface charge was studied by injecting uncoated and surfactant-coated hematite nanorice. The affinity of nanoparticles to flow media and the influence of particle size were explored through the injection of

Sn-Bi alloy nanoparticles. The injection of silica nanoparticles was aimed at testing the feasibility of transporting nanospheres through the pores of the greywacke rock core as it represents the kind of tight rocks found in geothermal reservoirs. The experiment was intended to bracket the size limits of the nanoparticles that may be able to flow through the pores. Note that the influence of flow velocity, solution pH, and ionic strength was not part of these experiments.

Generally, the objective of the experiment, the characterizations of the original nanofluid injected, effluent samples collected and cross-sections of the rock matrix are presented and discussed in the following sections.

3.5.1 Silver nanowire (AgNW) injection experiment results

The objective of this experiment was to investigate the transport of rod-like nanoparticles through reservoir rock. Specifically, we explored the implication that the shape of the nanoparticles might impact their recovery. The injected Ag nanowires had diameters in the range of 0.05 to 0.10 μm and lengths in the range of 5 to 10 μm . Their surface charge was negative (i.e., the same as the sandstone).

Ag nanowires were injected through the Berea sandstone core; however, they were not detected in the effluent. The effluent samples were analyzed and/or characterized using UV-vis spectrophotometry. Figure 3.11 shows the optical density measurements of the influent and selected effluent sample collected during injection. The influent had an optical signature (red curve) similar to typical Ag nanowires reported in the literature (Sun et al. 2002). The optical density of the selected effluent sample did not show any sign of Ag nanowires. The spectrum of all effluent samples exhibited the behavior of pure water (flat lines). Note that effluent sample curves contain no further details than being flat lines, indicating that these effluent samples were free of any Ag nanowires. This suggested that the Ag nanowires were not transported, but rather were trapped within the pore network of the sandstone core, most likely at the inlet pore throats.

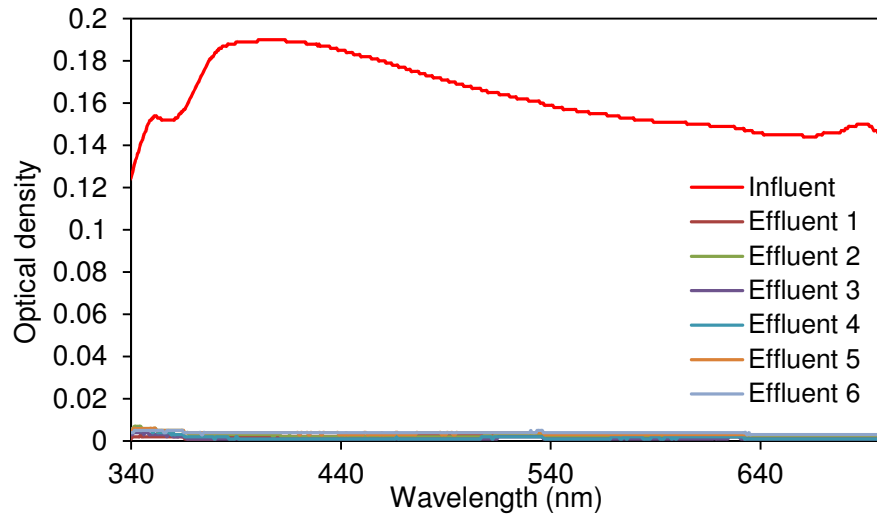


Figure 3.11: Optical density of Ag nanowires influent (red curve) and selected effluent samples. The optical density of the effluent samples presented as flat lines, indicating these samples are free of Ag nanowires.

The drop in the matrix permeability, as depicted in Figure 3.12, also suggested that some flow paths were blocked by the Ag nanowires. There was a drop in the permeability from approximately 94 to 51 md, or a reduction of approximately 45%. This drop began during the injection of the nanofluid and stabilized through the post-injection of the fifth pore volume. The core was backflushed by the injection of 11 pore volumes of pure water. The optical densities of representative backflushing samples of every pore volume were measured (not shown here). All exhibited the behavior of pure water, similar to that depicted in Figure 3.11, indicating that the nanowires remained in the core and were not backflushed out.

To further investigate the hypothesis regarding the entrapment of the Ag nanowires, a 3-mm slice was cut at the inlet section of the core. The core was then dried in the furnace at 80 °C for 24 hours. The permeability was remeasured to assess the effect of the nanowires on the core after removing the few millimeters slice. The permeability was restored to its original value by cutting off that slice. Figure 3.13 shows a comparison between the two measurements. The change in the gas permeability was within 2.7 % of original permeability measurement prior to nanofluid injection.

CHAPTER 3. PRELIMINARY EXPERIMENTATION WITH INJECTION OF NANOMATERIALS INTO POROUS ROCKS

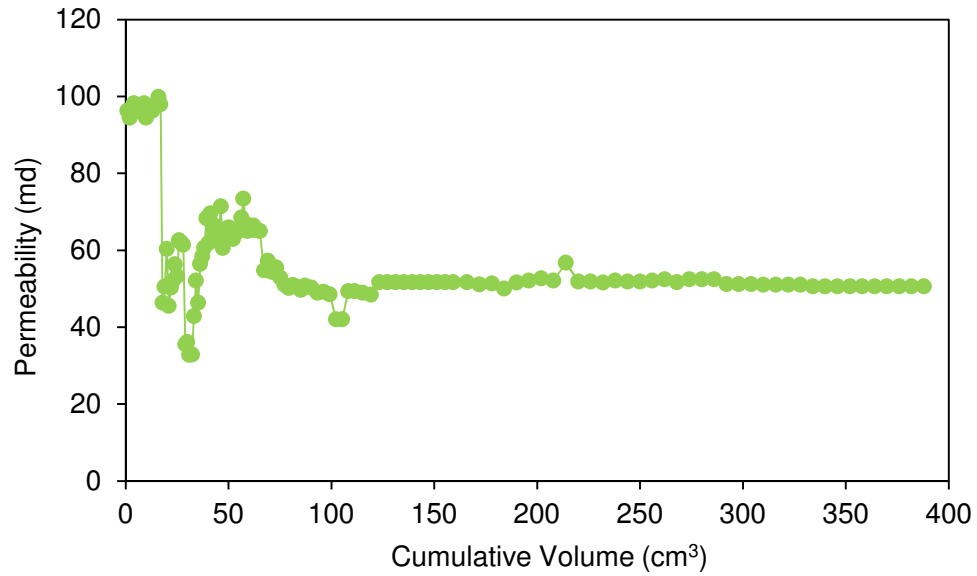


Figure 3.12: Permeability measurement during the Ag nanowires injection experiment. Permeability dropped during the injection of the nanofluid until it stabilized (plateau) at approximately 45% of initial permeability.

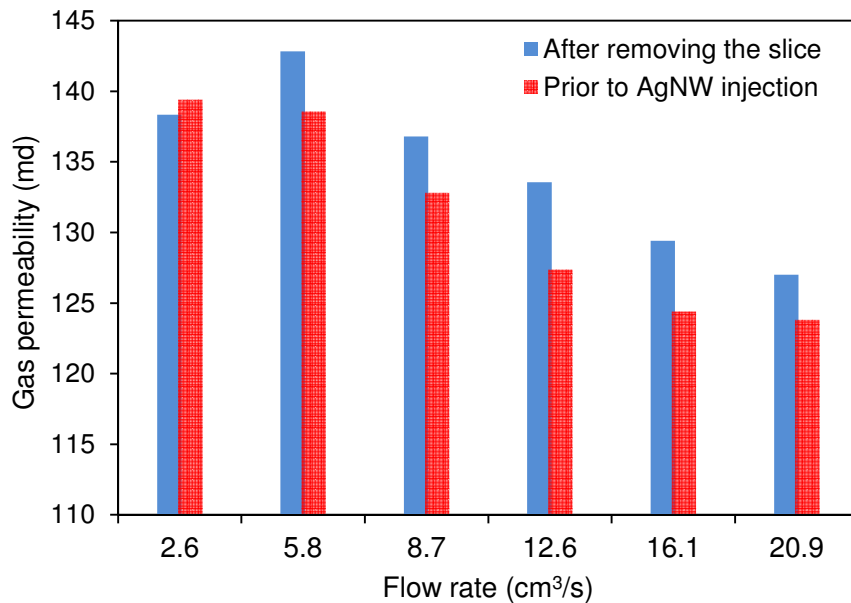


Figure 3.13: Gas permeability comparison before and after cutting the slice at the inlet.

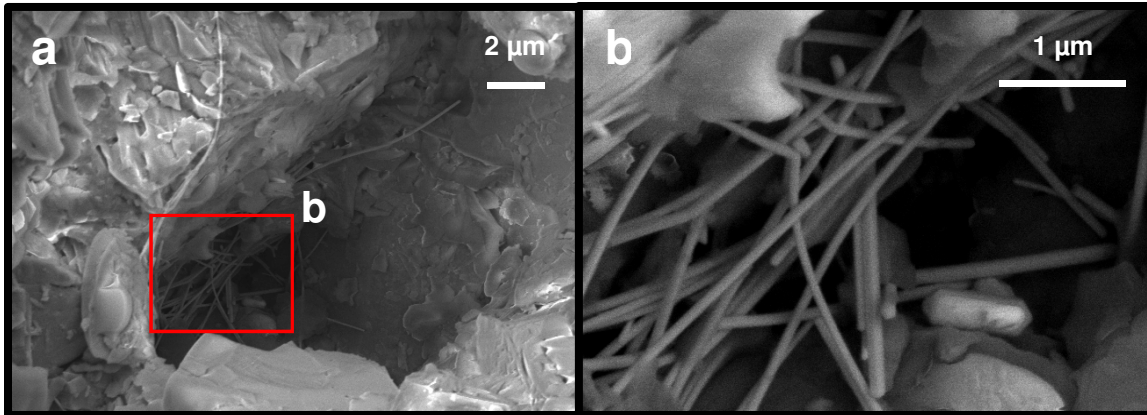


Figure 3.14: SEM imaging on the front side of the slice at different magnifications post the injection of AgNW into Berea II sandstone. The micrographs show the nanowires meshing and plugging at the pores.

The gas and equivalent liquid permeabilities were restored by cutting off the slice at the inlet. Therefore, it was highly suggestive that the nanowires were trapped at the inlet within the removed slice. SEM imaging confirmed this unambiguously. The analysis was performed on the front and back sides of the slice. Figure 3.14 shows SEM images of the front side. The Ag nanowires were clearly trapped at the front side. SEM micrographs (not shown) of the back side of the slice showed no sign of nanowires. This demonstrated that the nanowires did not pass through the pores of the core even for a few millimeters. It has been concluded that their geometry (longitudinal length) imposed constraint on their transport through the core, and thus rod-like nanoparticle of large aspect ratio (length to diameter ratio) may not be suitable as temperature nanosensors. To verify this hypothesis, an injection of spherical Ag nanoparticles into the same Berea sandstone (after removing the slice) was conducted.

3.5.2 Silver (Ag) nanosphere characterization and injection experiment results

The injection of silver nanospheres was carried out to investigate their transport through Berea sandstone. The retention of silver nanowires was mainly attributed to their shape.

Silver nanospheres of same material as the nanowires, but different shape (i.e. spherically shaped) were tested to explore this hypothesis further.

3.5.2.1 Ag nanoparticle characterization

The silver nanoparticles were synthesized by Clement Levard in the Department of Geological and Environmental Sciences at Stanford University. Silver nanoparticles were characterized in terms of size, surface charge (zeta potential), light absorption and pH levels using SEM imaging, zeta potential analysis, UV-vis spectrophotometry and pH meter, respectively. The spherically-shaped Ag nanoparticle size was approximately 0.04 μm , ± 0.01 (Figure 3.15), with an average zeta potential of approximately negative 17 mV at pH of 7.9. The nanoparticle suspension concentration used in the injection experiment was 0.5 mg/ml. Both the particles and the sandstone are of like charge. The zeta potential for Berea sandstone saturated with pure water (ionic strength of 10^{-6}) was assumed to be -76.3 mV, as suggested by Alkafeef et al. (1999). The Ag nanoparticle properties are summarized in Table 3.3. Pore-size-distribution measurement using mercury intrusion (Figure 3.1) showed that Berea sandstone has pore sizes in the range of 0.1 to 50 μm . Note that the size of these nanoparticles was within the size of the pore spaces available for their flow. Because the goal was to determine if the shape of the nanoparticles would affect their flow, the main difference over the Ag nanowires was the shape of the particles. UV-visible spectrophotometry was used to measure the absorption of the silver nanoparticles in the effluent samples and hence their concentrations. This is an essential step as it enables us to construct the return curve of concentrations verses volume injected. Several dilutions were prepared from the original silver nanofluid. The absorbance spectra were then measured at room temperature using a Shimadzu UV-1700 double-beam spectrophotometer with a 12 mm square polystyrene cuvette. All samples had been sonicated prior to analysis to disperse the particles. The optical (absorbance) signatures and calibration curve of the diluted silver nanofluid samples are shown in Figure 3.16. There is a linear relationship between the optical density and concentration indicating the applicability of Beer-Lambert Law.

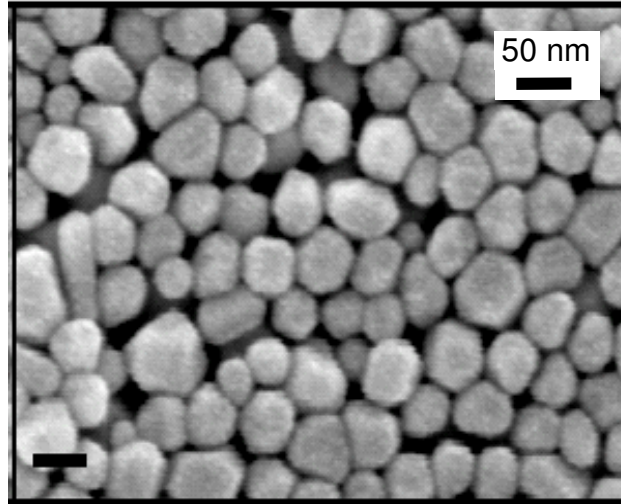


Figure 3.15: SEM image of the silver nanoparticles. (Levard, personal communication)

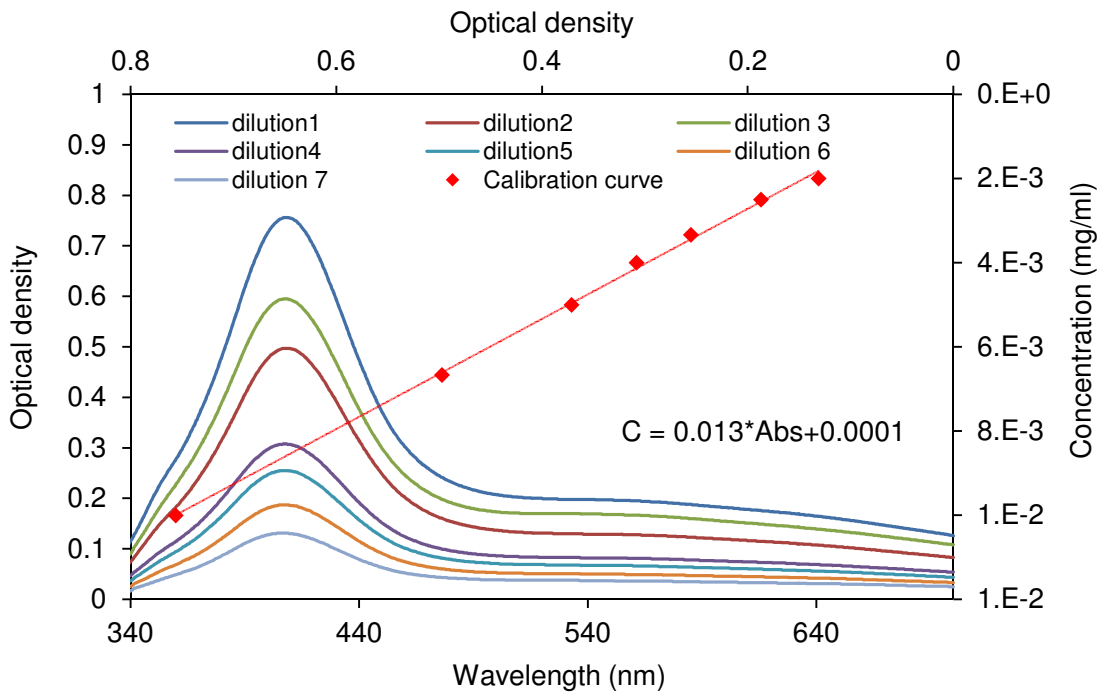


Figure 3.16: Optical density and calibration curve of diluted silver nanofluids of known concentrations. The maximum absorbance (peak) was at wavelength of 408 nm. Note the linearity of the calibration curve, indicating the applicability of Beer-Lambert Law. The calibration equation is showing in the graph. The secondary horizontal axis of optical density is associated with the secondary vertical axis of concentration.

3.5.2.2 Ag nanoparticle injection experiment results

The Ag nanoparticles were transported through the pore spaces of the rock and were detected in the effluents as seen in the micrograph in Figure 3.17b. The recovery of the silver nanoparticles can be observed visually (Figure 3.17a). Cloudy samples are concentrated with silver nanoparticles compared to transparent samples. It could also be seen that the nanoparticles were recovered following the post-injection of about 30% of the first pore volume of pure water and produced continuously until the bulk of these particles were displaced through the second pore volume.

The production-history (return) curve of the Ag nanoparticles was estimated, as depicted in Figure 3.18. The first breakthrough of nanoparticles occurred at approximately 30% of the first post-injected pore volume. The first nanoparticle breakthrough is when the relative concentration of recovered particles to influent concentration is 0.01 (i.e. $C/C_o = 0.01$). The maximum relative concentration was about 0.082. The recovered Ag nanoparticles C/C_o concentration values fell below 0.01 during the second injected pore volume, with moderate decline in concentration forming smooth and steady tail. The mass recovery of nanoparticles was approximately 25%, calculated by integrating the area under the return curve.

Filtration theory (Equation 2.1) predicted a high collision probability ($\eta_0 < 0.825\%$) of nanoparticles with grains, mainly due to particle diffusion. The contribution of other filtration mechanisms, interception and gravitational sedimentation, was negligible. Analysis data is summarized in Table 3.4. The Ag nanoparticles have the same density as the suspension fluid (water), which suggested gravity settling of particles is not likely. This can be realized by examining Equation 2.11, where identical densities of nanoparticles and suspension fluid would lead to zero settling or buoyancy scenario. Interception of particles in the submicron size range is not a significant transport mechanism.

CHAPTER 3. PRELIMINARY EXPERIMENTATION WITH INJECTION OF NANOMATERIALS INTO POROUS ROCKS

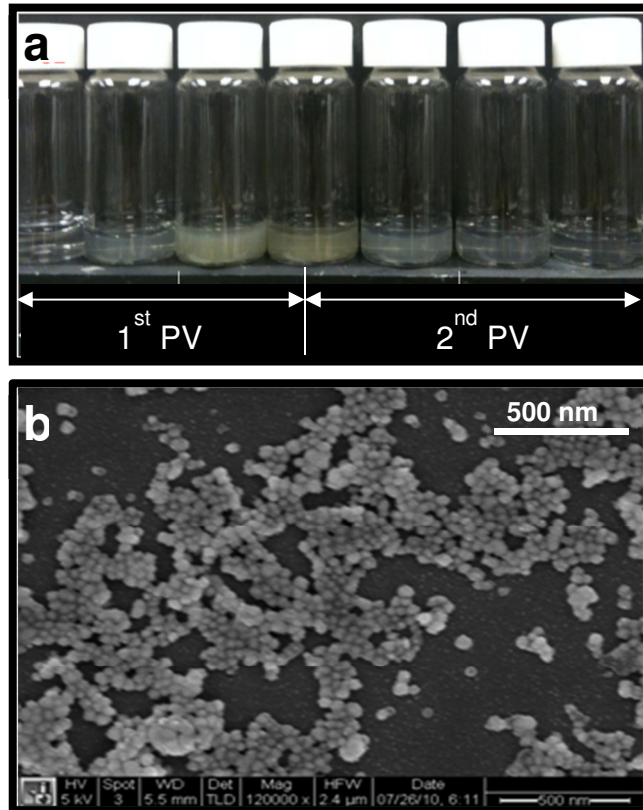


Figure 3.17: Silver nanoparticles detected at effluent (a) visually based on color (b) SEM image from the third post injected pore.

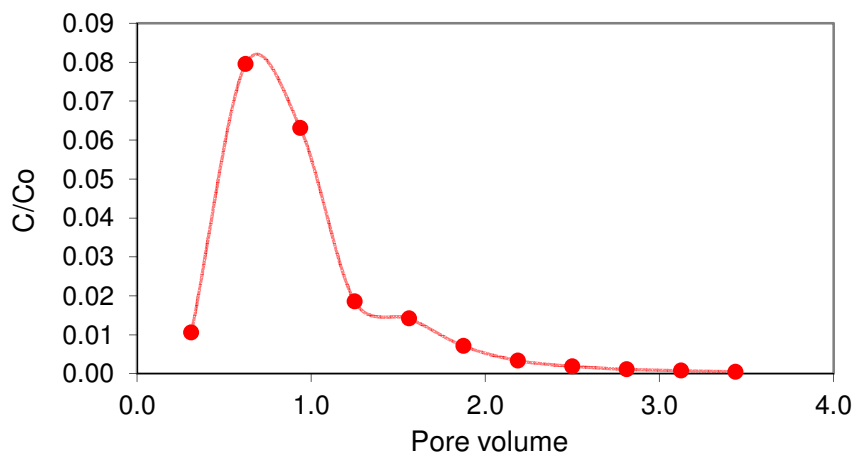


Figure 3.18: Production history (return curve) of silver nanoparticles.

CHAPTER 3. PRELIMINARY EXPERIMENTATION WITH INJECTION OF NANOMATERIALS INTO POROUS ROCKS

The dominance of transport by advection or diffusion can be estimated by comparing Peclet number (Pe) of tracers. Zvikelsky and Weisbrod (2006) evaluated the transport of particles and solutes through a fractured chalk rock sample. Peclet number of particles of the size range as Ag nanoparticles was in the order of 10^4 compared to that of solutes (in the order of 10^2), indicating that the transport within the fracture is primarily by advection. Based on flow conditions of Ag nanoparticles, Peclet number is about an order of magnitude lower (11.7) than that of solute in fracture, indicating that the transport within the pore network is diffusion-dominated. Peclet number of tracers flow through matrix to fracture should be lower since velocities in fracture are expected to be higher (higher Peclet number) than in matrix.

Table 3.4: Summary of Ag nanoparticle properties and analysis data^a

<i>Ag nanoparticle properties</i>				
d_p	ρ_p	c	ζ	pH
(nm)	(g/cm ³)	(mg/ml)	(mV)	
40 (± 10)	1.0	0.5	-17	7.9
<i>Analysis data</i>				
η_0	$\eta_{0,diff}$	α	η	Pe^b
(%)	(%)	(%)	(%)	
82.5	82.4	1.4	1.20	11.7

^a d_p is the particle diameter, ρ_p is the particle density, c is the Ag injected suspension concentration, ζ the particle zeta potential at measured pH. η_0 and $\eta_{0,diff}$ are the total single-collector contact efficiency and contact by diffusion mechanism, respectively (Equation 2.1), α is the attachment efficiency (Equation 2.4), η is the actual single-collector efficiency and Pe is Peclet number (Equation 2.10). Here, Hamaker constant for silver-water is 40×10^{-20} J (Israelachvili, 1992) at 21°C and average grain size for Berea sandstone of 150 μm (Churcher et al., 1991).

^bThe characteristic length used in Peclet number calculation was the average pore size of Berea sandstone (8.8 μm).

The low recovery was attributed to particle aggregation. The small particles are more susceptible to aggregation than larger ones. Large aggregates or clusters can be trapped physically at small pore throats. The low removal efficiency (Table 3.4) is because

CHAPTER 3. PRELIMINARY EXPERIMENTATION WITH INJECTION OF NANOMATERIALS INTO POROUS ROCKS

filtration theory does not account for particles removed by physical exclusion, phenomena observed by many investigators (e.g. Bradford et al., 2002). Estimation of total interaction energy between particles and rock surfaces (Fig. 3.19) indicated that the repulsive energy barrier is very shallow (below $6 k_B T$). Also, there exist attractive forces at the primary energy minima. Particles may attach to the pore walls and to each other at the primary energy minima. If particles collide with the pore walls, they may attach permanently, hence deposit within the pore space. Particles may also interact with among each other forming aggregates or clusters. Clusters moving through narrow pore throats will be excluded from the flow by physical entrapment because of their size and, thus, retained to a greater extent within the porous medium. Despite the modest recovery of these nanoparticles, it was clear that the shape was an important factor for their transport through the pores of the sandstone core (when compared to the silver nanowires). It was concluded that the mobility of rod-like silver nanoparticles was not feasible because of the physical constraint imposed by their shape.

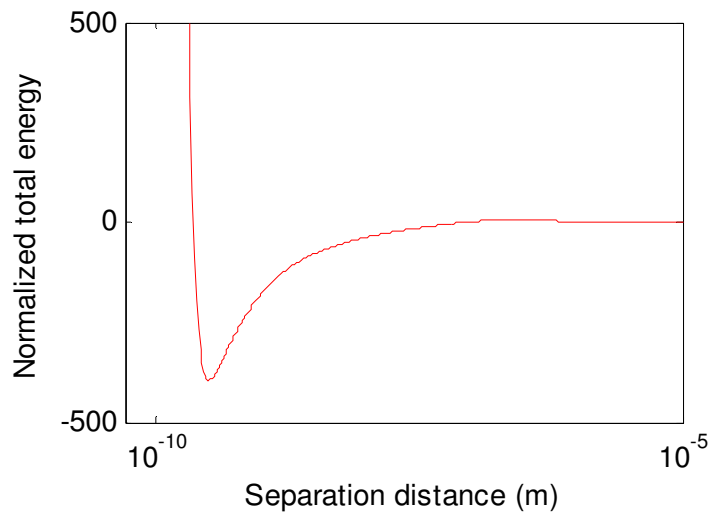


Figure 3.19: Total interaction energy between Ag nanoparticles and Berea core. The interaction energy is normalized to the thermal energy (Boltzmann constant and absolute temperature). The total interaction energy plot shows a shallow energy barrier below $6 k_B T$ with considerable attractive interaction at the primary energy minima.

3.5.3 Hematite (Fe₂O₃) nanorice characterization and injection experiment results

Injection of hematite nanorice was conducted to investigate their mobility within the pore spaces of Berea sandstone. The purpose was to investigate constraints imposed by the geometry and surface charge. The nanoparticle size was roughly 500 nm in length and 100 nm in diameter, resulting in an aspect ratio of 5:1. By comparison, the hematite nanorice was at least an order of magnitude shorter than the Ag nanowires injected previously. Thus, the nanorice was used to test the hypothesis made regarding the entrapment of the Ag nanowires because of their geometry (length).

The elongated shape of rod-shaped particles may cause them to have nonuniform surface potential (surface charge) that may result in clustering of the particles. Because hematite nanorice has a rod-like shape, it was used to investigate the effect of this issue by coating the hematite with different materials to alter their surface charges.

3.5.3.1 Hematite and coated hematite nanorice characterization

Hematite nanorice was synthesized by Stephen Connor and coated by Chong Liu in Material Science and Engineering at Stanford University. Coated and uncoated hematite were characterized in terms of size, surface charge (zeta potential) and pH using SEM imaging, zeta potential analysis and pH meter, respectively. The uncoated hematite size was roughly 0.50 μm in length and 0.10 μm in diameter (Figure 3.20), with an average zeta potential of approximately positive 59.3 mV at pH of 3.3. Summary of coated and uncoated hematite nanorice properties is provided in Table 3.5.

Note that there were three identical hematite samples each coated with different material. It was evident from the surface charge measurements that the coating materials have altered the surface charge of the original iron oxide nanorice. The original (uncoated) hematite nanorice carries a high positive charge of 59.3 mV with low pH of 3.3 compared to the samples coated with silica (negative 32.4 mV and pH of 5.56) and PVP surfactant

CHAPTER 3. PRELIMINARY EXPERIMENTATION WITH INJECTION OF NANOMATERIALS INTO POROUS ROCKS

(negative 9.5 mV and pH of 4.82). The iron oxide coated with triethanolamine (TEA) surfactant resulted in moderately positive charge of about 18.9 mV.

Table 3.5: Summary of coated and uncoated hematite nanorice properties^a

<i>Property</i>	d_p (nm)	c (mg/ml)	ζ (mV)	pH
<i>Uncoated hematite</i>	500×100	N/A	+59.3	3.30
<i>TEM coated hematite</i>	500×100	0.25	+18.9	4.50
<i>PVP coated hematite</i>	500×100	0.25	-9.5	4.82
<i>SiO₂ coated hematite</i>	600×200 ^b	N/A	-32.4	5.56

^a d_p is the particle diameter, ρ is the particle density, c is the hematite injected suspension concentration, ζ the particle zeta potential at measured pH. N/A denotes that measurement was not conducted.

^b Coating with SiO₂ has resulted in growth in particle length and diameter by approximately 50 nm.

Berea sandstone (-76.3 mV) and glass beads used during the hematite injection were negatively charged. Hematite coated with TEA carries a positive charge, although lower in magnitude, it is similar to the charge of uncoated hematite (i.e. positive charge). Therefore, studying the charge effect of particle transport would not be possible with the TEA coated hematite.

From the surface charge point of view, the hematite nanorice coated with SiO₂ was a very attractive candidate. Such particles carry the highest negative surface charge among the three samples. SEM imaging (Figure 3.21) showed that the hematite nanorice have a uniform SiO₂ coating of about 0.05 μm . As a result, the size of the hematite nanorice has changed from 0.50 μm and 0.10 μm to 0.60 μm and 0.20 μm in length and diameter, respectively. It was also observed that the nanorice did not retain their original spindle-like shape with sharp edges.

CHAPTER 3. PRELIMINARY EXPERIMENTATION WITH INJECTION OF NANOMATERIALS INTO POROUS ROCKS

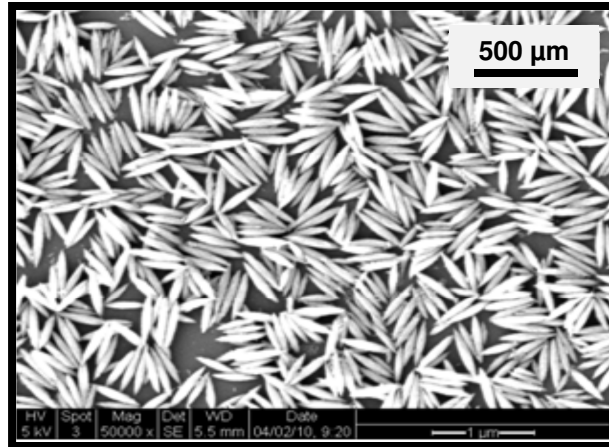


Figure 3.20: SEM image of uncoated hematite nanoparticles. Their shape bears remarkable resemblance to grains of rice.

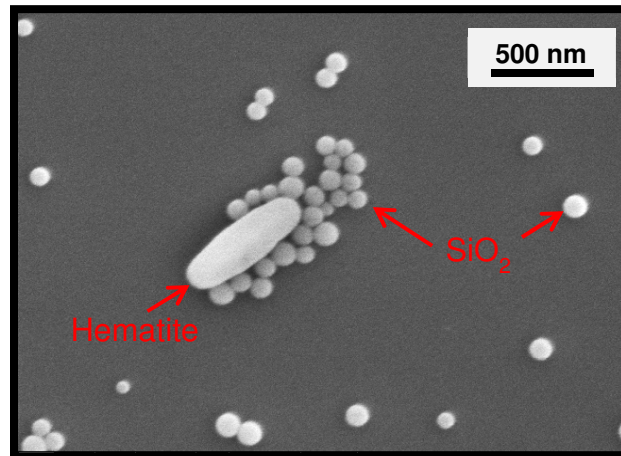


Figure 3.21: SEM image of SiO₂ coated hematite. Coated sample did not retain its spindle-like shape as a result of the 50 nm SiO₂ coat.

Further evaluation of the nanorice coated with SiO₂ showed that SiO₂ nanoparticles (about 100 nm in diameter) were dominating the sample. There were more SiO₂ nanoparticles than hematite. The existence of excess SiO₂ nanoparticles resulted from the coating process. Attempts to separate the SiO₂ nanoparticles were not successful. It was concluded that the hematite nanorice coated with SiO₂ and surfactant TEA were inappropriate for injection. However, hematite coated with surfactant PVP retained suitable characteristics in that it carried negative surface charge of 9.5 mV (Table 3.5).

CHAPTER 3. PRELIMINARY EXPERIMENTATION WITH INJECTION OF NANOMATERIALS INTO POROUS ROCKS

Similar to the experiments with Ag nanoparticles, UV-visible spectrophotometry was used to measure the absorption of the hematite nanorice in effluent samples and hence their concentrations using a calibration curve. The concentration of the hematite nanorice suspension was 0.25 g/cm^3 . The nanofluid was diluted 1 part of nanofluid to 2, 4, 9, 17, and 35 parts of ethanol. Dilutions were made using very accurate balance and pipette. The absorbance spectra were measured at room temperature using a Shimadzu UV-1700 double-beam spectrophotometer with a 12 mm square polystyrene cuvette. All samples had been sonicated prior to analysis to disperse the particles. The optical (absorbance) signatures of the diluted silver nanofluid samples and calibration curve are shown in Figure 3.22.

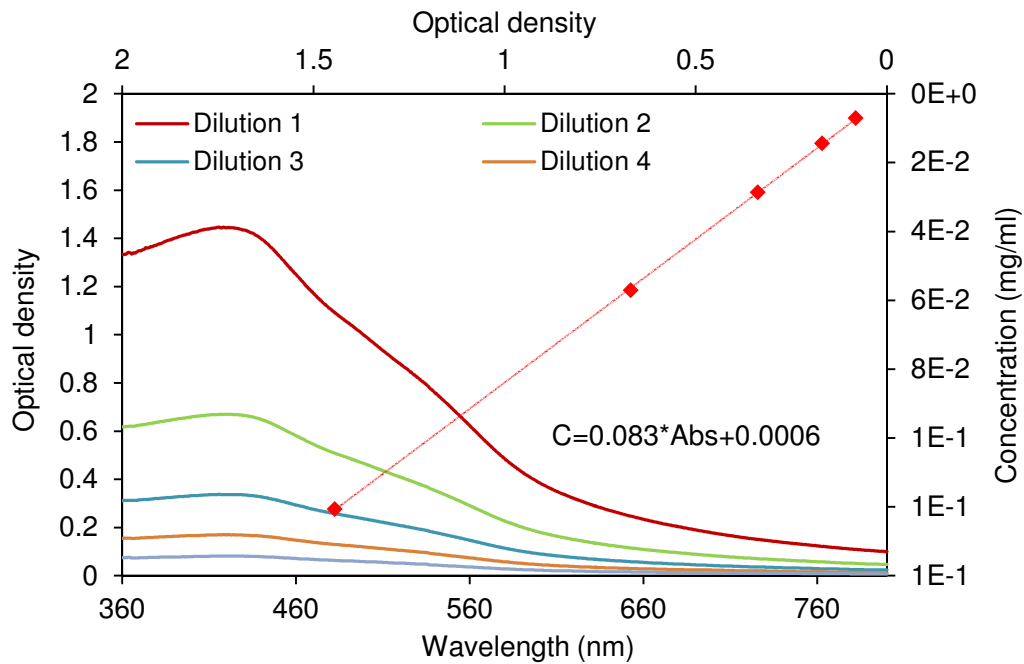


Figure 3.22: Optical density and calibration curve of diluted hematite suspension of known concentrations. The maximum absorbance (peak) was at wavelength of 420 nm. The calibration equation is showing in the graph. The secondary horizontal axis of optical density is associated with the secondary vertical axis of concentration.

3.5.3.2 Uncoated and PVP coated hematite injection experiment results

Uncoated hematite nanorice was injected into Berea sandstone to investigate the influence of surface charge incompatibility between particles and flow medium. Note that the uncoated hematite and Berea sandstone have a positive charge +59.3 mV and a negative charge -76.3 mV (Alkafeef et al., 1999), respectively.

DLS, UV-vis spectroscopy, and SEM were used to examine the effluent samples, however no hematite nanoparticles were detected. The hematite nanorice was, however, observed within the pores at the inlet side of the core, as illustrated by SEM micrographs in Figure 3.23a. Similar to the analysis of the Ag nanowires, a thin slice of the core at the inlet was cut and SEM imaging was performed on both sides. Hematite nanorice was observed on the front face (Figure 3.23a), but not on the back face (Figure 3.23b).

It was speculated that the entrapment of the nanorice resulted from interaction with core material, caused by either incompatibility of surface charges or chemical interaction of hematite with core constituents. The size of the nanorice (aspect ratio) and complexity of pore connectivity of Berea sandstone might have contributed to their entrapment; however, results of the nanorice injections into glass beads (explained later) suggested that surface-charge effect was dominating.

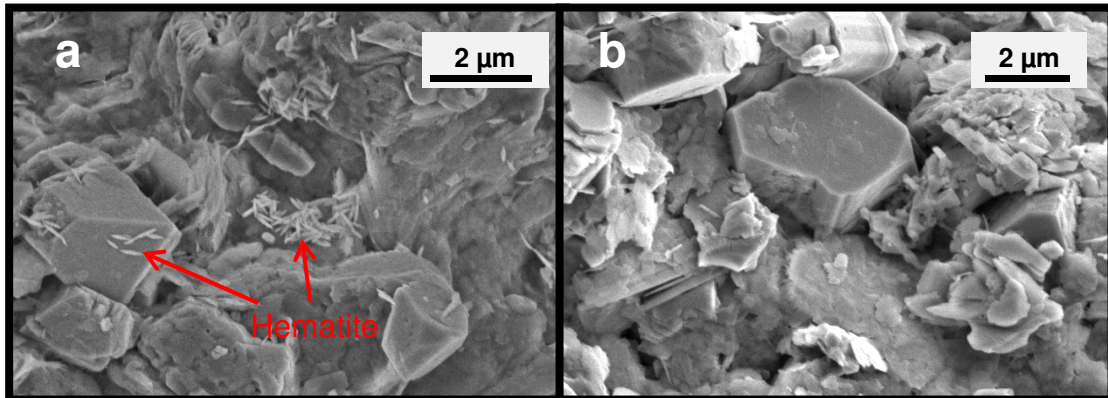


Figure 3.23: SEM imaging from within the pores of Berea sandstone at (a) front side, (b) back side (free of nanorice) of the slice at inlet side.

CHAPTER 3. PRELIMINARY EXPERIMENTATION WITH INJECTION OF NANOMATERIALS INTO POROUS ROCKS

Poulton and Raiswell (2005) reported that the natural spherical iron oxide (Fe_2O_3) nanoparticles (10–20 nm) in sediments tend to aggregate at the edges of clay grains, most likely because of their surface-charge characteristics. Tipping (1981) and Tipping and Cooke (1982) observed that iron oxides were negatively charged in fresh water, while the edge of clay has positive charge, which may explain the particle aggregation at that location. The micrographs in Figure 3.23 do not provide conclusive evidence of this interaction between the sandstone clays and the hematite nanorice. Nevertheless, this result suggested that there may be interaction between hematite nanorice and the sandstone core materials and/or among the nanorice in the form of particle aggregation. To investigate the interaction of hematite with core materials, the hematite nanorice was injected into a porous medium that consisted of a tube packed with glass beads (in the absence of core materials). The glass beads were negatively charged, so the incompatibility of surface charges still existed.

An extremely low particle count was observed using SEM imagery of several effluent samples at different post-injected pore volumes. The particles were found to be mostly aggregated on the surface or within the surface defects of the glass beads themselves (Figure 3.24). The optical density of the effluent samples could not be measured because of their low concentrations, and, thus, the concentration of hematite nanorice in the effluent relative to the concentration in the influent could not be determined. However, it was determined that in the absence of the clays (during injection into glass beads), the nanorice exhibited very low mobility and, thus, interaction with core materials was not the main factor behind the nanorice entrapment within pore spaces of Berea sandstone. Despite the fact that the pore connectivity in packed glass beads is less complex than that of Berea sandstone, and the pore sizes in packed glass beads are expected to be larger, the recovery of the hematite nanorice was negligible. This suggests that the entrapment of the nanorice was not caused by the particle size or aspect ratio. Therefore, it was concluded that the incompatibility of surface charges was limiting the transportation of the hematite nanorice through the sandstone and glass beads.

CHAPTER 3. PRELIMINARY EXPERIMENTATION WITH INJECTION OF NANOMATERIALS INTO POROUS ROCKS

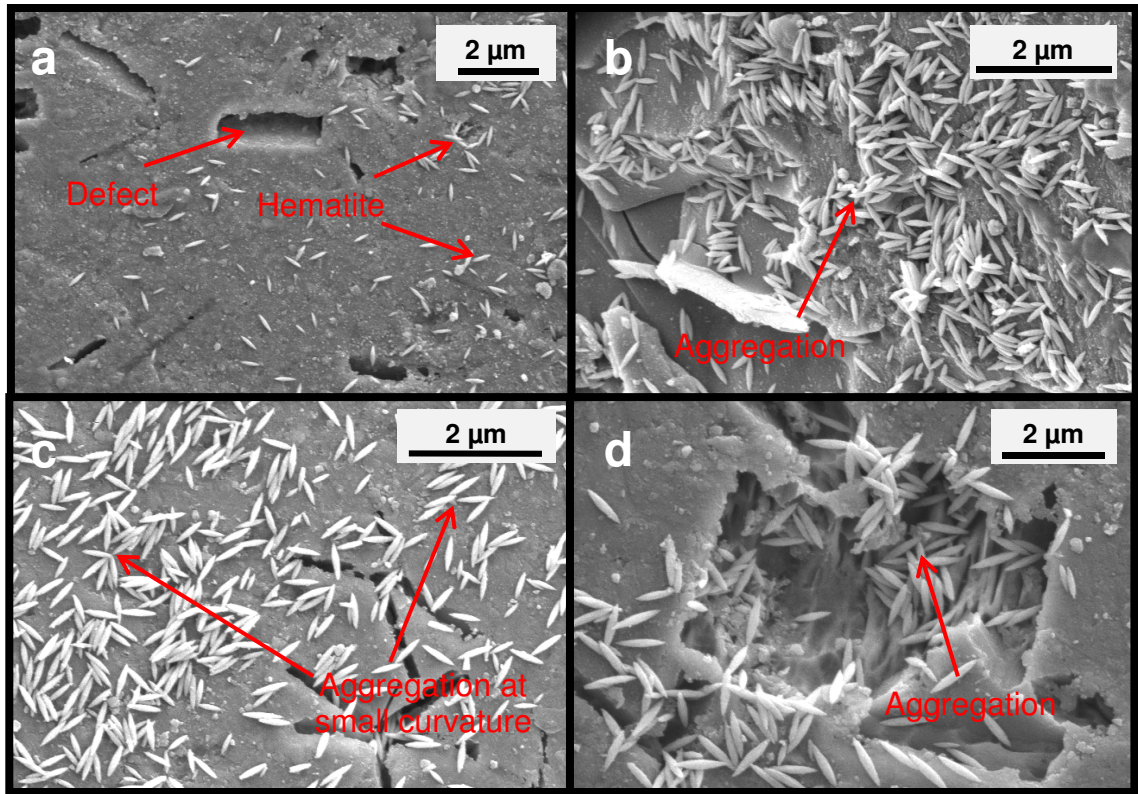


Figure 3.24: Hematite nanorice aggregation on the surface of glass beads at (a) and (b) inlet and (c) and (d) outlet side of the flow apparatus. Aggregation at the tip of the nanorice can be seen in image c.

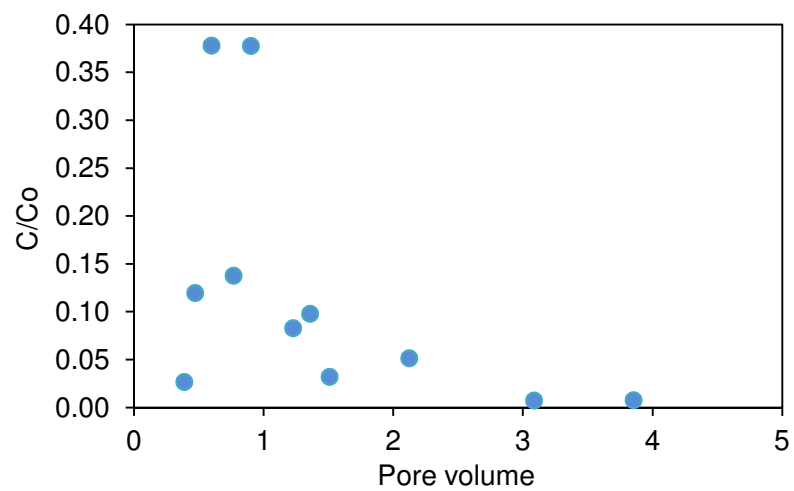


Figure 3.25: Production history (return) curve of PVP-coated hematite nanorice.

CHAPTER 3. PRELIMINARY EXPERIMENTATION WITH INJECTION OF NANOMATERIALS INTO POROUS ROCKS

To support this conclusion, the PVP-coated hematite nanorice was injected into a tube packed with glass beads. The PVP surfactant carried a negative charge of 9.5 mV with a pH of 4.8 compared with the uncoated nanorice (positive charge of 59.3 mV with a pH of 3.3). The coated nanorice was transported through the glass beads and was detected in the effluents. The first arrival of coated hematite was at about 39% of post-injected pore volume. The maximum relative concentration (C/C_0) was about 0.38, as depicted in Figure 3.25. The mass recovery of coated hematite nanorice amounted to approximately 23% of influent concentration. The hematite particles reached C/C_0 values lower than 0.1 following the first post-injected pore volume with fluctuating tail, which might indicate attachment and detachment of the hematite during transport. The relative concentration was then dropped to values below 0.007 subsequent to the third post-injected pore volume.

The low recovery was attributed to size exclusion (particle removal by physical entrapment because of size) caused by aggregation. As can be observed in Figure 3.24, the anisotropic hematite particles have a tendency to aggregate in clusters. Lu et al. (2002) reported that hematite nanorice often aggregate in large clusters as a result of anisotropic dipolar forces. This aggregation could limit the transport of the nanorice through pore networks, by bridging of the pores. Because nonspherical particles are anisotropic with respect to curvature, they are also anisotropic with respect to chemical potential, which is highest where the radius is smallest. Thus, nonspherical particles are more prone to aggregation than spherical ones with isotropic curvature. Furthermore, the aggregation can be expected to occur at high frequency where the radius of curvature is small to cover parts of the surface with high free energy. This can be observed in Figure 3.24c. As a result of aggregation, a large cluster forms. If the cluster flows along a streamline that passes through pore throats smaller than the size of the cluster, it will be excluded from the flow on the basis of its physical size.

While the recovery was not high, it was substantially higher than that achieved during the injection of the uncoated (positively charged) hematite, which confirms the influence of

surface charge on the transport of nanoparticles (the objective of these experiments). This also confirms that the recovery was less sensitive to the aspect ratio of hematite used in this study. If the hematite would be used as an inert core material of a core-shell nanosensor, its surface charge should be investigated carefully after attaching the shell material.

3.5.4 Tin-bismuth (Sn-Bi) alloy nanoparticle characterization and injection experiment results

The objective of these injection experiments was to study the flow mechanism of Sn-Bi nanoparticles through a porous medium. Ultimately, Sn-Bi alloy would be incorporated as a shell material in shell-core temperature nanotracers, thus its affinity to the flow medium was addressed. Because the Sn-Bi sample had a wide size distribution, the effect of polydispersity was also investigated. The nanoparticle suspensions were injected into a slim tube packed with glass beads and into a Berea sandstone core. The synthesized Sn-Bi nanoparticles were spherically shaped and negatively charged -30 mV, with a wide size distribution of particles from 0.05 to 0.60 μm as seen in the micrograph in (Figure 3.26). A summary of the Sn-Bi alloy nanoparticle properties and analysis data is provided in Table 3.5.

Sn-Bi nanoparticles were identified in a few effluent samples with very low concentrations. It was observed that only nanoparticles with diameters of 0.20 μm and smaller were transported within the pore spaces of the rock, as shown in the SEM image in Figure 3.27a. Note that the influent sample contained nanoparticles as large as 0.60 μm . It was speculated that larger particles (greater than 0.20 μm) were trapped at the inlet of the core. In fact, SEM imaging of the backflushed effluents showed that there was entrapment of various nanoparticle sizes, including the sizes greater than 0.20 μm (Fig. 9b). The rock filtered the injected nanofluid, allowing only certain particle sizes to flow through it. It should be noted that this is a qualitative analysis in which the determination of the relative number of particles recovered was not attempted.

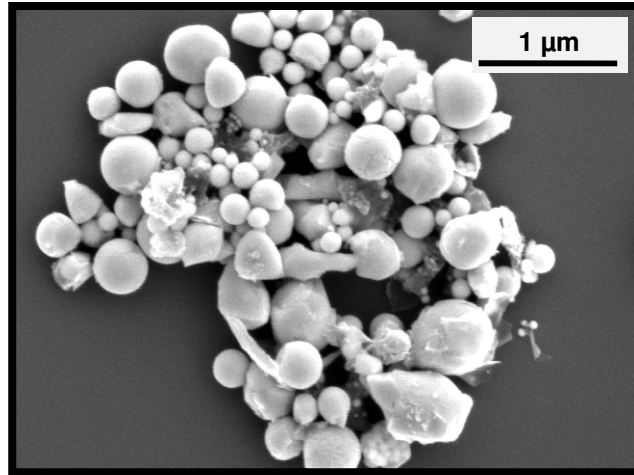


Figure 3.26: SEM image showing the polydispersity of the tin-bismuth nanoparticles. The nanoparticles range in size from 0.05 to 0.60 μm.

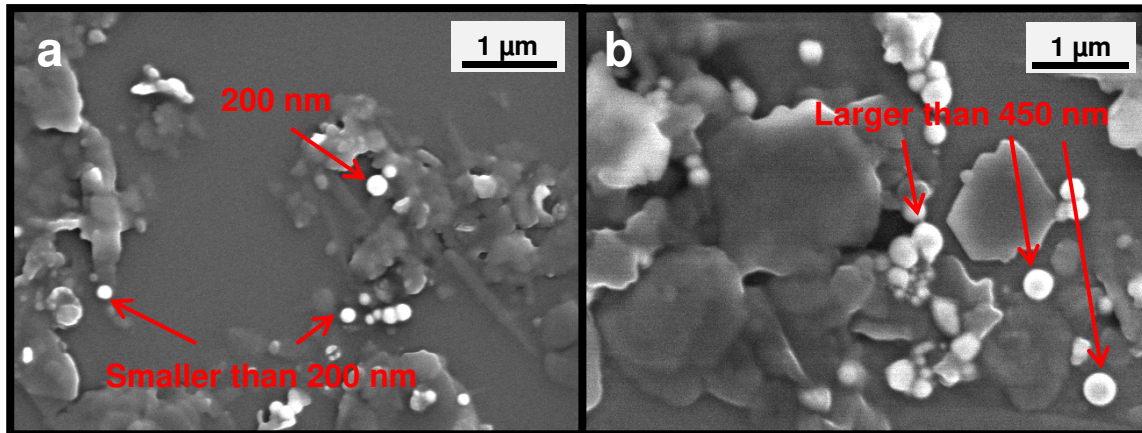


Figure 3.27: SEM imaging showing the Sn-Bi nanoparticles at the effluent during (a) injection and (b) backflushing of the Berea sandstone. Only particles smaller than 200 nm were transported through pore spaces, while larger particles were trapped at the inlet of the core and mobilized during backflushing.

The permeability measurements during the injection agreed with this finding. The permeability as a function of the injected volume is depicted in Figure 3.28. There was a sudden drop in permeability to approximately 55.3% of the original value (from 125.4 to 69.5 md), after which the permeability remained at that level during the first post-injected pore volume, indicating the partial plugging of the pores. Then, permeability started to increase until it reached a plateau at approximately 82.9% (103.9 md) of its value before

CHAPTER 3. PRELIMINARY EXPERIMENTATION WITH INJECTION OF NANOMATERIALS INTO POROUS ROCKS

the nanofluid injection. At this time, only nanoparticles of $0.20\ \mu\text{m}$ and smaller were observed in the effluent, using SEM imaging (Figure 3.27a). As mentioned earlier, the backflushing of the core remobilized some particles, and, as a result, the permeability of the rock improved slightly by 8% (i.e., a return to 90.8% or 113.6 md of its original value). However, permeability improvement (from 55.3 to 90.8% of original value) does not imply a good recovery of the injected nanoparticles. SEM imaging (Figure 3.29) of the rock pore spaces at the core inlet showed that many of these nanoparticles were deposited on the pore walls. Bridging and plugging of the Sn-Bi nanoparticles in the pore-throat entry was evident in those micrographs (Figure 3.30). Kanj et al. (2009) suggested that small particles at high concentrations might bridge across the pore throat. The authors also added that large particles could result in direct plugging of the pore entry. Both phenomena would impact the rock permeability negatively. Particles shown in Figure 3.30 could not be mobilized either by increasing the injection flow rate or by backflushing and were probably responsible for the permanent reduction in the rock permeability. The SEM analysis did not provide conclusive evidence of the mechanism of particle entrapment.

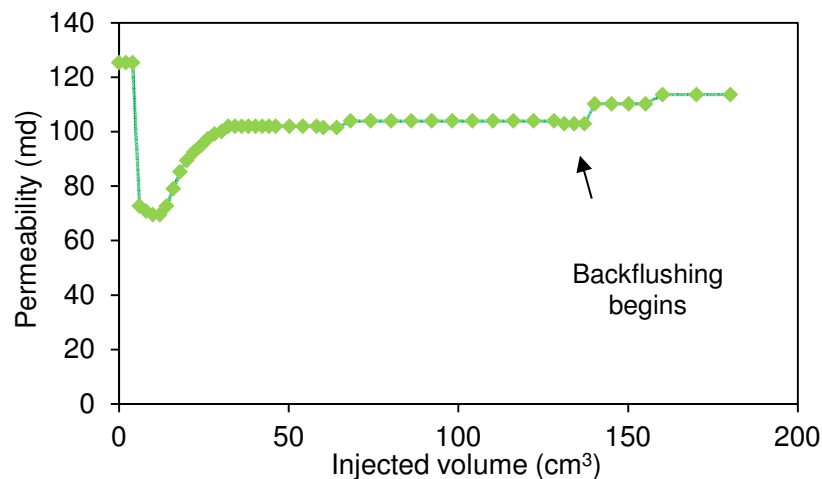


Figure 3.28: Permeability measurements during the injection of the Sn-Bi nanoparticles. The permeability value dropped significantly during the injection of the nanofluid, and then increased to plateau. Backflushing increased the permeability slightly.

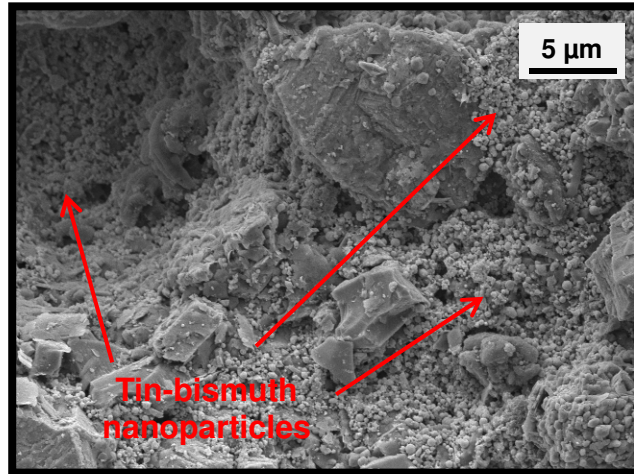


Figure 3.29: A micrograph from within the pore spaces at the inlet side of Berea sandstone used during the tin-bismuth injection. Nanoparticle entrapment is apparent. Sn-Bi nanoparticles covered most of the pore surfaces.

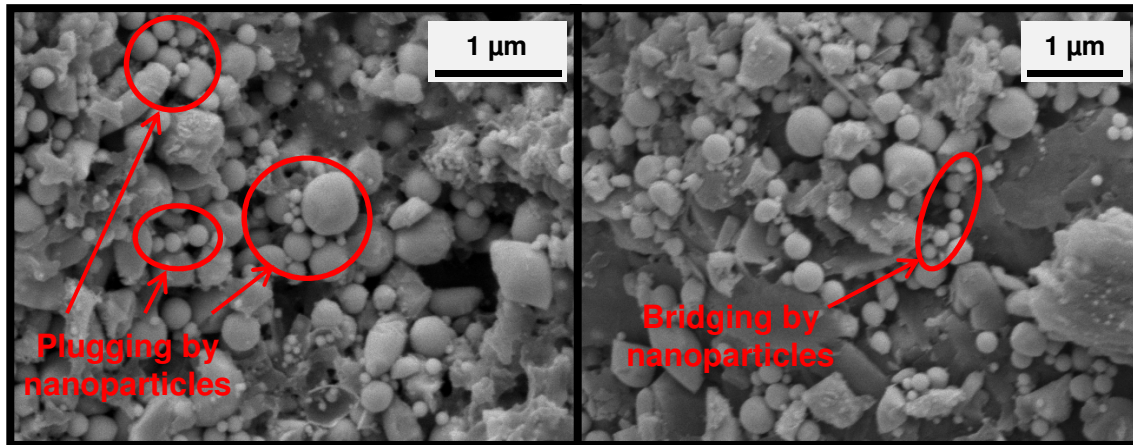


Figure 3.30: SEM images from within the pore spaces of the Berea sandstone. They demonstrate the bridging and plugging phenomena.

From filtration point of view, retention of the Sn-Bi nanoparticles by interception may not be significant, given their small size (the largest particle is 0.60 μm). Particle filtration by diffusion and gravity settling is more probable. Both mechanisms are dependent on particle size and fluid velocity. Smaller particles would diffuse more and settle less than larger particles. The dominance of diffusion based on particle size can be

CHAPTER 3. PRELIMINARY EXPERIMENTATION WITH INJECTION OF NANOMATERIALS INTO POROUS ROCKS

seen in calculated Peclet number (Table 3.6). There is an order of magnitude difference in Peclet number (83.31-999.70) for particle size in this range. Similarly, the settling velocity, and hence settling length, is more than two orders of magnitude higher for larger particles. The large contrast between the density of the Sn-Bi nanoparticles and suspension fluid (i.e. water) suggested that particles may settle due to gravity. This is particularly important for larger particles. The settling length of particles larger than 200 nm is in the range of 100.25 to 902.29 μm , based on the water pore velocity and resident time. The largest pore size is about 50 μm obtained pore size distribution measurement using mercury intrusion method (Figure 3.1). This suggested that particles larger than 200 nm settled immediately at the inlet pores. This is consistent with the SEM analysis and the fact that backflushing remobilized settled particles.

Table 3.6: Summary of Sn-Bi alloy nanoparticle properties and analysis data^a

<i>Sn-Bi alloy nanoparticle properties</i>				
d_p	ρ_p	c	ζ	pH
(nm)	(g/cm ³)	(mg/ml)	(mV)	
50-600	8.57	N/A	-30	7.2
<i>Analysis data</i>				
v	τ	U_s	L_s	Pe^b
(cm/min)	(min)	($\mu\text{m}/\text{min}$)	(μm)	
0.50	10.14	0.62-89.02 ^c	6.27-902.29 ^c	83.31-999.70 ^c

^a d_p is the particle diameter, ρ_p is the particle density, c is the Ag injected suspension concentration, ζ the particle zeta potential at measured pH, v the pore water velocity, τ is the resident time, U_s is settling velocity of particles (Equation 2.11), L_s is the settling length or distance (Equation 2.12) and Pe is Peclet number (Equation 2.10).

^bThe characteristic length used in Peclet number calculation was the average pore size of Berea sandstone (8.8 μm).

^cValues within this range depending on the particle size.

Physical exclusion or straining is unlikely to play a significant role in Sn-Bi nanoparticle deposition within the pore network. Previous investigators have suggested that straining is more important in porous media when the ratio of particle to the median grain size is

CHAPTER 3. PRELIMINARY EXPERIMENTATION WITH INJECTION OF NANOMATERIALS INTO POROUS ROCKS

larger than 0.05 (Sakthivadivel, 1966 and 1969), 0.2 (Herzig et al., 1970), 0.18 (Matthess and Pekdeger, 1985) and 0.008 (Xu et al., 2006). The Sn-Bi nanoparticle size range to median grain size (150 μm for Berea sandstone used in this study) was in the range of 0.0003 to 0.004. Based in published metrics, the straining of Sn-Bi nanoparticles in this size range is not probable. Based on the Sn-Bi nanoparticle injection, the observed ratio of particle to grain size, larger than which straining is expected, should be 0.0013 (0.20 μm particle divided by 150 μm grain diameter), because particles size of 0.20 μm and smaller were the only particles recovered.

As discussed later in Section 3.5.5, the spherical silica nanoparticles with narrow size distribution and surface charge compatible to that of the rock were transported successfully through the pore spaces of Berea sandstone. The Sn-Bi nanoparticles exhibit similar properties in terms of shape and surface charge (negatively charged), except that the Sn-Bi nanoparticles had a wider distribution of sizes between 0.05 to 0.60 μm . Thus, particle shape and surface charge should not impose flow constraints. The testing program suggested by Kanj et al. (2009) for nanoparticle flow in porous media emphasizes particle size, influent concentration, and affinity of particles to rock matrix. In the case of Sn-Bi injection, although the influent sample had wide distribution of particle sizes that might have introduced difficulty for their delivery, the Sn-Bi nanoparticles affinity and/or concentration may be the primary cause of their entrapment.

Further investigation of particle affinity to Berea sandstone was carried out by injecting the same sample with the same concentration into a slim tube packed with glass beads. This allowed testing the transport of the Sn-Bi nanoparticles in the absence of the core material. One pore volume of the nanofluid was injected at the rate of 0.5 cm^3/min , followed by continuous injection of pure water at the same rate. Several effluent samples were collected and analyzed by SEM imaging.

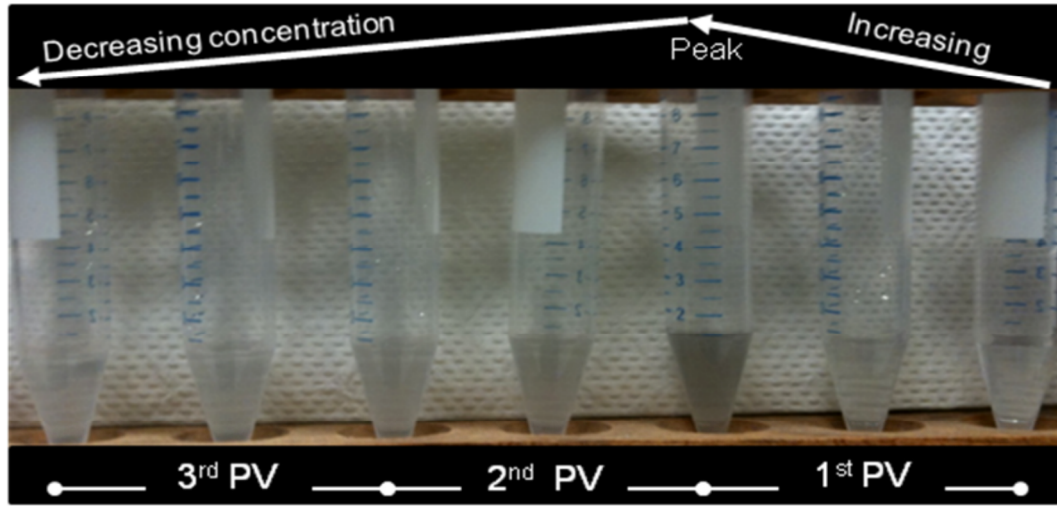


Figure 3.31: Visual characterization of effluent samples for their Sn-Bi nanoparticles content based on color.

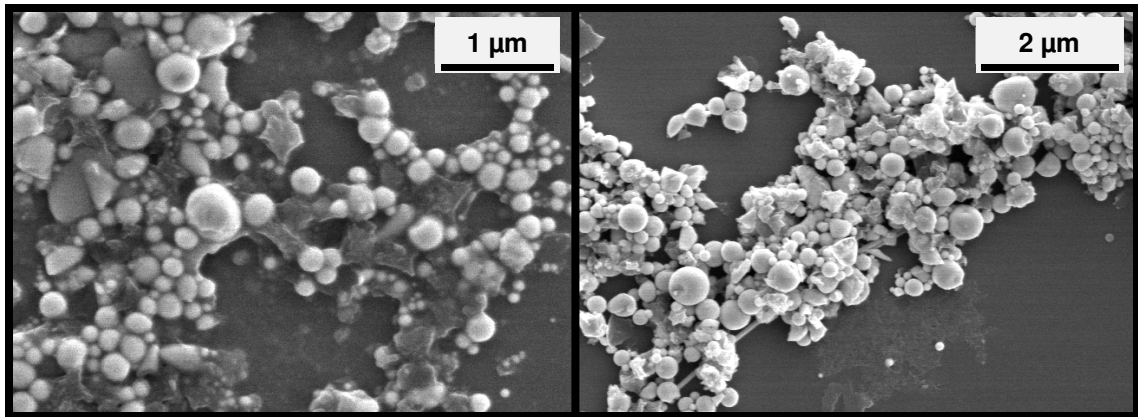


Figure 3.32: Micrographs of effluent collected during the injection of Sn-Bi nanoparticle into slim tube packed with glass beads.

It was found that the Sn-Bi nanoparticles of all sizes flowed through the slim tube. The increasing concentration of the nanoparticles in the effluent was observed visually through the injection of the first post-injected pore volume, as illustrated in Figure 3.31. SEM imaging confirmed this finding as depicted in Figure 3.32.

Thus, it was demonstrated that the spherically shaped Sn-Bi nanoparticles can be recovered following their injection into glass beads without being trapped within the flow

conduits, but not through the pore network of the rock (which has much smaller pores). This might be attributed to an affinity of these nanoparticles to the sandstone rock matrix and the wide size distribution imposing constraints to their flow. The complexity of the rock pore network compared with the large pores in the glass beads was not taken into consideration during this analysis. It should be noted that the pore network in glass beads is expected to be less complex compared with that of a natural rock, such as Berea sandstone. The pore sizes are also predicted to be larger than those in real rocks. This might aid the transport of large particles during the glass-bead injection.

3.5.5 Silica (SiO₂) nanoparticle characterization and injection experiment results

An objective of these transport experiments was to investigate the use of SiO₂ nanoparticles to characterize fractured reservoirs. An initial investigation of the feasibility of synthesizing SiO₂ nanoparticles with dyes attached using a temperature-sensitive covalent linkage was performed (Section 6.3). We demonstrated temperature sensitivity based on an observable change in the fluorescence spectrum of the dye upon heating. Protected DNA, another potential temperature nanosensor, is encapsulated inside SiO₂ nanoparticles (Section 6.5). Therefore, we focused initially on the transport of inert SiO₂ particles, as a precursor for the transport of the functional dye-attached and/or encapsulated DNA silica particles.

The silica particles were transported through Berea and greywacke sandstones as well as a long sand-packed tube. Based on our findings thus far, spherically-shaped particles of certain size with surface charge similar to that of the flow medium are more likely to be transported with lower probability of attenuation within the porous medium. The SiO₂ nanoparticles used in these transport experiments were negatively charged nanospheres with size distribution as depicted in Figure 3.33. SiO₂ particles with an average size of 100 nm and 350 nm were injected into Berea sandstone and sand-packed tube, respectively.

CHAPTER 3. PRELIMINARY EXPERIMENTATION WITH INJECTION OF NANOMATERIALS INTO POROUS ROCKS

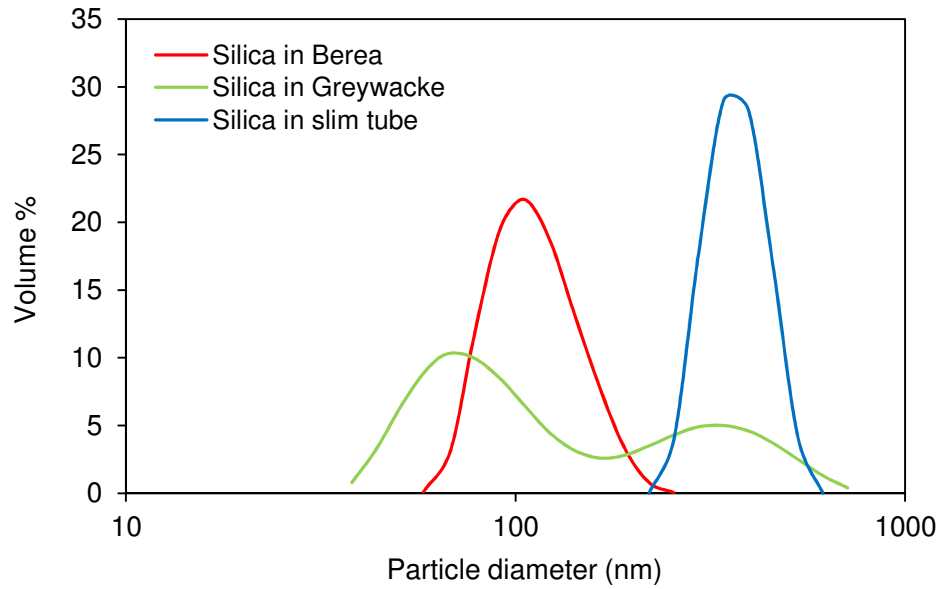


Figure 3.33: Size distribution by volume percentage of the SiO_2 particles suspensions used during injection into Berea, greywacke sandstones and sand packed tube. Note the Bimodal distribution of the nanofluid suspension injected into greywacke core. The measurements were performed using DLS.

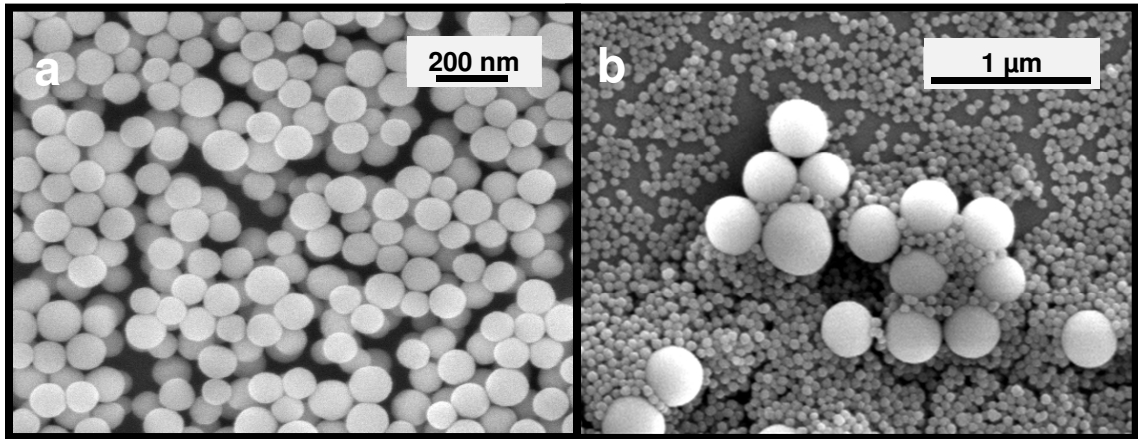


Figure 3.34: Micrographs of the (a) $0.10 \mu\text{m}$ and (b) 0.07 to $0.35 \mu\text{m}$ SiO_2 nanospheres influent.

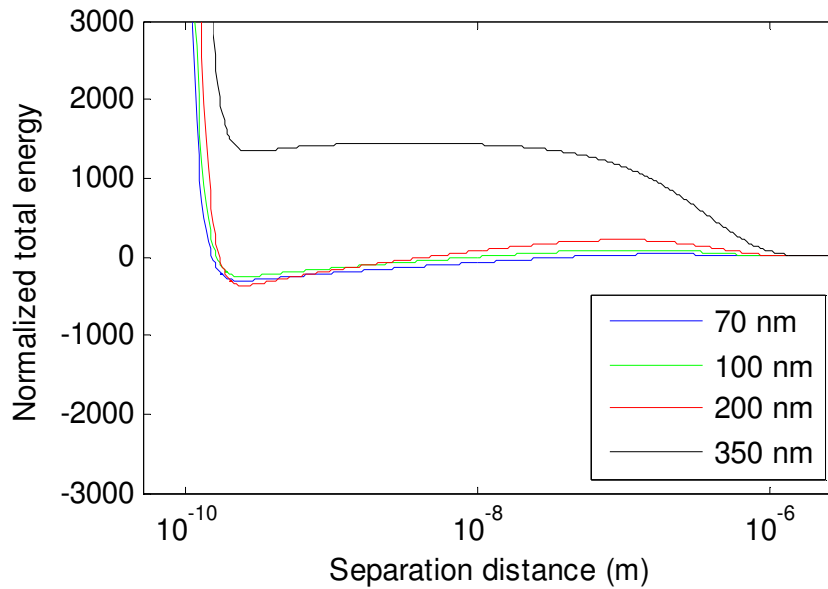


Figure 3.35: Total interaction energy between SiO_2 particles and rock surfaces. The interaction energy is normalized to the thermal energy (Boltzmann constant and absolute temperature). Hamaker constant used is 6.0×10^{-21} J as per Israelachvili (1992) for $\text{SiO}_2/\text{SiO}_2$ nanoparticle in water. The total interaction energy plot shows a shallow energy barrier below as the particle size decreases.

The nanofluid suspension prepared for the greywacke experiment was a mix of 1, 0.3 and 0.2 ml of 0.07, 0.20 and 0.35 μm nanoparticles, respectively. The intention here was to have fewer of the big particles. SEM imaging (Figure 3.34) was used to confirm the particles size. The zeta potential of the 0.07, 0.10, 0.20 and 0.35 μm particles was -21.3, -29.1, 32.4 and 73.4 mV. The total interaction energy between the SiO_2 particles and rock surfaces can be seen in Figure 3.35. The energy barrier is significantly shallower for 0.07, 0.10 and 0.20 μm silica particles and decreases with decreasing particle size. Particle aggregation may occur for particles smaller than 0.35 μm due to the shallow energy barrier and/or the existence of attractive forces at the primary energy minima.

3.5.5.1 Berea, silica (SiO_2) nanoparticle injection experiment results

SiO_2 nanoparticles were flowed successfully through the Berea sandstone core. The injected nanoparticles were transported through the pore spaces of the rock and were detected in the effluent. The recovery of the nanoparticles following their injection was

CHAPTER 3. PRELIMINARY EXPERIMENTATION WITH INJECTION OF NANOMATERIALS INTO POROUS ROCKS

verified. It has been demonstrated that they were not trapped in the pore spaces by hydraulic, chemical or electrostatic effects. The concentration of influent was unknown and therefore the return concentration of the SiO₂ particles was not quantified. Filtration theory predicted that the probability of SiO₂ transport by diffusion, interception and gravity settling was low. Transport by gravity and interception was negligible because the particles are small and have density similar to suspension fluid. The total single-collector efficiency was 9.48 %, mainly by diffusion, as estimated by Equation 2.1. Peclet number suggested that the flow was advection dominated ($Pe \approx 160$). Unless local heterogeneity of charge among particles or particles and sandstone exists, particles should remain stable in suspension prior to injection and particles may not attach electrostatically to pore walls. The interaction energy between particles and pore wall would be a factor of two higher than energy barrier among particles shown in Figure 3.35. This is because interaction expressions are modified to approximate sphere-plate system.

Straining of the 0.10 μm SiO₂ was not likely to occur. The particle to median grain diameter ratio was about 6.67×10^{-4} . This ratio is orders of magnitude smaller than ratios suggested by other investigators (Sakthivadivel, 1966 and 1969; Herzig et al., 1970; Matthess and Pekdeger, 1985; and Xu et al., 2006) where straining is expected to play an important role in deposition of particles within porous media. Also, the average pore throat, 8.8 μm as estimated by mercury intrusion method, of Berea sandstone used during the SiO₂ transport was about 88 times larger than the average SiO₂ particle diameter.

The effluent samples were examined for the existence of the nanoparticles using the DLS technique and a more precise approach using SEM imaging of the effluent confirmed this finding. It is worth mentioning that larger size particles than those injected were detected by DLS in some of the early effluent samples. An example of the size distribution based on the volume percentage of particles is illustrated in Figure 3.36. Particle aggregation was not expected as discussed above. It was believed that these particles were the core fines which were produced from within the rock pore spaces.

CHAPTER 3. PRELIMINARY EXPERIMENTATION WITH INJECTION OF NANOMATERIALS INTO POROUS ROCKS

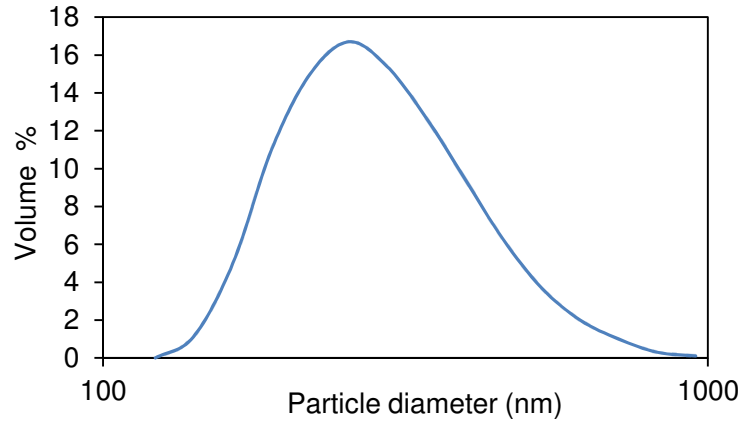


Figure 3.36: Particle size distribution by volume percentage of effluent sample containing core fines and debris.

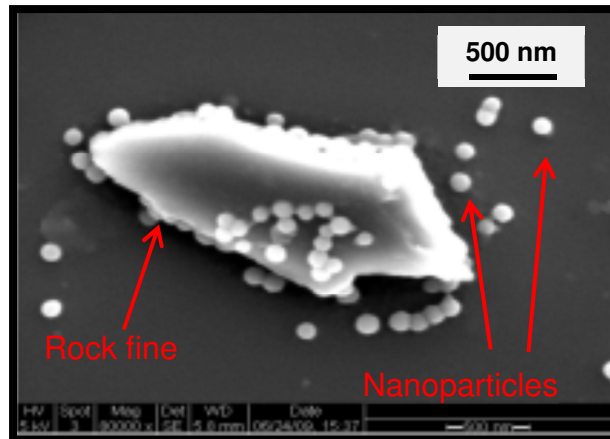


Figure 3.37: SEM image of rock fine relative to injected SiO_2 nanoparticles.

To verify this hypothesis, SEM images of the same sample were taken as shown in Figure 3.37. The presence of such fines has resulted in the size distribution estimated by light scattering technique shown in Figure 3.36. The nanoparticles were easily distinguishable from the core fines and debris due to their size and spherical shape, even though all were made of same material as the rock itself.

These large particles have shown up immediately after the injection of nanofluid suspension. Traces of these particles have been detected using DLS within the first post-injected pore volume of deionized water with a decreasing trend. The large particles were

CHAPTER 3. PRELIMINARY EXPERIMENTATION WITH INJECTION OF NANOMATERIALS INTO POROUS ROCKS

produced only in the early part of the injection. Following that, the 100 nm SiO₂ nanoparticles began to breakthrough. The nanoparticles continued to flow until their concentration at later effluent samples had fallen below the detection limit of the DLS instrument. Note that DLS measurement is not concentration measurement. DLS only provides particle size distribution versus light intensity. Based on the light scattering measurements, the intensity of the incident light should remain relatively unchanged for every particle size regardless of the sample concentration (unless the sample is too concentrated). In this case, the intensity of around 20 % (± 3 %) was measured at the particle size of the nanofluid injected (0.10 μm), as shown previously in Figure 3.33. Therefore, effluent samples collected during post-injection of deionized water that contain any nanoparticle concentrations within the detection limits of instrument used should have the same intensity for that particular particle size.

The particle size distribution was conducted for all effluent samples. Then each particle size was plotted individually. Only particle sizes around the peak of the distribution was plotted since data at the shoulders of distribution is a result of calculation performed by the software that could be in misleading. Figure 3.38 shows the production history of the 100 nm particle size. Each data point in this graph was obtained from different effluent sample. The plot demonstrates that the 0.10 μm SiO₂ particles were identified in several effluent samples collected during the injection experiment, confirming their transport.

Subsequent to the analysis of the effluent, the interior of the rock itself was examined. Specifically, middle and outlet slices (Figure 3.39) were examined most closely because nanoparticles present in those sections had clearly passed the inlet. Figure 3.40 shows SEM image of the pore spaces at the middle section of the core. The SiO₂ nanoparticles were visible as little white spheres. These spheres were approximately 100 nm in diameter. This demonstrated unambiguously that the nanoparticles had been transported through the pore network of the reservoir rock.

CHAPTER 3. PRELIMINARY EXPERIMENTATION WITH INJECTION OF NANOMATERIALS INTO POROUS ROCKS

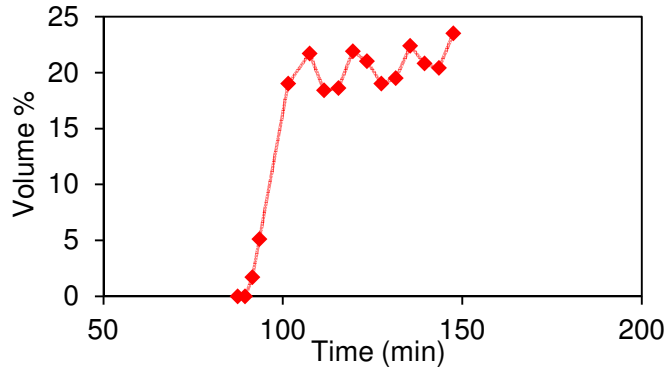


Figure 3.38: Production history of the 0.10 μm SiO₂ particles using DLS. Note that this is not concentration or return curve. DLS only identify the existence of particle based on its size. Each data point in this figure is taken from different effluent sample for the same particle size.

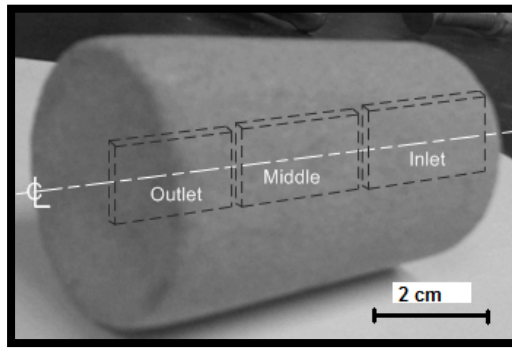


Figure 3.39: Rock sections for SEM analyses.

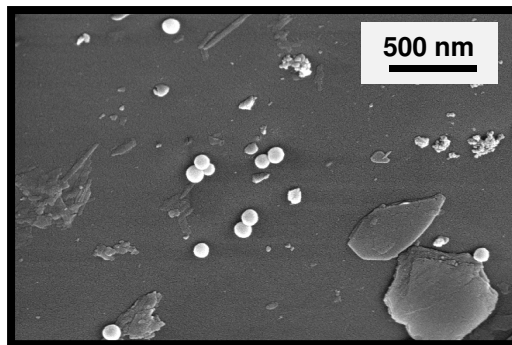


Figure 3.40: Nanoparticles at the middle section of the rock. Nonspherical objects are the natural fines and debris from the rock itself.

3.5.5.2 Sand-packed tube silica (SiO₂) nanoparticle injection experiment results

A second experiment was conducted using a different flow apparatus, a 10 meter long sand-packed slim tube, to study the transport and recovery of injected SiO₂ nanoparticles through a longer flow path. This experiment imitates near field interwell distance as in conventional interwell tracer tests.

The SiO₂ nanoparticles were detected at the effluent, confirming their transport. The permeability was unaltered during and after the injection of the nanofluid suspension with minimal change of about ± 4 darcy (Figure 3.41).

The influent concentration was unknown so the return concentration curve was not determined. The recovery of the SiO₂ particles through the sand packed tube is expected to be higher than previous injection into Berea sandstone. The pore network in the sand tube is likely to be less complex than Berea sandstone. This would facilitate the transport of particles. The sand grain size used was approximately 1000 μm , as opposed to the average grain size of Berea sandstone (150 μm). The removal efficiency decreases with increasing grain size. In this case, the total single-collector efficiency was less than 1%.

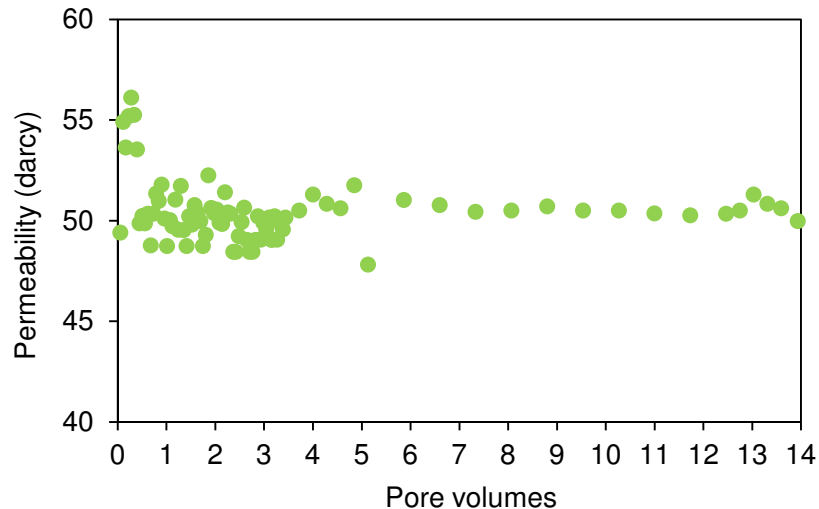


Figure 3.41: Permeability measurements during, after as well as during backflushing of the slim tube. Note the very frequent sampling at the beginning of the injection.

CHAPTER 3. PRELIMINARY EXPERIMENTATION WITH INJECTION OF NANOMATERIALS INTO POROUS ROCKS

The water pore velocity used during injection was at least two orders of magnitude higher than injection velocity during Berea injection. This implies that particles will experience less diffusion and therefore shorter resident time and lower probability to interact with porous media. The strong repulsive energy barrier between particles and pore wall will also force particle to follow streamlines, and hence lower probability of attachment to pore wall.

Similar to the DLS analysis performed on the effluent samples collected during the SiO₂ particle injection into Berea sandstone, the intensity of around 30 % was measured at the particle size of the influent injected (0.35 μm), as shown in Figure 3.33. The light intensity of effluent samples is plotted against post-injected pore volumes in Figure 3.42. It is evident from Figure 3.42 that the nanoparticles exist in the effluent samples with the same intensity of the SiO₂ nanofluid influent (i.e. 30 %). The nanoparticles were identified following the post-injection of about half a pore volume of pure water and produced continuously until the bulk of these particles were displaced through the second pore volume. The increasing content of nanoparticles within that pore volume can be observed visually as shown in Figure 3.43. Cloudy samples are characterized by being highly concentrated with SiO₂ nanoparticles (as opposed to semitransparent samples).

Scanning electron imaging confirmed the variation in the particle concentrations. A series of SEM images (Figure 3.44) were taken for samples a, b and c of Figure 3.43. These images show the difference in particle count or concentration clearly. Note that the volume of each sample was identical and micrographs were taken at the same magnification.

Thus, it was demonstrated that the spherically shaped SiO₂ nanoparticles could be recovered following their injection not only through short core plugs but also through a long flow path without being trapped within the flow conduits.

CHAPTER 3. PRELIMINARY EXPERIMENTATION WITH INJECTION OF NANOMATERIALS INTO POROUS ROCKS

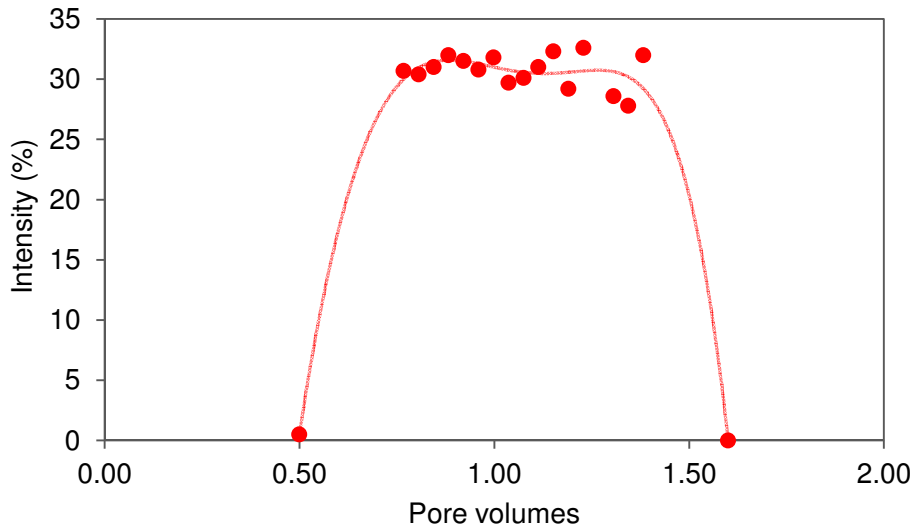


Figure 3.42: Production history of the $0.35 \mu\text{m}$ SiO_2 particles using DLS. Note that this is not concentration or return curve. Particle recovery was during the second post-injected pore volume. The first data point in the plot was from the effluent sample after which particles were detected. The last data point is from effluent after which particles were not detected.

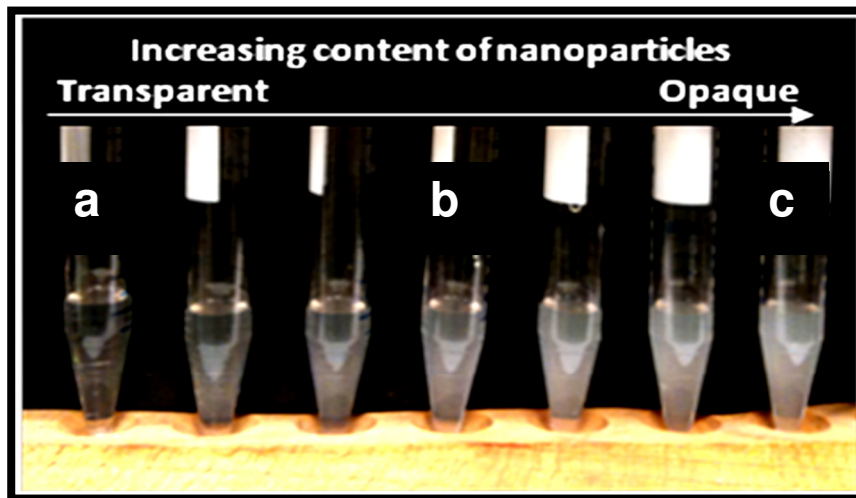


Figure 3.43: Visual characterization of effluent samples for their SiO_2 nanoparticles content based on color.

CHAPTER 3. PRELIMINARY EXPERIMENTATION WITH INJECTION OF NANOMATERIALS INTO POROUS ROCKS

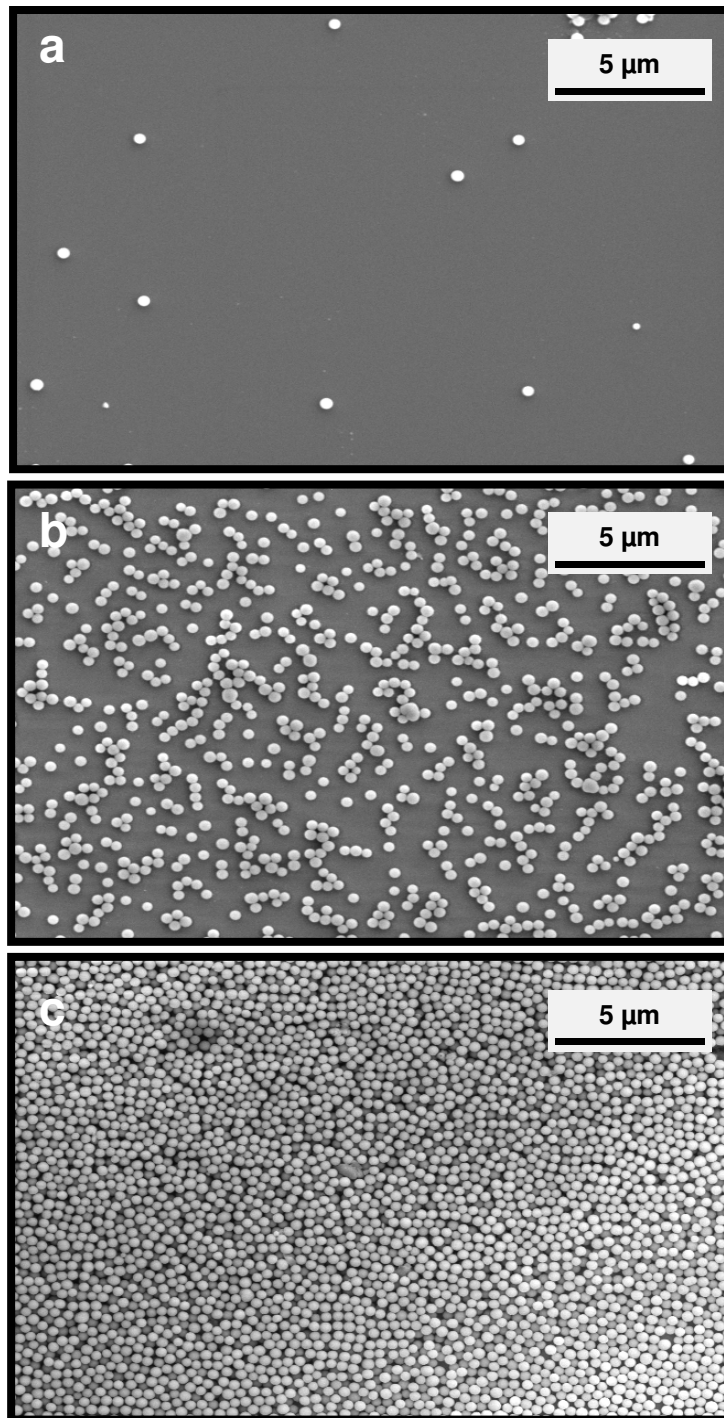


Figure 3.44: SEM images of effluent samples a, b and c of Figure 3.43.

3.5.5.3 Greywacke, silica (SiO₂) nanoparticles injection experiment results

The injection of SiO₂ nanoparticles was aimed to test the feasibility of transporting SiO₂ nanospheres through the pores of the greywacke rock core as it represents the kind of tight rocks found in geothermal reservoirs. The experiment was intended to bracket the size limits of the nanoparticles that may be able to flow through the pores.

Silica (SiO₂) nanoparticles were identified in some of the effluent, but not all. The interior of the rock itself was examined. There were no signs of the injected nanoparticles inside the pores. The SiO₂ nanoparticles had a wide distribution of sizes between 70 to 350 nm. The average and largest pore sizes were predetermined by mercury injection (Figure 3.1) and found to be 0.06 and 0.15 μm, respectively. Note that the average pore size is smaller than the smallest injected particle (i.e. 0.07 μm). It was suggested that particles of all sizes were physically trapped at small pores. Subsequent particles will be redirected to large continuous pores. In the best case scenario, particles sizes below 0.15 μm would flow through such pores. SEM analysis (e.g. Figure 3.47) showed that the effluent contained particles larger than 0.15 μm. This is physically impossible because a particle cannot access flow conduits smaller than the particle itself. We speculated that the particles might have slipped through at the space between the core wall and core-holder rubber sleeve due to insufficient confining pressure (1000 psig).

The small particle size (submicron range) and the low water pore velocity (1.60×10^{-3} cm/min) suggested that the flow was diffusion-dominated, given that the particles could access the pore network. The importance of particle transport due to advection or diffusion can be evaluated by Peclet number. Based on the pore velocity and using the average pore size of 60 nm as the characteristic length, Peclet number was found to be in the range between 2.54×10^{-3} to 1.45×10^{-2} for particle size in the range from 0.07 to 0.35 μm. Peclet number was significantly below 1.0, indicating diffusion-dominated flow.

The injection into the greywacke core was conducted in the following fashion. The core was first preflushed with deionized water, and then the nanofluid was injected. Following

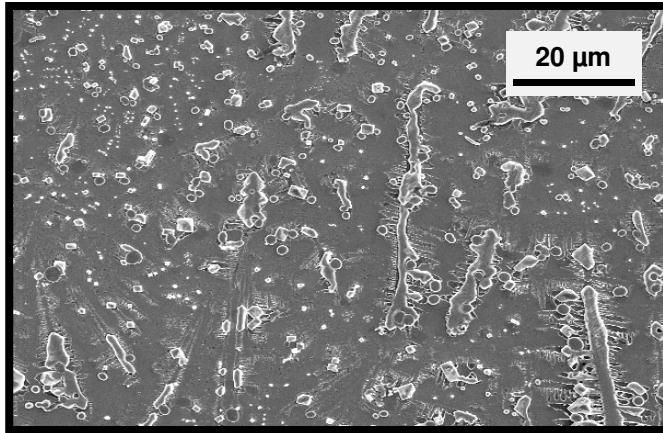


Figure 3.45: Core fines and debris in preflush effluent sample prior to SiO_2 injection.

that, several pore volumes of distilled water was post injected. Figure 3.45 shows SEM images of the particle-free deionized water (preflush) evaporated solution placed on silicon substrate. It appeared that all the white colored material was the rock fines and debris. No sign of any round particles was seen, which was expected since no introduction of the nanofluid had taken place yet. This confirmed that the core fines were not round in shape and should not be confused with SiO_2 nanoparticles. On other words, any spherically shaped objects should be interpreted as injected SiO_2 nanoparticles. This gave confidence in the characterization of the effluent samples throughout the experiment as well as the rock pore space itself.

The analyses of selected, but representative, effluent samples were continued. Dynamic light scattering did not work with any of the effluent samples. Several factors, such as presence of dust and aggregates of small particles ($0.07 \mu\text{m}$) or high concentration of particles in solution, might have made the samples unsuitable for DLS measurements. Samples were filtered using 0.8 and $0.2 \mu\text{m}$ syringe filters and/or diluted in order to eliminate some of these causes, however, the samples were still not suitable for the analysis. This was not given a big attention at this time because a more precise characterization approach (SEM imaging) was readily available. Therefore, subsequent effluent samples were analyzed by SEM imaging only. SEM micrographs (Figure 3.46) showed irregularly shaped small particles in the order of $0.10 \mu\text{m}$ in size. The existence

CHAPTER 3. PRELIMINARY EXPERIMENTATION WITH INJECTION OF NANOMATERIALS INTO POROUS ROCKS

of smaller particles suggested that the nanoparticles were crushed under high pressure (700 psig in this case). If this was the case, it would be difficult to distinguish between broken pieces of the silicon oxide nanoparticles and core fines using this type of analysis (SEM imaging). To verify if particles were collapsed due pressure and to avoid confusion with rock debris, a pressure test on a sample of nanofluid containing 350 nm silicon oxide nanoparticles was conducted outside the core.

A few milliliters of pure nanofluid with particles in the size range of 350 nm were pressurized outside the core (in a clean container). The maximum pressure was 2000 psig applied in steps of 500 psig at a time. At every step, a sample was collected and prepared for SEM analysis. To optimize the analysis time, SEM imaging was performed at the highest and second highest pressure samples (i.e. samples pressurized to 1500 and 2000 psig). The silicon oxide nanoparticles did not exhibit any distortion or damage.

It should also be pointed out that this test did not take into consideration the effect of the tortuous paths within the rock pore network. It might be possible that elevated pressure, along with the physical bombardment of the particles as they transported through tortuous path, could cause particle damage. A sample at the fifth post-injected pore volume showed unusual particle shapes (Figures 3.47 and 3.48). The nanoparticles appeared to be

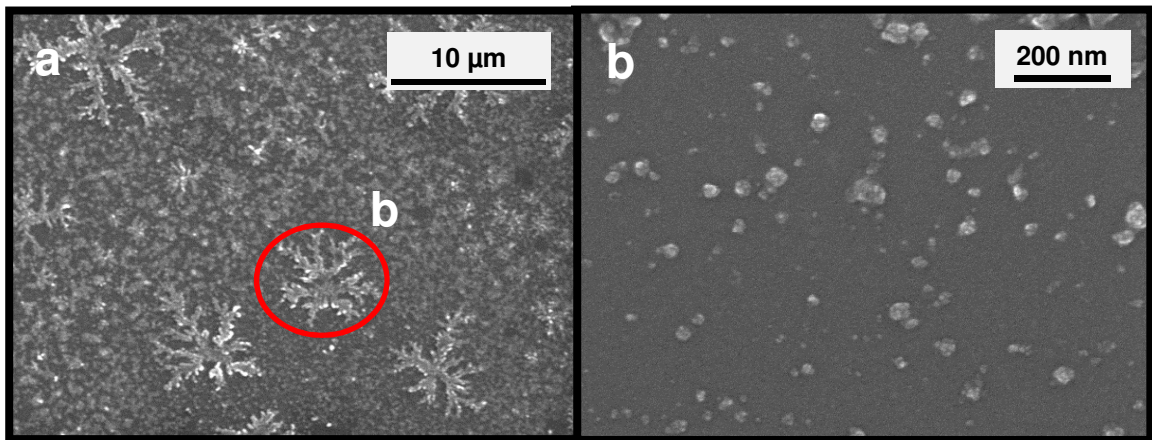


Figure 3.46: (a) Effluent sample during injection of nanofluid, (b) close-up image.

CHAPTER 3. PRELIMINARY EXPERIMENTATION WITH INJECTION OF NANOMATERIALS INTO POROUS ROCKS

round in shape on one side while having a cut from the other side. The size of these particles agreed with the size of injected nanoparticles. In addition, the roundness of these particles on one side strongly suggested that these were not core debris but injected nanoparticles. The distortion of the nanoparticle shape has not been explained at this time.

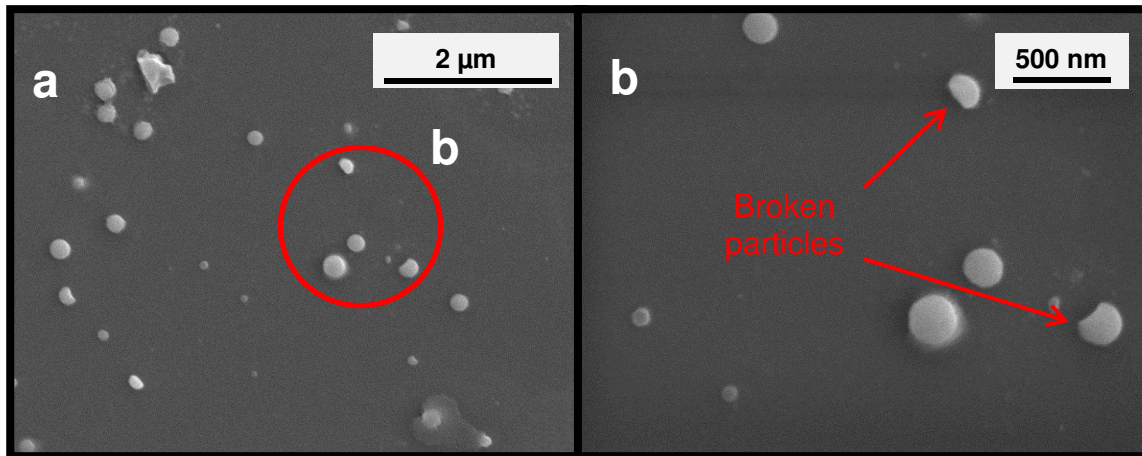


Figure 3.47: (a) Effluent sample at the fifth post-injected pore volume showing SiO_2 nanospheres with broken side, (b) close-up image.

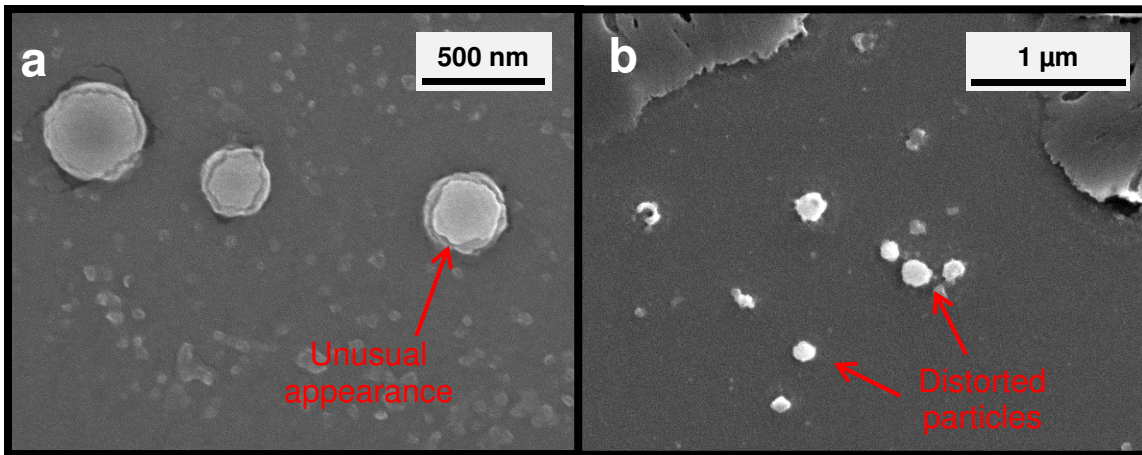


Figure 3.48: SEM images showing SiO_2 nanospheres, (a) unusual appearance, (b) distorted particles.

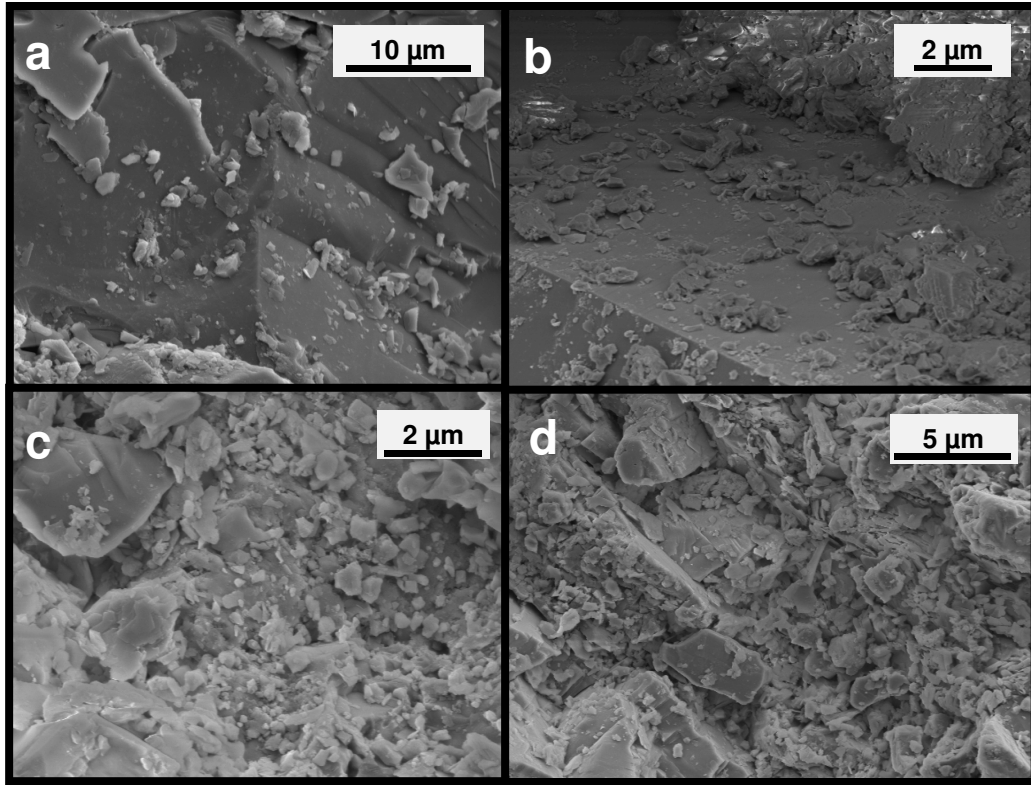


Figure 3.49: SEM images of the pore spaces of greywacke core sections at, (a) inlet, (b) middle, (c) and (d) outlet.

The interior of the rock itself was examined. Specifically, inlet, middle and outlet slices were examined most closely. Figure 3.49 shows an SEM image of the pore spaces at all three sections of the core. The SiO_2 nanoparticles were not visible. The core has many fines and debris which made it difficult to identify the nanoparticles.

This experimentation with the greywacke core involved many uncertainties. The unusual shape and distortion of the nanoparticles were identified at various pore volumes. The particles either have a cut in one side (Figure 3.47), unusual appearance or distortion (Figure 3.48). It was also suspected that nanofluid might have slipped through the space between the core and the core-holder sleeve. This could happen if the confining pressure was insufficient to seal the core. The core-holder used has a maximum allowable pressure of about 1000 psig. Due to these uncertainties, the results of this experiment were inconclusive.

3.6 Chapter summary

To investigate the feasibility of using nanosensors to determine reservoir properties in general and fracture-network properties in particular, it was necessary to verify their transport through typical formation rock. Initial testing with nanoparticles was also required to develop the understanding of best injection procedures, sampling strategies, and characterization techniques. Accordingly, various laboratory-scaled coreflooding experiments with inert nanoparticle suspensions were conducted.

In this chapter, it has been shown that the size and/or size distribution, shape, and surface charge of the particles were influential parameters governing the transport of nanoparticles through porous media.

- **Shape:** As change in particle shape (i.e. rod-like to sphere) upon heating was a potential sensing mechanism, the significance of the nanoparticle shape on its transport was explored by flowing Ag nanowires through the pore spaces of Berea sandstone. The Ag nanowires were trapped at the inlet of the core and could not flow through. Subsequently, spherically-shaped Ag nanoparticles of the same material were injected into the sandstone. It was found that the Ag nanospheres were able to flow with 25% recovery. The low recovery was attributed to the aggregation of the particles that resulted in entrapment because of the shallow repulsive energy barrier and attractive forces in the primary energy minima. It has been concluded that the rod-like nanoparticles with large aspect ratio would not be suitable as temperature nanosensors, due to difficulty imposed by shape on their mobility within the pore spaces of the rock core.
- **Surface charge:** The effect of surface-charge on the transport of nanoparticles was studied by injecting hematite nanorice into sandstone. Initially, the hematite nanorice sample had a surface charge opposite of that found in the sandstone. Analysis of the effluent and pore spaces showed that the nanorice was trapped within the pores and was not detected in the effluent. Testing on a tube packed

CHAPTER 3. PRELIMINARY EXPERIMENTATION WITH INJECTION OF NANOMATERIALS INTO POROUS ROCKS

with glass beads (in the absence of core materials) revealed that nanorice still experienced low mobility. We modified the hematite surface charge by coating the particles with surfactant. As a result, the hematite nanorice flowed with 23% recovery. Despite the modest recovery, it was concluded that the affinity of the nanorice to the porous medium was related primarily to its surface charge. It was also concluded that hematite could be used as a core material of a core-shell nanosensor; however, modification of surface properties (surface charge) upon attachment of shell material should be evaluated to ensure compatibility with the flow medium.

- Particle size: It has also been shown that there was an optimum particle size for the transport of Sn-Bi alloy nanoparticles through Berea sandstone. The rock filtered the injected nanofluid, allowing only certain particle sizes to flow through it, as opposed to the glass-bead injection, in which Sn-Bi particles of all sizes were produced. Testing with glass beads has also confirmed that the Sn-Bi nanoparticles had affinity to the rock materials. Therefore, using the growth in size of the Sn-Bi particles as a characteristic of temperature measurement may result in entrapment of particles larger than an optimum particle size relative to the rock pore spaces.

CHAPTER 4

EXPERIMENTAL INVESTIGATION OF PARTICLE TRANSPORT THROUGH FRACTURED MEDIA

4.1 Background

Fluid flow through natural and engineered geothermal reservoirs as well as carbonate oil formations is fracture-dominated. In the development of such reservoirs, the characterization of the size, shape and connectivity of fractures is crucial. Research studies have been devoted to develop methods to characterize fracture networks within a reservoir. Temperature measurements acquired by nanosensors may be used to infer information about fracture properties. In order for temperature nanosensors to map the reservoir temperature distribution and ultimately to characterize the fracture network, they must be transported through the fractured reservoir without major retention within the formation pores and/or fractures. Therefore, particle mobility through fractured rocks was investigated. Specifically, various laboratory-scaled core-flooding experiments with inert silica particle suspensions were conducted. Silica particles were injected into fractured greywacke and Berea sandstones as well as a glass fracture model. We investigated the influence of size, fluid velocity and concentration on particle transport under unfavorable attachment conditions.

The following sections will provide the details of the particles and flow medium characterizations, experimental apparatus, results and discussion.

4.2 Characterizations of silica particle suspensions and flow media

4.2.1 Silica particles

Fluorescent silica particles (purchased from Corpuiscular Inc., New York, USA) were used in this experimental study. Because two of the potential temperature-sensitive particles investigated in this research study were silica based (dye-attached silica and silica-encapsulated DNA), inert silica particles were used for this transport study.

Fluorescent silica particles were characterized in terms of size and shape, zeta potential and light emission (fluorescence). The size and shape of the particles were characterized using an optical microscope and scanning electron microscope (SEM). Zeta potential was measured using Zetasizer manufactured by Malvern Instruments. The emission spectrum was obtained using Fluorescent Spectrometer (Fluorolog) manufactured by Horbia.

Three silica microsphere suspensions, each labeled with different fluorescent dye of blue, green and red color were used. The blue and green samples were shown to have uniformly shaped spheres with a narrow size distribution with an average particle size of approximately 2 and 5 μm , respectively. The red silica spheres were polysized. The red silica sample had spheres with diameters ranging from 5 to 31 μm . The particle size was confirmed by SEM, as shown in Figure 4.1. The size was also verified by optical microscopy but images are not included. These particles had a density in the range between 2.0 to 2.2 g/cm^3 . The concentration of injected suspension varied between experiments. The excitation and emission of the blue, green and red fluorescent dyes were at wavelengths of 360/430 nm, 480/530 nm and 554/577, respectively. The emission spectra showing the peak of emission of the blue, green and red fluorescent silica particles are depicted in Figure 4.2. The effluent concentration after injecting the silica suspensions was estimated by measuring the emission intensity of the fluorescence. First, a calibration curve was constructed by acquiring the emission spectra of several dilutions of known concentration. The concentration of collected effluents was then determined using this linear correlation based on their emission intensity (Figure 4.3).

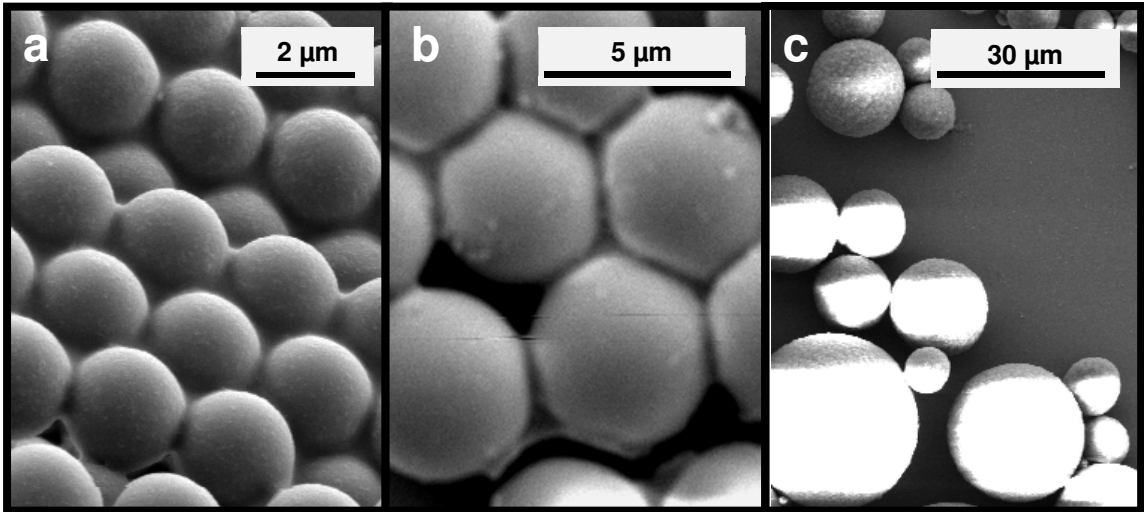


Figure 4.1: SEM micrographs of (a) blue, (b) green and (c) red fluorescent silica particles. The shape uniformity of the silica particles is evident. The blue and green particles have a uniform size, whereas the red particles have a wide size distribution.

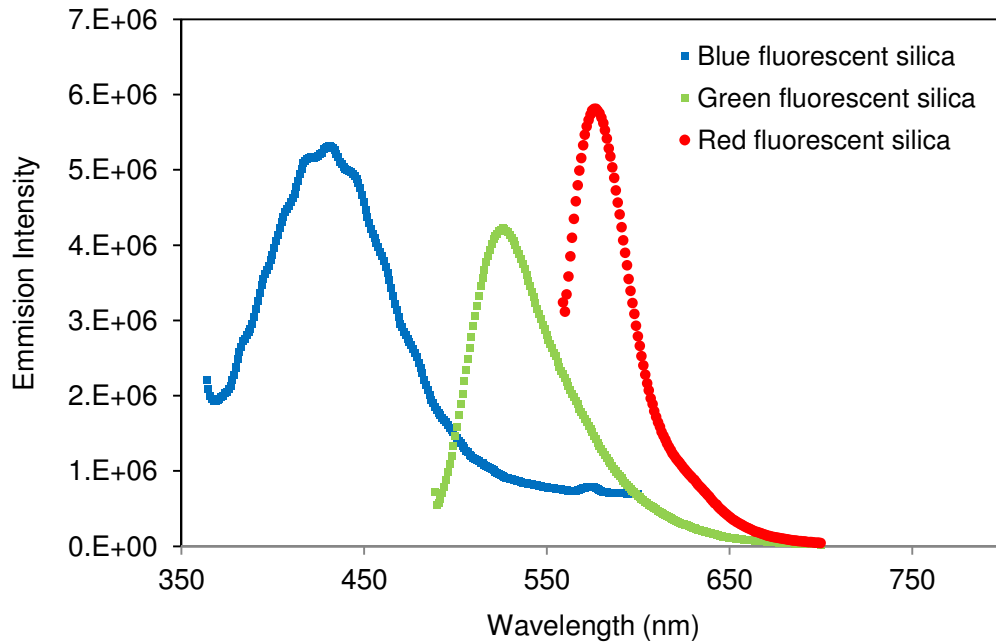


Figure 4.2: Emission spectrum of the blue, green and red fluorescent silica particles. The peak emission of the blue, green and red dye is at wavelength 430, 530 and 577 nm, respectively.

CHAPTER 4. EXPERIMENTAL INVESTIGATION OF PARTICLE TRANSPORT THROUGH FRACTURED MEDIA

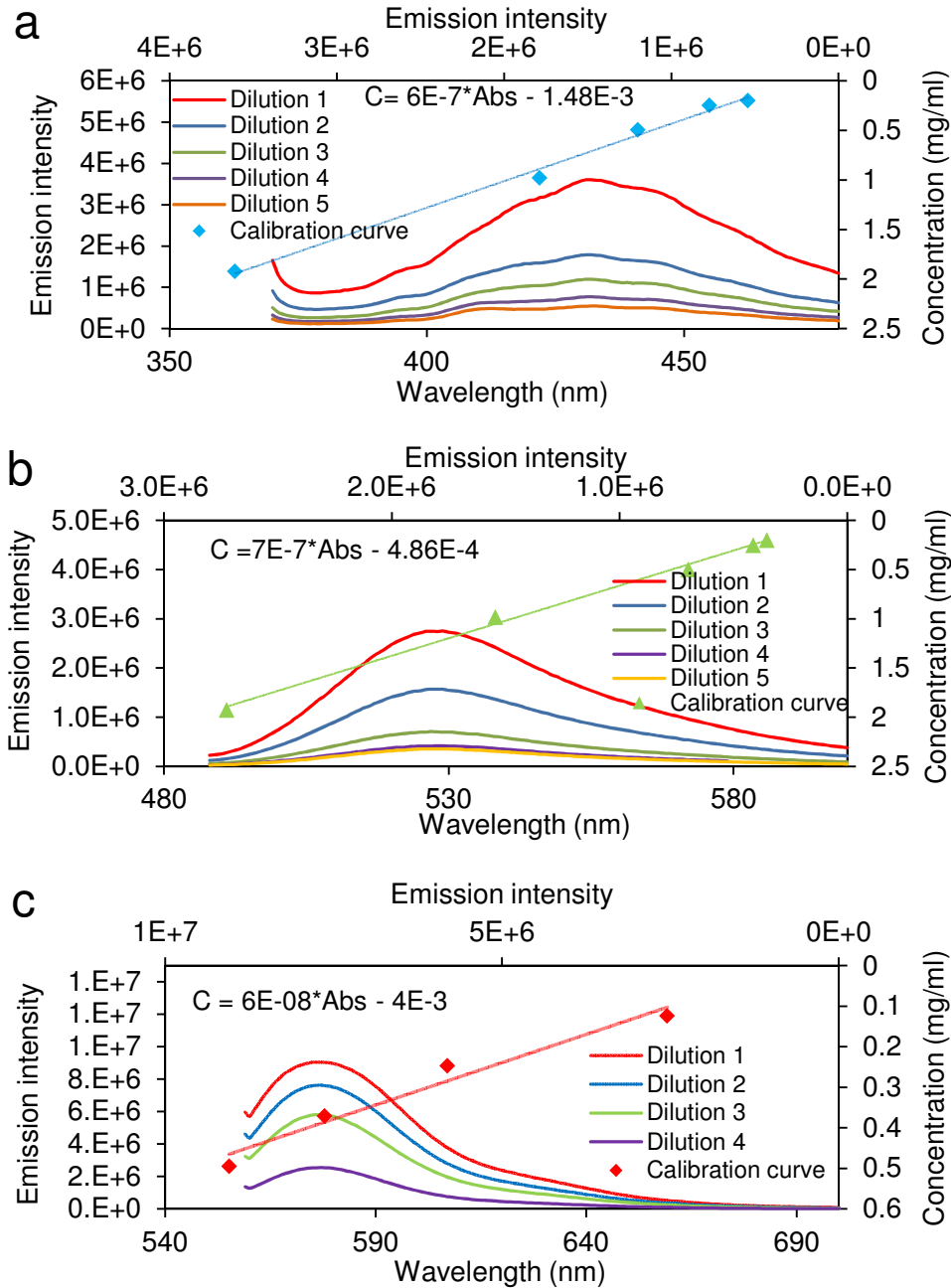


Figure 4.3: Fluorescent emission and calibration curve of (a) blue, (b) green and (c) red silica microparticle samples of known concentrations. The maximum emission (peak) was at wavelength of 430, 530 and 577 nm for blue, green and red silica suspensions. Note the linearity of the calibration curve, indicating the applicability of Beer-Lambert Law. The calibration equation is showing in each graph. The secondary horizontal axis of optical density is associated with the secondary vertical axis of concentration.

CHAPTER 4. EXPERIMENTAL INVESTIGATION OF PARTICLE TRANSPORT THROUGH FRACTURED MEDIA

The particles employed were negatively charged as specified by the manufacturer. Five different measurements of zeta potential (ζ) (i.e. conversion of electrophoretic mobility to zeta potential using the Smoluchowski approximation and Henry's Equation (Equation 3.5) were performed and the average zeta potentials were found to be -40.2 mV (standard deviation: 0.41 mV), -80.2 mV (standard deviation: 1.77 mV) and -56.3 mV (standard deviation: 1.32 mV) for the blue, green and red fluorescent silica particles, respectively. The total interaction energy between silica particles is estimated using Equations 2.7-2.9, and plotted in Figure 4.4. All particles exhibited high repulsive energy barrier above $1000 k_B T$, which should render them free from aggregation and/or attachment to rock walls.

In addition to silica microparticles, silica nanoparticles were also used in this study, only through the fractured greywacke rock. The average particle size (350 nm) was determined by DLS and confirmed by SEM. The nanoparticles were negatively charged with zeta potential of -73.4 mV. These silica particles are the same as those used during the injection into 10 m long sand packed slim tube, as described earlier in Section 3.5.5.

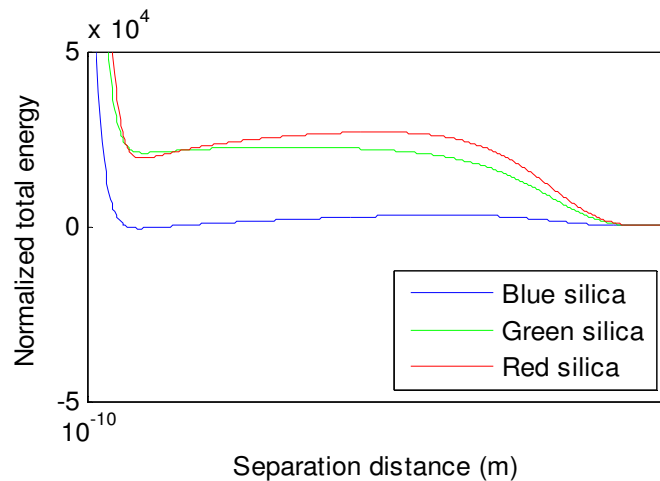


Figure 4.4: Total interaction energy between silica particles and surfaces. The interaction energy is normalized to the thermal energy (Boltzmann constant and absolute temperature). Hamaker constant used is 6.0×10^{-21} J as per Israelachvili (1992) for $\text{SiO}_2/\text{SiO}_2$ particles in water. The total interaction energy plot shows a strong energy barrier above $1000 k_B T$ for all particle sizes.

4.2.2 Characterization of flow media

Standard experiments to characterize the fractured rocks and glass fracture model were performed, including the porosity, permeability and hydraulic aperture measurements. Silica suspension injection was carried out using two different cores; fractured Berea and greywacke rock samples as well as a glass fracture model. The glass fracture model was designed originally to study the multiphase flow of gas and liquid phases through fractures. The apparatus was designed and fabricated by a previous researcher Gracel Diomampo during her master degree research in Stanford (Diomampo, 2001), as described later in Section 4.3.2. Fractured media dimensions, porosity, permeability, pore volume and hydraulic aperture calculations are summarized in Table 4.1.

Silica nanoparticles and silica particles of different concentrations (blue, green and red suspensions) were transported through the fractured greywacke core. Only blue silica suspension was injected into the glass model to investigate the effect of fracture wall roughness. In the case of fractured Berea, the blue and green silica suspensions were transported at various fluid velocity and concentrations.

4.2.2.1 Pore size distribution

The pore size distribution of the core samples was measured by the mercury (Hg) intrusion method. The intrusion of mercury was performed using the AutoPore IV 9500 Mercury Porosimeter manufactured by Micromeritics. The pore size distribution of greywacke core is similar to that shown earlier in Figure 3.1, with an average pore size of 60 nm. The glass fracture model contains no porous medium. The pore size distribution of Berea sandstone (Figure 4.5) was obtained from the capillary pressure-saturation curve measured by mercury intrusion and Laplace's equation of capillarity. According to this approach, the Berea sandstone has pores in the range from few nanometers (5 nm) to as large as 50 μm in diameter, with the majority below 25 μm (d_{90}). The average pore size (d_{50}) or (d_{50}) was approximately 15.44 μm . The pore distribution also indicated that 10% of the total pores are smaller than 8 μm (d_{10}).

CHAPTER 4. EXPERIMENTAL INVESTIGATION OF PARTICLE TRANSPORT THROUGH FRACTURED MEDIA

Table 4.1: Fractured rocks and glass fracture model characterization data^a

Property	Fractured greywacke	Fractured glass model	Fractured Berea
d (cm)	5.08	10.16 ^b	3.78
L (cm)	3.02	30.48	2.56
Φ_{sat} (%)	2.96	100.00	22.00
θ (degrees)	40.00	0	0
k_f (darcy)	79.48	272.35	328.79 (1.21) ^d
k_m (darcy)	1.5×10^{-7e}	N/A ^c	0.51
b (μm)	30.68	56.79	62.40 (3.79) ^f
d_{pore} (μm)	0.06	N/A	15.50
PV (cm^3)	1.81	1.76	6.30

^a d and L are the core diameter and length, respectively, Φ_{sat} is porosity by resaturation, θ is fracture orientation angle in degrees, k_f and k_m are the water permeability of fracture and matrix, respectively, b is the fracture hydraulic aperture, d_{pore} is mean pore size, PV is pore volume and N/A indicates that measurement is not applicable.

^bNote that this dimension is the glass model width.

^cThe glass model contains no matrix (only fracture).

^dThe value between parentheses is the fracture permeability assuming no matrix (which is not true). This is used to estimate the lower limit of fracture aperture.

^eThe matrix permeability of greywacke core was measured as explained in Section 3.3.2.

^fThe aperture value outside the parentheses is based on parallel flow, the value inside the parentheses assumes the fracture permeability is equivalent to total permeability (this value represent the lower limit of fracture aperture).

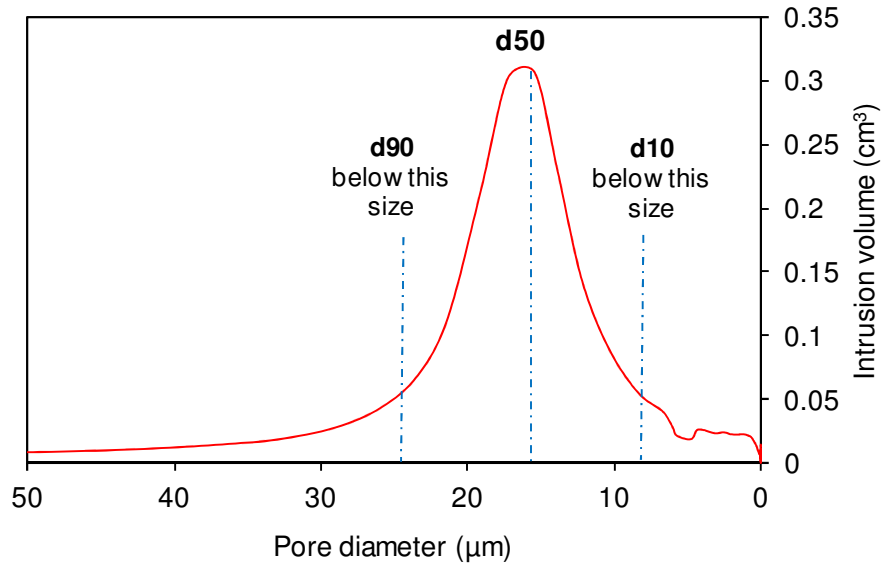


Figure 4.5: Pore size distribution of fractured Berea sandstone obtained by mercury intrusion method. The core sample has an average pore size of 15.44 μm .

4.2.2.2 Fractured rocks and glass fracture model permeability measurements

The fractured rock samples and glass model were characterized in terms of porosity, pore volume, liquid permeability and fracture hydraulic aperture. Gas permeability measurement was not attempted. Note that the permeability equipment used was the same as explained in Section 3.3.2, unless indicated otherwise. The following sections provide specific details of standard tests (porosity and permeability) carried out for the fracture systems under investigation.

4.2.2.2.1 Fractured greywacke permeability measurements

The core sample tested was a fractured greywacke from The Geysers geothermal field. The physical properties of the rock can be found in Table 4.1. The core sample was fitted between the two end-pieces and wrapped with Teflon shrink tube. An electric heating gun was used to bond the assembly together. To achieve proper sealing, the heat was applied evenly starting bottom up in a round motion. The holding or confining pressure supplied by the shrink tube is expected to be below 10-15 psig. The assembly was positioned horizontally and polyethylene tubes (0.3175 cm in diameter) and fittings were used to

CHAPTER 4. EXPERIMENTAL INVESTIGATION OF PARTICLE TRANSPORT THROUGH FRACTURED MEDIA

connect the water pump and pressure manometer to the core assembly (Figure 4.6). As only a very low differential pressure was required to flow fluid through the fractured core, the inlet pressure was measured using a manometer tube rather than a transducer. The flow rate (using water pump, Dynamax, Model SD-200, manufactured by Rainin Instrument Company) was measured using a balance (Mettler balance, Model PE 300) and stop watch. The accuracy of the pump flow rate and balance were 0.01 cm³/min and 0.01 g, respectively. Before saturation, the core was dried at 75°C under vacuum pressure of 0.09 MPa for about 3 days, using a vacuum oven. Then, the core and related system were saturated with deionized water. Initially, the system was evacuated using a vacuum pump (Welch Vacuum Pump, Model No. 8915A) under vacuum pressure of about 13 millitorr for about 4 hours. The vacuum pump was connected to the system from the inlet side of the core. A water column used to saturate the system was attached at the outlet side of the core assembly. The water column was positioned on a scale to observe the weight change and hence the water volume entered the system. The pore volume of the fractured core sample was determined by subtracting the dead volume of connecting tubes, fittings and end pieces from the total volume displaced from the saturation water column. The pore volume and porosity were calculated using equations outlined in Section 3.3.2 (Equations 3.7 to 3.9).

The hydraulic aperture of the fracture was determined using the cubic law. The cubic law is given as (Van Golf-Racht, 1982):

$$q = \frac{b^2}{12} \frac{bW \cos^2 \theta}{\mu} \frac{\Delta p}{L} \quad (4.1)$$

$$k_f = \frac{b^2}{12} \quad (4.2)$$

where q is the volumetric flow rate in cm³/s, b is the fracture aperture in meters, W is the fracture width (same as core diameter) in meter, θ the fracture orientation angle, Δp is the pressure drop across the core sample in Pascal, L is the length of the fracture in meter, μ is the test fluid (water) viscosity in Pascal second and k_f is the fracture permeability in m² (9.86×10⁻¹³ m² is equivalent to 1 darcy).

CHAPTER 4. EXPERIMENTAL INVESTIGATION OF PARTICLE TRANSPORT THROUGH FRACTURED MEDIA

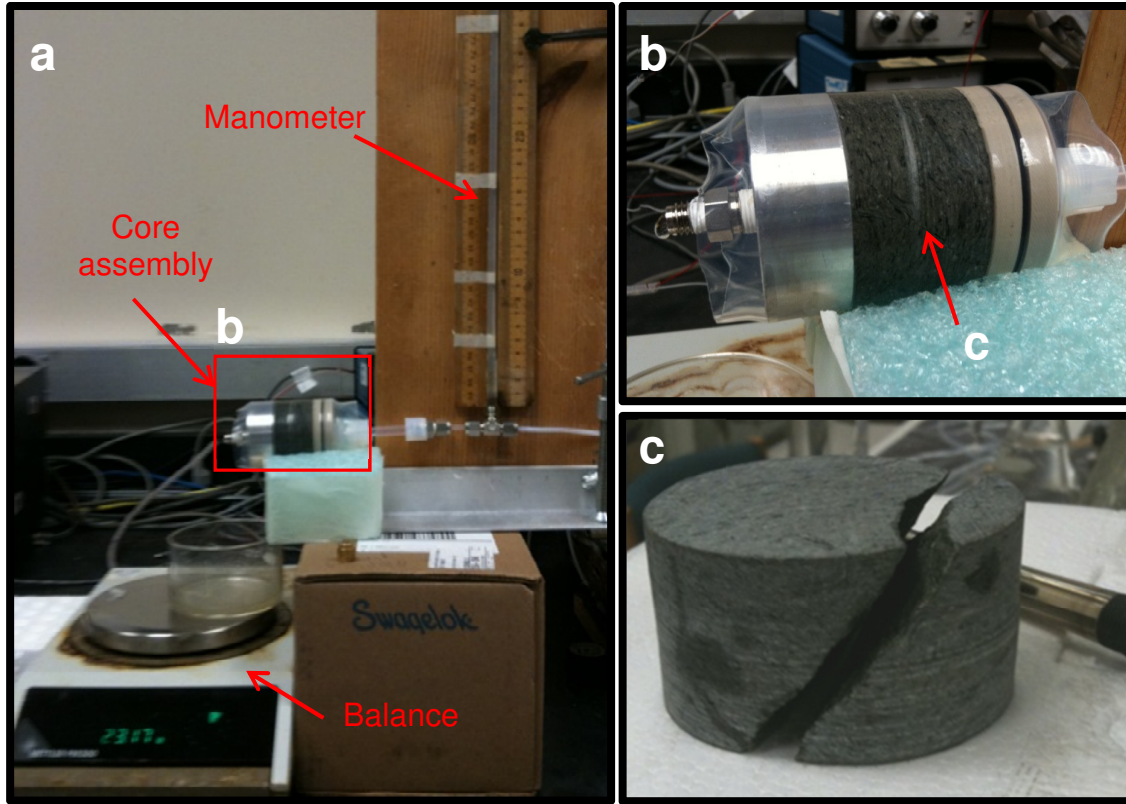


Figure 4.6: A picture of the experimental setup used during the permeability measurement of the fractured greywacke core, (a) showing manometer (pressure), core assembly and balance (flow rate), (b) close-up image showing the core assembly and (c) an image of the fractured greywacke core showing the orientation of the fracture.

The fracture permeability was measured and found to be approximately $79.48 (\pm 3)$ darcy, corresponding to hydraulic fracture aperture of about $30.68 \mu\text{m}$. The fracture orientation angle used in the permeability and/or fracture aperture calculation is about 40 degrees. The validity of Darcy law was confirmed by the linear relationship between the flow rate and pressure drop across the core, as shown in Figure 4.7

CHAPTER 4. EXPERIMENTAL INVESTIGATION OF PARTICLE TRANSPORT THROUGH FRACTURED MEDIA

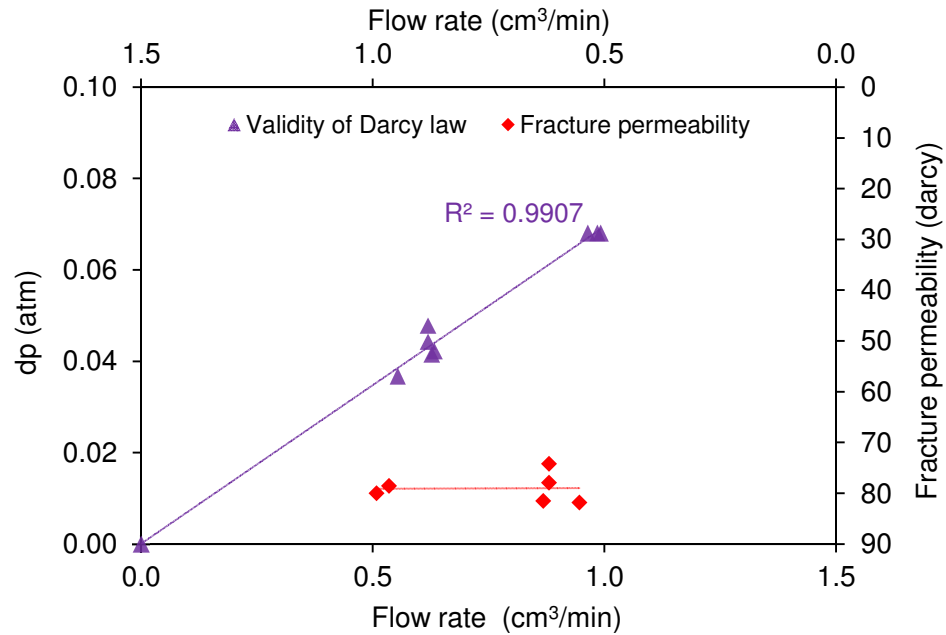


Figure 4.7: Fracture permeability as function of flow rate, with an average fracture permeability of about 79.48 darcy. Note that the angle by which the fracture is orientated is about 40 degrees. The validity of Darcy law under experimental conditions was confirmed through the linearity between flow rate and pressure drop (the secondary horizontal axis of flow rate is associated with the secondary vertical axis of fracture permeability).

4.2.2.2.2 Glass fracture model permeability measurements

Prior to permeability or hydraulic aperture measurements, the fracture was saturated with the testing fluid (i.e. deionized water). Air removal via vacuum and resaturation with water was not possible because the system was not designed to withstand vacuum. Instead, the saturation was achieved by first saturating the system with CO₂ then deionized water, as CO₂ dissolves easier in water than air. The fracture apparatus was also tilted by 45 degrees for gravity to aid the saturation process.

The hydraulic aperture of the fracture was determined using the cubic law (Equation 4.1). The aperture of the fracture was set by installing stainless steel shims with specific thickness as the fracture spacer. Initially, shims with thickness of 51 μm and 102 μm were used. For both cases, the hydraulic aperture measurements were found to be around

CHAPTER 4. EXPERIMENTAL INVESTIGATION OF PARTICLE TRANSPORT THROUGH FRACTURED MEDIA

185 μm , indicating that the aperture measurements were insensitive to shim size of at least 102 μm or smaller. Fracture permeability measurements with the 102 μm shims installed can be seen in Figures 4.8.

It was observed that the absolute permeability was changing with flow rate for fracture pressures below about 0.5 psig. It was implied that the fluid was lifting the glass as it flowed through the fracture. At pressures greater than 0.034 atm, the glass was lifted to its maximum height defined by the confinement of the metal frame. At this pressure range, the fracture permeability was constant and found to be around 3100 darcy.

Due to the inconsistency between the measured fracture hydraulic aperture (185 μm) and shim size (102 μm), further investigation was carried out. The hydraulic aperture was measured after the removal of the shims. In this case, only the o-ring exists between the glass and aluminum plates. It was found that the hydraulic aperture of the fracture to be around 57.25 μm with an average permeability of 272.35 darcy. This implied that the o-ring was compressed to a minimum height of about 57 μm . When shims were installed, additional thickness of shims was added. If fracture surfaces were perfectly flat, the measured fracture aperture should be the sum of the o-ring and shim thicknesses (i.e. 102 μm plus 57 μm or total of 159 μm). The difference between measured aperture and expected value (about 26 μm) was attributed to measurement error or a result of irregularities of flat surfaces. The fracture permeability measurements without shims can also be seen in Figures 4.8. To avoid uncertainty of aperture measurements, it was decided to use the model without shims during injection of microparticles. That required the influent sample to have particles smaller than 57 μm .

To confirm the validity of Darcy's law (i.e. flow in fracture is laminar and that inertia effect is negligible), we examined the linearity between single-phase pressure drop and flow rate. Figure 4.9 shows a linear relationship between the pressure drop and flow rate, indicating the negligible effect of inertia.

CHAPTER 4. EXPERIMENTAL INVESTIGATION OF PARTICLE TRANSPORT THROUGH FRACTURED MEDIA

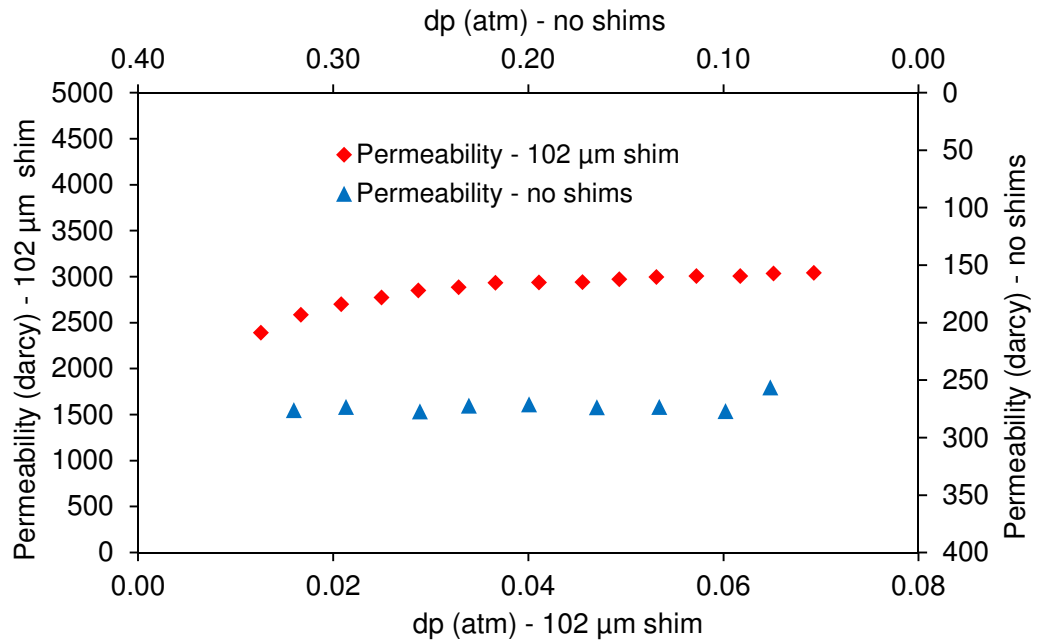


Figure 4.8: Fracture permeability of the glass fracture model, with and without 102 μm shims.

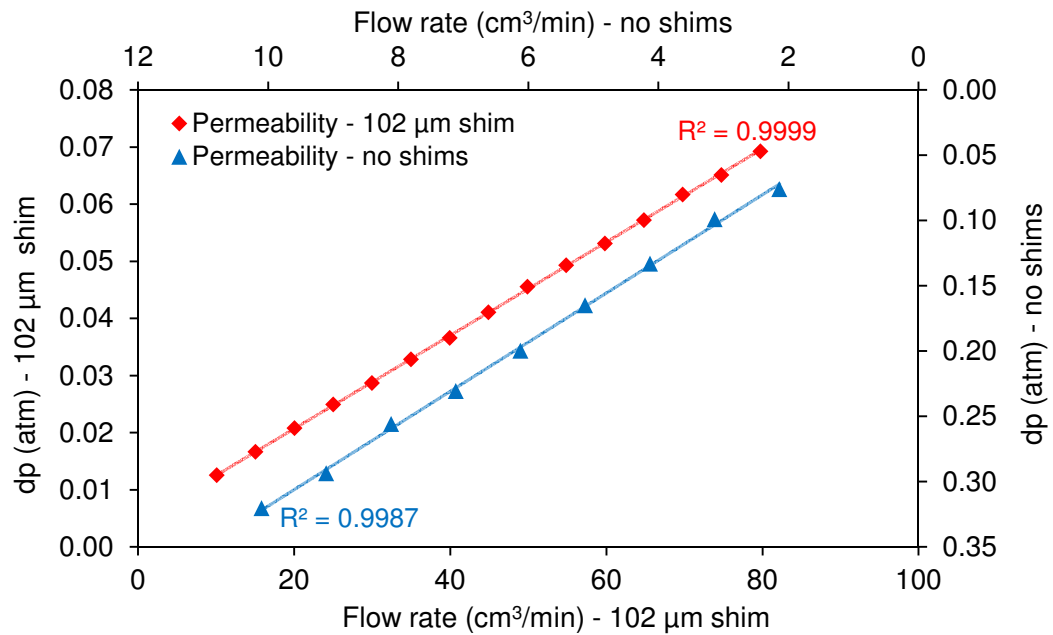


Figure 4.9: Validity of Darcy law under experimental conditions was confirmed through the linearity between flow rate and pressure drop.

CHAPTER 4. EXPERIMENTAL INVESTIGATION OF PARTICLE TRANSPORT THROUGH FRACTURED MEDIA

4.2.2.2.3 Fractured Berea permeability measurements

The physical properties of fractured Berea sandstone core plug used are summarized in Table 4.1. The core plug was fired at 700°C for 2 hours. This firing process was implemented to stabilize the indigenous fines and produces strongly water-wet conditions (Syndansk, 1980; Shaw et al., 1989). Prior to saturation, the core plug was dried under vacuum pressure of 0.09 MPa at 70°C for 24 hours using a vacuum oven. The core was then saturated with testing fluid (i.e. ultrapure water prepared using Q-Millipore) inside the core-holder. The saturation was accomplished by evacuating the system (core plug and connecting tubing) to vacuum pressure below 50 millitorr. The system was left under vacuum for about 4 hours to ensure complete evacuation. The pure water was then introduced and the remaining vacuum was released to aid the process of saturation.

The rock sample was characterized in terms of its porosity, matrix permeability, grain density and pore size distribution. The porosity of the core plug was measured by resaturation of the core (weight difference before and after saturation with testing fluid of known density), helium expansion (gas pycnometer), and mercury intrusion methods and found to be 22%, 21.4% and 20.3%, respectively. The grain density measured by the gas pycnometer was 2.67 g/cm³ and that by mercury intrusion was 2.57 g/cm³. Matrix permeability was measured by introducing flow at different flow rates. The average matrix permeability was approximately 0.51 darcy.

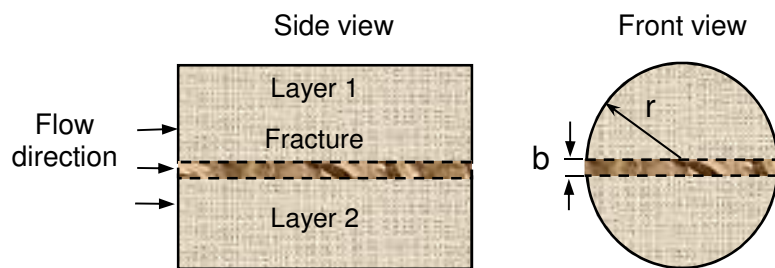


Figure 4.10: Schematic of the sandstone core plug with the location of the fracture. The fracture extends from the inlet to the outlet. The fracture was created by saw-cutting the core into two pieces at the center.

CHAPTER 4. EXPERIMENTAL INVESTIGATION OF PARTICLE TRANSPORT THROUGH FRACTURED MEDIA

The fracture was created by saw-cutting the core plug into two pieces at the center. A schematic of the core showing the location of the fracture can be seen in Figure 4.10. The two pieces were then held together using heat-shrink tubing. The hydraulic aperture of the fracture was estimated by considering the flow in parallel layers. Under conditions of flow in parallel layers, the pressure drop across each layer is the same. The total flow rate is the sum of flow rate in each layer. That is:

$$q_t = q_1 + q_2 + q_f \quad (4.3)$$

using Darcy's Law of incompressible horizontal fluid flow $q = kA(\Delta p)/\mu L$,

$$k_t A_t = k_1 A_1 + k_2 A_2 + k_f A_f \quad (4.4)$$

Because $k_1 = k_2 = k_m$ and assuming $A_t = A_1 = A_2 = \pi r^2$, $k_f = b^2/12$ (cubic law) and $A_f = 2br$, then Equation (4.4) becomes:

$$b = \sqrt[3]{6\pi r(k_t - k_m)} \quad (4.5)$$

where r is the radius of the core plug in meter, k_t and k_m are the total and matrix permeability in square meters, respectively. Note that the matrix permeability (k_m) was determined before cutting the fracture. The hydraulic aperture of the fracture varied between 17.9 to 62.4 μm at different confining pressure ranging from 8.5 to 50 atmospheres. All particles injections were performed under confining pressure of 8.5 atmospheres. The maximum hydraulic aperture in these experiments was estimated to be 62.4 μm ($k_t=1.23$ darcy) using flow in parallel layers (Equation 4.5). The minimum aperture was approximated to be 3.79 μm by assuming the fracture permeability to be equal to the total permeability (1.23 darcy). The total permeability (fracture and matrix) as a function of flow rate, and the relationship of flow rate to pressure drop can be seen in Figure 4.11.

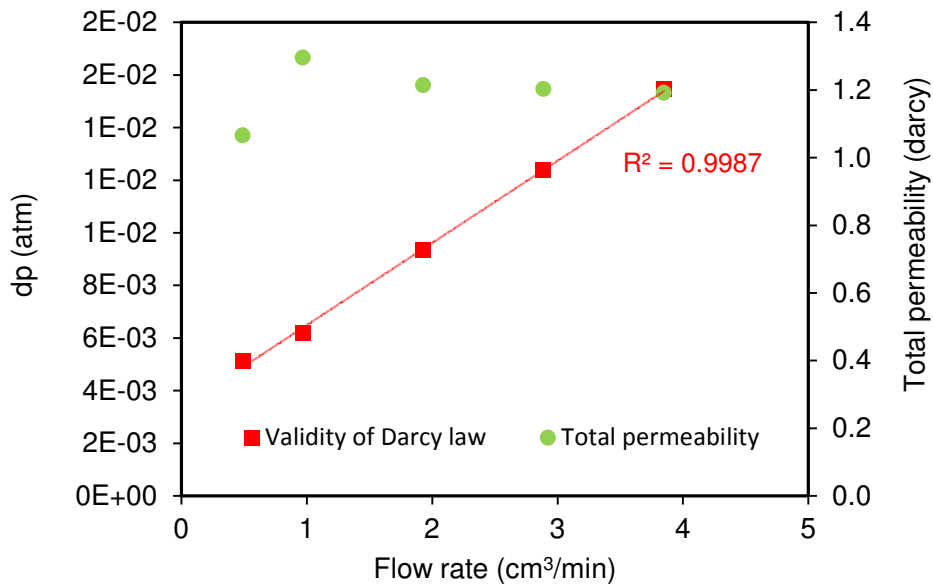


Figure 4.11: Total permeability measured at different volumetric flow rates. The validity of Darcy's law is also verified through the linear relationship between pressure drop and volumetric flow rate.

4.3 Particle suspension injection methods

The injection process and sampling strategies in all experiments were similar, however, they differed in some aspects such as total pore volume injected, flow rates and sampling frequency. A summary of the injection experiment flow parameters can be seen in Table 4.2.

4.3.1 Fractured greywacke experimental setup and injection method

The testing apparatus allows for a switch to injection of particle-free deionized water, without interrupting the flow. The particle suspension was contained in a syringe downstream from the water pump (Figure 4.12). All equipment was the same as those used during permeability measurements.

CHAPTER 4. EXPERIMENTAL INVESTIGATION OF PARTICLE TRANSPORT THROUGH FRACTURED MEDIA

Table 4.2: Summary of fractured rocks and glass model flow experiments parameters^a

Flow medium	SiO ₂ suspension	q (cm ³ /min)	v _m (cm/min)	v _f ^{d,e} (cm/min)	V _{NP} (cm ³)	c (mg/cm ³)
Fractured Greywacke	SiO ₂ NP ^c	0.50	0.62	32.08	1.00	N/A
	Blue	0.68	0.84	43.63	1.00	0.49
	Blue	0.68	0.84	43.63	1.00	0.98
	Green	0.78	0.96	50.05	1.00	0.49
	Green	0.78	0.96	50.05	1.00	0.98
	Red	1.00	1.23	64.16	1.00	0.49
	Red	1.00	1.23	64.16	1.00	0.98
Glass model	Blue	0.50	N/A ^b	8.78	1.00	0.49
Fractured Berea	Blue	1.00	0.41	7.39	2.50	0.49
	Blue	1.00	0.41	7.39	2.50	0.98
	Blue	1.00	0.41	7.39	2.50	1.92
	Blue	3.00	1.22	22.06	2.50	0.49
	Blue	3.00	1.22	22.06	2.50	0.98
	Blue	3.00	1.22	22.06	2.50	1.92
	Green	1.00	0.41	7.39	2.50	0.49
	Green	1.00	0.41	7.39	2.50	0.98
	Green	1.00	0.41	7.39	2.50	1.92
	Green	3.00	1.22	22.06	2.50	0.49
	Green	3.00	1.22	22.06	2.50	0.98
	Green	3.00	1.22	22.06	2.50	1.92
	Green	10.00	4.05	73.38	2.50	0.49

^aHere q is the volumetric flow rate, v_m and v_f average fluid pore velocity in matrix and fracture, V_{NP} is the injected particle suspension volume and c is the particle suspension mass concentration

^bN/A denotes that the measurement is not applicable or could not be determined.

^cNP stands for Nanoparticles.

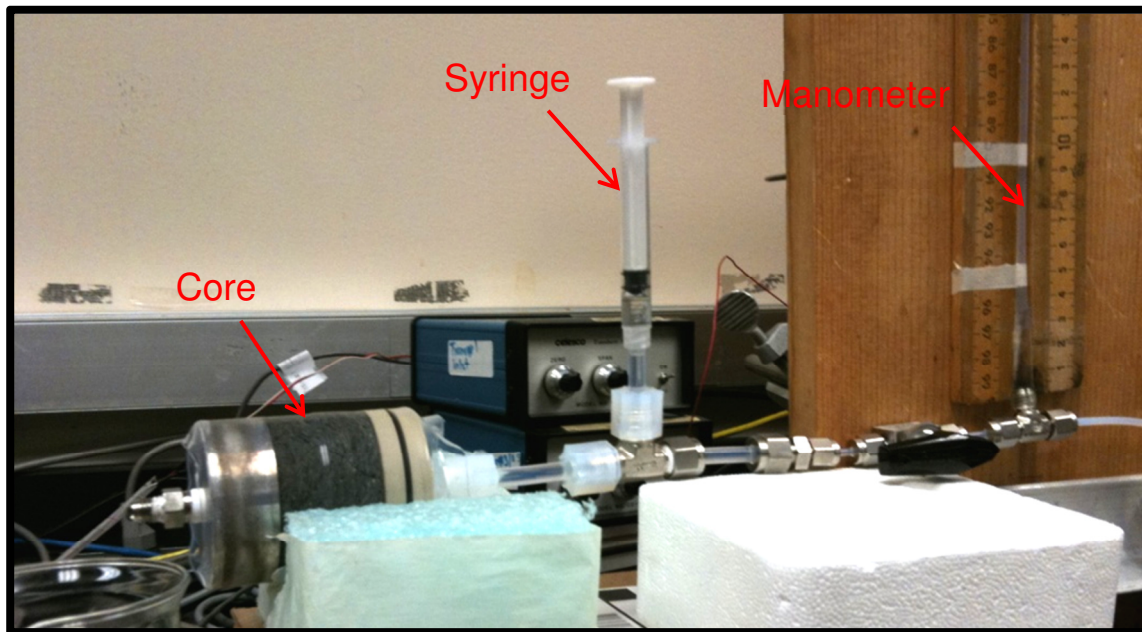
^dThe water velocity inside the fractured greywacke core was calculated based on total flow. All water is assumed to flow through the fracture (no flow through the matrix) since the matrix has very low permeability in the sub-millidarcy range (1.5×10^{-4} md, Table 3.1) and applied differential pressure used during injection of particles was a fraction of one atmospheric unit.

^eThe water velocity inside the fractured Berea core was calculated based on the fractional flow rate that enters the fracture (17% of the total flow) based on the permeability data.

CHAPTER 4. EXPERIMENTAL INVESTIGATION OF PARTICLE TRANSPORT THROUGH FRACTURED MEDIA

The particles were injected using the syringe. All silica suspensions (blue, green, and red fluorescent samples) were diluted to two distinct mass concentrations (i.e., $C = 0.5 \text{ mg/cm}^3$ and $2C = 1 \text{ mg/cm}^3$), resulting in six influent samples (two blue, two green, and two red). The volume injected into the fractured core sample was one cubic centimeter. Prior to the injection of particle suspensions, the samples were sonicated (using Branson 2510 Bath Sonicator). The core was preflushed with several pore volumes of deionized water. Following the injection of the particles (1 cm^3), a continuous flow of deionized water was introduced.

Before the injection of silica microspheres, silica nanoparticles (volume injected 1 cm^3 of unknown concentration at $0.5 \text{ cm}^3/\text{min}$) were transported through the fractured greywacke core. The objective of this experiment was to investigate the transport of silica nanoparticles through fractured greywacke core, providing a baseline for subsequent injections of the fluorescent silica microspheres.



4.12: A picture of the silica particle injection apparatus showing the manometer and syringe used for pressure measurements and particle suspensions injection, respectively.

CHAPTER 4. EXPERIMENTAL INVESTIGATION OF PARTICLE TRANSPORT THROUGH FRACTURED MEDIA

The sequence by which the transport of the silica particles through the fractured greywacke core was investigated is as follows. Initially, the blue and green microsphere suspensions of mass concentration C were injected, followed by the injection of the blue and green microsphere suspensions of mass concentration $2C$. Following each injection, effluent samples were collected. Because of the polydisperse nature of the red silica particles and concerns regarding plugging of the fracture by larger spheres, red particle suspensions (C and $2C$) were injected at the end.

4.3.2 Glass fracture model description and injection method

The testing apparatus was similar to the permeability measurement experiment, but modified slightly to allow for the injection of microparticles. The particle suspension was injected into the glass model through an injecting loop. The pressure difference across the length of the fracture was obtained using low capacity differential transducers. Two liquid-filled differential transducers (Validyne Transducer, model DP-215, range 0-1.5 psi and 0-5 psi) were attached to inlet and outlet pressure ports. Both differential pressure transducers were calibrated using a standard pressure gauge with an accuracy of 0.1 psi. The pressure calibration curves (not shown) indicated a good agreement between the standard pressure gauge and the differential pressure transducers. A water pump (Dynamax, Model SD-200) was used to inject particle suspension (through the injection loop) and post-inject deionized water into the fracture model. The water pump was also calibrated, using a balance (Mettler, model PE 300) and stop watch, and measured flow rates were consistent with those specified on the pump.

The fracture model consists of a smooth glass plate placed on top of an aluminum flat surface. The seal was achieved by placing an o-ring (Viton 1/8" thick #2-272) between the glass (top) and aluminum (bottom) plates. Also, a metal frame was bolted to the bottom plate to improve the seal. The metal frame was designed with supporting beams to prevent glass deformation due to system pressure. The spacing between these two surfaces is the simulated fracture of predetermined width and length (10.16 cm by 30.48 cm). The fracture model is pictured in Figure 4.13.

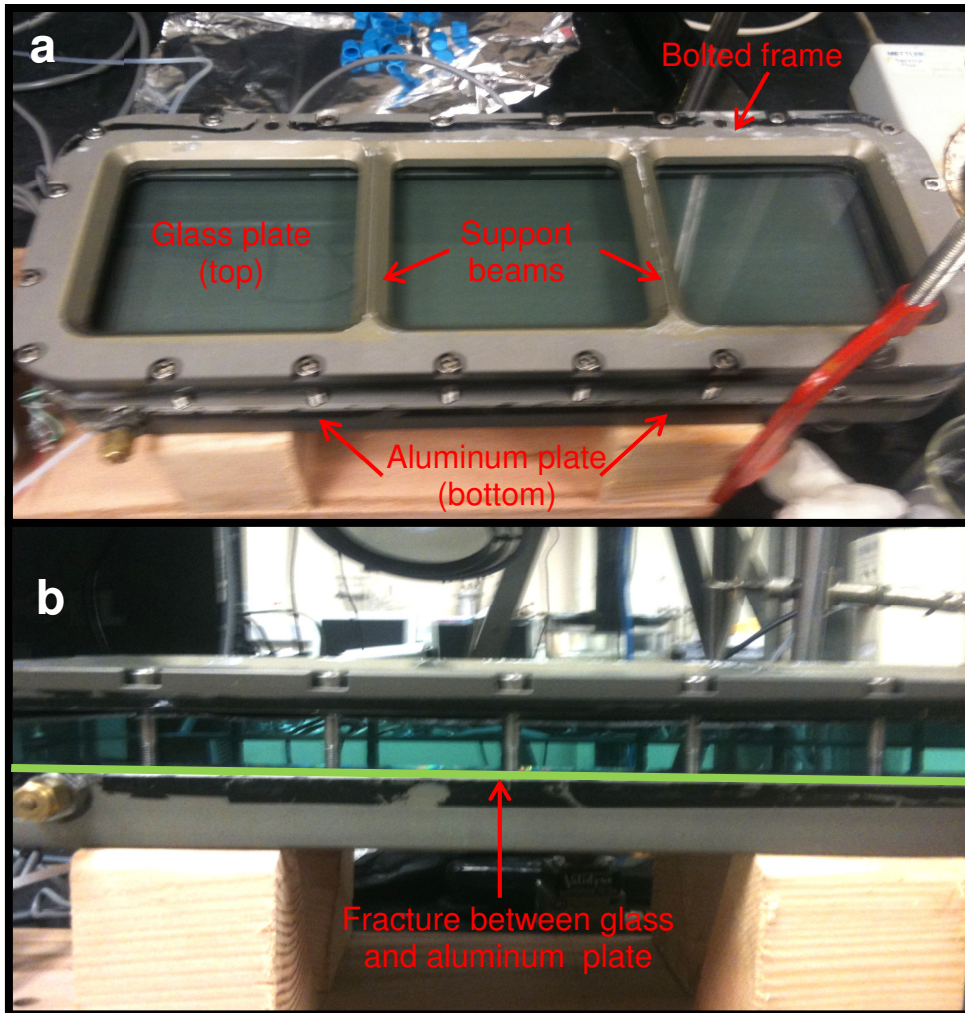


Figure 4.13: Pictures of fracture glass model, showing (a) the bolted frame, top glass and bottom aluminum plates and (b) the fracture location.

Because the fracture apparatus was originally designed to study two-phase flow, each fluid enters the fracture through two separate inlet ports, a total of 123 capillary ports, each 0.51 mm in diameter. These ports were aligned to the fracture surface alternately. Four pressure ports with a diameter of 0.51 mm were drilled at locations throughout the fracture area. Temperature ports were also drilled, but not used during particle injection experiments. Ports were drilled with a needle-size drill to minimize surface discontinuity. The fluids exit the fracture through a single outlet. A schematic diagram of the fracture apparatus is depicted in Figure 4.14.

CHAPTER 4. EXPERIMENTAL INVESTIGATION OF PARTICLE TRANSPORT THROUGH FRACTURED MEDIA

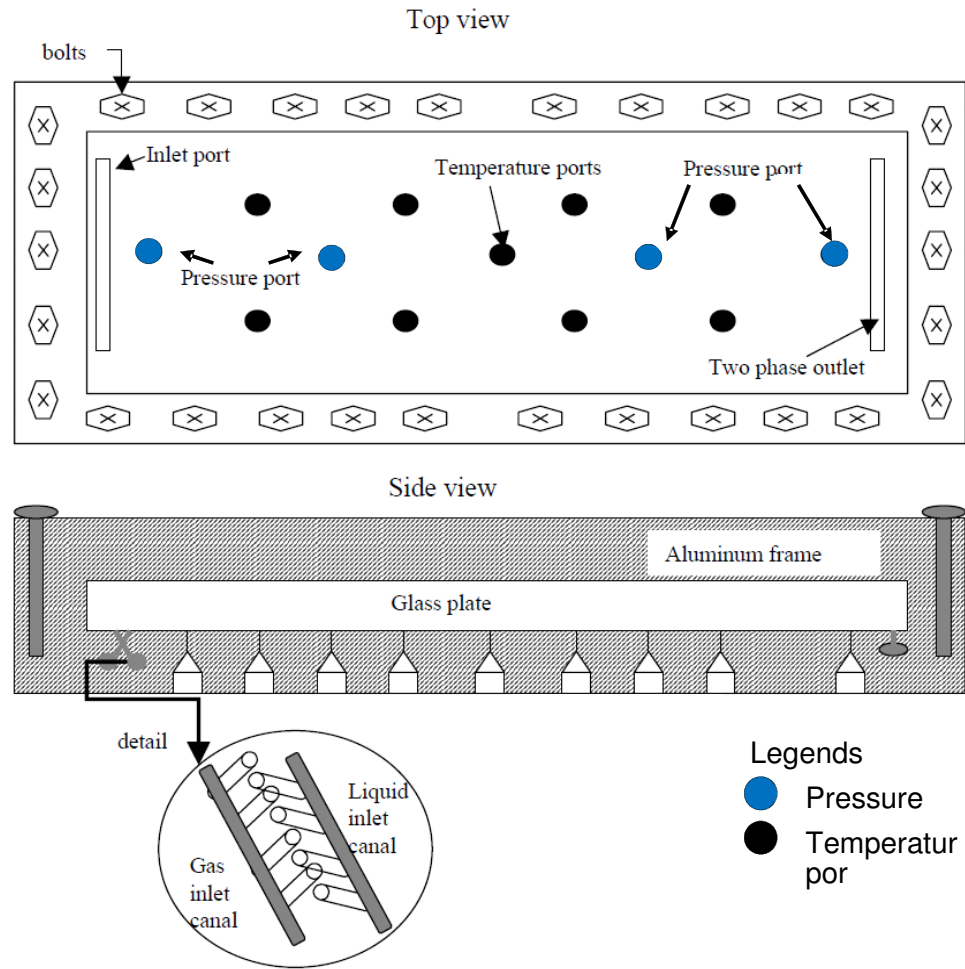


Figure 4.14: Schematic of the fracture apparatus (adopted from Diomampo, 2001).

4.3.3 Fractured Berea experimental setup and injection method

A schematic of the experimental apparatus employed for the silica particle transport through fractured Berea sandstone is shown in Figure 4.15. The apparatus consists of ultrapure water container, water pump, injection loop, syringe, differential pressure transducer and a core-holder. Effluent samples were analyzed by standalone fluorometer. Water ($\rho_w = 0.997 \text{ g/cm}^3$, $\mu_w = 0.982 \text{ cp}$ at 21°C) used throughout the experiments was purified using Millipore (A10) equipped with $0.220 \text{ }\mu\text{m}$ filter, and deaerated at 50 millitorr vacuum for at least 30 minutes prior to use. Particles were injected using a syringe through the injection loop. The injection loop allowed an alternating injection of

CHAPTER 4. EXPERIMENTAL INVESTIGATION OF PARTICLE TRANSPORT THROUGH FRACTURED MEDIA

particle suspension and particle-free water, without interrupting the flow. Volumetric flow rates were varied between 1 to 10 cm³/min using a pump equipped with standard head manufactured by Dynamax. The pump flow rate was calibrated using stop watch and balance (Mettler PM300) with 0.01 gram accuracy. The differential pressure across the core plug was measured using differential pressure transducer (Validyne Model DP215-50) with low pressure rating diaphragm. The transducer was calibrated with standard pressure gauge with accuracy of 1.25% of full range.

Prior to the injection of the particle suspensions, the core was preflushed with pure water. The preflushing samples were analyzed to determine the existence of any naturally occurring particles. The injection sequence involved the introduction of the particle suspension slug followed by a continuous injection of pure water. In particular, the volume of particle suspension injected in to the core was 2.5 cm³. Subsequently, a continuous flow of pure water (post-injection) was carried out. Depending on the experiment, a few pore volumes of pure water were injected while the effluent samples were collected. The total time of the experiment, flow rates and frequency of sampling were also experiment dependent.

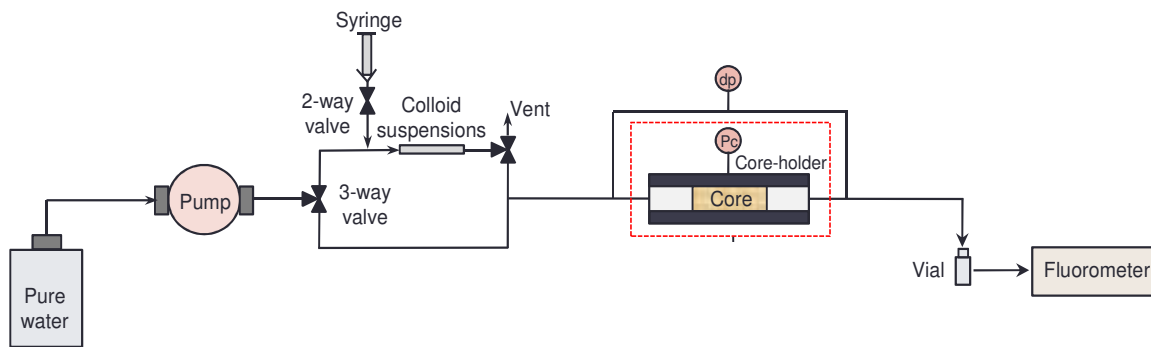


Figure 4.15: Schematic of the experimental apparatus employed in the silica particle transport.

CHAPTER 4. EXPERIMENTAL INVESTIGATION OF PARTICLE TRANSPORT THROUGH FRACTURED MEDIA

To investigate the influence of particle size, concentration and fluid velocity on the transport of particle through the core plug, 13 injections were conducted. For each particle size, every suspension concentration (C, 2C and 4C) was injected at 1 and 3 cm³/min. In addition, the 5 µm particle suspension at concentration (C) was injected at 10 cm³/min. The breakthrough curves of the silica particles were determined by measuring the emission spectrum and correlating it to the effluent concentration using a calibration curve.

4.4 Results and discussion

This section provides the results of the silica particles injection experiments carried out on fractured Berea and greywacke core samples and the glass fracture model. We investigated the effect of the particle size and suspension concentration on their transport through the fractured greywacke core. The fracture aperture caliper concept (estimating the fracture aperture based on the largest recovered particle) was demonstrated through the injection of the polydisperse red silica particles. The fractured Berea sandstone was also used to study the effect of particle size, suspension concentration and fluid velocity of particle recovery. Berea sandstone represents a fracture-matrix system, whereas fractured greywacke represents flow mostly in fractures because of its tight matrix. The glass model experiment was conducted to verify the effect of fracture surface roughness using the blue silica suspension.

In the following sections, the results of fractured greywacke and Berea experiments are presented. The results of the glass fracture model are used to support findings of the fractured core experiments. Experiments results are then discussed in terms of the effect of hydrodynamic conditions (fluid velocity) and particle size and concentration on particle transport.

4.4.1 Fractured greywacke core experiment results and discussion

This section provides the results of the injection of fluorescent silica particles into the fractured greywacke core. The details of using particles as fracture calipers are also

presented. The results are summarized in Table 4.3. Prior to the injection of silica microspheres, silica nanoparticles were first transported. The objective of the silica nanoparticle injection experiment was to confirm their transport through the fractured greywacke core, providing a baseline for subsequent injections of the fluorescent silica particles. The silica nanoparticles flowed through the fractured greywacke core successfully. The nanoparticles had an average particle size of 0.35 μm . The effluent samples were examined for the presence of the nanoparticles using the light scattering technique. Effluent samples showed particle size distributions that were identical to the particle size distribution of the injected influent.

4.4.1.1 Impact of particle size and input concentration of on particle recovery

The return curves for the blue, green and red silica particles showed a very fast arrival. The first arrival of the particles occurred within 0.02 and 0.09 pore volumes from the start of their injection. This shows that the recovered particles were moving through the fracture, not the core matrix. The pore-size distribution of greywacke sandstone (see Figure 3.1) indicated that the largest pore throat is 0.150 μm . The largest pore is significantly smaller than the smallest the silica particles (2 μm). The first arrival of blue silica particles was at 0.104 min. The blue silica particles were producing at constant levels with no identifiable concentration peak. The breakthrough curves (Figure 4.16) of the green and red silica particles show that the first arrivals were at 0.123 and 0.029 min, respectively. The relative concentration of the green silica particles decreased to below 0.001 of injection concentrations following the post-injection of about four pore volumes of water. Backflushing samples (at sixth pore volume and beyond) showed very low concentration of green particles, indicating that particles were not depositing at the inlet of the fracture. The relative concentration of the red particles decreased below 0.004 of injected concentrations at the sixth post-injected pore volume, with slight fluctuation in the relative concentration of the backflushing samples (beyond the sixth and third post-injected pore volumes for the 2C and C suspension concentration injections). The cumulative relative concentrations were gradually increasing until the end of the post-injection and/or backflushing.

CHAPTER 4. EXPERIMENTAL INVESTIGATION OF PARTICLE TRANSPORT THROUGH FRACTURED MEDIA

Table 4.3: Results of fractured greywacke and Berea rock samples^a

<i>Flow medium</i>	<i>SiO₂ suspension</i>	<i>q (cm³/min)</i>	<i>c (mg/ml)</i>	<i>τ (min)</i>	<i>(C/C_o)_{max}</i> -	<i>(C/C_o)_{cum}</i> -
<i>Fractured greywacke</i>	<i>Blue</i>	0.68	0.49	0.10	0.48	N/A
		0.68	0.98	0.10	0.17	N/A
	<i>Green</i>	0.78	0.49	0.12	0.40	0.93
		0.78	0.98	0.12	0.55	0.82
	<i>Red</i>	1.00	0.49	0.03	0.03	0.08
		1.00	0.98	0.03	0.09	0.21
<i>Glass model</i>	<i>Blue</i>	0.5	0.49	0.57	0.65	0.76
<i>Fractured Berea</i>	<i>Blue</i>	1.00	0.49	0.12	0.26	1.01
	<i>Blue</i>	1.00	0.98	0.18	0.23	0.78
	<i>Blue</i>	1.00	1.92	0.24	0.16	0.47
	<i>Blue</i>	3.00	0.49	0.04	0.24	0.99
	<i>Blue</i>	3.00	0.98	0.06	0.21	0.86
	<i>Blue</i>	3.00	1.92	0.08	0.14	0.52
	<i>Green</i>	1.00	0.49	0.36	0.06	0.13
	<i>Green</i>	1.00	0.98	0.31	0.08	0.19
	<i>Green</i>	1.00	1.92	0.48	0.04	0.09
	<i>Green</i>	3.00	0.49	0.12	0.19	0.64
	<i>Green</i>	3.00	0.98	0.10	0.21	0.58
	<i>Green</i>	3.00	1.92	0.16	0.18	0.52
	<i>Green</i>	10.00	0.49	0.03	0.36	1.01

^aHere q is the volumetric flow rate, c is the particle suspension mass concentration, τ is the first arrival time of particles, $(C/C_o)_{max}$ is the maximum recovered relative concentration and $(C/C_o)_{cum}$ is the cumulative relative concentration.

^bN/A denotes that the measurement could not be determined.

The maximum $(C/C_o)_{max}$ and cumulative $(C/C_o)_{cum}$ relative concentration of the silica particles varied according to suspension concentration and particle size with average values as listed in Table 4.3. Generally, the particle recovery was increasing with

CHAPTER 4. EXPERIMENTAL INVESTIGATION OF PARTICLE TRANSPORT THROUGH FRACTURED MEDIA

increasing injected suspension concentration (except for the blue particles), and decreasing with increasing particle size. Similar findings with regard to the influence of injected suspension concentration to particle recovery were reported in the literature (e.g. Tan et al., 1994; Liu et al., 1995; Bradford and Bettahar, 2006). Higher particle concentrations produced more rapid filling of favorable attachment sites than lower particle concentrations, and therefore resulted in greater breakthrough concentrations. Conversely, the recovery of the blue silica particles exhibited the opposite trend. The recovery of particles was lower with increasing input mass concentration. This behavior suggested that there was particle/particle interaction, causing the particles to aggregate.

As the suspension concentration increases, more particles are present, resulting in larger aggregates or clusters. Note that although the mass concentrations of all particle suspensions were the same, the number concentration (number of particles per unit volume) was different. For the same mass concentration, the number concentration of the 2 μm particles is 15.6 times more than that of the 5 μm particles. The rate of particle collision, which is often used as a precursor to aggregation, varies proportional to approximately the square of the number concentration. Therefore, for the same mass concentration, smaller particles are expected to aggregate at much faster rate than larger particles (i.e. the 2 μm particles would aggregate 244 times faster than the 5 μm particles). Although particle suspensions were sonicated prior to injection, there was still a chance for the blue silica particles to aggregate sooner, at least when compared to the green and red particles. It was speculated that the 2 μm blue particles were aggregating to form larger clusters. When these clusters flow through areas of narrower aperture (areas in which fracture surfaces are closer to each other), they will be trapped because of their physical size. With the tendency to aggregate, the higher the concentration, the larger is the size of the clusters and therefore the retention was enhanced. This could explain the lower breakthrough concentrations of the 2 μm particles at higher input concentration. The extent to which the 2 μm particles were straining with increasing concentration was confirmed by direct observation using micromodels. Further details can be found in Section 5.5.1.

CHAPTER 4. EXPERIMENTAL INVESTIGATION OF PARTICLE TRANSPORT THROUGH FRACTURED MEDIA

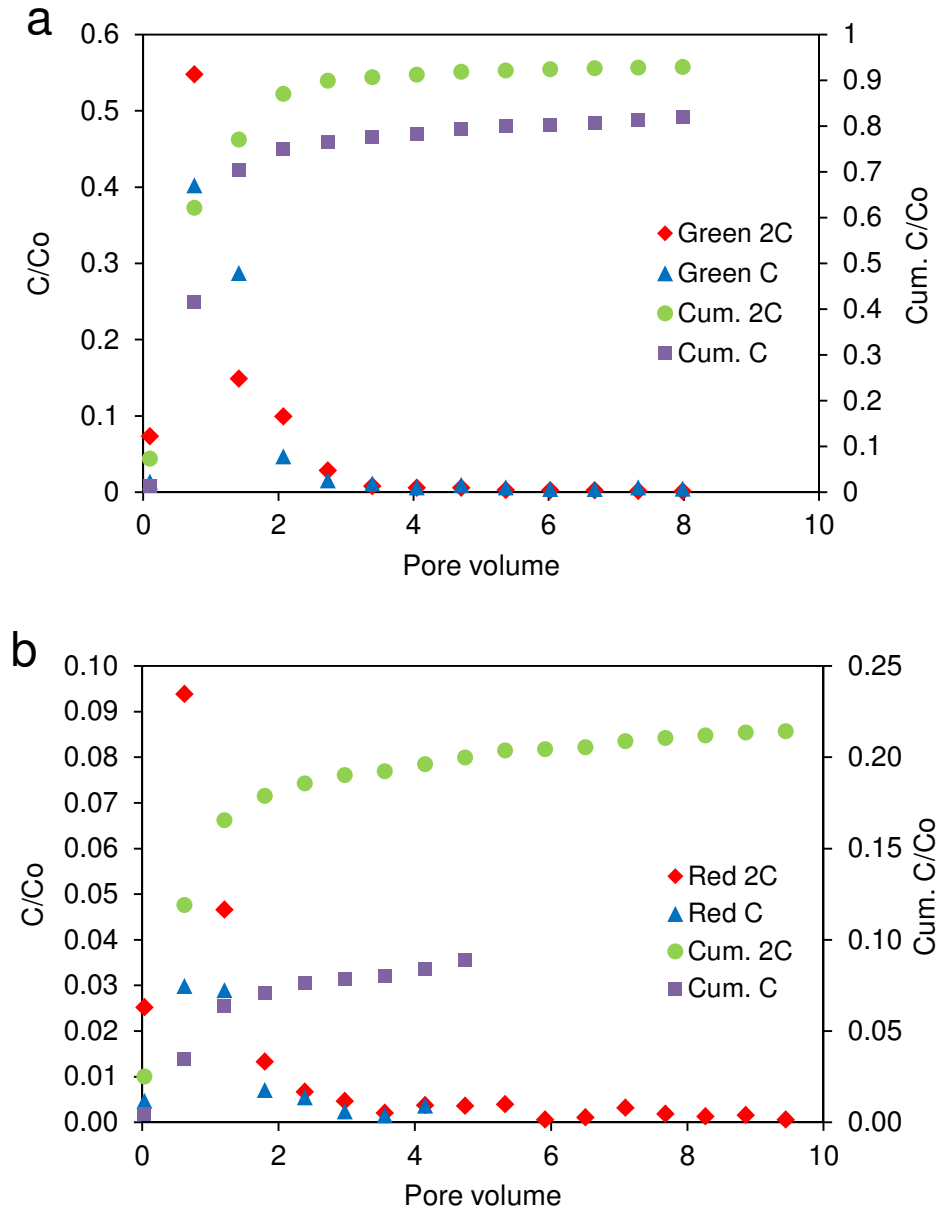


Figure 4.16: Relative concentrations of (a) green and (b) red silica particles at two different suspension concentrations following their injection through fractured greywacke sandstone. The cumulative relative concentration is also included. For the green particles, data points beyond the sixth pore volume represent backflushing samples. For the red particles, backflushing samples start at the sixth pore volume and third pore volume for the 2C and C suspensions, respectively.

CHAPTER 4. EXPERIMENTAL INVESTIGATION OF PARTICLE TRANSPORT THROUGH FRACTURED MEDIA

For the 5 μm particles, the estimation of the total interaction energy (Figure 4.4) among the green particles suggests a high repulsive-energy barrier, along with the lower rate of collision would prevent the particles from aggregation. Instead, the particles will repel from fracture surfaces and from each other and remain disperse in solution. We speculated that the retention of the green particles within the fractured medium was related to transport by gravitational sedimentation. Note that the density of the silica particles is more than twice that of the injected water (i.e., 2.2 g/cm^3). During transport by sedimentation, a particle moves across streamlines because of gravitational forces and associated settling velocity until it collides with the fracture surface. The calculated settling velocity, for creeping flow, of the 5 μm particles is around 16.4 $\mu\text{m}/\text{sec}$. Based on the fracture data and injection rate (i.e. 0.78 cm^3/min), the 5 μm particles are expected to settle 54 μm (twice the estimated fracture aperture) within the fracture. This suggests that these particles were rolling along the fracture surface. Given their large size relative to the fracture aperture, and the high repulsive energy interaction, drag forces at the fluid velocity used during injection might be sufficient to roll the particles. The effect of fluid velocity was not assessed because the objective of the fracture experiments was to investigate only the influence of the particle size and its relation to fracture aperture. The influence of the fluid velocity on particle transport was investigated during the injection into the fractured Berea sandstone. Therefore, it was concluded that the low recovery of the green particles was primarily a result of gravity settling.

Owing to the existence of surface irregularities in fractures, it is very possible that a flow channel in the fracture at or below the size of injected particles exists along a preferential flow path. Consequently, entrapment of particles because of their physical size will result in their accumulation at narrow aperture areas and, therefore, the total blockage of that flow path. Blocked flow paths are a dead end for subsequent particles, which eventually results in reduction of particle recovery. The permeability measurements (i.e., pressure data) support the fact that the number of conductive flow paths available to particles decreased because of blockage. Figure 4.17 shows the permeability measurements conducted before and during the injection of the blue and green particles at two different

CHAPTER 4. EXPERIMENTAL INVESTIGATION OF PARTICLE TRANSPORT THROUGH FRACTURED MEDIA

suspension concentrations through the fractured greywacke core. The permeability continued to decrease as more particles were injected. The permeability decreased to approximately 22 darcy by the end of the blue particle (of Concentration C) injection. This reduction in permeability indicates a certain degree of blockage that occurred in some of the preferential flow paths. After that, the permeability decreased slightly as more particles were injected (during the injection of blue and green silica particles at concentration of 2C). The slight decrease in permeability following the injection of concentrated suspensions can be explained by the fact that small flow paths were already plugged during previous injections (injection of blue and green suspensions at concentration C), and the flow of subsequently injected particles was redirected to areas of wider apertures at which trapping by particle size is least expected.

A test injection of blue silica particles into the glass fracture model was conducted to investigate the effect of fracture surface irregularities (varying aperture) on particle recovery. The glass fracture model represents a smooth-walled fracture with constant aperture throughout the fracture width and length. In other words, preferential flow paths, if they exist, should have aperture size similar to the rest of the fracture (i.e. 56.79 μm , Table 4.1). The blue silica suspension ($C = 0.49 \text{ mg/ml}$) used during the glass model injection was the same as that used during injection into the fractured greywacke core under similar volumetric flow rate ($q = 0.5 \text{ cm}^3/\text{min}$). The average residence time of water was about five times larger than in the fractured greywacke ($\tau = 0.57$ versus 0.10 min), allowing more time for the silica particles to interact with the glass model fracture walls in cases where the particles have an affinity to glass and/or aluminum walls. The maximum relative concentration of recovered blue particles was about 0.65 (Table 4.3), 17% more than measured during injection into the fractured greywacke under the same experimental conditions. The permeability of the glass fracture model remained unaltered. Note that the greatest reduction in permeability of the fractured greywacke core injection occurred during the transport of the blue silica suspension of concentration C (permeability decreased from 61 to 40 darcy). The results of the glass model support

CHAPTER 4. EXPERIMENTAL INVESTIGATION OF PARTICLE TRANSPORT THROUGH FRACTURED MEDIA

the hypothesis that fracture aperture irregularities at preferential flow path may affect recovery of the transported particles.

The recovery of the larger polydisperse red particles was significantly lower than the blue and green particles. For example, the cumulative relative concentration of red and green particles at concentration C was approximately 0.08 and 0.93, an order of magnitude difference. This is consistent with the fact that increasing particle size (far from an optimum size) had an inverse effect on particle recovery. The red silica suspension had particles of sizes very comparable to the estimated hydraulic fracture aperture (i.e. aperture of $30.68\ \mu\text{m}$ versus particle size of $31\ \mu\text{m}$). Thus, it was anticipated that more of the red particles would be physically trapped at the matrix inlet pores and/or in the fracture. It was also observed that increasing the input concentration resulted in higher recovery (Figure 4.16b). The main objective of the red particle injection was to investigate the fracture caliper concept by relating the size of the largest recovered particle to fracture aperture. This will be explained later, in Section 4.4.1.3.

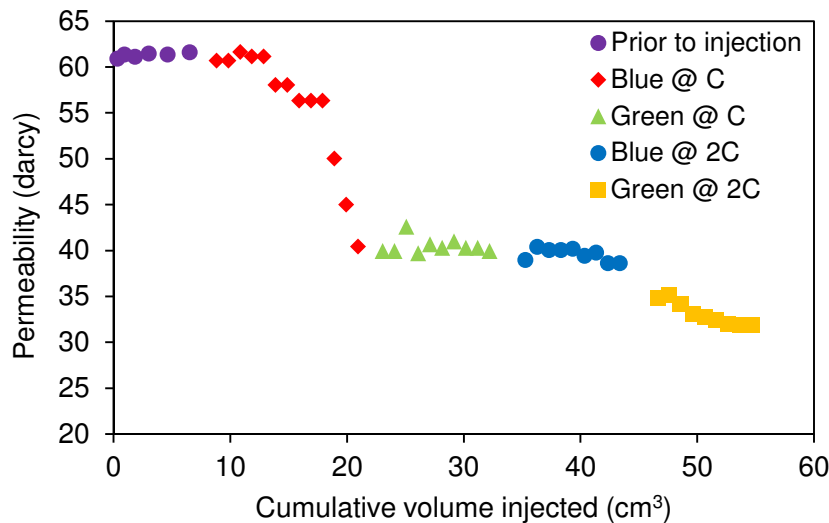


Figure 4.17: Permeability measurement before and during the injection of the blue and green silica particles at different concentrations into fractured greywacke core. The permeability is decreasing as more particles are injected.

4.4.1.2 Particle deposition and transport mechanisms

Particles can be physically deposited on fracture surfaces or matrix pores due to their size, diffusion, interception and gravitational sedimentation. As mentioned earlier, particle transport through the greywacke matrix was not anticipated because the largest available pore size is significantly smaller than the smallest particle injected. Also the early breakthrough of particles suggested that their transport was mainly through the fracture. The ratio of the blue and green particle size to fracture aperture was 0.065 ($2\ \mu\text{m}$ divided by $30.68\ \mu\text{m}$) and 0.163 ($5\ \mu\text{m}$ divided by $30.68\ \mu\text{m}$), respectively, indicating that there should be sufficient space for particle flow. Note that the calculated hydraulic aperture integrates the effect of larger and smaller aperture regions. So it is very possible for the fracture to particle size ratios to be much larger in certain regions of the fracture. Herzig et al., (1970) suggested that straining is important in porous media when the particle to grain size ratio is greater than 0.2. Zvikelsky and Weisbrod (2006) modified this rule of thumb to indicate the significance of straining of particles inside the fracture. They suggested that straining is important if the particle to grain size ratio is greater than 0.02, by assuming that the pore size is about 10% of grain size. Both the blue and green silica particles exhibited particle to grain size ratio larger than 0.02 by at least a factor of three, suggesting that straining may occur within the fracture. It was concluded earlier that the blue particles were aggregating forming large clusters. The size of the cluster may have been larger than the fracture aperture, leading to physical filtration due to size, and thus higher particle deposition inside the fracture. Flushing following the injection of the green silica showed the backflushing effluent samples to have negligible concentration (Figure 4.16a). This suggests that there was no substantial remobilization of the green particles, thus no significant straining. The concentration of the red particles in backflushing samples was fluctuating (Figure 4.16b) indicating some release of particles. Straining of the red particles was therefore likely to occur, especially for particles that have size comparable to the fracture aperture. In fact, the red suspension was designed to have particles as large as the fracture aperture in order to test the fracture caliper concept.

CHAPTER 4. EXPERIMENTAL INVESTIGATION OF PARTICLE TRANSPORT THROUGH FRACTURED MEDIA

Deposition of particles due to interception was unlikely to be important. Particle interception is highly dependent on fluid velocity. Higher fluid velocity would result in lower probability of filtration by interception. Fluid velocities used during the injection of blue, green and red silica suspensions were 43.63, 50.05 and 64.16 cm/min (Table 4.2), respectively, yet there was lower recovery of larger particles. The influence of fluid velocity was studied further during particle injection into fractured Berea sandstone (see Section 4.4.2.1).

Particle deposition by diffusion and gravitational sedimentation can be assessed using the length scale analysis suggested by Becker et al. (1999). According to the length scale model, the particle deposition was due mainly to gravity settling. In general, diffusion of particles in the micron size range is known to be insignificant. A summary of length scales and Peclet number is provided in Table 4.4. The L_s/L_D and $L_s/0.5b$ ratios were significantly larger than 1.0, suggesting that the transport by gravity settling is dominating and the lower surface of the fracture is accessible (the $L_s/0.5b$ is also greater than 1.0). The settling distances of 120.74 and 113.80 μm for the green and red particles are about four times the fracture aperture size (30.68 μm). Therefore, it is likely that the particles were rolling along the lower surface of the fracture. The high density of the particles (2.2 g/cm^3) relative to suspension fluid (i.e. water with density of 1.0 g/cm^3) also suggests settling.

The dominance of particle transport by advection or diffusion was evaluated using the Peclet number. The calculated Peclet numbers for all particle sizes under the hydrodynamic experimental conditions were in the order of 10^5 to 10^7 . These values are orders of magnitudes higher than 1.0, indicating advection-dominated transport. The extremely low diffusion coefficients (2.15×10^{-13} , 8.62×10^{-14} and 4.31×10^{-14} m^2/s for blue, green and red particles), calculated using Equation 2.2, and the hydrodynamic forces (lift forces) acting on the finite size of the particle may force the particles to follow high velocity streamlines within the fracture, and hence faster breakthrough. For instance, the red particles were traveling at a velocity that was about 2.11 times the average

CHAPTER 4. EXPERIMENTAL INVESTIGATION OF PARTICLE TRANSPORT THROUGH FRACTURED MEDIA

velocity of water. Advection-dominated transport of particles through fractures is well documented by other investigators (e.g. Riemus 1995; Cumbie and McKay, 1999; McCarthy et al., 2002).

Table 4.4: Summary of calculated length scales and Peclet number for blue, green and red silica particles in fractured greywacke core^a.

Flow medium	SiO ₂ suspension	U _s (μm/s)	L _s (μm)	L _s /L _D	L _s /0.5b	Pe
Fractured greywacke	Blue	2.63	16.39	9.97	1.07	8.95x10 ⁵
	Green	16.35	120.74	107.02	7.87	1.90x10 ⁶
	Red ^b	65.40	113.80	293.86	7.42	1.61x10 ⁷

^aHere U_s is the particle settling velocity (Equation 2.11), L_s is the length scale of Stoke settling of spherical particle (Equation 2.12), L_D is the length scale of diffusion (Equation 2.13), b is the fracture hydraulic aperture and Pe is Peclet number (Equation 2.10)

^bParameters were calculated based on nominal size of 10 μm.

4.4.1.3 Fracture aperture estimation using particles (Fracture caliper concept)

We demonstrated the feasibility of transporting nanoparticles and/or microparticles through a fractured greywacke core. In terms of characterizing the fractures in the rock, which is a primary objective of the project, the preliminary experiments showed promise. The preliminary testing involved injection of silica nanoparticles through Berea sandstone. The details for the preliminary experimental work can be found in Section 3.5.5.1. It was found that the nanoparticles passed through pores of sizes larger than themselves, but were unable to pass into the smaller natural fractures that existed within the rock structure (Figure 4.18). A smaller nanoparticle could have entered the fracture, providing a direct correlation between the recovered particle size and fracture aperture. Therefore, it would be possible to use nanoparticles as a fracture-aperture caliper.

An investigation into the idea of using particles to measure the fracture aperture was carried out by injecting the polydisperse (diameter ranging from 5 to 31 μm) red silica particle suspension (Figure 4.19a) into the fractured greywacke core. It was found that

CHAPTER 4. EXPERIMENTAL INVESTIGATION OF PARTICLE TRANSPORT THROUGH FRACTURED MEDIA

only particles with diameters smaller than 23 μm (Figure 4.19b) were transported through the fracture. This suggested that the fracture had an aperture of at least 23 μm . This result was in agreement with the hydraulic-fracture-aperture measurement (i.e., 30.68 μm) and demonstrates the possibility of using particles to estimate the size of the fracture opening.

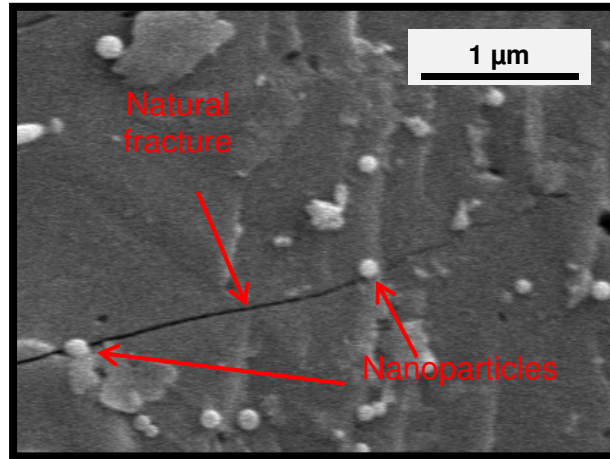


Figure 4.18: Micrograph of the interior of Berea sandstone showing natural fracture with two 100 nm SiO_2 nanoparticles at its entry. Smaller nanoparticles would have entered the fracture providing direct fracture aperture measurement based on recovered particle size.

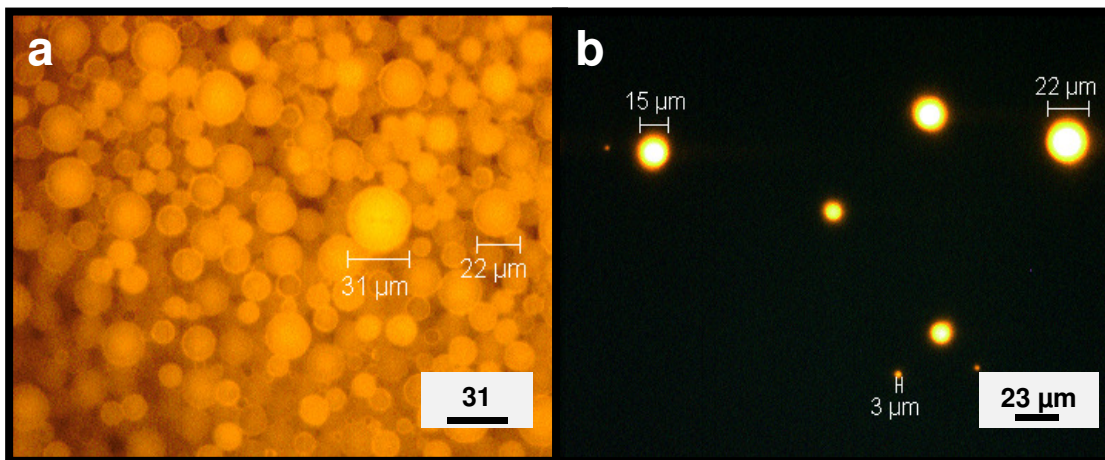


Figure 4.19: Optical images for red fluorescent silica particles of (a) influent, (b) effluent samples. Only particles of about 23 μm flowed through the fracture of predetermined aperture of 30.68 μm .

4.4.2 Fractured Berea core experiment results and discussion

The transport of silica particles was investigated by flow experiments in the fractured Berea sandstone core plug. For this purpose, the particle suspension concentration, particle size and fluid velocity were varied. The effluent breakthrough curves of blue (2 μm) and green (5 μm) silica particles are presented in Figure 4.20 and 4.21, respectively. Fluid injection rates and resident times, maximum and cumulative relative concentrations are also summarized in Table 4.3.

4.4.2.1 Influence of particle size, input concentration and fluid velocity on particle recovery

Several observations can be made based on these breakthrough curves. The breakthrough time for both particle sizes was very similar. The return curves for both particle sizes showed a very fast arrival. The first arrival of the 2 and 5 μm particles occurred within 0.02 to 0.04 and 0.03 to 0.08 pore volume from the start of their injection. This suggests that the recovered particles were, at least initially, moving through the fracture and large pores. The transport of latex particles in fractured media using micromodels (Section 5.5.2) confirmed visually that particles favored flow through the fracture and hence had earlier breakthrough time. In the case of the 2 μm particles, the cumulative relative concentration was increasing gradually (Figure 4.20b) until the end of the experiment. For the 5 μm particles, the cumulative relative concentration reached a plateau (Figure 4.21b) at the first post-injected pore volume when injected at 3 cm^3/min , and half pore volume when injected at 1 cm^3/min . The maximum relative concentration $(C/C_o)_{\text{max}}$ of the 2 and 5 μm particles was in the range between 0.14 to 0.26 (Figure 4.20a) and 0.04 to 0.21 (Figure 4.21a), respectively, and peak of maximum relative concentration occurred at about half pore volume. Large particles exhibited lower recovery than smaller particles. The breakthrough curves of the 2 μm particles showed modest decline in relative concentrations, resulting in a smooth and steady tail, relative to the sharp drop in the relative concentrations of the 5 μm particles, except for the 5 μm particles at suspension concentration of C injected at 3 and 10 cm^3/min . These breakthrough curves exhibited fluctuating tails.

CHAPTER 4. EXPERIMENTAL INVESTIGATION OF PARTICLE TRANSPORT THROUGH FRACTURED MEDIA

For the 2 μm silica particles (Figure 4.20), the recovery was inversely proportional to particle suspension concentration, and directly proportional to fluid velocity. Recovery was strongly sensitive to concentration, and slightly sensitive to fluid velocity. Similar behavior was observed during the injection of the 2 μm silica particles into fractured greywacke core (Section 4.4.1.1), and confirmed directly using micromodels (Section 5.5.1). The recovery was decreasing with increasing input concentration. This represents an opposite trend to observations reported in literature (e.g. Tan et al., 1994; Liu et al., 1995; Bradford and Bettahar, 2006). It was concluded that the 2 μm particles were aggregating, and thus straining inside the fracture. The higher the mass concentration, the more particles were present. If particles have an affinity to aggregation, large particle clusters would form and therefore higher attenuation of particles would occur within the fracture. The fact that particle recovery was not sensitive to fluid velocity supports this conclusion, because particle removal by physical straining is known to be insensitive to fluid velocity. Detachment of particles by rolling, sliding or lifting was considered insignificant because increasing fluid velocity (drag forces) did not result in considerable recovery enhancement. The recovery of the 5 μm silica particles was more sensitive to fluid velocity than concentration. In general, the particle recovery (Figure 4.21b) was found to have a linear relationship with the fluid velocity used during injection. For example, the recovery of the 5 μm diameter particle particles had increased from below 20% to higher than 64% (about three times higher by increasing fluid velocity by factor of three). Further increase in fluid velocity (10 cm^3/min) had resulted in complete recovery of the 5 μm diameter silica particles. Large particles follow fast-moving streamlines (central streamlines) and therefore they are held away from grain or fracture walls. As fluid velocity decreases, the drag force exerted on particles by moving fluid also decreases, allowing gravity to play a larger role. Particles may also diffuse away from fast-moving streamlines toward the fracture walls, or near grains at the fracture-matrix interface, but this is not expected to play a dominant role in the transport of micron-scale particles. Based on all the experimental data, it was hypothesized that gravitational sedimentation was playing an important role in the particle transport.

CHAPTER 4. EXPERIMENTAL INVESTIGATION OF PARTICLE TRANSPORT THROUGH FRACTURED MEDIA

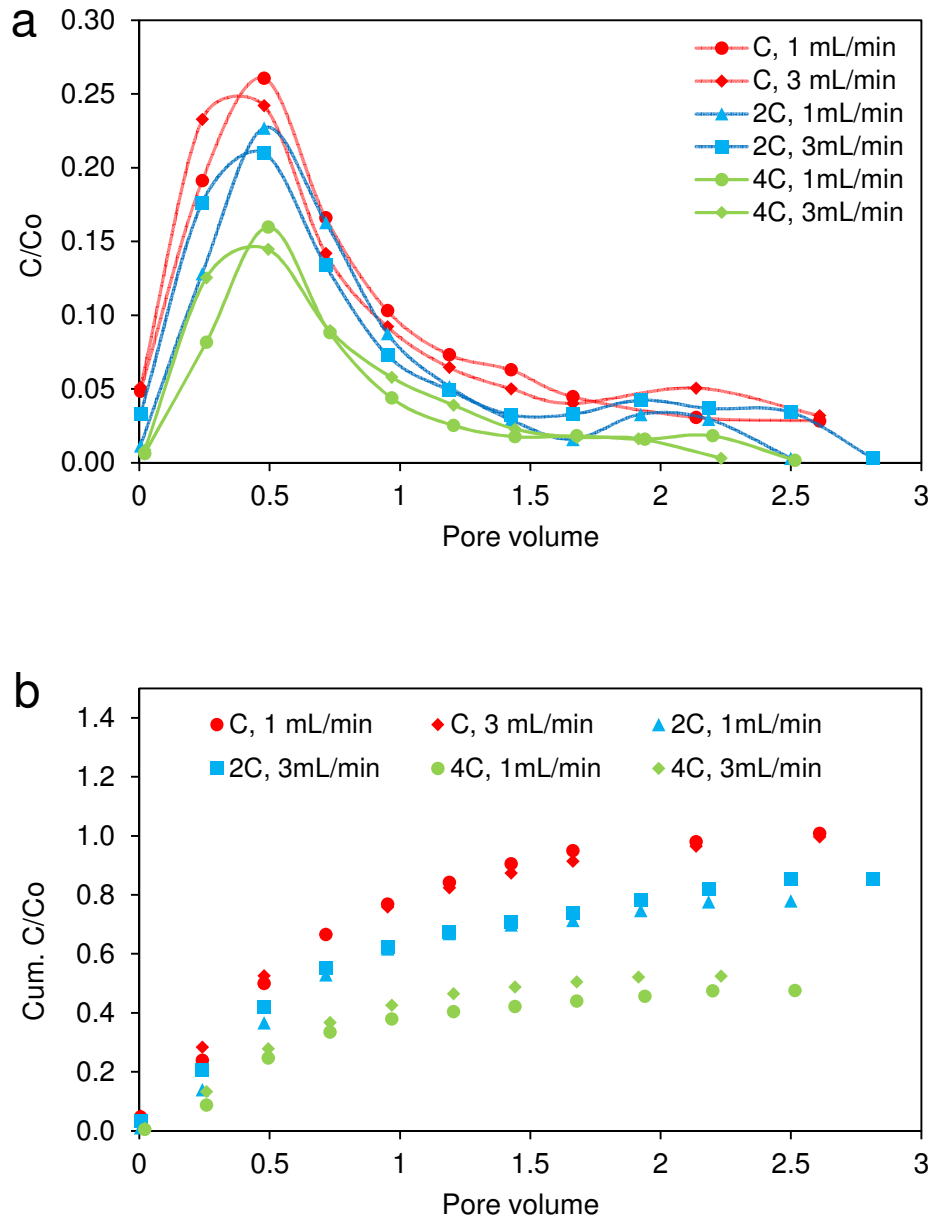


Figure 4.20: Breakthrough curves of blue (2 μm) silica particles transported in fractured Berea sandstone showing (a) the maximum and (b) cumulative relative concentration. Note the steady decrease in the relative concentration for all breakthrough curves, and the gradual increase of the cumulative relative concentration until the end of the injection. The return curves were more sensitive to suspension concentrations than fluid velocity.

CHAPTER 4. EXPERIMENTAL INVESTIGATION OF PARTICLE TRANSPORT THROUGH FRACTURED MEDIA

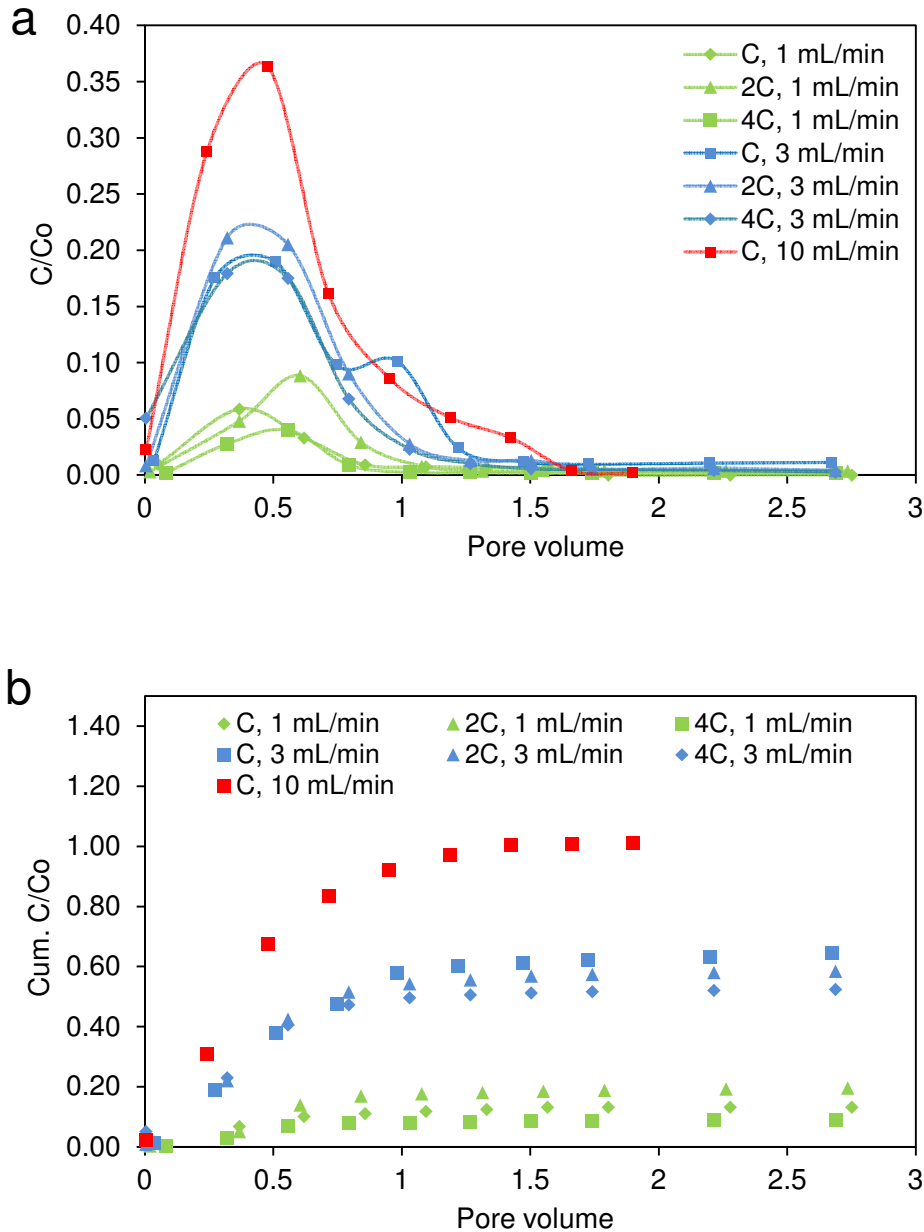


Figure 4.21: Breakthrough curves of green (5 μm) silica particles transported in fractured Berea sandstone showing (a) the maximum and (b) cumulative relative concentration. Most breakthrough curves exhibited a sharp decrease in relative concentrations, except for the silica suspensions of concentration C injected at 3 and 10 cm³/min. The cumulative relative concentrations reached a plateau at different pore volumes depending on the injection flow rate. The return curves were more sensitive to fluid velocity than suspension concentrations.

4.4.2.2 Filtration theory prediction of transport mechanisms within the rock matrix

Based on the refined correlation for single-collector contact efficiency (η_0), the probability of collision of the silica particles with a grain can be estimated using Equation (2.1). Figure 4.22 represents the total single-collector contact efficiency, and the magnitude of individual collision mechanisms (diffusion, interception and sedimentation), calculated for the silica particles used in this study, with particle density of 2.2 g/cm^3 , average grain size for Berea sandstone of $150 \text{ }\mu\text{m}$ (Churcher et al., 1991) with porosity of 21%, fluid velocity of $6.84 \times 10^{-5} \text{ m/s}$ (corresponds to $1 \text{ cm}^3/\text{min}$), temperature of $21 \text{ }^\circ\text{C}$, Hamaker A constant for silica-water-silica system in the order of $6 \times 10^{-21} \text{ J}$ (Grabbe and Horn, 1993) and particle size ranging from 0.01 to $10 \text{ }\mu\text{m}$. At particle size of $2 \text{ }\mu\text{m}$, the total probability of collision was approximately 5.77%, of which interception and gravitational sedimentation contributed around 3.16% and 1.74%, respectively. Note that collision probability by interception is about twice that by gravity sedimentation at $6.84 \times 10^{-5} \text{ m/s}$ (the smallest fluid velocity used in this study). In contrast, the filtration theory predicted that the transport mechanism of the $5 \text{ }\mu\text{m}$ diameter particles was dominated by the gravitational sedimentation and interception. The probabilities of collision based on gravity and interception accounted for 10.66% and 11.65% of the overall probability (22.74%), respectively. Transport by diffusion was negligible for both particle sizes. Note that filtration theory does not account for straining, which was supposed to have caused the $2 \text{ }\mu\text{m}$ particles to deposit within the porous medium and/or at narrower fracture aperture regions. Bradford et al. (2002) reported that experimental data and filtration theory prediction were not in agreement. They attributed such discrepancies to the fact that filtration theory does not account for straining.

Recall that the silica particles have density of about 2.2 g/cm^3 , more than twice that of the suspension water, meaning that these particles are subjected to a force due to gravity. The gravitational force on a particle is directly proportional to particle mass (and thus the cube of the particle diameter), so the $5 \text{ }\mu\text{m}$ particles are more greatly affected by gravitational settling than the $2 \text{ }\mu\text{m}$ particles. This helps to explain why the recovery of $5 \text{ }\mu\text{m}$ particles was much more sensitive to fluid velocity than the $2 \text{ }\mu\text{m}$ particles. Because

CHAPTER 4. EXPERIMENTAL INVESTIGATION OF PARTICLE TRANSPORT THROUGH FRACTURED MEDIA

the transport of 5 μm particles is likely to be dominated by gravitational sedimentation (which can be offset by increasing fluid velocity) and the trapping of the 2 μm particles is likely to be dominated by aggregation (which may not necessarily be offset by increasing fluid velocity), it makes sense that the recovery of the 5 μm particles was more sensitive to fluid velocity than that of the 2 μm particles. Furthermore, the fluid drag force acting on a spherical particle is directly proportional to the fluid velocity and the diameter of particle. Larger particles will be experience greater drag forces, and thus, they will be mobilized or detached more effectively from contact surface as velocity increases (Ryan and Elimelech, 1995). The lift force that also counters the adhesive force is also function of the fluid velocity. The combined effect of fluid velocity on those forces caused larger particles to be more sensitive to fluid velocity. Finally, as a result of increasing fluid velocity, the volume of low velocity regions (referred to as stagnant flow regions) will decrease, which will limit collision of particles between fracture surface crevasses or at the pore walls.

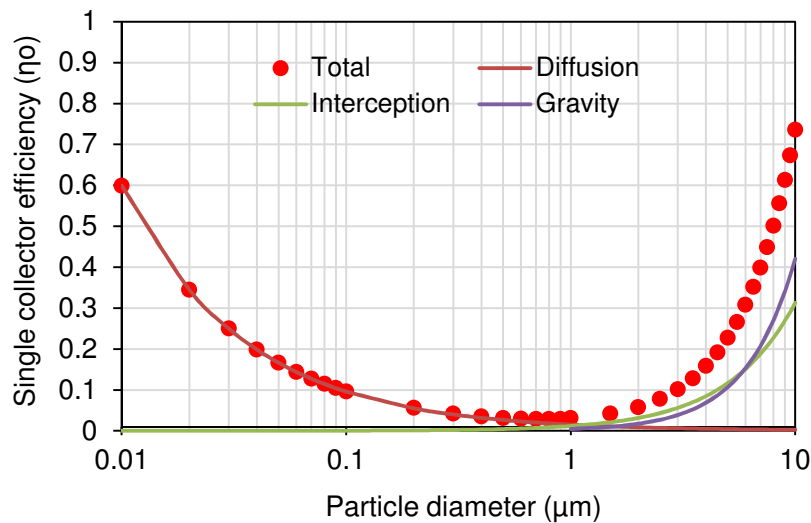


Figure 4.22: Semilog plot of single-collector contact efficiency, with respective contribution of each transport mechanism, calculated for silica particles used in this study. Hamaker constant $A_H=6\times 10^{-21}$ J, $T= 21$ °C, $\rho_p= 2.2$ g/cm³, $d_c= 150$ μm , $f= 21\%$, $v= 6.84\times 10^{-5}$ m/s.

CHAPTER 4. EXPERIMENTAL INVESTIGATION OF PARTICLE TRANSPORT THROUGH FRACTURED MEDIA

Keller and Auset (2006), when studying the transport of polystyrene particles of various sizes (0.05, 1, 2.5 and 5 μm) through micromodels, estimated the relative importance of the contributing transport mechanisms as function of fluid velocity using Equation (2.1). Due to the fact that their polystyrene particles had density similar to that of injection water (1.05 g/cm^3), the probability of collision based on gravity for all particle sizes was assumed to be insignificant. The transport mechanisms were predicted to be due to diffusion and interception, with interception being the dominant controlling mechanism. In the case of the silica particles used in this study, the effect of gravitational sedimentation is very prominent, especially at lower fluid velocities, as depicted in Figure 4.23. For the 2 μm particles, the collision probability as a result of gravity and diffusion decreases by a factor of three as water pore velocity increases from 6.84×10^{-5} to 2.04×10^{-4} m/s (corresponding to flow rates of 1 and 3 cm^3/min), while probability of interception remained relatively the same. For the 5 μm particles, collision probability due to gravity diminished from 10.64% to 0.84% as water pore velocity increased an order of magnitude (6.84×10^{-4} m/s). Diffusion had no role in their transport at that fluid velocity, but collision by interception with grain or crevasses in fracture wall was probable. By comparison, fluid velocity played a more important role in offsetting gravity sedimentation for larger particles than smaller ones (from 10.64% to 0.84% for 5 μm and 1.73% to 0.52% for 2 μm , i.e. a factor of 6). This is consistent with the fact that larger particles were more susceptible to gravitational and fluid drag forces than smaller particles.

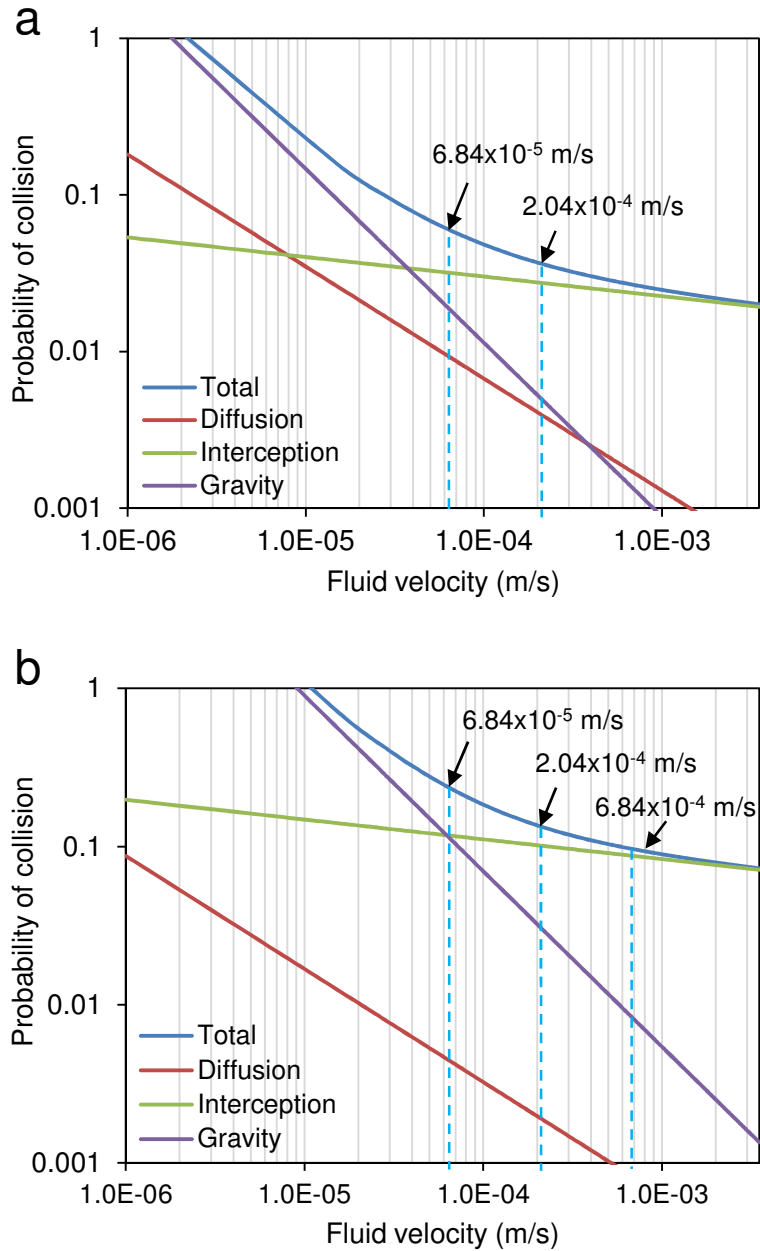


Figure 4.23: A log-log plot of the effect of fluid velocity on the physical transport mechanisms of diffusion, interception and gravitational sedimentation for silica particle of size (a) 2 μm and (b) 5 μm . Parameters used here are the same as those used in Figure 4.22.

CHAPTER 4. EXPERIMENTAL INVESTIGATION OF PARTICLE TRANSPORT THROUGH FRACTURED MEDIA

The values of the attachment efficiency (α), the probability that collisions of a particle with a grain collector (or fracture wall in this study) will result in attachment, were calculated using Equation (2.4) and values are listed in Table 4.5. The attachment efficiency values, for all experiments with changing particle sizes, concentrations and fluid velocities varied from 0.0014 to 0.086. Other studies conducted in sand columns (Keller et al., 2004; Bradford et al., 2002 and 2006) or sediment cores (Dong et al., 2002) reported values comparable to the values found in this study. The attachment efficiency in this study generally increased with increasing concentration of the particle suspension. The values of actual-collector removal efficiency (η), also listed in Table 4.5, behaved somewhat differently. The actual efficiency values increased with concentrations (the larger the number of particles, the higher the probability of collision) and decreased with increasing fluid velocities (except for one data point). This was anticipated because the silica particles at sizes of 2 and 5 μm are expected not to diffuse much but rather follow the higher velocity streamlines, and thus the probability to collide with the fracture or grain walls is lower at higher velocities. Filtration theory accounts for the dependency of particle and grain sizes in the actual-collector removal efficiency and that of surface chemistry in the attachment efficiency. It should be mentioned that all experiments were conducted under unfavorable attachment conditions (i.e. at low ionic strength, $I=10^{-6}$, using pure water) to minimize the physicochemical factors that determine particle immobilization. According to filtration theory, the attachment efficiency should not change with varying particle and grain sizes for experiments conducted at the same set of chemical conditions. Deviation from this condition suggests that significant straining may be occurring (Bradford et al., 2006). In this work, variability of the attachment efficiency values was observed.

CHAPTER 4. EXPERIMENTAL INVESTIGATION OF PARTICLE TRANSPORT THROUGH FRACTURED MEDIA

Table 4.5: Summary of attachment, single-collector contact and actual efficiencies calculated for silica particles injection experiments into the fracture Berea core^a

Flow medium	d_p (μm)	c (mg/ml)	v_m (m/s)	η_0 %	$\alpha \times 10^2$ -	$\eta \times 10^3$ -
Fractured Berea	2	0.49	6.84×10^{-5}	5.77	0	0
	2	0.98	6.84×10^{-5}	5.77	2.13	1.23
	2	1.92	6.84×10^{-5}	5.77	6.46	3.73
	2	0.49	2.04×10^{-4}	3.67	0.14	0.05
	2	0.98	2.04×10^{-4}	3.67	2.12	0.78
	2	1.92	2.04×10^{-4}	3.67	8.69	3.19
	5	0.49	6.84×10^{-5}	22.74	4.43	10.08
	5	0.98	6.84×10^{-5}	22.74	3.56	8.08
	5	1.92	6.84×10^{-5}	22.74	5.26	11.96
	5	0.49	2.04×10^{-4}	13.53	1.63	2.21
	5	0.98	2.04×10^{-4}	13.53	1.97	2.66
	5	1.92	2.04×10^{-4}	13.53	2.37	3.21
	5	0.49	6.84×10^{-4}	9.66	0	0

^aHere d_p is the particle size, c is the particle suspension concentration, v_m is the water pore velocity in matrix, η_0 is the single-collector contact efficiency (Equation 2.1), α is the attachment efficiency (Equation 2.4) and η is the actual single-collector removal efficiency (Equation 2.3).

Ryan and Elimelech (1996) reported that the existence of repulsive forces between particles and surfaces of porous media would result in inaccurate prediction of attachment efficiency. The total interaction energy between particles was calculated using Equations (2.7, 2.8 and 2.9) and plotted in Figure 4.4. In this calculation, the measured zeta potentials of -40.2 and -80.23 mV for 2 and 5 μm particles were used. The zeta potential for Berea sandstone saturated with pure water (ionic strength of 10^{-6}) was assumed to be -76.3 mV as suggested by Alkafef et al. (1999). The rock zeta potential was very similar to the zeta potential of the 5 μm particles and almost double that of the 2 μm particles. The estimation of the total interaction energy indicated that the attractive forces of van der Waals were negligible. This was indicative that the silica particles did not interact

CHAPTER 4. EXPERIMENTAL INVESTIGATION OF PARTICLE TRANSPORT THROUGH FRACTURED MEDIA

with Berea sandstone surfaces via the secondary energy minimum. Both particle sizes showed a repulsive energy barrier, considerably higher for the 5 μm diameter particles. Unless these forces are overcome by gravitational forces, particle attachment would be unfavorable. This may also explain the variability of attachment efficiency when calculated for different particle sizes under the same set of chemical conditions.

Surface chemistry or functional groups on the particle surface may result in acid-base energy interactions. These acid-base interactions (not accounted for by classical DLVO theory) describe the hydrogen bonding properties of interacting surfaces with water. Water molecules structure themselves by hydrogen bonding upon interaction, resulting in attractive particle-surface and particle-particle interactions for hydrophobic particles and repulsive particle-surface and particle-particle interactions for hydrophilic particles. The silica particles used in this study retain hydrophilic properties at the experiment pH as provided by the manufacturer, and thus repulsive hydrophilic interactions were expected. The 5 μm particles may have had a sufficiently large repulsive energy barrier to hinder particle aggregation. When particles are at close proximity to each other while entering a pore throat or near a fracture wall, they may repel each other until one or the other flows through or physically strains based on their size. If aggregation is occurring, particles attach to each other to form a cluster. The size of the cluster is dependent on the number of particles forming that cluster; the more particles available, the larger the cluster size. Thus, size exclusion may occur not based on the size of the individual particle but the size of the cluster. The cluster would be excluded from all pores smaller than its own size. Evidence of increasing straining as a function of increasing mass concentration of the 2 μm particles was confirmed visually during the micromodel flow experiments which are discussed later in Chapter 5. Clustering was observed visually in the micromodel experiments, despite the fact that very low ionic strength water (pure water) was used. Keller and Auset (2006) observed particle clustering at the same conditions.

4.4.2.3 Particle removal by physical straining

Unlike attachment, where a particle requires one solid-water interface to attach to a surface, straining involves at least two solid-water interfaces or surface roughness (Bradford et al., 2006). Straining or size exclusion inside the fracture may be present, either in areas between fracture surfaces or at the fracture-matrix interface. When fracture surfaces come into contact, irregularities of those surfaces (crevasses) result in a fracture with varying aperture. Areas where surfaces are further apart are candidate sites for particle attachment (one solid-water interface), while closer surfaces (two solid-water interfaces) promote straining. The removal mechanisms by collision with attachment to fracture walls or straining between fracture surfaces are analogous to those occurring within a pore throat. We shall discuss some of the criteria suggested by other authors with regard to particle straining inside pore structure and employ whichever applicable to assess straining occurring in the fracture area. In this regard, the fracture was treated as a single pore with a maximum width of 62.4 μm as calculated from flow in parallel layers using Equation 4.5 or a minimum width of 3.79 μm as estimated by the cubic law assuming that the fracture permeability is equal to the total permeability. This is a conservative estimate because matrix permeability is high (approximately 0.51 darcy).

The general disagreement between prediction of filtration theory and experimental work (Bradford et al., 2002) was attributed to the fact that the filtration theory does not take into account the influence of pore structure on particle removal by straining. Xu et al. (2006) studied the effect of straining on the mobility of particles within groundwater aquifers and granular filters. They suggested that accurate description of particle mobility requires considering the effects of straining when the ratio of particle diameter to the median grain size (d_p/d_{50}) exceeds 0.008. Bradford et al. (2007) investigated the influence of (d_p/d_{50}) on the recovery of latex particles on the basis of straining under unfavorable attachment conditions. They reported that as (d_p/d_{50}) ratio increased, the recovery declined and more particles were deposited, especially adjacent to the sand column inlet. For example, for the (d_p/d_{50}) ratio of 0.007, 0.008, 0.013 and 0.020 (at fluid velocity of 0.1 cm/min), the peaks of the return curves were approximately at 100%, 70%, 20% and

CHAPTER 4. EXPERIMENTAL INVESTIGATION OF PARTICLE TRANSPORT THROUGH FRACTURED MEDIA

10%, respectively. It is well understood that smaller grain size corresponds to smaller pore size for certain types of grain packing. For the Berea sandstone used in this study, an average grain size of 150 μm was assumed, as per Churcher et al. (1991). Considering the silica particles of 2 and 5 μm , the ratio of (d_p/d_{50}) would be 0.013 and 0.033, respectively. This suggested that the silica particles that entered the pore network at the inlet or fracture-matrix interface were likely to be trapped due to straining, especially larger particles. Additionally, the pore network in sedimentary rocks such as Berea sandstone would have far more complex pore connectivity which might lead to additional reduction in effective pore size at pore junctions. In other words, this criterion is regarded as conservative when applied to sedimentary rocks. However, because the recovery of the 5 μm particles was changing (increasing) with increasing fluid velocity, straining was unlikely to be the main removal mechanism of the 5 μm particles. It should be mentioned that the estimated hydraulic aperture represents an average value of large and small aperture regions. Therefore some local straining may be present.

The ratio of throat size to particle size (T/C) was used as a criterion by Auset and Keller (2006). They performed experiments in micromodels with porous medium only (no fracture), the results of which suggested that the T/C of 1.8 and smaller would result in particle removal solely by straining. For T/C ratios between 1.8 and 2.5, interception and straining were observed. For higher T/C, straining was not observed. For Berea sandstone, we applied the T/C criteria based on the pore size distribution range obtained from capillary pressure data (Figure 4.5) and particle sizes (2 and 5 μm) used in this study. Recall that the Berea sandstone has pore sizes in the range of 0.005 to 50 μm , with an average pore size of 15.5 μm . According to this criterion, the threshold pore size for the straining of 2 μm particles is 5 μm (2.5 times 2 μm), and that of 5 μm particles is 12.5 μm (2.5 times 5 μm). In other words, in pores that are smaller than this threshold size, the particles may be trapped within the porous medium primarily due to straining. Aggregation of the 2 μm particles (as we concluded earlier) would result in clusters larger than the threshold pore size of 5 μm , hence straining at the pore network. The

CHAPTER 4. EXPERIMENTAL INVESTIGATION OF PARTICLE TRANSPORT THROUGH FRACTURED MEDIA

threshold pore size of the 5 μm particles was very comparable to the average pore size (15.5 μm), indicating a high probability of straining at most of the pores.

Similarly, the T/C criteria can be applied to evaluate straining within a fracture by treating the fracture regions with small apertures as pore throats. Our estimate of the fracture hydraulic aperture indicated that the apertures could be as small as 3.79 μm in areas of closely matching fracture surfaces. This aperture size (or throat) would result in T/C ratio of 1.9 and 0.8 for particle sizes of 2 and 5 μm , respectively, suggesting a high probability of straining at narrower aperture regions. The criteria provided by Herzig et al., (1970) and modified by Zvikelsky and Weisbrod (2006) suggested that straining is more important within the fracture if the ratio of the particle to fracture aperture exceeds 0.02. Considering the silica particles used in this study, the ratio of the 2 and 5 μm particles to the smallest aperture (3.79 μm) was 0.5 and 1.3, respectively. Therefore straining is possible at narrower fracture regions. Owing to the complexity of the pore network and the existence of surface irregularities in fractures, it is very possible that a pore throat (or a flow channel in the fracture) at or below the threshold size exists along a preferential flow path. Consequently, straining of particles will result in their accumulation at pore junctions and, therefore, the total blockage of the connecting pore. Blocked pores are a dead end for subsequent particles, which eventually results in reduction of particle recovery. The permeability measurements (i.e. pressure data) support the fact that the number of conductive flow paths available to particles decreased due to blockage. Figure 4.24 shows an example of the permeability measurements conducted during the injection of the 2 μm silica particles at flow rate of 3 cm^3/min using three different suspension concentrations. The permeability continued to decrease as particle concentration increased. Although it was a slight decrease, it indicated a certain degree of blockage (i.e. incomplete straining). Bradford et al. (2002) reported that incomplete straining would have less pronounced reduction in permeability because it occurred in only part of the pore network. The decrease in permeability was consistent with the decline in recovery (the rock is less permeable as more particles retained inside). Also, the rate of reduction in permeability (from initial values to the end of injection) was

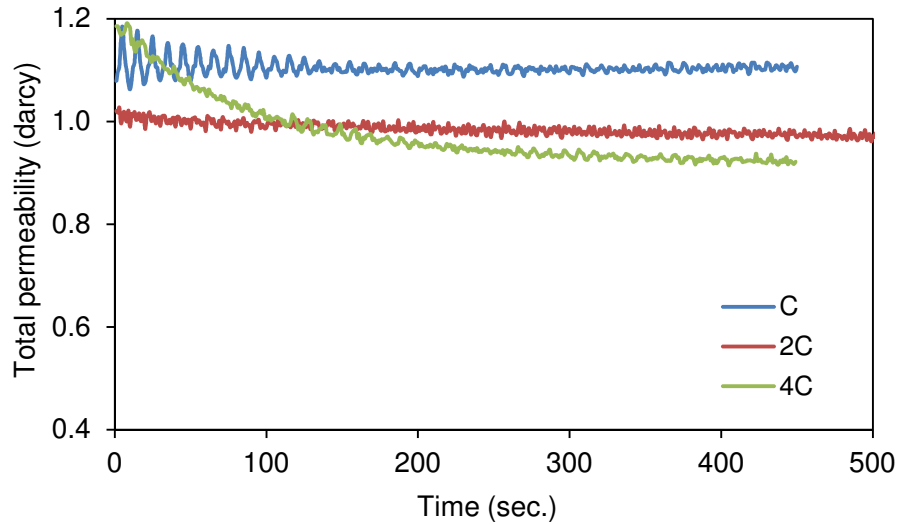


Figure 4.24: Permeability measurements during the injection of the $2 \mu\text{m}$ silica particles at different suspension concentrations, C, 2C and 4C. Flow rate was $3 \text{ cm}^3/\text{min}$. The rate of reduction in total permeability was the highest during the injection of silica suspension with highest mass concentration.

closely related to the amount of recovered particles. This means the permeability decreased faster as more particles were introduced to the porous medium, possibly due to blockage by aggregation and straining. The rate of reduction was the largest (from 1.2 to 0.92 darcy) during the injection of particle suspension with the highest concentration, the experiment in which only 53% of the influent concentration was recovered. The reduction rate was shallower (from 1.02 to 0.97 darcy) during the injection of particle concentration of (2C), where recovery was 85%. For the injection of the most dilute suspension (C), the permeability remained almost constant with an average value of about 1.10 darcy, after a slight decrease at the beginning of the experiment.

4.4.2.4 Particle deposition and transport mechanisms inside the fracture

Particle deposition within the fracture due to straining was discussed in the previous section (Section 4.4.2.3). It was concluded that the $2 \mu\text{m}$ particles were straining within the fracture aperture due to particle aggregation. This conclusion was supported by the visual observation using the micromodels as explained in Chapter 5. Also, the recovery of the $2 \mu\text{m}$ particles was not affected by increasing the fluid velocity, suggested that

CHAPTER 4. EXPERIMENTAL INVESTIGATION OF PARTICLE TRANSPORT THROUGH FRACTURED MEDIA

particle or particle aggregates were straining within the fracture. Although local straining of the 5 μm particles may occur, physical straining was unlikely to be the main removal mechanism. The recovery of the 5 μm particles was very sensitive to fluid velocity, suggesting that interception and gravitational sedimentation played significant role in large particles deposition within the fracture aperture. Both transport mechanisms are dependent on the fluid velocity and particle size. Size and charge exclusion (defined and explained in Section 2.1.2.1) would force large particles (particles in the micron size range) to follow fast moving streamlines, away from fracture walls. Because of the large size of the 5 μm particles compared to fracture aperture, particles are excluded from low flow regions following fluid streamlines. The like charge between the particles and fracture surface (both were negatively charged) would cause particles to repel away from fracture walls into fast moving streamlines. The total interaction energy estimated for silica particles (Figure 4.4) showed that the repulsive energy barrier extends for one micron in the solution. This means particles should not be able to access the region near fracture walls for at least two microns, but rather follow central streamlines. The enhanced particle velocity would reduce the probability of particle deposition by interception. Therefore it is not likely that interception would be a significant deposition mechanism.

The large density difference (1.2 g/cm^3) between the silica particles and suspension fluid (i.e. pure water) suggests particle settling. Transport by gravitational sedimentation is highly dependent on fluid velocity and particle size, decreasing with increasing fluid velocity and increasing with increasing particle size. Similar to the analysis performed for silica particles transport through the fractured greywacke (Section 4.4.1.2), the magnitude by gravitational sedimentation transport is dominating relative to particle diffusion as evaluated using the length scale analysis suggested by Becker et al. (1999). Summary of length scales and Peclet number can be found in Table 4.6. According to the length scale model, the 2 μm particles would settle at distances of 57.61 and 19.31 μm at injection rates of 1 and 3 cm^3/min , respectively. However, the lower surface of the fracture was not accessible by particles at the higher flow rate because the $L_s/0.5b$ is below 1.0., and

CHAPTER 4. EXPERIMENTAL INVESTIGATION OF PARTICLE TRANSPORT THROUGH FRACTURED MEDIA

therefore particles may not settle. Although settling was predicted at the lower flow rate, increasing flow rates (from 1 to 3 cm³/min) did not result in significant change in recovery, suggesting that if particles were settling, it is unlikely to be significantly.

For the 5 μm particles, the length scale analysis suggested that gravitational forces were dominating. The settling distance of 36.27 μm was estimated when particles were injected at flow rate of 10 cm³/min (where the highest recovery was observed). Particles may have settled initially, and then rolled along the fracture surface due to the effective drag forces. This might explain the fluctuating tail of the return curve (Figure 4.21). Under the same experimental conditions, the 5 μm particles should settle at distances of 360.04 and 120.66 μm compared to the 2 μm particles with settling distances of 57.61 and 19.31 μm at flow rates of 1 and 3 cm³/min, respectively. The settling distances of the 5 μm particles were at least twice the fracture aperture. Therefore it was concluded that these particles were rolling along the lower surface of the fracture for much of their travel time. Their large size relative to the fracture dimensions suggests that drag forces should be efficient at rolling them, especially with the strong repulsive surface interaction between particles and the fracture walls.

Table 4.6: Summary of calculated length scales and Pe number for 2 and 5 μm silica particles in fractured Berea core^a.

q (cm ³ /min)	d_p (μm)	U_s (μm/s)	L_s (μm)	L_s/L_D -	$L_s/0.5b$ -	Pe -
1	2	2.63	57.61	18.70	1.85	3.37×10 ⁵
3	2	2.63	19.31	10.83	0.62	1.00×10 ⁶
1	5	16.35	360.04	184.80	11.54	8.42×10 ⁵
3	5	16.35	120.66	106.98	3.87	2.51×10 ⁶
10	5	16.35	36.27	58.65	1.16	8.36×10 ⁶

^aHere U_s is the particle settling velocity (Equation 2.11), L_s is the length scale of Stoke settling of spherical particle (Equation 2.12), L_D is the length scale of diffusion (Equation 2.13), b is the fracture hydraulic aperture and Pe is Peclet number (Equation 2.10).

CHAPTER 4. EXPERIMENTAL INVESTIGATION OF PARTICLE TRANSPORT THROUGH FRACTURED MEDIA

The values of Peclet number (Table 4.6) were very high, suggesting advection flow inside the fracture. Under advection-dominated flow, particles will tend to move along central streamlines. The observed fast breakthrough of particles also implies that particles were following fast-moving streamlines. Table 4.7 provides a comparison between observed particle velocity (calculated based on the fracture length and first arrival time of particle) and the average water velocity inside the fracture. The 2 and 5 μm particles were flowing at velocity that was 2.01 and 1.21 times greater than the average water velocity within the fracture, respectively. The maximum velocity of fluid moving between two parallel plates, separated by constant distance, is 1.5 times the average fluid velocity. Deviation from this factor ($v_{max}=1.5v_f$) is expected because of the variation in the fracture aperture (wide and narrow aperture regions). The enhanced transport of particles through fractured porous media was observed by other investigators (Toran and Palumbo, 1992; McKay et al., 1993a and 1993b; Hinsby et al., 1996; Becker et al., 1999; Knapp et al., 2000; Zvikelsky and Weisbrod, 2006).

Table 4.7: Comparison between observed particle velocity and the average water velocity inside the fracture during silica injection into fractured Berea core^a.

q (cm^3/min)	d_p (μm)	v_p^b (cm/min)	v_f (cm/min)	v_p/v_f -
1	2	14.04	7.39	2.01
3	2	41.89	22.06	2.01
1	5	8.42	7.39	1.21
3	5	25.14	22.06	1.21
10	5	83.63	73.38	1.21

^aHere q is the volumetric flow rate, d_p is the particle size, v_p is the measured particle velocity, v_f is the average water velocity inside the fracture, v_p/v_f is the ratio of particle to water velocity inside the fracture.

^bNote that the first arrival time used in calculating the particle velocity was the average arrival time measured for particles of the same size injected at the same flow rate at different suspension concentration.

4.5 Chapter summary

This chapter focuses on the investigation of the transport mechanisms of silica particles in fractures, as a precursor for their use as nanosensors. Experiments were conducted by injecting fluorescent silica particles of different sizes (2 μm , 5 μm and polysized sample of sizes ranging from 5-31 μm), with varying suspension concentrations and/or fluid velocities, through a fractured greywacke and a fractured Berea sandstone core plug. The rapid breakthrough of particles in the core indicated that their transport was mainly through the fracture. Trapped particles were most likely retained in the small pore spaces in the core matrix and fracture walls in regions with small apertures. It was concluded that gravitational sedimentation, aggregation (only for the 2 μm particles) and straining due to particle or cluster size were the main particle trapping mechanisms.

It was observed that the recovery of the 2 μm particles following their injection into fractured greywacke and Berea cores was affected adversely by suspension concentrations (decreasing recovery with increasing suspension concentration). It was found that the increasing concentration of the 2 μm particles resulted in more pronounced aggregation, which led to trapping by straining. This conclusion was supported by the degree and rate of reduction in permeability occurring at higher concentration, and visual observations during micromodel flow experiments described in Chapter 5. This finding would be significant in the design of a tracer test using these particles as nanosensors.

The recovery of the 5 μm particles was influenced more by fluid velocity than by suspension concentration. This effect was attributed to the degree by which larger particles were influenced by the hydrodynamics of the system (drag and gravitational forces) compared to smaller particles. Silica particles have mass density higher than water. Particles are inclined to settle as the density difference between particles and suspension fluid increases. Because two of the investigated temperature sensors were silica based particles, it is crucial to design or synthesize the silica particles to have lower density and/or increase the fluid velocity to offset gravitational forces.

CHAPTER 4. EXPERIMENTAL INVESTIGATION OF PARTICLE TRANSPORT THROUGH FRACTURED MEDIA

The feasibility of estimating the fracture aperture by correlating the size of the largest recovered particles to the fracture opening through the injection of a polydisperse sample into fractured greywacke core was demonstrated. It was observed that the largest recovered particle size was within 75% of the estimated hydraulic aperture size.

CHAPTER 5

PORE SCALE OBSERVATION OF PARTICLE TRANSPORT IN FRACTURE-MATRIX SYSTEMS

5.1 Background

Micromodels were used to assess the flow mechanism of particles, at the pore scale, within the fracture and fracture-matrix interface. Particle transport in porous and fractured systems is usually investigated through sand columns, consolidated rock cores and field studies (e.g., Hornberger et al., 1992; Harvey et al., 1995; Reimus, 1995; Vilks and Bachinski, 1996; Vilks et al., 1997; Becker et al., 1999; Cumbie and McKay, 1999; Bradford and Bettahar, 2005; Zvikelsky and Weisbrod, 2006). Results of these studies are interpreted based on the evaluation of breakthrough curves that represent an average behavior of the particle transport. The use of micromodels provides direct observation of the internal processes and transport mechanisms at pore scale (Keller and Auset, 2007). In general, pore-scale studies used micromodels that consist of a homogeneous periodic network of generic shapes (squares, circles or irregularly-shaped repeated patterns) representing a porous network (e.g., Chen et al., 2002; Lanning and Ford, 2002; Sirivithayapakorn and Keller, 2003; Auset and Keller, 2004). Auset and Keller (2006) investigated the impact of particle size on transport through saturated porous media at the microscale. The authors showed the applicability of classical filtration theory to describe the governing transport mechanisms of particles through porous media, under certain throat to particle ratio. Smaller ratios result in straining (trapping of particle in a pore throat that is smaller than the particle itself) for which the filtration theory does not account.

CHAPTER 5. PORE SCALE OBSERVATION OF PARTICLE TRANSPORT IN FRACTURE-MATRIX SYSTEMS

In this work, the main purpose of the microscale experiments was to visualize particle transport processes in fractured porous media. The influence of fractures in enhancing particle transport and the impact of particle diameter on its transport were observed visually. The micromodel experiment results were used to help explain findings from the core-flooding experiments that were discussed in Chapter 4. Specifically, the 2 μm silica particles at two different concentrations (0.49 and 1.92 mg/ml, the same mass concentrations as used during the fractured greywacke and Berea experiments) were transported through micromodels representing a fracture-matrix system. The objective was to investigate the effect of concentration on particle straining or plugging that led to an opposite effect of suspension mass concentration on particle recovery than observed by other investigators in the literature. Impact of particle size on particle transport was examined using 2, 4.5, 6 and 10 μm fluorescent carboxylate-modified latex (CML) particles. The latex particles were also used to visually confirm the enhanced particle migration in the fracture.

The following sections provide the details of the particle characterization, micromodel fabrication and characterization, experimental apparatus, particle injection method, results and discussion.

5.2 Characterizations of microparticle suspensions

Two different particle suspensions were used during the micromodel experiments. One used the blue fluorescent silica particles (2 μm in diameter), and the second used fluorescent carboxylate-modified latex (CML) particles of different sizes purchased from Polysciences, Inc. The blue silica particles were the same as those injected into the fractured greywacke and Berea cores. Characterization of the blue silica particles can be found in Section 4.2.1.

Fluorescent CML particles (excitation/emission: 441/486 nm) were 2, 4.5, 6 and 10 μm in size. Two polydispersed samples were prepared by mixing particles of different sizes. Mix 1 was a mix of the 2, 4.5, 6 and 10 μm particles, while Mix 2 contained the 2, 4.5

CHAPTER 5. PORE SCALE OBSERVATION OF PARTICLE TRANSPORT IN FRACTURE-MATRIX SYSTEMS

and 6 μm particles only. The latex particles were uniformly shaped spheres with a narrow size distribution, except for the 6 μm . The 6 μm particle suspension showed traces of larger particles (two or three times the nominal size). The particle size was confirmed by SEM, as depicted in Figure 5.1. The size was also verified by optical microscopy but images are not included. These particles had a density of 1.05 g/cm^3 , very similar to that of water. Physical and chemical properties of the particles are listed in Table 5.1.

CML particles have carboxyl surface functional groups that give the particles hydrophilic surfaces and a negative charge at pH higher than 5. The hydrophilic and negatively charged surfaces of CML particles minimize their aggregation over a wide range of chemical conditions such as higher ionic strengths (Wan and Wilson, 1994b; Becker et al., 1999). Four different measurements of zeta potential (ζ) (i.e. conversion of electrophoretic mobility to zeta potential using the Henry equation (Equation 3.5) were performed and the average zeta potentials with standard deviation are presented in Table 5.1. Particle suspensions were at the same number concentration (number of particles per unit volume) to reduce the probability of aggregation of the smaller particles relative to the larger ones. This is because the rate of collision, which is often a precursor to aggregation, is roughly proportional to the square of number concentration. The particle suspensions were thoroughly sonicated (using Branson 2510 bath Sonicator) and well dispersed immediately prior to injection.

The sum of electrostatic double layer, van der Waals and Born interactions between the particles and the micromodel surface (zeta potential for silicon micromodel saturated with ultrapure water of ionic strength in the order of 10^{-6} is about -30 mV as per Baumann and Werth, 2004), was approximated using the expression in Gregory (1981) (Equation 2.7), Hogg et al. (1966) (Equation 2.8) and Ruckenstein and Prieve (1976) (Equation 2.9), respectively, and can be seen in Figure 5.2. For all particle sizes, there exists a high repulsive energy barrier.

CHAPTER 5. PORE SCALE OBSERVATION OF PARTICLE TRANSPORT IN FRACTURE-MATRIX SYSTEMS

Table 5.1: Summary of physical and chemical properties of CML particles^a

Nominal particle size (μm)	Particle size distribution (μm)	Particle density (g/cm^3)	Number concentration (# particle/ cm^3)	pH	Zeta potential (ζ) (mV)
2	1.83 (± 0.022)	1.05	7.54×10^6	8.6	-49.9 (± 0.51)
4.5	4.46 (± 0.13)	1.05	7.55×10^6	8.9	-54.7 (± 0.80)
6 ^b	6.33 (± 0.36)	1.05	7.55×10^6	8.2	-67.5 (± 0.48)
10	10.08 (± 0.97)	1.05	7.51×10^6	8.5	-70.6 (± 0.55)

^aThe particle size distribution and density were provided by the manufacturer, Polysciences, Inc. (polyscience.com). The zeta potential was measured using Zetasizer (Malvern Instruments LTD).

^bSEM micrographs showed tracers of particles 2 to 3 times larger than nominal size.

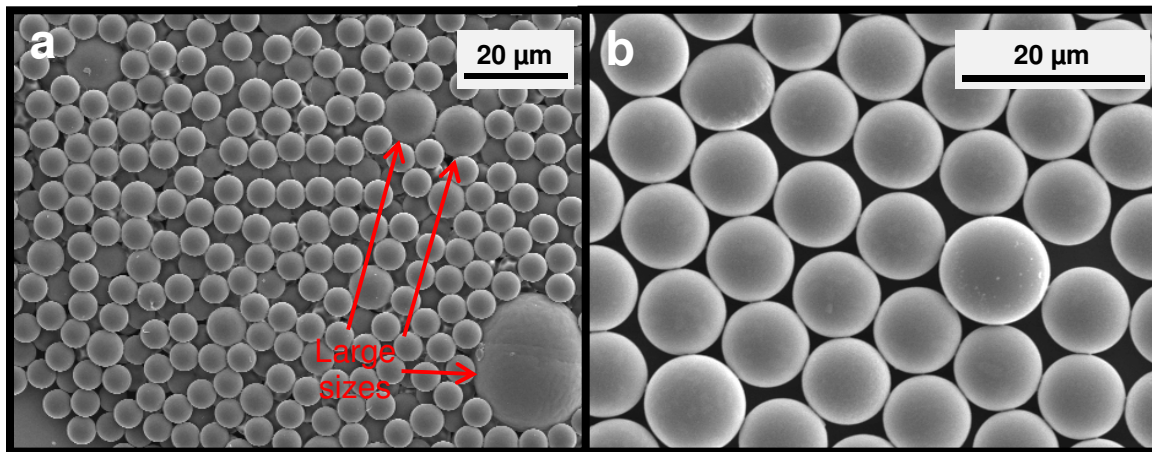


Figure 5.1: Example micrographs of (a) 6 μm and (b) 10 μm latex particles. Image (a) shows particles 2 to 3 times larger in diameter than nominal size, whereas image (b) confirms a uniform size of the 10 μm particles. Micrographs of the 2 and 4.5 μm particles are not shown; however, they exhibited the similar characteristics to the 10 μm (uniform shape and size).

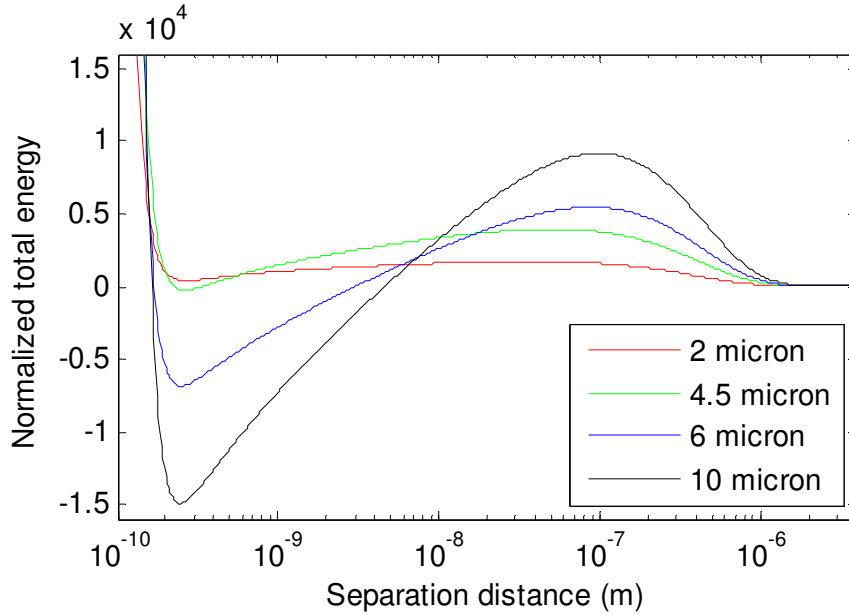


Figure 5.2: XDLVO interaction energy between latex particles and silicon micromodel. The interaction energy is normalized to the thermal energy ($k_B T$). Here Hamaker constant for latex-water-quartz is $4.04 \times 10^{-21} \text{ J}$ (Israelachvili, 1992), T is 293K.

5.3 Micromodel fabrication and characterization

Micromodels have been developed to allow for flow visualization at the pore scale (Buckley, 1991). Micromodels are transparent networks of porous structures and channels. The porous structures can be an artificial pattern such as straight or staggered cylinders to simulate grains, or images based on real pore network found in natural rocks. Micromodels are two-dimensional systems and care must be taken when extrapolating the results to three-dimensional systems.

Micromodels used in this study were fabricated in the Stanford Nanofabrication Facility (SNF). A detailed step-by-step fabrication program can be found in Appendix A.

The following sections provide a full characterization of the micromodels used in this study, including permeability measurements. The micromodel fabrication process is also described.

5.3.1 Micromodel characterization

Micromodels with two different designs (fracture location and pore network structures) were used. One (Micromodel A) was used during the injection of the silica particles, and the other (Micromodel B) was used during the injection of the latex particles. The micromodels used in this work were of the type described by Rangel-Germán (2002). Micromodel A and B were made of 4-inch silicon wafers, K Prime, 4P <100> B S42565.

5.3.1.1 Micromodel A

A pore network of a repeated pattern obtained from an SEM image of a sandstone thin section (Figure 5.3a) was used. Continuity of repeated patterns was ensured by manipulating the image digitally (Figure 5.3b).

Into Micromodel A were etched pore patterns with two flow channels (fractures) (Rangel-Germán, 2002). Each pattern was about 490 μm by 400 μm repeated more than 100 times across each side of the 5 cm by 5 cm matrix region (Table 5.2). A schematic of the micromodel is shown in Figure 5.4.

Grain sizes were ranging from 30 to 300 μm and porosity was about 47% measured using image analysis (Inwood, 2008). The absolute permeability was measured by Inwood, (2008) and found to be approximately 1 darcy. The absolute (water) permeability was remeasured at various flow rates ranging from around 0.04 to 0.27 cm^3/min . Higher flow rates were not used to avoid overpressurizing the micromodel. Initially, the micromodel and connecting tubes were all fully saturated with ultrapure water. Complete saturation of the micromodel was confirmed via image analysis. Darcy's Law of incompressible horizontal fluid flow was used to calculate the absolute permeability. Validity of Darcy's Law was confirmed by linearity between flow rates and pressure drop as shown in Figure 5.5. The area used was the cross-sectional area at the fracture-matrix interface (i.e. 5 cm by 0.0025 cm, length and depth of Micromodel A). The average water permeability was found to be approximately 1.09 darcy (Figure 5.5), in agreement with previous measurements carried out by Inwood (2008).

CHAPTER 5. PORE SCALE OBSERVATION OF PARTICLE TRANSPORT IN FRACTURE-MATRIX SYSTEMS

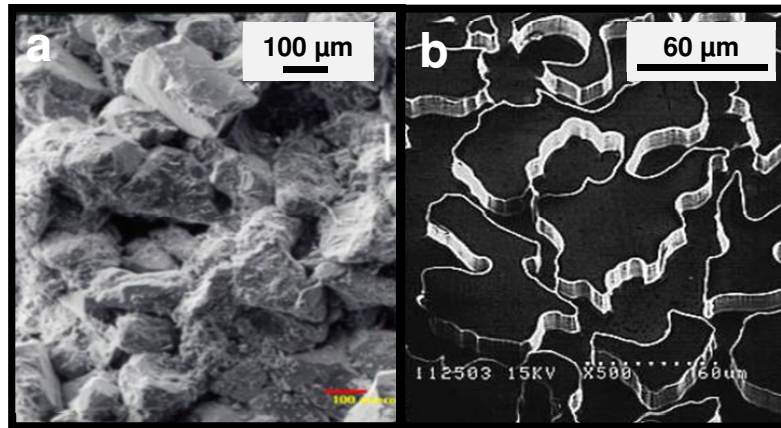


Figure 5.3: Sandstone thin section (a) SEM, and (b) digitally manipulated images used in the design of Micromodel A (Rangel-Germán, 2002).

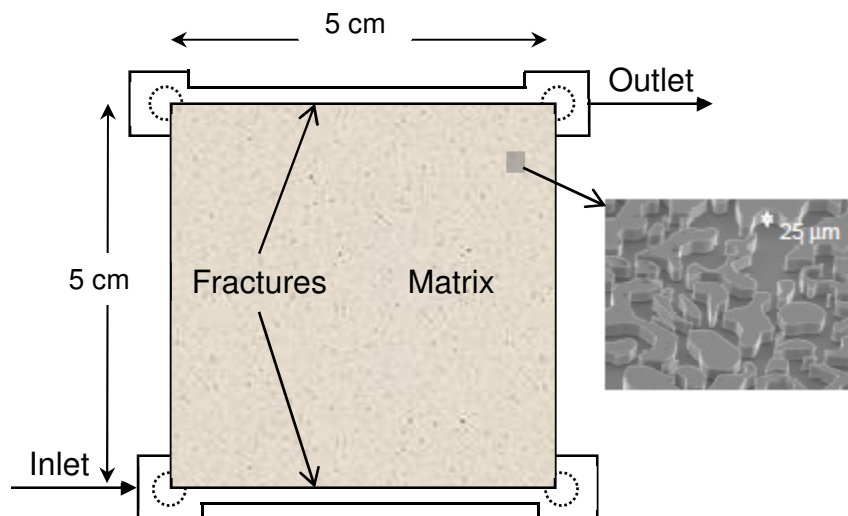


Figure 5.4: Schematic of Micromodel A showing the repeated pattern and fracture channels (Rangel-Germán, 2002). Note that inlet and outlet port location were modified from the original design.

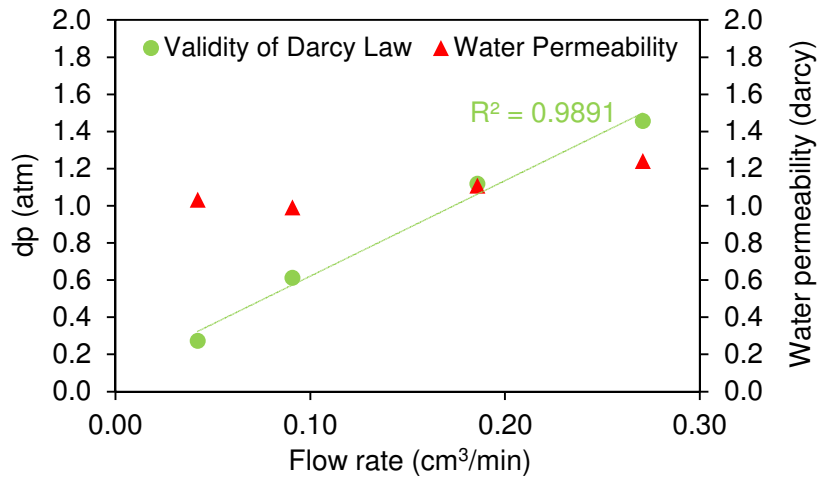


Figure 5.5: Water permeability of Micromodel A measured at various volumetric flow rates showed an average value of approximately 1.09 darcy. This is in agreement with measurement performed by Inwood (2008). The linearity between the flow rates and pressure drop indicated the validity of Darcy Law.

5.3.1.2 Micromodel B

Each model consists of five separate flow regions: flow region 1 contains matrix only, flow regions 2 to 5 consists of a single fracture of different aperture size (5, 15, 25 and 50 μm) surrounded by matrix on both sides. The depth of the pores and/or fracture channel was controlled by etching time (because etching rate is relatively constant). In this study, we used two different depths. Scanning electron microscopy (SEM) was used to measure the channel depth. The SEM measurement showed that micromodels B1 and B2 were 13.4 μm (± 0.6) and 6.4 μm (± 0.7) deep, respectively. The physical properties of Micromodel B are summarized in Table 5.3. The heterogeneous pore network representation was obtained from a thin section of real sandstone. The pattern is about 5250 μm by 4786 μm repeated five times horizontally. Continuity of repeated patterns was ensured by manipulating the image digitally. A schematic of Micromodel B showing the flow regions, micrograph of the pore network and an image of the fracture with surrounding porous medium can be seen in Figure 5.6.

CHAPTER 5. PORE SCALE OBSERVATION OF PARTICLE TRANSPORT IN FRACTURE-MATRIX SYSTEMS

Table 5.2: Summary of physical properties of Micromodel A^a

A_m (cm^2)	A_f (cm^2)	Φ^b -	PV (cm^3)	k_w (darcy)	d_g^b (μm)	z (μm)
5x5	5x0.1	0.47	0.029	1.09	30-300	25

^aHere A_m is the matrix area, A_f is the fracture area, Φ is the micromodel porosity, PV is the pore volume, k_w is the absolute (water) permeability, d_g is the grain size and z is the micromodel depth.

^bPorosity and grain size range was determined by image analysis (Inwood, 2008).

Table 5.3: Summary of physical properties of Micromodel B^a

Micromodel	z (μm)	Φ^b -	PV (cm^3)	d_g^b (μm)	d_p^c (μm)	b^d (μm)
B1	13.4 (± 0.6)	0.315	1.06×10^{-4}	60.9	9.58	5, 15, 25 and 50
B2	6.4 (± 0.7)	0.315	5.07×10^{-5}	60.9	9.58	5, 15, 25 and 50

^aHere, z is the depth of Micromodel B, Φ is the micromodel porosity, PV is the pore volume, d_g is the grain size based on relative grain size, d_p is the average pore size and b is the fracture aperture.

^bPorosity and grain size was determined by image analysis.

^cThe average pore size was obtained from mercury intrusion data measured for the real sandstone, from which the micromodel image was transferred.

^dThe fracture aperture was varied with single size for each flow region.

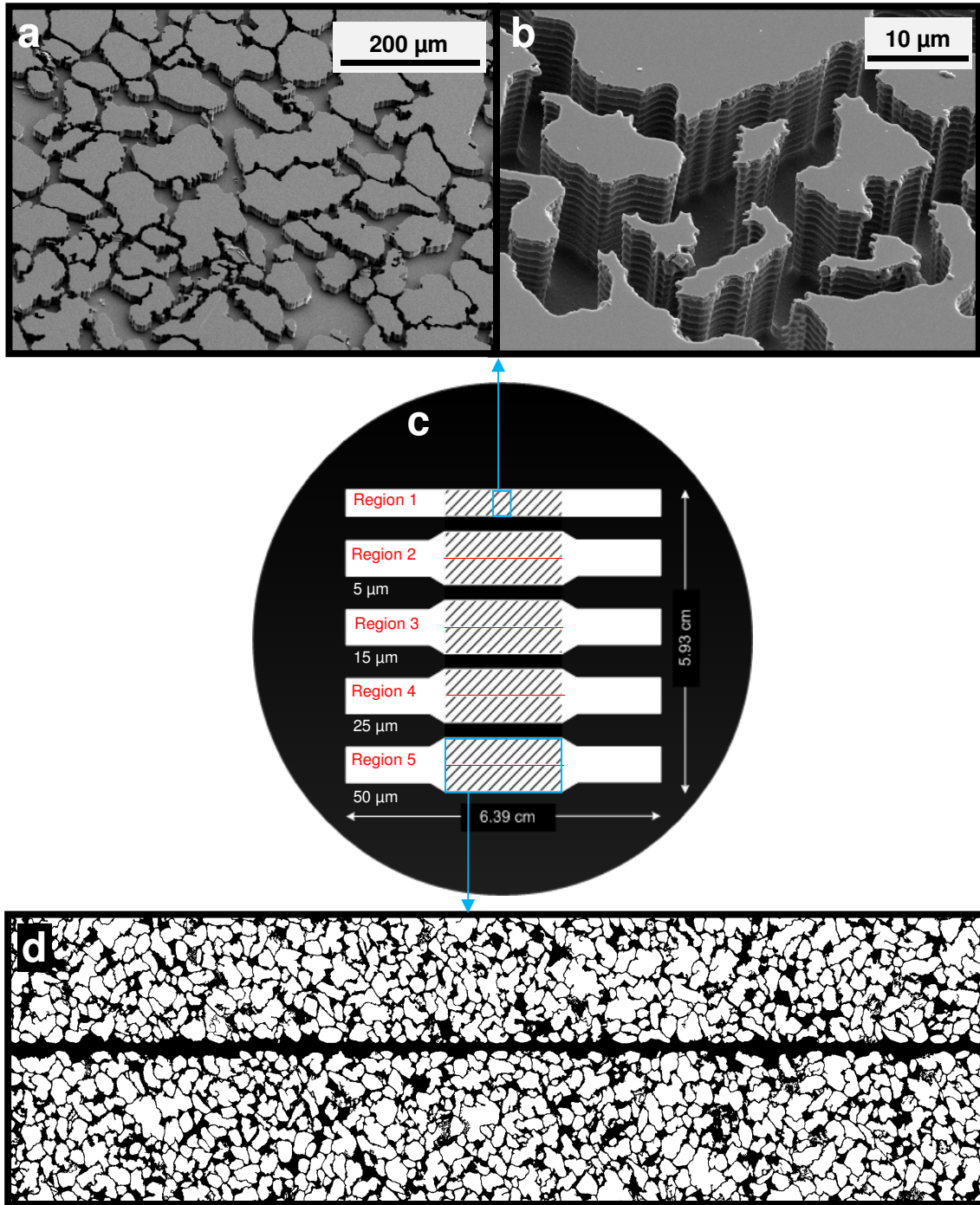


Figure 5.6: (a) SEM image of the porous medium, (b) a close-up image showing the heterogeneity and surface roughness of the grains, (c) schematic of Micromodel B showing the flow regions, fracture channels (in red) and (d) an image of the fracture surrounded by porous medium.

CHAPTER 5. PORE SCALE OBSERVATION OF PARTICLE TRANSPORT IN FRACTURE-MATRIX SYSTEMS

Grain sizes of the micromodel were ranging from 3.7 to 133.2 μm , with a considerable number of small grains. The average grain size based on the relative grain area was approximately 60.9 μm (Figure 5.7). The porosity was calculated as the ratio of pore void area to total area using image analysis, and found to be 31.5%. The pore size distribution (Figure 5.8) was obtained from the capillary pressure-saturation curve measured by mercury intrusion and Laplace's equation of capillarity, using the real sandstone from which the pore network image was obtained. The average pore size in the micromodel is about 9.53 μm .

The permeability of the porous medium was estimated by the Kozeny-Carman equation (Bear, 1988) and verified experimentally by measuring pressure drop at specified volumetric flow rates and the application of Darcy's law (Equation 3.10). The experimental setup used during permeability measurement was the same as that used for particle injection (Figure 5.12). The Kozeny-Carman equation is given as:

$$k_{kc} = \frac{d_m^2}{180} \frac{\phi^3}{(1 - \phi)^2} \quad (5.1)$$

where k_{kc} is the matrix permeability estimated by Kozeny-Carman equation in square meters, d_m is the mean size of the solid matrix in meters (estimated from the equivalent volume of the grain and the volume of a sphere) and ϕ is the porosity of the porous medium obtained by image analysis. It was found that the matrix permeability from Equation (5.1) is about 0.39 and 0.24 darcy for micromodels B1 and B2, respectively. Matrix, fracture and total permeability of micromodels B1 and B2 are summarized in Table 5.4.

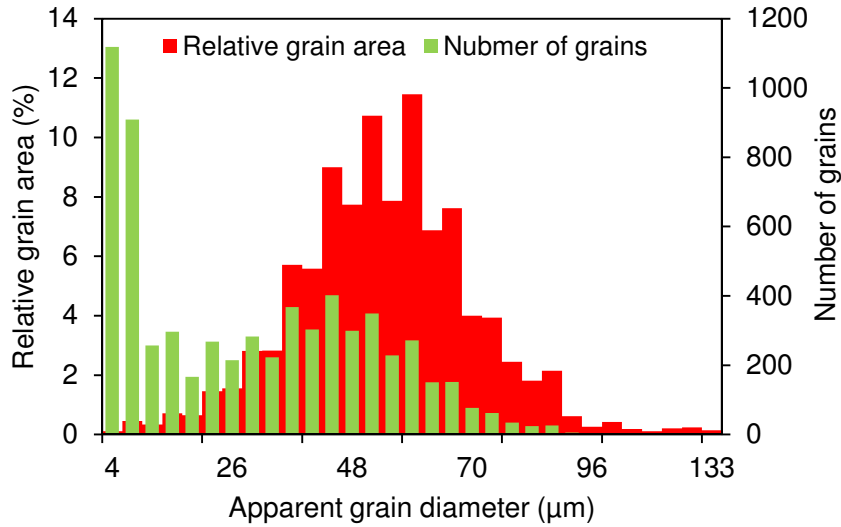


Figure 5.7: Grain size distribution based on the relative grain area and number of grains, obtained by image analysis. The relative grain area distribution indicated that the average grain size was about 60.9 μm .

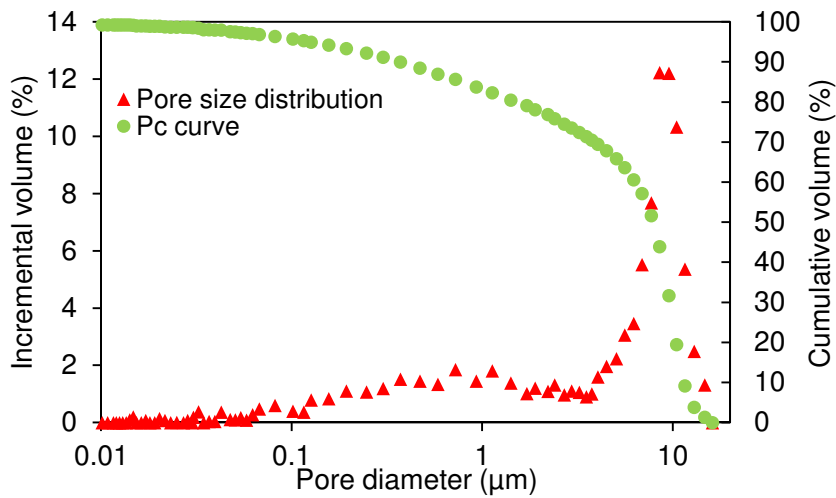


Figure 5.8: Pore size distribution of the pore network obtained by mercury intrusion, indicating an average pore diameter of about 9.53 μm .

CHAPTER 5. PORE SCALE OBSERVATION OF PARTICLE TRANSPORT IN FRACTURE-MATRIX SYSTEMS

Table 5.4: Summary of matrix and fracture permeability for micromodel B1 and B2^a

Fracture aperture (μm)	Micromodel B1 (darcy)			
	Cubic law		Poiseuille's law	
	k_m	k_f	k_m	k_f
15	0.40	15.27	0.51	8.16
25	0.38	15.27	0.51	13.60
50	0.35	15.27	0.51	27.20
k_{kc}		0.39		
$k_{\text{matrix only}}$		0.30		
Fracture aperture (μm)	Micromodel B2 (darcy)			
	Cubic law		Poiseuille's law	
	k_m	k_f	k_m	k_f
15	0.22	3.48	0.18	3.90
25	0.21	3.48	0.18	6.50
50	0.21	3.48	0.18	12.99
k_{kc}		0.24		
$k_{\text{matrix only}}$		(-) ^b		

^aHere k_m is matrix permeability (Equation 5.2), k_f is fracture permeability (Equation 5.3 or 5.4 for cubic and Poiseuille's law, respectively), k_{kc} is Kozeny-Carman matrix permeability (Equation 5.1) and $k_{\text{matrix only}}$ is the matrix permeability using flow region 1 where there was not fracture. "-" indicates that measurement was not performed. Note that permeability was calculated based on the average measured depth of the micromodels, 13.4 μm and 6.4 μm for micromodel B1 and B2, respectively.

^bThis measurement was attempted but was not successful.

The matrix permeability measurements were conducted in flow region 1 (no fracture) as seen in Figure 5.6c, at varying volumetric flow rates between 0.0001 to 0.0005 cm^3/min . Figure 5.9 shows matrix permeability and pressure drop at different flow rates. The average matrix permeability was approximately 0.30 darcy for Micromodel B1. The measurement of matrix permeability of Micromodel B2 was attempted, but was not successful due to the higher pressure drops at shallower depth that resulted in wafer breakage at the flow rates used (flow rates lower than 0.0001 cm^3/min).

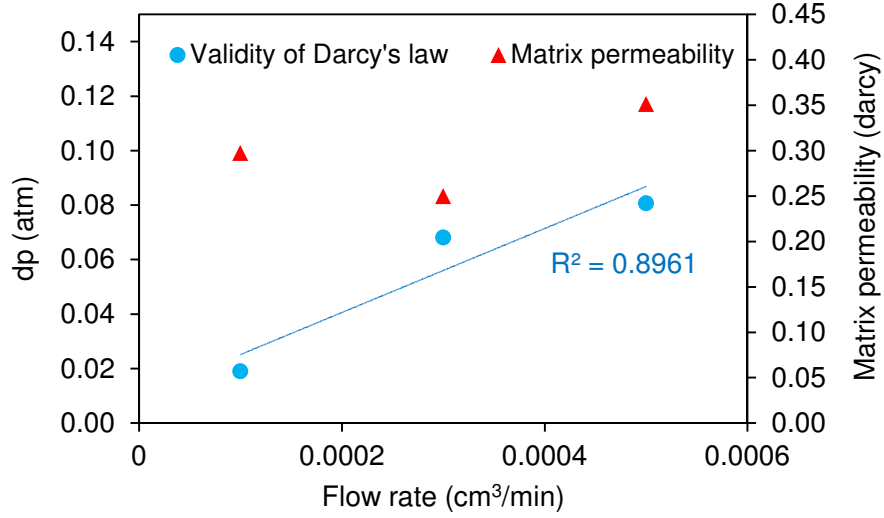


Figure 5.9: Matrix permeability of Micromodel B1 and pressure drop at various volumetric flow rates. The average matrix permeability was about 0.3 darcy. The pressure drop with relation to volumetric flow rate was relatively linear, indicating applicability of Darcy's law at experimental flow conditions.

The matrix permeability was also estimated by measuring the total permeability of fracture-matrix system (regions 2 to 5 in Figure 5.6c), considering flow in the parallel-plate fracture model and the application of Darcy's law of incompressible horizontal fluid flow, the matrix permeability can be expressed as:

$$k_m = \frac{k_t A_t - k_f A_f}{2A_m} \quad (5.2)$$

where k_m is matrix permeability measured experimentally, k_t is the equivalent permeability of flow in parallel layers, k_f is the fracture permeability. The fracture permeability was approximated based on the fracture shape using the cubic law (Snow, 1968) simulating flow between two parallel plates when the depth to aperture ratio was smaller than 1.0, or Poiseuille's law (Sutera and Skalak, 1993) simulating flow in a tube when the depth to aperture ratio was close to 1.0. The fracture permeability based on cubic law and is given as:

CHAPTER 5. PORE SCALE OBSERVATION OF PARTICLE TRANSPORT IN FRACTURE-MATRIX SYSTEMS

based on cubic law,
$$k_f = k_{f,cubic} = \frac{b^2}{12} \quad (5.3)$$

based on Poiseuille's law,
$$k_f = k_{f,Poiseuille's} = \frac{b^2}{8} \quad (5.4)$$

Note that b in Equation 5.4 was calculated based on the equivalent area of the channel and the area of a circle (equivalent radius).

The micromodel orientation with respect to a fracture in a block of fractured rock is illustrated schematically in Figure 5.10. Because the micromodel is a slot perpendicular to the block fracture with depth similar to the fracture aperture, the fracture permeability in Equation 5.3 was calculated using the depth of the micromodel instead. Because the fracture depth of the micromodel is measured by SEM, k_f can be calculated directly.

The matrix and total permeability assuming cubic or Poiseuille's law in calculating fracture permeability, for Micromodel B1 and B2, are shown in Figure 5.11. The permeability data suggested that there was a small difference in the permeability values (below 30 md) when the fracture was treated as parallel plate or tube for Micromodel B2.

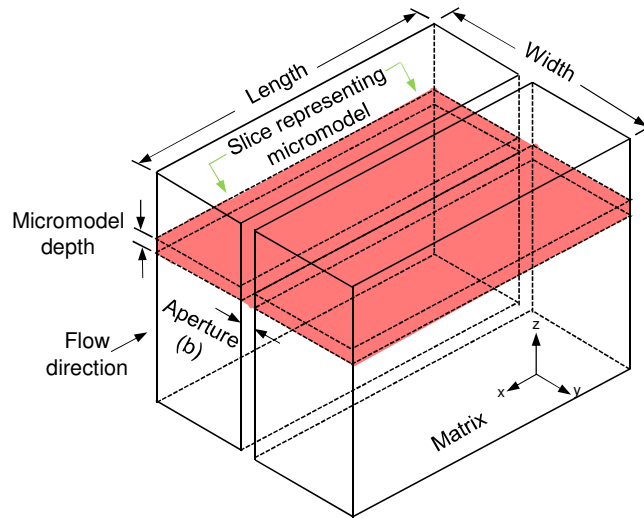


Figure 5.10: Schematic of block of fractured rock showing the micromodel orientation with respect to the fracture.

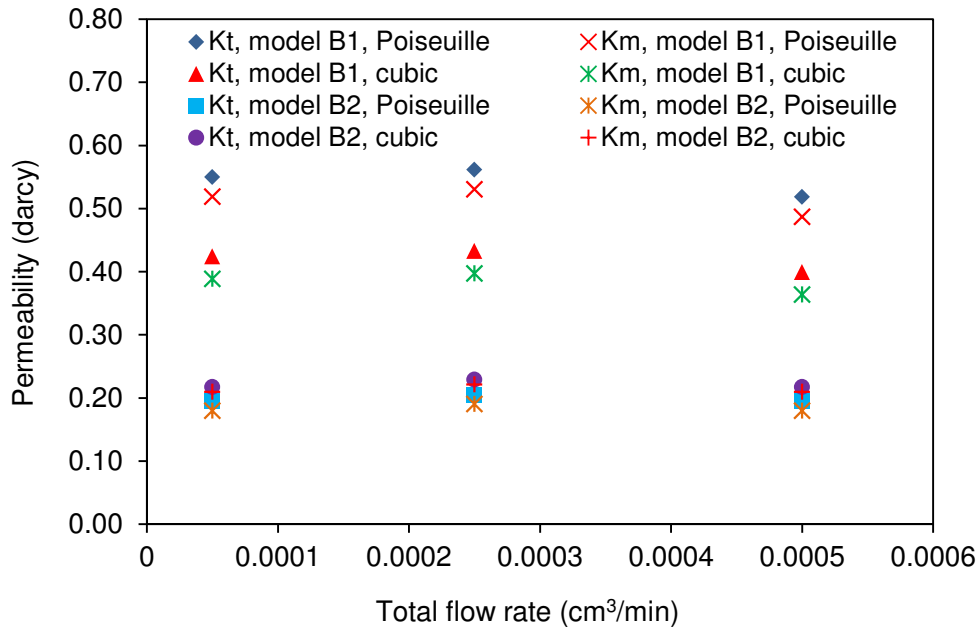


Figure 5.11: Total and matrix permeability measured at various volumetric flow rates for Micromodels B1 and B2, assuming a parallel plate fracture (cubic law) and flow in tube (Poiseuille's law). Note that the total and matrix permeability of Micromodel B2 did not change much when treating the fracture as parallel plate or tube. All these measurements were conducted in flow region 4, with fracture aperture of 25 μm .

The change was greater in case of Micromodel B1 (around 125 md). The ratio of the fracture depth to equivalent radius (when the fracture is assumed as tube) was about 76% and 90% for Micromodel B1 and B2, respectively, which was consistent with fact that the permeability of Micromodel B2 was not very sensitive to which fracture model had been used. A summary of measured matrix and fracture permeability of micromodels B1 and B2 for different fracture apertures is presented in Table 5.4.

5.3.2 Micromodel fabrication

The fabrication of a micromodel begins with construction of a mask. The pore network image is reproduced as chrome on glass substrate. The grains on the glass replica are opaque while pores spaces are transparent. The image on the mask is transferred to the silicon wafer (4-inch silicon wafers, K Prime, 4P <100> B S42565) using a photoresist material (Hornbrook, 1991). Prior to the photoresist coating, the silicon wafer is

CHAPTER 5. PORE SCALE OBSERVATION OF PARTICLE TRANSPORT IN FRACTURE-MATRIX SYSTEMS

dehydrated in an oven at 150°C for about 30 minutes. Dehydration involves priming the wafer with hexamethyldisilazane (HMDS) to improve the photoresist adhesion to the wafer.

A coating of the photoresist (Shipley 3612) is spun onto the wafer, resulting in 1.6 µm thick photoresist layer. The wafer is then baked at 90°C for 2 minutes until dry. The wafer is exposed to the mask using a Karluss MA-6 contact mask aligner. During exposure, ultraviolet light is passed through the mask, leaving only the photoresist coating at grains. A soft contact program with 2.6 seconds exposure time and 40-µm gap width is selected. The silicon wafer is developed using Shipley MF-26A surfactant to remove unexposed photoresist, and then baked at 110°C for 2 minutes. After developing, the image transfer is completed and the wafer is removed from the photolithography area and is ready for etching.

The pore network image is dry-etched using an inductive charged plasma deep reactive ion etcher. The etch process alternates between the passivating C₄F₈ plasma and the silicon etching SF₆ plasma. The wafer is etched to a desired depth. To isolate the individual flow channels, a borofloat glass wafer of 10.16 cm diameter and 0.1 cm thick, is bonded anodically to the silicon wafer. Prior to bonding, wafers are cleaned in sulfuric acid/hydrogen peroxide (9:1 H₂SO₄:H₂O₂) solution bath at 120°C for 20 minutes, followed by six-cycle deionized water rinse and spin dry. In this work, 0.15 cm inlet and outlet ports were drilled, in the Stanford crystal shop, into the bonded glass substrate.

The anodic bonding forms an irreversible bond between the glass and unetched portions of the silicon wafer. The bonding process involves a hotplate, electrodes and power supply. The materials are arranged from bottom up: anode, etched silicon wafer, glass wafer and cathode (Hornbrook, 1991). The bonding process starts by placing a clean silicon wafer (etched face up) on the hotplate preheated to 350°C for about 30 minutes. The wafer is dusted using compressed ultrapure air to ensure that the etched side is particle-free. A clean glass wafer is then placed carefully on top of the silicon wafer. An aluminum plate wrapped with a copper mesh is positioned above the wafers. The hotplate

is connected to one electrode (anode) of the power supply, while the positive electrode (cathode) is connected to the aluminum plate. The power supply is brought to 1000 volts and left for about 45 minutes (Rangel-Germán, 2002). The bonding is observed as gradual change in color of the wafer, bonded areas appear black whereas unbounded regions appear light gray (Hornbrook, 1991).

5.4 Micromodel experimental setup and injection method

A schematic of the experimental apparatus employed for the particle transport is shown in Figure 5.12. The apparatus consists of syringe pump (Cole Parmer, series 74900), reflective light microscope (Leica DM 2500 M) and differential pressure transducer (Validyne Model DP215-50). Images of particles in the micromodel were obtained using a high speed digital camera (Leica DFC400) controlled by Leica Application Suite (LAS) image analysis software. During the particle injection experiments, images were acquired at specific times at different sections of the micromodel with 10X and 20X objectives (plus 10X eyepiece). The micromodel was placed in a horizontal position on top of the microscope stage. The inlet and outlet ports were fitted with special nanoport connection assemblies (Nano-Port model N-333 Headless, 0.15 cm diameter) for chip-base application (i.e. flat glass wafer) manufactured by IDEX Health and Science. The nanoports were attached to the glass wafer via an adhesive ring provided by the manufacturer according to the following procedure. First, the bonding surfaces were cleaned with isopropyl alcohol. A gasket seal was then inserted on the recess in the bottom of the port and the adhesive ring centered on the glass wafer. Finally, the port was clamped to the glass wafer and placed in an oven at a temperature of 170°C for one hour to develop a complete bond between the ports and wafer. Water used throughout the experiments was purified using Millipore (A10) equipped with 0.220 μm filter, boiled and vacuumed at 50 millitorr vacuum pressure for at least 30 minutes prior to use.

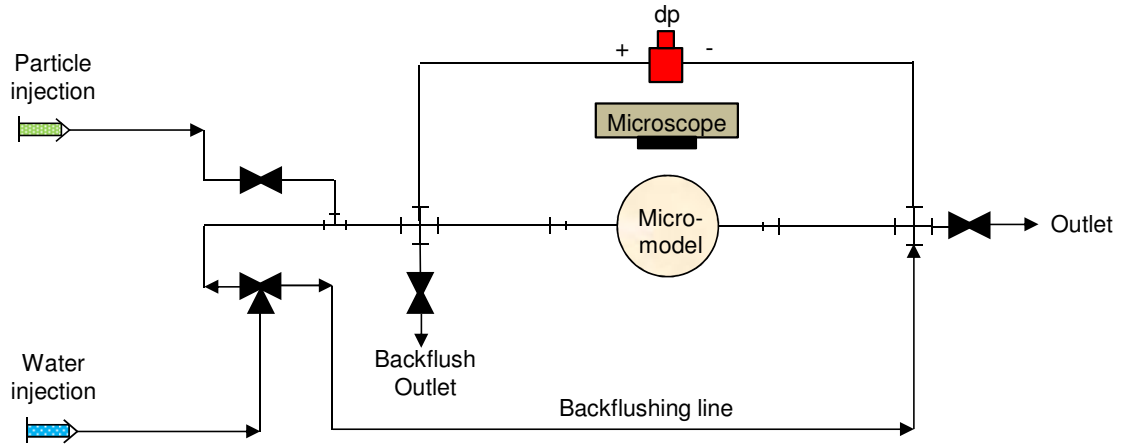


Figure 5.12: Schematic of the experimental apparatus employed in the particle transport through micromodels.

5.4.1 Silica particle Micromodel A injection method

The aim of these microscale experiments was to visualize particle transport processes, and to help explain findings from the core-flooding experiments (silica particles into fractured greywacke and Berea sandstones, as described in Chapter 4). Micromodel A was used to assess the flow mechanism of silica particles, particularly the influence of suspension concentration on recovery and straining, within the fracture and fracture-matrix interface.

A volumetric flow rate of $0.001 \text{ cm}^3/\text{min}$ was used to prevent damage to the silicon micromodel due to excessive pressure, and to allow for visual observation through the microscope during the particle flow within the pores. This flow rate corresponds to an average water pore velocity of about $0.17 \text{ cm}/\text{min}$ and residence time of 29.38 min . The study was conducted at saturated conditions. Before initiating the particle transport experiments, the micromodel was saturated fully with pure water. Several pore volumes of pure water were flushed through the model, and complete saturation was confirmed by image analysis. Only particles of $2 \text{ }\mu\text{m}$ diameter at concentrations of 0.49 and $1.92 \text{ mg}/\text{ml}$, were injected into the micromodel. A precursor injection of silica nanoparticles (350 nm , -73.4 mV) was conducted under same flow conditions. Silica nanoparticles

were the same as those used during silica injection into sand-packed slim tube (particle characterization can be found Section 3.5.5).

5.4.2 CML particle Micromodel B injection method

CML particles of different sizes were transported through Micromodel B to investigate the influence of particle size on its transport and visually confirm enhanced particle transport by fractures.

The transport experiments were all conducted at saturated conditions. The micromodels were saturated by flowing pure water (Q-Millipore) until full saturation was achieved. The saturation of shallower models (Micromodel B2) was accomplished by flushing with CO₂ followed by continuous flow of water. The pore volume of Micromodel B1 and B2, calculated based on 15 μm fracture aperture and excluding the inlet and outlet port volumes, were approximately 1.06×10^{-3} and 5.09×10^{-4} cm³, respectively. Note that the pore volumes will increase slightly for larger fracture apertures (25 and 50 μm). The particle injection flow rate was varied from 5×10^{-5} to 3×10^{-3} cm³/min, depending on the fracture aperture size. Several particle sizes were injected at two different flow rates to examine the effect of fluid velocity on transport. Table 5.5 provides a summary of water velocity and average water residence time in fracture during particle injection into Micromodels B1 and B2.

CHAPTER 5. PORE SCALE OBSERVATION OF PARTICLE TRANSPORT IN FRACTURE-MATRIX SYSTEMS

Table 5.5: Summary of water velocities and average resident time in fracture for micromodel B1 and B2^a

<i>Micromodel B1</i> (depth: 13.4 μm)									
Cubic law					Poiseuille's law				
b (μm)	d_p (μm)	$v_{f,l}$ (cm/min)	$\tau_{f,l}$ (min)	$v_{f,h}$ (cm/min)	$\tau_{f,h}$ (min)	$v_{f,l}$ (cm/min)	$\tau_{f,l}$ (min)	$v_{f,h}$ (cm/min)	$\tau_{f,h}$ (min)
15	6	2.61	0.92	3.39	0.71	1.39	1.72	1.81	1.32
25	2	1.30	1.84	16.94	0.14	0.77	3.09	10.06	0.24
25	4.5	2.61	0.92	12.77	0.19	2.32	1.03	11.38	0.21
25	6	2.61	0.92	25.54	0.09	2.32	1.03	22.75	0.11
25	10	2.61	0.92	78.18	0.03	2.32	1.03	69.64	0.03
25	^b Mix 1	2.61	0.92	-	-	2.32	1.03	-	-
25	^b Mix 2	2.61	0.92	-	-	2.32	1.03	-	-
50	10	2.61	0.92	78.18	0.03	4.64	0.56	139.29	0.02
50	^b Mix 2	2.61	0.92	-	-	4.64	0.52	-	-

<i>Micromodel B2</i> (depth: 6.4 μm)									
Cubic law					Poiseuille's law				
b (μm)	d_p (μm)	$v_{f,l}$ (cm/min)	$\tau_{f,l}$ (min)	$v_{f,h}$ (cm/min)	$\tau_{f,h}$ (min)	$v_{f,l}$ (cm/min)	$\tau_{f,l}$ (min)	$v_{f,h}$ (cm/min)	$\tau_{f,h}$ (min)
15	6	2.08	1.15	297.24	0.01	2.33	1.03	332.63	0.01
25	4.5	2.38	1.01	297.24	0.01	4.44	0.54	554.38	4×10^{-3}
25	6	0.53	2.88	0.83	4.03	1.11	2.16	8.87	0.27
50	6	2.38	1.01	297.24	0.01	8.87	0.27	1108.77	2×10^{-3}

^aSubscripts f,l and f,h in $V_{f,l}$ and $V_{f,h}$ refer to low-and high water velocity inside fracture, respectively. $\tau_{f,l}$ and $\tau_{f,h}$ refer to water travel time in fracture during injection experiments at two different flow rates. b is fracture aperture and d_p is particle size. “-“ indicates that this injection experiment was not performed.

^bMix 1 contains particle sizes of 2, 4.5, 6 and 10 μm . Mix 2 contains only the 2, 4.5 and 6 μm particles.

5.5 Results and discussion

This section provides the results of the 2 μm silica and the CML particles injection through Micromodel A and B, respectively.

5.5.1 Silica particle injections into Micromodel A

The 2 μm silica particles at two different suspension concentrations (0.49 and 1.92 mg/ml) were injected at flow rate of 0.001 cm^3/min (pore velocity of 0.17 cm/min). The particles were transported through the fracture, but trapped along the fracture-matrix interface (Figure 5.13). The particles were aggregating and therefore straining at pore throats. The particles were not able to infiltrate through the matrix for more than a few grains downstream of the fracture-matrix interface, depending on the concentration. Fluorescent emission measurement and SEM imaging showed that the effluent samples were free of particles. Note that straining was more pronounced with increasing concentration, which resulted in significant particle deposition. Particle deposition was a function of suspension concentration. Particles were aggregating; forming large clusters because more particles were present at high suspension concentration. This was consistent with the recovery measurements (i.e. the recovery of the 2 μm particles was decreasing with increasing particle concentration during core-flooding experiments).

Further investigation of particle straining was carried out by injecting silica nanoparticles of an average size of 0.35 μm (about six times smaller than the 2 μm particles). The silica nanoparticles were negatively charged (zeta potential of -73.4 mV) with surface chemistry similar to the 2 μm particles. The silica nanoparticles transported across the micromodel. The existence of the silica nanoparticles in the effluent was confirmed by SEM. The recovery of nanoparticles was not determined because the influent concentration was unknown and because the nanoparticles were not fluorescent. Visual observation of the nanoparticles was not possible due to the physical limitation imposed by the light optics to resolve particles at that size. This injection was conducted as a precursor only, so further details are omitted.

CHAPTER 5. PORE SCALE OBSERVATION OF PARTICLE TRANSPORT IN FRACTURE-MATRIX SYSTEMS

In the case of the 2 μm particles, by visual observation (Figure 5.13), it was evident that significant straining had occurred, with some attachment. Attachment aided straining because particle attachment decreased the effective pore throat size for subsequent particles to flow in a given pore throat. The particle attachment to fracture walls was also observed (Figure 5.13a, c). Flushing in both directions at high velocity did not remobilize the particles, suggesting permanent attachment of particles to the grains and/or fracture wall. At injection rate of 0.001 cm^3/min , the residence time in the micromodel is estimated to be about 29.38 min, which was considerably longer than resident times of the silica particles in fractured greywacke (0.1 min) and Berea (0.04 to 0.24 min) core experiments, thus allowing more time for particle-wall interactions.

Fracture walls in the micromodel (silicon-glass walls) are considerably smoother and more uniform compared to the fracture in the real rock (e.g. fractured Berea sandstone). In fractured rocks, fracture walls are expected to have some degree of surface roughness. Rougher grain surfaces are expected to be more efficient particle collectors. Auset and Keller (2006) observed significant influence of rough grain surface in particle capturing. Irregularities in matching fracture surfaces would result in varying size and orientation of flow paths, resulting in a larger collision probability, and a higher overall probability of attachment to fracture walls. Thus, the particle attachments to the fracture walls in Berea core were expected to be more pronounced than in the micromodel. Filtration theory, using single-collector contact efficiency, suggested that the probability collision of the 2 μm particles (density of 2.2 g/cm^3) with varying collector (grain) size from 30 to 300 μm (as per the fabrication of the micromodel) was below 13% (Figure 5.14). Note that under these experimental conditions, the probability of collision decreased by 50% with increasing grain size (from 13% to 6%) at the same fluid velocity. According to filtration theory, gravitational sedimentation dominates the transport of particles for the majority of the grain size distribution of the micromodel. Transport by interception and Brownian diffusion was estimated to decrease with increasing grain size, with the former decreasing more rapidly with increasing grain size.

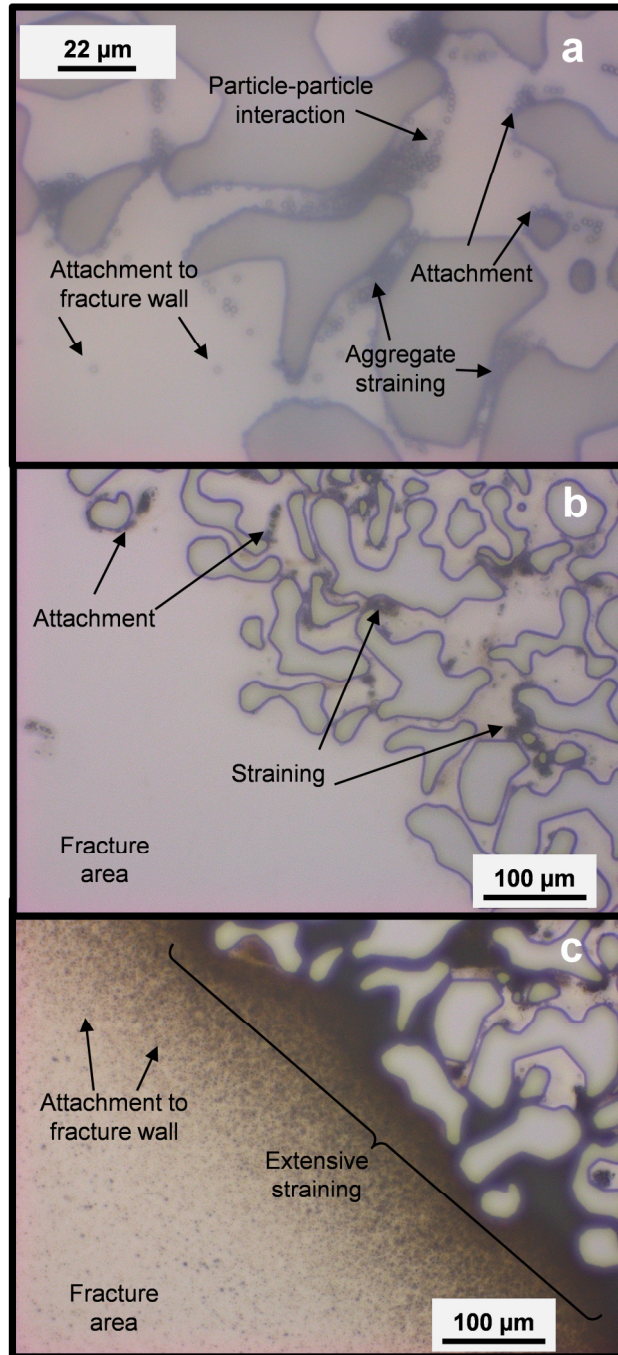


Figure 5.13: Image (a) showing particle-particle interaction (aggregation), particle attachment to grain surface and straining. Images (b) and (c) are showing straining during the injection of suspension concentration 0.49 and 1.92 mg/ml, respectively. Particle straining at the fracture-matrix interface is prominent with increasing suspension concentration.

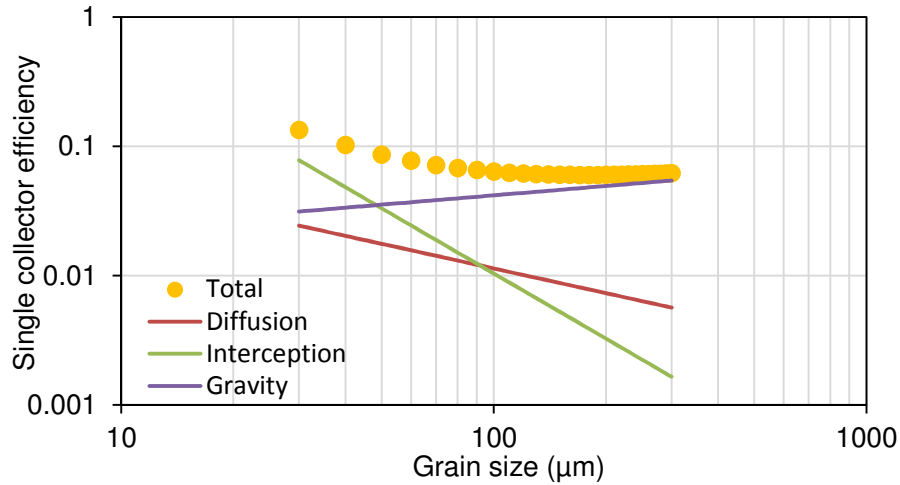


Figure 5.14: A log-log plot showing the effect of grain size on the physical transport mechanisms of diffusion, interception and gravitational sedimentation for silica of particle size $2 \mu\text{m}$ in Micromodel A. Hamaker constant $A_H=6 \times 10^{-21} \text{ J}$, $T= 21 \text{ }^\circ\text{C}$, $\rho_p= 2.2 \text{ g/cm}^3$, $f= 21\%$, $v= 2.84 \times 10^{-5} \text{ m/s}$.

Most of Micromodel A inlet pore throats are about 8 to 12 μm , corresponding to T/C ratios higher than 4. Keller and Auset (2006) showed experimentally that filtration theory is appropriate for T/C ratios greater than 2.5, but not at lower T/C ratios where straining was occurring. In this experiment, although the T/C ratio based on the individual particle size was greater than 2.5, straining of aggregates was occurring. This is because the size of the aggregate would be larger than the size of the individual particle. Predicting particle removal by filtration theory would not be accurate because filtration theory does not account for straining (Bradford et al., 2002).

The ratio of particle to grain size is in the range of 0.0067 to 0.067. At grain sizes of 250 μm and smaller, the particle to grain size ratio exceeded the value of 0.008, threshold proposed by Xu et al. (2006), above which straining affects particle mobility. This implies that straining dominated the transport in the micromodel. This is also consistent with the findings of Bradford et al. (2007) in their study of transport of latex particles through sand columns, each packed with single grain size sand (ratios in the range of 0.007 to 0.02 with respective recovery diminishing from 100% to 10%). Thus,

heterogeneity of the pore network in our micromodel, represented by the mixture of grain sizes, augmented the effect of straining. In order to predict of particle recovery successfully, the influence of the spatial distribution of pore or grain size must be included.

5.5.2 CML particle injections into Micromodel B

The impact of particle size in transport through fractured porous media was investigated using Micromodel B. Enhancement of particle transport through the fracture was confirmed visually. CML particles of sizes in the range of 2-10 μm were transported through fractures of different apertures (15, 25 and 50 μm). Note that particle sizes in the submicron range were not used due to limitations of the reflective light microscopy to see particles at that size.

This study showed that particle transport is facilitated by the presence of fractures. Although expected, the experiments confirmed (by direct visual observation) that particles flow mainly through the fracture especially for larger particles. This is because of the high flow velocity within the fracture relative to the surrounding porous medium. The velocity field was calculated by solving the Navier-Stokes equation numerically for laminar flow using COMSOL Multiphysics. The velocity field was solved for 1177 μm by 450 μm section of Micromodel B that included the fracture and surrounding matrix. The geometry of the micromodel was hand-traced using eMachineShop CAD Software. The resulting velocity field can be seen in Figure 5.15. The simulated velocity field indicated that the high velocity streamlines were inside the fracture. The calculated velocities were higher than the velocities measured experimentally, because the velocity field was calculated for two-dimensional space whereas the micromodel is a three-dimensional space. Also, the pressure gradient used in this calculation was not measured at the inlet and outlet faces of the simulated section. Although the calculated velocities were not matching, this result showed qualitatively that the highest velocities are within the fracture.

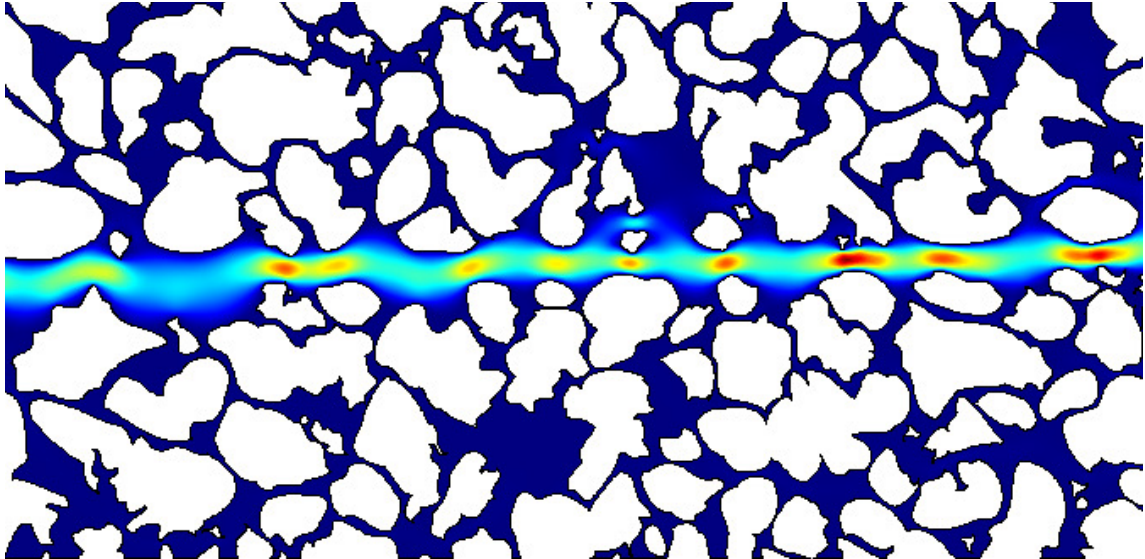


Figure 5.15: Two-dimensional velocity field for section of Micromodel B. Blue color indicates slow fluid velocity, red color indicates higher velocity.

Table 5.5 provides a summary of water velocity and residence time within fractures during particle injection into Micromodels B1 and B2. For example, the average water velocity within the 25 μm aperture fracture relative to matrix of micromodel B1 is about 12.5. Particles tend to travel along fast moving streamlines, experience fewer detours to adjacent matrix grains and hence shorter travel time and enhanced transport velocity; phenomena observed by many investigators by interpreting breakthrough curves (e.g., Reimus, 1995; Becker et al., 1999; McKay et al., 2000, 2002; Zvikelsky and Weisbrod, 2006). This was consistent with the fast arrival of silica particles during the experiments in fractured greywacke and Berea sandstones (refer to Chapter 4).

The particle velocity during its transport through the fracture was estimated by tracking the particles manually as they flowed across the captured frame. Each video was split into frames. The particle velocity was determined statistically by tracking approximately 40 particles at different parts of the recorded video. The individual particle velocity was then calculated based on the time it spent to leave the frame (of length 1177 μm). Table 5.6 summarizes particle velocity of selected injections (where fracture plugging did not occur). A comparison between particle velocity and the maximum velocity of fluid

CHAPTER 5. PORE SCALE OBSERVATION OF PARTICLE TRANSPORT IN FRACTURE-MATRIX SYSTEMS

between two parallel-plates and within a tube is also provided. The particle velocity was 1.05 to 2.12 and 0.73 to 2.33 times the average water velocity inside the fracture assuming parallel-plate (maximum velocity is 1.5 times the average water velocity) or tube (maximum velocity is 2.0 times the average water velocity) fractures, respectively. In fractures where the aspect ratio of aperture to micromodel depth was greater than 1.5, particles velocities were very close to the maximum water velocity assuming parallel-plate fracture. In the case in which the fracture aperture (15 μm) was comparable to the micromodel depth (13.4 μm), the particle velocity was better matched to the maximum water velocity assuming Poiseuille's law (circular channel). The particle velocity was approximately 0.045 cm/s compared to a maximum water velocity of 0.040 cm/s. This observation confirmed that particles follow midstream velocity lines when migrating through a fracture, as reported by other researchers (e.g., Reimus, 1995; Becker et al., 1999; McKay et al., 2000, 2002; Zvikelsky and Weisbrod, 2006). The combined effect of charge and size exclusion may result in an enhanced velocity of particles (Becker et al., 1999).

The total interaction energy between the particles and the micromodel surface can be seen in Figure 5.2. For all particle sizes, there exists a high repulsive energy barrier that extends approximately 1 μm into solution. This indicates that particles would not be able to access flow paths within a couple of micrometers of fracture walls, which would force particles to travel through the center of the fracture along fast moving streamlines. This is the effect of charge exclusion. Particles in the micron size range, such as those used in this study, are prone to migrate through large flow paths (the fracture). For instance, the Peclet number for the 10 and 4.5 μm particles at the same velocity decreased from 1.35×10^6 to 6.08×10^5 (44%) solely because of the size of the particle. Diminishing Brownian diffusion rate associated with larger particles would prevent them from diffusing out of high velocity streamlines, and thus excluding them from low velocity hydrodynamic boundary layers along the fracture walls. This is the effect of size exclusion.

Table 5.6: Particle velocity of selected injection^a

d_p (μm)	b (μm)	Micromodel -	v_p (cm/s)	$v_{f,max1}$ ^e (cm/s) <i>Poiseuille's law</i>	$v_{f,max2}$ ^f (cm/s) <i>Cubic law</i>
2	25	B1	0.028	0.026	0.030
4.5	25	B1	0.059	0.078	0.060
4.5	25	B2	0.054	0.148	0.060
6	15	B1	0.045	0.040	0.064
6	25	B1	0.091	0.078	0.065
6	50	B2	0.056	0.292	0.060
6	25	B2	0.023	0.040	0.021
10	50	B1	0.069	0.154	0.065
Mix 2 ^b	50	B1	0.074	0.140	0.065
Mix 2 ^c	50	B1	0.056	0.140	0.065
Mix 2 ^d	50	B1	0.051	0.140	0.065

^aHere b is the fracture aperture, d_p is the particle size, v_p is the particle velocity inside the fracture, $v_{f,max1}$ and $v_{f,max2}$ are the maximum water velocity inside the fracture assuming tube and parallel-plate fracture, respectively.

^bThe velocity of the 2 μm particle size.

^cThe velocity of the 4.5 μm particle size.

^dThe velocity of the 6 μm particle size.

^eThe maximum water assuming a circular channel (tube) fracture is 2.0 times the average water velocity inside the fracture.

^fThe maximum water velocity assuming a parallel-plate fracture is 1.5 times the average water velocity inside the fracture.

Physical size exclusion or straining at matrix grains was observed visually for all particle sizes. Note that discussion hereafter refers to flow experiments conducted through Micromodel B1 (depth of 13.4 μm), unless otherwise indicated. Particles accumulated at the first few rows of pore throats. Particle accumulation was more significant as particle size increased. Blocked pore throats become dead ends for subsequent particles until a filter cake of particles forms at the inlet grains. Although the 6 and 10 μm particle straining was expected, at average pore throat of 9.53 μm , the micromodel experiments

CHAPTER 5. PORE SCALE OBSERVATION OF PARTICLE TRANSPORT IN FRACTURE-MATRIX SYSTEMS

showed the overwhelming fraction of particles depositing at the inlet pore spaces (Figure 5.16). This is consistent with the findings of Auset and Keller (2006). Particle retention in the porous matrix was a function of relative particle size (i.e. pore throat-particle ratio (T/C), where T is the average pore throat size of 9.53 μm obtained by mercury intrusion). For example, the T/C ratio of particle size 6 and 10 μm was 1.6 and 1.0, respectively, at which straining was expected and observed.

In addition, straining was also the primary deposition mechanism at matrix grains during particle transport at volumetric flow rates an order of magnitude higher. The fact that particle deposition at grains was independent of flow rate was indicative of straining. Most of the 6 and 10 μm particle transport occurred through the fracture. The impact of the flow medium depth on particle transport is illustrated in Figure 5.17. The optical images were taken from the transport experiments of the 6 μm particles through Micromodel B1 (aperture 25 μm) and B2 (aperture 25 μm), where Micromodel B1 is two times deeper than Micromodel B2. All flow parameters were the same for these two flow experiments. One can observe the size of the filter cake of particles straining at the inlet grains in Micromodel B2. Note that the fracture channel was not plugged during these experiments and particle transport continued mainly through the fracture. The amount of straining at the inlet grains of the matrix of the shallower micromodel was more pronounced. This observation signifies that particle transport differs greatly as a function of the physical dimensions of the flow conduits (pore space or fracture channel).

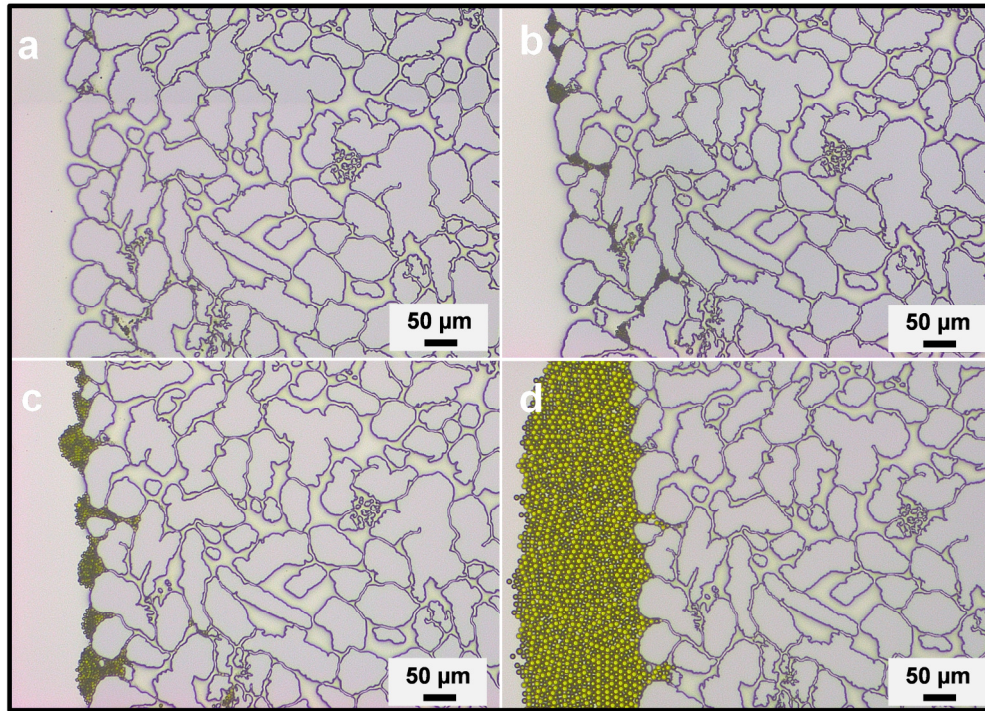


Figure 5.16: Optical images obtained at the inlet pore spaces during the transport of particle size (a) 2, (b) 4.5, (c) 6 and (d) 10 μm through Micromodel B1. These images were captured at the same location at the end of the flow experiments, showing the overwhelming straining as particle size increases. Images taken at magnification of 100X.

The 2 μm particles ($T/C = 4.8$), on the other hand, transported across the entire porous medium. Particle removal at this size was mainly at a few rows of pore spaces at the inlet side. Visual observation suggested that interception was the filtration mechanisms at the matrix side (not fracture vicinity). Particle removal by the porous medium decreased with increasing flow rate, indicating that the deposition mechanism was flow dependent. Figure 5.18 shows snapshots at the end of the 2 μm particle experiments at two different volumetric flow rates (5×10^{-5} and 5×10^{-4} cm^3/min , an order of magnitude apart). It was evident that particle deposition mechanism was flow dependent. Interception and gravity settling are highly dependent on fluid pore velocity. Transport by gravitational sedimentation may have contributed to particle deposition at the low flow rate injection. Transport by gravitational sedimentation could not be observed visually during the transport.

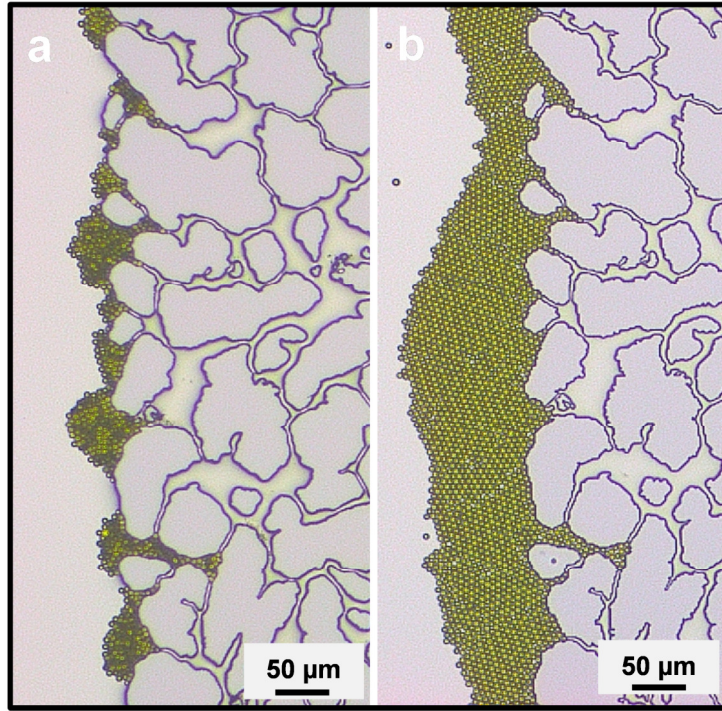


Figure 5.17: Optical imaging of the $6\ \mu\text{m}$ particles straining during their transport into (a) Micromodel B1 (aperture $25\ \mu\text{m}$) and (b) Micromodel B2 (aperture $25\ \mu\text{m}$), showing the influence of the physical dimensions (or depth) of flow conduit on particle transport.

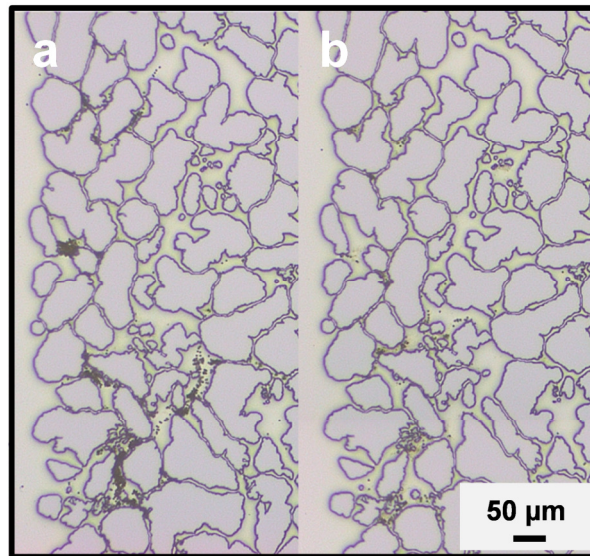


Figure 5.18: Optical images captured at the end of the $2\ \mu\text{m}$ particle experiments at (a) 5×10^{-5} and (b) $5 \times 10^{-4}\ \text{cm}^3/\text{min}$ injection rates. This confirmed that the particle deposition mechanism was flow dependent.

CHAPTER 5. PORE SCALE OBSERVATION OF PARTICLE TRANSPORT IN FRACTURE-MATRIX SYSTEMS

The existence of the fracture facilitated the transport of all the particles used in this study, except for the cases of the 10 and 6 μm particles in Micromodels B1 and B2, respectively. These experiments will be discussed later in this section. Note that larger particles were straining near the porous medium inlet causing dead-end pores. Due to this and the high velocity in the fracture relative to surrounding matrix, particle transport was restricted to be through the fracture. This was consistent with the finding of Bradford et al. (2002 and 2003) of particle transport in a sand column. They reported that straining was depth-dependent because straining at inlet grains created dead ends, forcing subsequent particles through a larger continuous pore network. Among all the particles, the 2 μm particles were observed to diffuse into surrounding pores along the sides of the fracture, especially during the low flow rate injection. Also, particles were found to deposit at the sides of the fracture. One explanation is that particles were moving across streamlines due to gravity settling. The length scale analysis (Table 5.7) suggested that, during the low flow rate injection, the 2 μm particles had L_S/L_D ratio greater than 1.0 and they would have a settling distance of about 13.2 μm . The settling distance was very comparable to the depth of the model (13.4 μm). The particles may have settled to the lower fracture surface at first, and then rolled along the fracture with the aid of drag forces, while others remained still at stagnant flow areas around the fracture. Figure 5.19 is an optical image showing particles depositing within neighboring pore spaces and along the sides of the fracture. Increasing the flow rate by an order of magnitude resulted in L_S/L_D ratio of 0.5, indicating that settling was unlikely to be significant at that flow rate. It was also unlikely that the 2 μm particle attenuation at the fracture sides was due to straining and/or interception. The depth of the fracture (smallest dimension of the fracture channel) is about 6.7 times larger than the particle size. Backflushing with flow rates orders of magnitude higher than injection rates in both directions did not remobilize these particles. Their small size compared to the fracture dimensions and lack of remobilization at high velocity suggested that neither interception nor straining was the main deposition mechanisms within the fracture region.

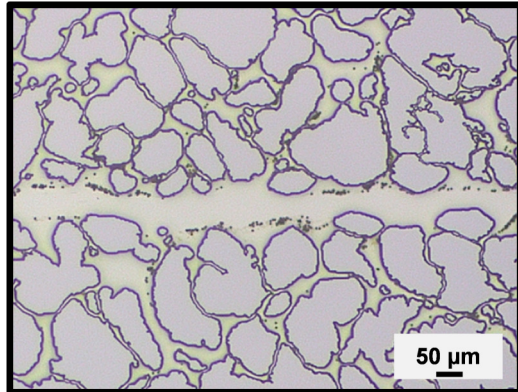


Figure 5.19: Optical image at the 25 μm aperture fracture during the injection of 2 μm particles at low flow rate (Micromodel B1), showing particle entering the matrix and depositing at the sides of the fracture.

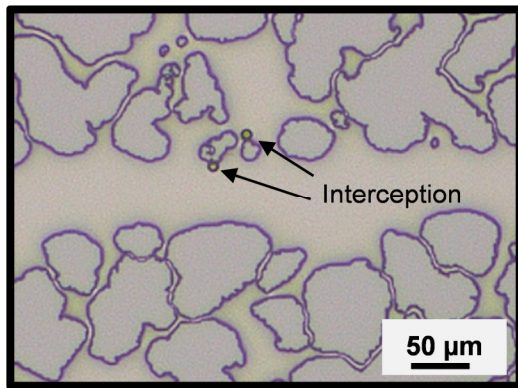


Figure 5.20: An optical image showing an example of particle interception by a grain at the fracture-matrix interface.

There was no noticeable diffusion of particles from the fracture to the matrix during the transport of the 4.5 and 6 μm particles. However, some particles were intercepted by adjacent grains (Figure 5.20). Particles also diffuse into pores of stagnant flow regions. Settling was probable at low flow rate injections (according to the length scale model), however, experiments did not show conclusive evidence of this deposition mechanism. It can be concluded these particles were rolling along the fracture surface for much of their travel time. Their size relative to the fracture dimensions suggest that drag forces should be quite efficient at rolling them along, particularly considering the prevailing chemically repulsive surface interactions in ultrapure water.

CHAPTER 5. PORE SCALE OBSERVATION OF PARTICLE TRANSPORT IN FRACTURE-MATRIX SYSTEMS

Table 5.7: Summary of calculated length scales and Peclet number for different particles, apertures and channel depths^{a,b}

<i>Micromodel B1</i>						
b (μm)	d_p (μm)	v_f (cm/min)	L_s (μm)	L_s/L_D -	$L_s/0.5b$ -	Pe -
15	6	2.61	45.7	18.5	6.8	1.1×10^6
25	2	1.30	13.2	1.9	2.0	1.4×10^5
25	2	16.94	1.0	0.5	0.2	1.8×10^6
25	4.5	2.61	33.4	10.3	5.0	6.1×10^5
25	4.5	12.77	6.8	4.7	1.0	3.0×10^6
25	6	2.61	59.5	21.1	8.9	8.1×10^5
25	6	25.54	0.9	6.8	0.8	7.9×10^6
25	10	2.61	165.1	75.8	24.6	1.4×10^6
25	10	78.18	5.5	13.8	0.8	4.1×10^7
50	10	2.61	165.1	75.8	24.6	1.4×10^6
<i>Micromodel B2</i>						
b (μm)	d_p (μm)	v_f (cm/min)	L_s (μm)	L_s/L_D -	$L_s/0.5b$ -	Pe -
15	6	2.08	74.5	23.7	23.3	3.1×10^5
25	4.5	2.38	3.4	10.8	11.5	2.6×10^5
25	6	0.53	186.2	37.4	58.2	1.2×10^5
50	6	2.38	65.2	22.1	20.4	4.4×10^7

^aHere b is the fracture aperture, d_p is the particle size, v_f is fluid velocity inside the fracture, L_s is Stoke settling length, L_D is the diffusion length and Pe is Peclet number.

^bNote that these calculations assume parallel plate fracture.

Only the 10 μm particles were physically captured during their transport through the 25 μm aperture fracture of Micromodel B1 (Figure 5.21a). The size of the particles was comparable to the depth of the fracture channel, with relative depth to particle ratio of 1.3. The 10 μm particles also strained within the 50 μm aperture of Micromodel B1. According to the T/C metrics, particles were expected to strain. Crevices and irregular asperities of the fracture lower surface (surface roughness) would contribute to higher retention of particles. Auset and Keller (2006) observed greater retention of particles in their rough wall grain micromodel due to surface asperities. Removal of the 10 μm particles by gravity settling was believed to be insignificant. Their settling length during low flow rate experiment is 165.1 μm , approximately 12 times the fracture depth. An order of magnitude increase in flow rate, where the lower surface of fracture is not

CHAPTER 5. PORE SCALE OBSERVATION OF PARTICLE TRANSPORT IN FRACTURE-MATRIX SYSTEMS

accessible, did not prevent the particles from straining at the fracture. Similar to the 4.5 and 6 μm particles, the 10 μm particles were transported initially by rolling along the lower surface of the fracture until strained at narrower fracture aperture. Drag forces should be more effective as particle size increases, because of the larger projected area of the particle against the flow. Nevertheless, particles were still physically trapped within the fracture. The insensitivity in particle transport to changing fluid velocity was indicative of straining.

To further investigate the influence of the relative particle size on particle removal in fractures, we transported particles of 6 μm in diameter through a fracture of shallower depth (Micromodel B2: 6.4 μm deep). This combination (particle size to depth) exhibits a similar ratio (ratio of 1.1) to that of the 10 μm particle in Micromodel B1 (ratio of 1.3). The 6 μm particles were found straining only in the fracture with aperture of 15 μm (Figure 5.21b). Interestingly, straining within the fracture occurred when the relative aperture to particle size ratios of the 6 μm particles in the 15 μm aperture and the 10 μm particles in 25 μm aperture were the same (ratio of 2.5). No straining was observed during the transport of the 6 μm particles in fractures with apertures of 25 or 50 μm . This finding suggested that the removal of particles in fractures is a function of fracture aperture and width. It was also observed that plugging inside the fracture occurred at a common location. There may be a shallower region and/or surface asperities, which aided the straining process at that location. Real-time observation showed that the plugging process within the fracture was initiated by the trapping of a few particles. Subsequent particles collided with the stationary particles and/or fracture surface. Because particles and surfaces are of like charge, the energy of collision between particles must have been greater than the electrostatic repulsion forces, thus leading to permanent attachment.

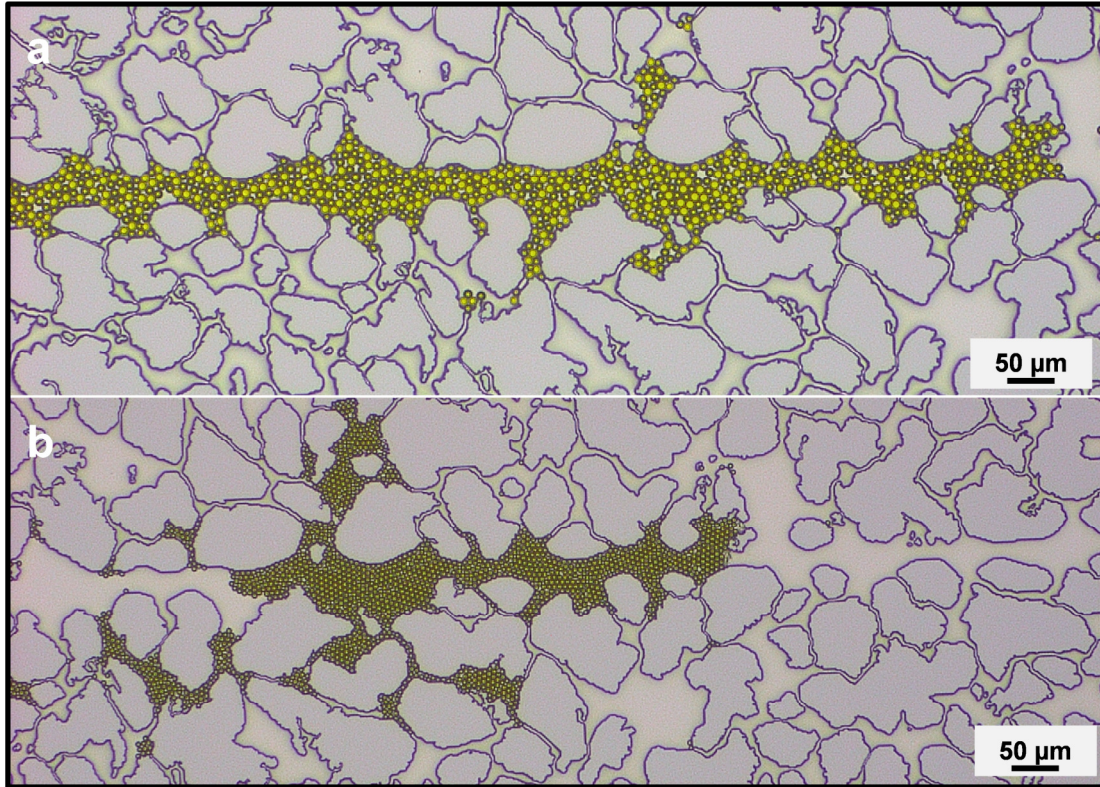


Figure 5.21: Optical images at the end of injection showing particle size of 10 and 6 μm plugging the (a) 25 μm aperture in micromodel B1 and (b) 15 μm aperture in micromodel B2, respectively. Images taken at magnification of 100X. This finding illustrated the effect of both fracture dimensions on particle transport.

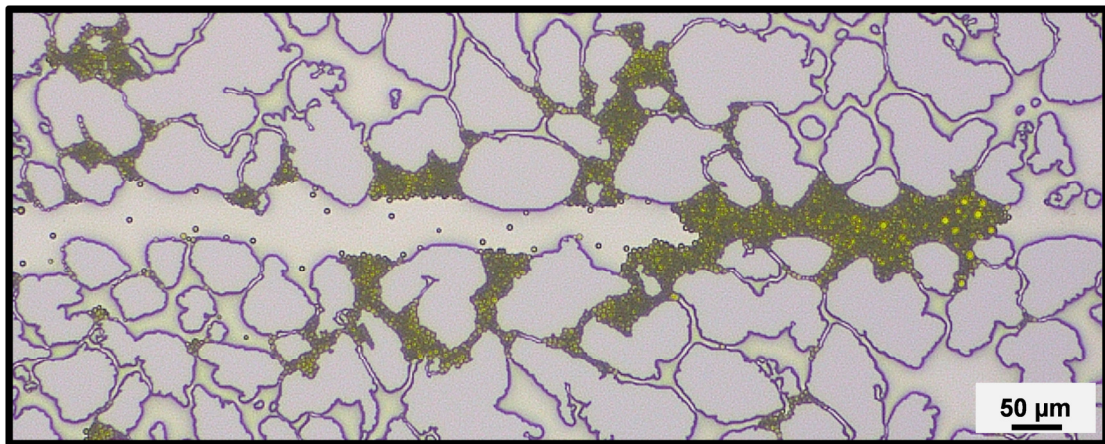


Figure 5.22: An optical image showing the plugging of the 25 μm fracture (Micromodel B1) by particles of the polydisperse (Mix 2) sample. This image also shows particles flowing through the surrounding grains and plugging small pore throats.

The effect of polydispersity of the sample (mixture of sizes) was investigated using Mix 1 and 2 polydisperse samples. The particle suspension of Mix 1 resulted in fracture plugging. This was not surprising because the mixture contained the 10 μm particles. The 10 μm particles were straining at the fracture of Micromodel B1 as shown in Figure 5.21a. Particles of Mix 2, which does not contain the 10 μm particle size, were trapped in the fracture of 25 μm aperture (Figure 5.22) but transported through the 50 μm fracture aperture. Note that the 2, 4.5 and 6 μm particles, when injected separately, were transported through the 25 μm fracture. It was only when they mixed and injected together, fracture plugging occurred. This suggested that polydispersity of particle suspension may impose difficulty on particle transport. The fact that the same polydisperse sample was transported across the wider fracture (50 μm) of the same depth also confirmed our previous finding that particle deposition within the fracture is a function of fracture aperture and width.

5.6 Chapter summary

Direct observation of particle transport through a fracture-matrix system was achieved using micromodels. Micromodel experiments were conducted to verify previous observations of particle transport into fractured cores. It was confirmed visually that the 2 μm silica particles were aggregating and straining at the inlet grains of the matrix. Increasing particle suspension concentration resulted in excessive straining. This was consistent with the observations during the transport of the 2 μm silica particles through fractured Berea core.

Micromodels were also used to investigate the influence of particle size on transport through fractured systems at pore scale. Four different sizes (2, 4.5, 6 and 10 μm) of fluorescent carboxylate-modified latex (CML) particles were used during these experiments. The experiments confirmed by visual observation that fractures are favorable conduits for particle transport. Particle velocity measurements showed that

CHAPTER 5. PORE SCALE OBSERVATION OF PARTICLE TRANSPORT IN FRACTURE-MATRIX SYSTEMS

particles were flowing along the fast moving streamlines with velocities comparable to maximum velocity of bulk fluid assuming parallel-plate fracture model.

Smaller particles (2 μm) were transported through both the pore spaces and fracture. Removal of particles at this size was caused by interception in the porous medium. Increasing flow rate resulted in less deposition on grain walls. Deposition of these particles at stagnant flow regions along the fracture sides was observed. Straining of larger particles (4.5 and 6 μm) at the inlet face of the porous medium was evident. These particles were transported through the fracture. Deposition of particles of these sizes was due mainly to interception by matrix grains. The 10 μm particles were not transported through the fracture of depth to particle and aperture to particle ratio of 1.3 and 2.5, respectively. They were deposited in the fracture as well as in the matrix. Significant straining of the 10 μm particles was observed at the matrix inlet, forming a filter cake of particles. The relative size of those particles to the average pore size (9.53 μm) suggested physical exclusion. Attenuation of these particles within the fracture was initiated by straining and then attachment due to collision with energy higher than the repulsive energy barrier. Results of the 6 μm particle transport experiments through the 15, 25 and 50 μm fracture apertures differed greatly as a function of the aperture to particle ratio. Straining occurred only during particle transport through the 15 μm aperture. Similar results (straining) were observed with the transport of the 10 μm particles at the same depth to particle and aperture to particle ratio (1.3 & 2.5 and 1.1 & 2.5 for the 10 and 6 μm particles, respectively). The difference in the magnitude of straining of the 6 μm particles at matrix inlet grains in Micromodels B1 and B2 was very significant. These results showed the impact of the relative size of particles to fracture dimensions on their transport.

Results of this chapter have positive implication on particle transport through fractured reservoirs. First, particles need not be sized to the nanoscale as fractures are usually larger than nanometers. Second, the existence of fractures should facilitate the particle mobility between wells, even for microscale particles.

CHAPTER 6

POTENTIAL TEMPERATURE-SENSITIVE NANOSENSOR CANDIDATES

6.1 Background

The focus of this research study was to investigate a temperature-sensitive nanosensor that undergoes detectable and irreversible changes at a specific temperature. Furthermore, the nanosensor must be mobile to infiltrate through the rock pore spaces and fractures in order to map the reservoir temperature. Functionalizing and transporting nanoparticles require a novel synthesis and deep understanding of controlling transport and/or deposition mechanisms.

In the previous chapters, we have described the investigation of the transport of particles of different materials, physical and chemical properties and flowed through various flow media such as sand or glass bead packed tubes, porous and fractured cores and at microscale using silicon micromodels. This chapter describes the preliminary testing that was carried out for four potential temperature-sensitive nanoparticles; namely, tin-bismuth alloy, dye-attached silica, thermochromic polymer and silica-encapsulated DNA particles. A combined heat and flow test was performed for the thermochromic polymer and silica-encapsulated DNA particles only. The others were tested for temperature sensitivity without simultaneously being flowed through porous medium.

In the following sections, the heat and/or transport tests of the temperature nanosensor candidates will be discussed.

6.2 Tin-bismuth (Sn-Bi) alloy nanoparticle heat test

The concept of using tin-bismuth alloy particles as temperature sensors was suggested by Stephen Connor from the Material Sciences and Engineering Department at Stanford University. The tin-bismuth heating experiment was performed by Morgan Ames (Ames, 2011). Parts of this section was written by Morgan Ames and adopted from our joint paper Alaskar et al. (2011). The sample synthesis, characterization and transport experiments can be found in Sections 3.2.1.4 and 3.5.4. The sensing mechanism of tin-bismuth alloy nanoparticles was the melting of particles at tunable temperatures between 139°C and 271°C by adjusting the alloy composition, as shown in the phase diagram in Figure 6.1. A simple sensing scheme of melting and subsequent particle growth was conceived. The growth of native gold nanoparticles upon melting in geologic Arsenian pyrite has been observed by Reich et al. (2006) using transmission electron microscopy during in situ heating to 650°C. It was shown that when the gold nanoparticles melted, they became unstable, leading to diffusion-driven Ostwald ripening and ultimately resulting in the coarsening of the size distribution. Upon melting, it was hypothesized that the tin-bismuth alloy would experience a change in its size distribution in a fashion similar to the gold nanoparticles.

Another conceivable sensing scheme is using the tin-bismuth alloy as shell material of core-shell particles. The shell, when melted, may undergo a phase change that would result in a permanent and identifiable change in its optical properties. When the tin-bismuth sample is exposed to heat of a temperature within the melting range, its color is expected to change (change in optical density). The thermal sensitivity by melting and growth in particle size or change in color was tested using a bench heating apparatus. The sample was heated using a heating mantle connected to a temperature controller with a feedback thermometer, as shown in Figure 6.2. The tin-bismuth nanoparticles were heated while suspended in mineral oil to avoid boiling as mineral oil has a higher boiling temperature than that used during the heating test.

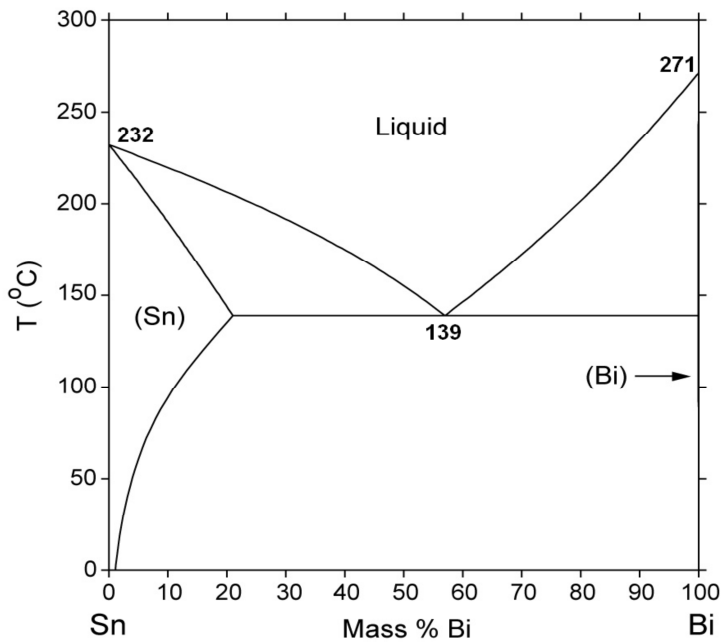


Figure 6.1: Phase diagram of tin-bismuth. Reproduced from National Institute of Standards and Technology (NIST).

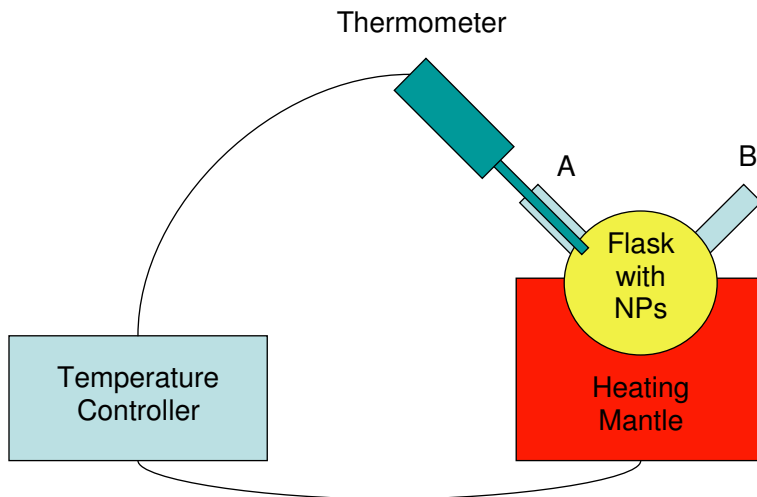


Figure 6.2: Experimental apparatus for tin-bismuth heating experiment. Experimental setup and heating experiments were carried out by Morgan Ames.

A thermometer (at port A) was used to measure the mantle temperature during the course of this experiment. The sample was heated in steps to the expected melting point of 139°C. The sample was monitored for a color change near the expected melting point, and when none occurred, the sample was heated in steps to 210°C. No color change ever occurred, but the heating was stopped to prevent the mineral oil from burning. Also, it is likely that melting occurred regardless of the absence of color change.

The sample was then washed and centrifuged several times with a 1:1 mixture of hexane and acetone, rinsed in a solution of 0.1 M PVP in ethanol, and finally suspended in ethanol. The centrifuge setting was 6000 rpm for 15 minutes each time. This sample was characterized using DLS and SEM imaging.

The DLS measurement showed that the heated tin-bismuth sample had grown in size with an average modal value of 0.321 μm . A comparison between the particle size distribution before and after heating can be seen in Figure 6.3. There was a noticeable shift in the average size distribution, represented by the peak of distribution, of the heated sample by approximately 0.08 μm . The secondary peak could be indicative of aggregates forming as a result of particle fusion upon melting. Evidence of melting and fusion of the tin-bismuth nanoparticles was confirmed by SEM as depicted in Figure 6.4. These results suggest that temperature sensing by melting and growth of the tin-bismuth nanoparticle is feasible.

While the fusion of melted particles could account for the shift in particle size distribution, it was difficult to observe the growth in size of individual particle from the SEM results due to the wide particle size distribution. To avoid this ambiguity, heating experiments were repeated by heating the tin-bismuth particles directly on a silicon substrate using a hot-plate. During this test, the tin-bismuth alloy particles in the micron size range (as large as 50 μm) were used. Their large size allowed for characterization using an optical microscope. Figure 6.6 shows an individual particle size comparison of the tin-bismuth alloy particles before and after heating to a temperature of 250°C for 2 hours. The optical images indicated that particles had grown in size by 15 to 51% over

the course of 2 hours at 250°C, confirming their thermal sensitivity. SEM imaging (Figure 6.7) was also used to confirm that the shape of the particles remain spherical (particles were not flattened from sphere to disk shape due to heat). Based on all heat experiments results, it can be concluded that the tin-bismuth alloy particles exhibited a observable change (growth in particle size) in response to temperature.

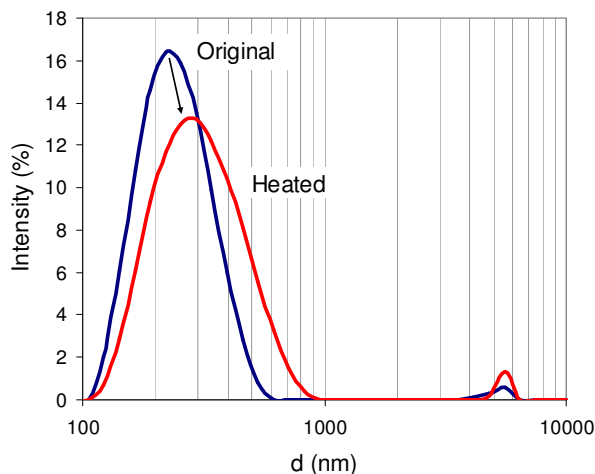


Figure 6.3: Comparison of particle size distribution of original and heated tin-bismuth sample. There is an increase in the average size of about 0.080 μm after heating. The secondary peak is indicative of large aggregate caused by particle fusion upon melting.

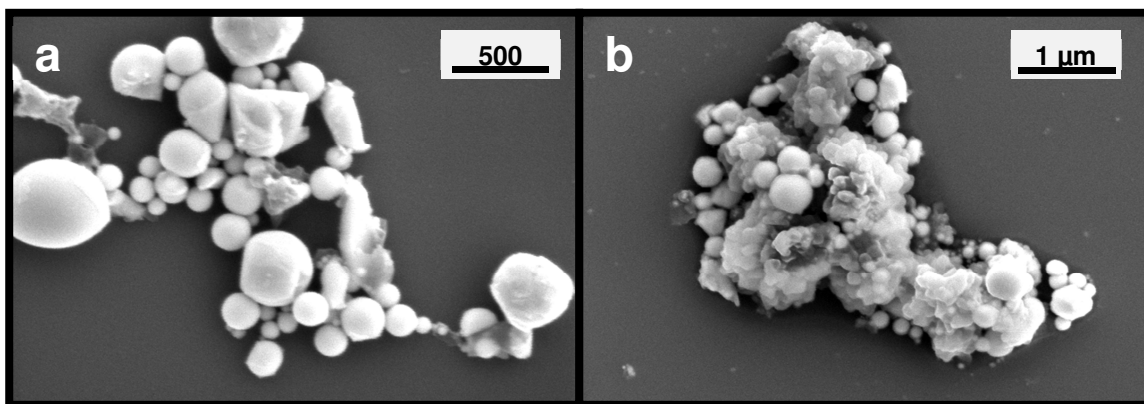


Figure 6.5: Micrographs of tin-bismuth nanoparticles (a) before and (b) after heating. The sample was heated to 210°C. The melting and fusion of particles were evident.

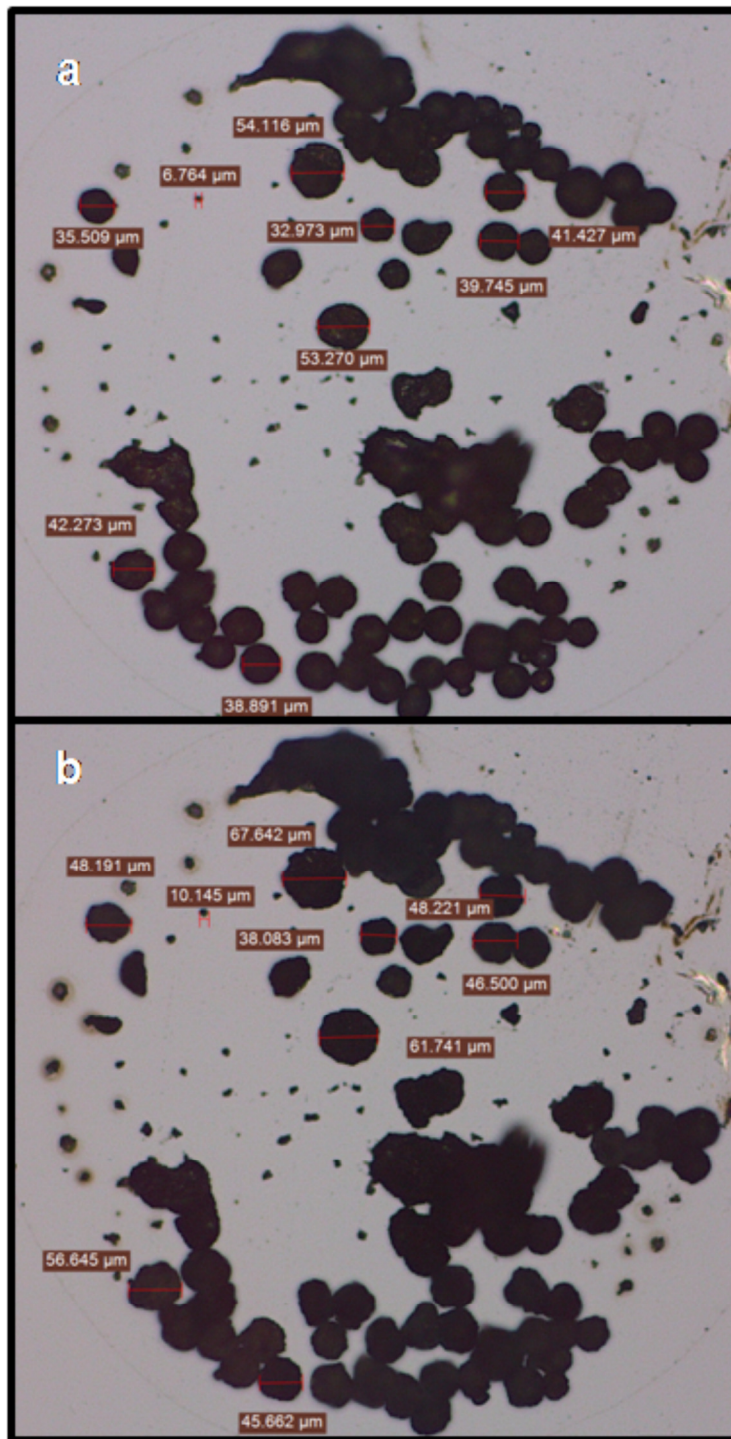


Figure 6.6: Optical images of the tin-bismuth alloy (a) before and (b) after heating (250°C for 2 hours) showing the growth of the individual particle size.

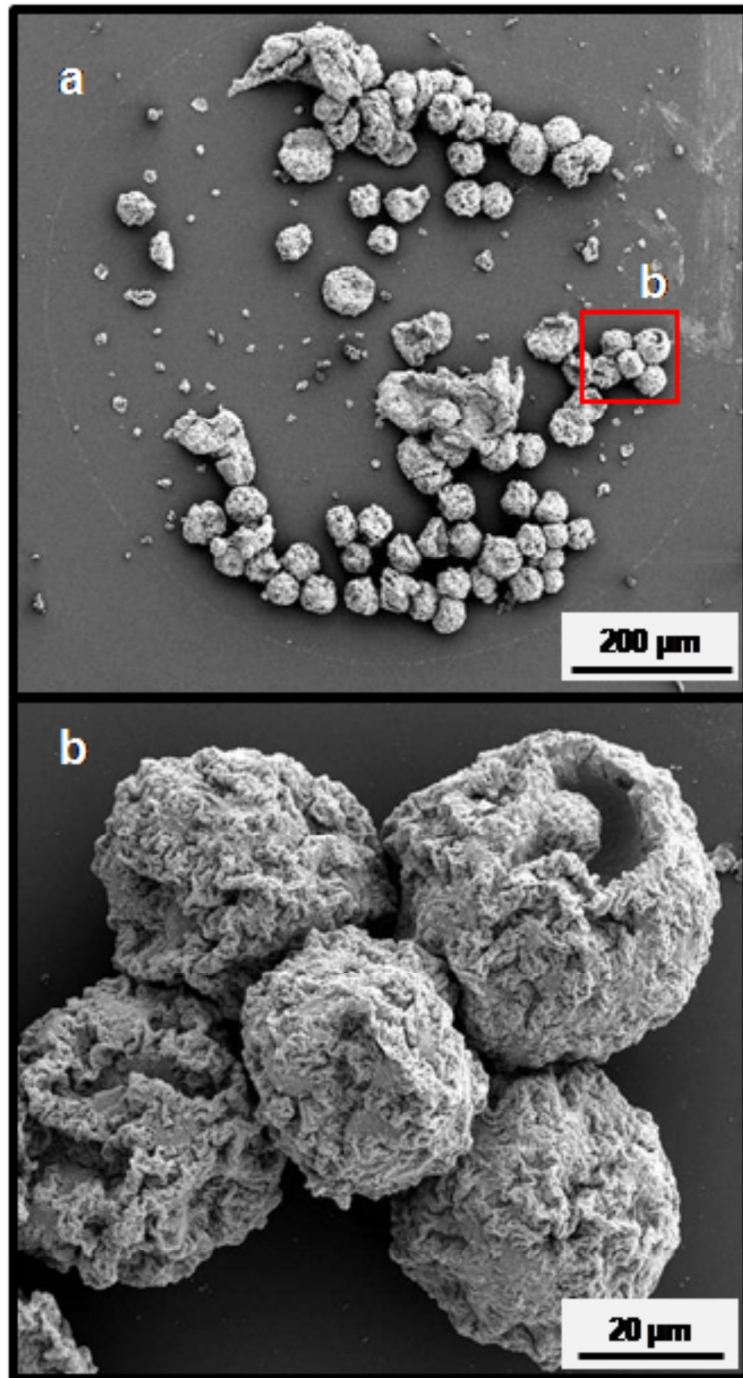


Figure 6.7: SEM images of the tin-bismuth alloy particles after heating at 250°C for 2 hours. The micrographs shows that the alloy particles were not flattened due to heat, but still hold their spherical shape.

6.3 Dye-attached silica nanoparticle heating experiment

The dye-attached silica synthesis, characterization, heating experiment and fluorescent emission spectra measurement were performed by Chong Liu from the Department of Materials Science and Engineering at Stanford University, who also wrote parts of this section. This section was adopted from our joint paper, Alaskar et al. (2011). As silica particles have been proven to have transported through sandstone core successfully, we changed their surface properties to explore their temperature response. According to the report by Wu et al. (2008), when free fluorescent dye molecule was attached to the surface of silica nanoparticles, through energy transfer, the fluorescent properties of these molecules were changed. Therefore, when the covalent bond between fluorescent dye molecule and surface-modified silica nanoparticle is broken under high temperature, the difference of fluorescent behavior before and after heating experiment can be detected. The characteristic of the temperature measurement is the observable change in the fluorescent emission spectrum of the attached dye before and after exposure to heat.

6.3.1 Synthesis of fluorescent dye-attached silica nanoparticles

A schematic representation of silica nanoparticle surface modification and dye attachment is depicted in Figure 6.8. First, silica nanoparticles (Nanogiant, LLC) were modified by attaching an amino group to their surfaces. In a typical reaction, 0.5 ml of 3-Aminopropyltriethoxysilane (APTS) was added to 100 mg silica nanoparticle suspended in 25 ml of toluene under nitrogen and heating to $\sim 95^{\circ}\text{C}$ for 4 hours. The resulting particles were washed by centrifugation in ethanol and acetone (10 min at 4,400 rpm). Then the particles were dried overnight at $\sim 95^{\circ}\text{C}$. The particles were about 350 nm in diameter. Second, the dye molecule (Oregon 488, Invitrogen) was attached to the modified silica particle surface. A suspension of 1.0 mg of the amino-modified silica nanoparticles in a mixture of 1 ml of ethanol and 15 μl of a 10 mmol/l phosphate buffer (pH 7.3) was reacted with 12.7 μl of dye molecule solution (1 mg/ml water solution) in dark for 3 hours at room temperature. The resulting particles were washed by centrifugation (10 min at 4,400 rpm) in ethanol and acetone.

Surface modification and dye attachment reaction was also performed on a monolayer of silica nanoparticles on quartz substrate using the same experimental parameters. In other words, two dye-attached silica particles samples were prepared; one sample where particles were suspended in solution (water) and a second sample in which particles were deposited on quartz substrate.

6.3.2 Dye-attached silica nanoparticle characterization

Fluorescent microscopy and fluorescent spectroscopy were used to characterize and verify the dye attachment to the silica nanoparticles. Fluorescent microscopy characterization as shown in Figure 6.9 was conducted using the substrate base dye-attached silica nanoparticle sample. The whole substrate was fluorescing (some spots were brighter because more fluorescent molecules were being attached, suggesting a successful attachment of the dye to the silica particles).

The fluorescence spectra of free dye molecule solution, silica nanoparticle suspension, dye-attached silica nanoparticles in solution and on substrate (prior to heating) were measured as shown in Figure 6.10. All samples were excited at wavelength of 400 nm. The Oregon 488 dye has its maximum emission peak at wavelength of 530 nm (Figure 6.10a). The fluorescent spectrum of bare silica nanoparticles (no dye-attachment) was acquired as a control and found to have no fluorescent response. After the dye-attachment, on the other hand, two emission peaks were observed at wavelengths of 425 and 530 nm (Figure 6.10b).

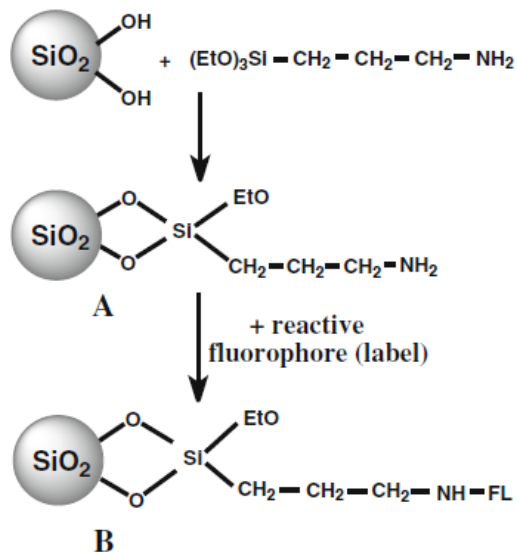


Figure 6.8: Schematic representation of silica nanoparticle surface modification and dye attachment. Adopted from Saleh, et al. (2010).

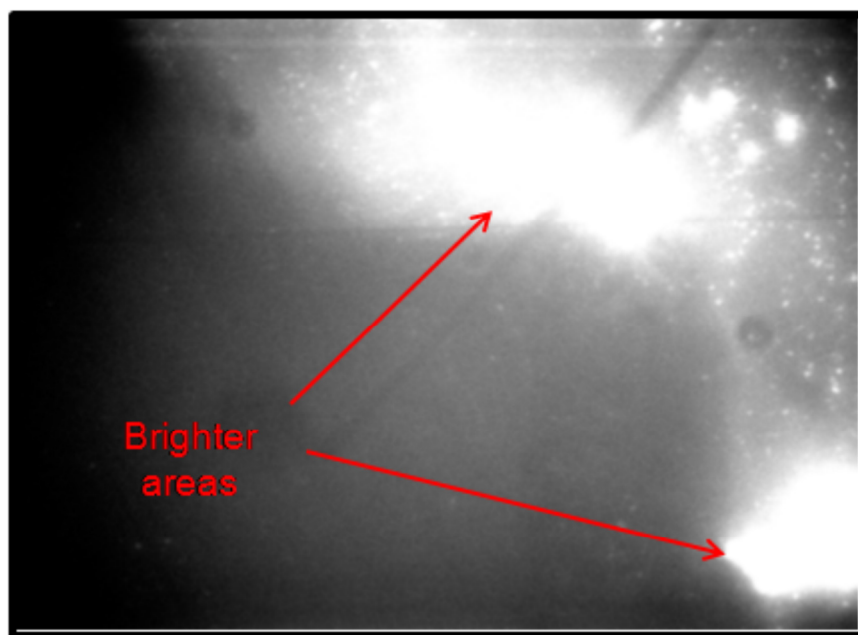


Figure 6.9: Fluorescent microscopy image of dye-attached silica nanoparticles on quartz substrate. The whole substrate was bright (compared to black). Brighter areas indicated that there were more fluorescent molecules at these locations.

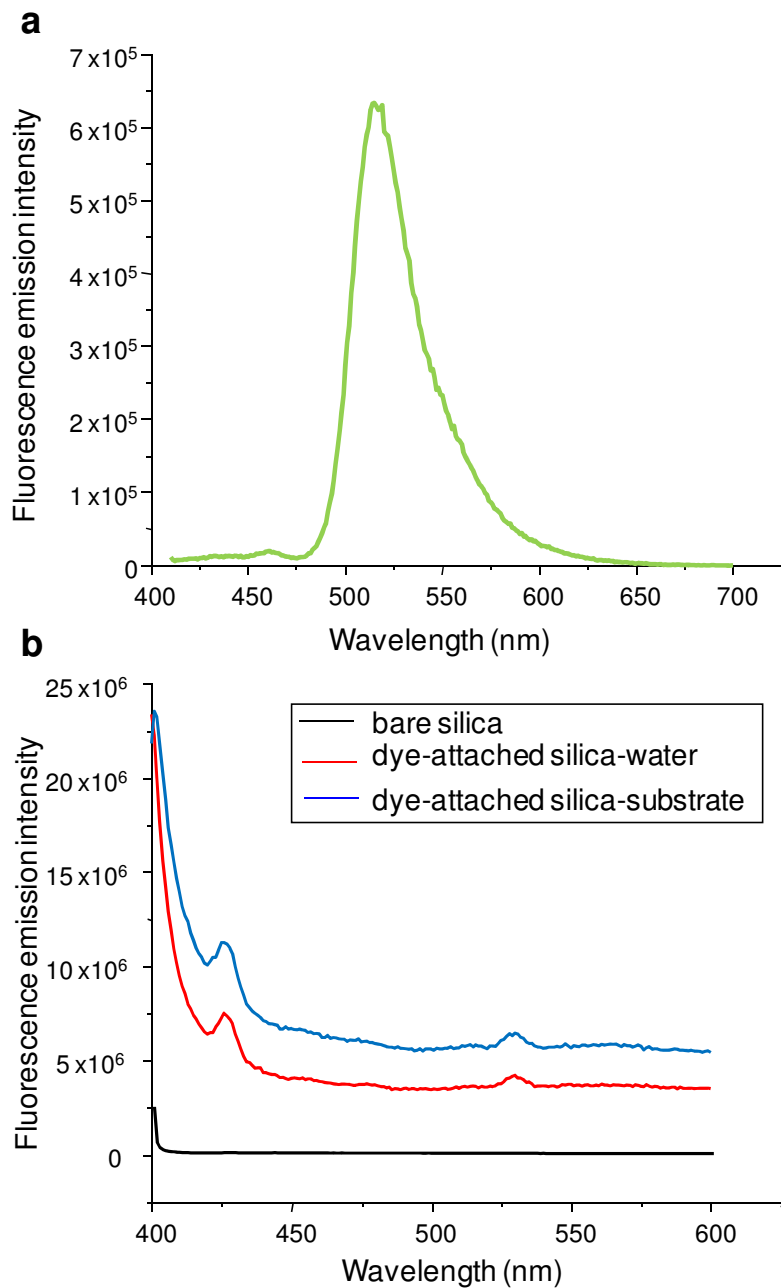


Figure 6.10: Fluorescence spectrum of (a) Oregon 488 dye molecule solution and (b) bare silica (no dye attachment) nanoparticles as control, dye-attached silica nanoparticles in water and dye-attached silica nanoparticles on quartz substrate. All samples were excited at wavelength of 400 nm. The dye-attached samples showed two peaks at 425 and 530 nm, compared to the free dye (Oregon 488) which has one peak at 530 nm.

6.3.3 Heating experiment of dye-attached silica nanoparticles

A heating experiment was conducted on the dye-attached silica nanoparticles that were deposited on quartz substrate. The substrate was placed on a hot-plate at a temperature of 200°C for 15 min. Then substrate was soaked and washed in ethanol and acetone and then was left to dry in air. Figure 6.11 shows the fluorescent spectra of the dye-attached silica sample prior and after the heat test. An excitation wavelength of 360 nm was used for both samples. It was observed that the heated sample had a wide peak at 425 nm that was very different than that before heating. Besides that, shoulder peaks at 380 nm and 475 nm and a peak at the spectrum tail (575 nm) were also observed for both samples. The observable change in the emission peak between the heated and unheated sample can be used as a characteristic of temperature measurement. Therefore, the dye-attached silica nanoparticles could potentially be used as a temperature nanosensor for subsurface reservoirs.

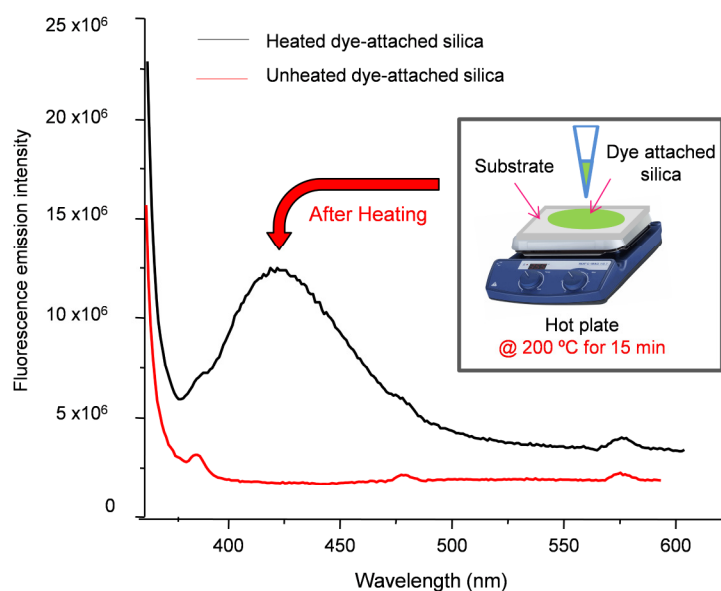


Figure 6.11: Fluorescence spectrum of the dye-attached silica nanoparticle before (red) and after (black) heating at 200°C for 15min. The samples were excited at wavelength of 360 nm. The change in the fluorescent spectrum can be readily distinguished as an indication to a temperature exposure.

6.4 Thermochromic microparticles

Chromogenic materials undergo a change in their color in response to electrical, optical or thermal stimulus (Seeboth et al., 2007). Colored chromogen compound that contains chromophore atoms are responsible for the visible color change in chromogenic materials. The color change arises when the visible light is transmitted or reflected by the chromogen (Bamfield, 2001). Among the different categories of chromogenic materials, thermochromics plays an important role in a wide range of applications (Seeboth et al., 2007).

Thermochromic materials change their color due to change in temperature, a phenomena known as thermochromism (Bamfield, 2001). There are two primary types of thermochromics, liquid crystals and leuco dyes. Liquid crystals change color based on specific light wavelength reflection from their structures. The most common commercial applications include forehead thermometers, fish-tank thermometers and stress testers (White and LeBlanc, 1999). Liquid crystals are used for precise temperature measurement and are difficult to work with as they require specialized manufacturing techniques. Leuco dyes, on the other hand, are easier to synthesize but less accurate than liquid crystals. Leuco dyes, usually organic, involve a mixture of at least two chemical components in order to achieve a thermal response. They are widely used in advertising, consumer packaging, security labels, toys and textiles (White and LeBlanc, 1999). The main shortcoming of the liquid crystals and leuco dyes is the reversibility to original color upon cooling, which hinder them to be useful temperature sensors in subsurface reservoir applications.

Another class of thermochromic materials known as thermochromic permanent change ink is a high temperature activated irreversible thermochromic ink. These pigments have a wide temperature reaction range (60 to 200°C) that may be suitable for geothermal applications. Thermochromic inks are manufactured in industrial quantities, which make them attractive for reservoir application.

The following sections describe the preliminary testing of the temperature sensitivity and transport of irreversible thermochromic ink.

6.4.1 Irreversible thermochromic ink bench heat tests

Tested samples were acquired from LCR Hallcrest LLC. The irreversible color change ink is supplied in two forms: inks and concentrate. The concentrates are used in the formulation of inks using water-based resins (product specification sheet, Appendix C). Ink testing was carried out using the concentrate format.

The pigment concentrates are in the form of ground crystalline solids suspended in water. The suspension concentration was 39% ($\pm 2\%$) solids. The pigment concentrate is slightly alkaline with a pH in the range of 6-8 at start of printing, and has a density between 1.0-1.1 relative to water (product specification and material safety data sheets, Appendix C).

The temperature sensitivity was verified using a bench heat test. Two samples were tested, black and magenta concentrates. The reaction temperature of the black and magenta concentrates was 90 and 60°C, respectively. These samples were selected to avoid complication in the heat testing due to water boiling. Although these temperatures were below the temperature range of interest for geothermal applications, their use served the purpose of investigating the concept of using irreversible thermochromic as temperature sensor in subsurface reservoirs.

As per the manufacturer, the color density of the thermochromic concentrates should increase with increasing temperature, with distinct color change at the rated temperature and full shade at temperatures of 10 to 20°C above the rated temperature. A faint color change is expected to occur at about 10 to 30°C below the rated temperature (product technical data sheet, Appendix C) Therefore, the temperature response was tested at different temperatures below and above the rated or reaction temperature. The black and magenta concentrates were heated to temperatures ranging from 60 to 100°C with 10°C increments, and 75 to 135°C with increments of 20°C, respectively. The samples were contained in a 1/8-inch coiled stainless steel tube. The coiled tube was then submerged in

CHAPTER 6. POTENTIAL TEMPERATURE-SENSITIVE NANOSENSOR CANDIDATES

an oil bath (Polyscience heat circulator model 1147 with working temperature from ambient to 200°C) at desired temperature for 3 minutes. The heat interval (3 minutes) was selected to match the heat test duration performed by the manufacturer on the same samples (product color comparison chart, Appendix C). Prior to heating, each sample was diluted one part to 10 parts of pure water (1:10 dilution). The coiled tube can be seen in Figure 6.12. The pressure gauge was used to monitor pressure build up for heat tests at or above 100°C. Before transferring the heated sample into a glass vial, the sample was cooled in air to ambient temperature.

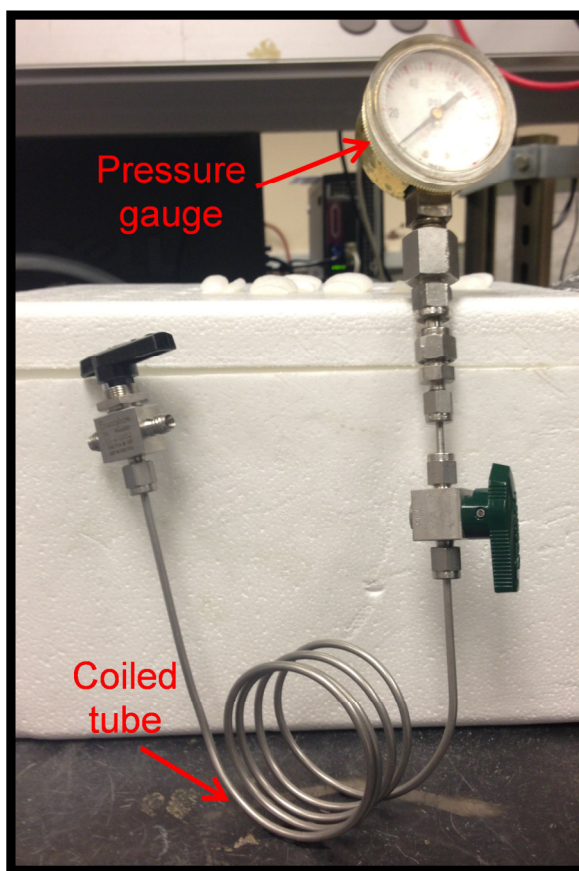


Figure 6.12: A picture of the coiled tube used during the bench heat test of the irreversible thermochromic ink. The coiled tube is submerged in oil bath heated to desired temperature.

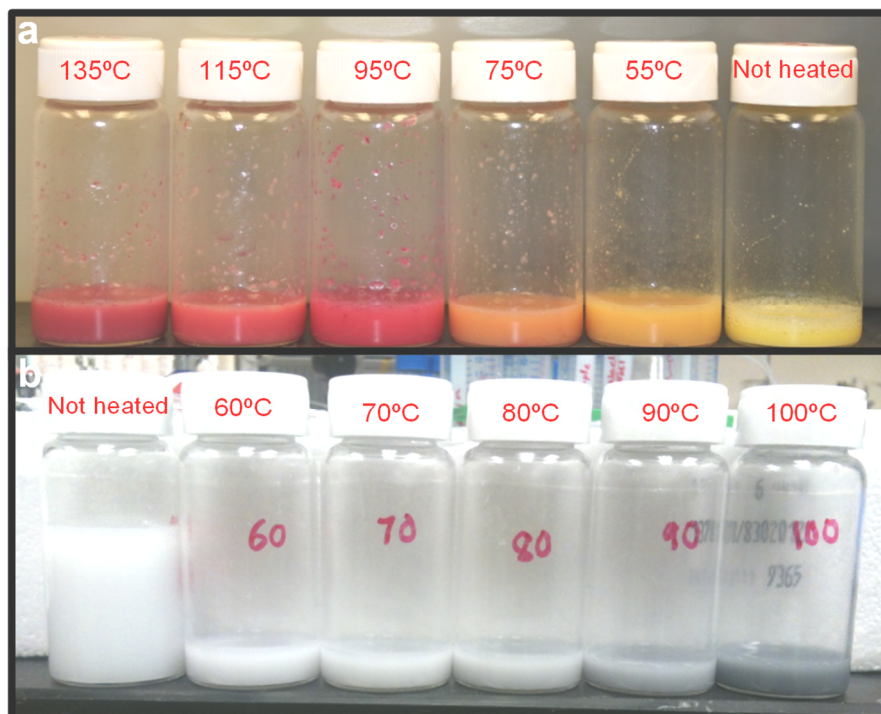


Figure 6.13: Snapshots of (a) black and (b) magenta irreversible thermochromic ink samples heated for 3 minutes at different temperatures below and above reaction temperature. The density or intensity of the sample color is increasing with increasing temperature. The color is fully developed at about 35°C and 10°C above the rated temperature of the black and magenta concentrate samples, respectively.

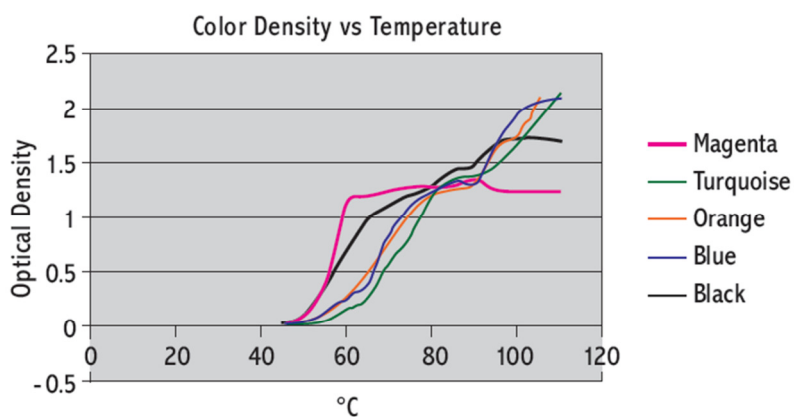


Figure 6.14: Color density as function of temperature of various irreversible thermochromic inks heated for 3 minutes. This test was performed by the manufacturer (Adopted from the product color comparison chart).

Snapshots of heated samples can be seen in Figure 6.13. It was observed that the black and magenta samples began to change color at 20°C and 5°C below the rated temperatures, respectively. The black sample showed a distinct change in color at about 10°C above the rated temperature, while the magenta sample reached a fully developed color at 35°C higher than the rated temperature. The color intensity was increasing with increasing temperature for both samples. These observations are in qualitative agreement with the manufacturer data. Figure 6.14 shows the change in color density as function of temperature for various irreversible thermochromic inks. Note these samples were test prints. Heat tests using the permanent thermochromic samples in concentrate format such as those used here are expected to have a degree of variation in color intensities.

For example, the magenta color was not fully developed at around the rated temperature (60°C), although the test print results (Figure 6.14) indicated that the color density reached a plateau beyond the sample rated temperature. Similarly, the color intensity of the black concentrate was gradually increasing with increasing temperature. The distinct color change occurred at higher than the rated temperature. It needs to be clear that these observations are based on visual comparisons not actual optical density measurements.

It was observed that the particles have irregular shapes and a wide size distribution (Figure 6.15a). The particles were ground crystalline solids. Upon heating, the melted particles were more spherical in shape with particle size of 2 μm in diameter and smaller. This is evident in the micrograph in Figure 6.15b.

The bench heat tests clearly confirmed the temperature sensitivity of the irreversible thermochromic concentrates. Because these particles will be flowing through the reservoir rock pore spaces, it was essential to test their temperature sensitivity while transported through a porous medium. Thus a combined heat and transport test was conducted. The magenta particle suspension was transported through a column packed with glass beads. The details of this injection are provided in the next section.

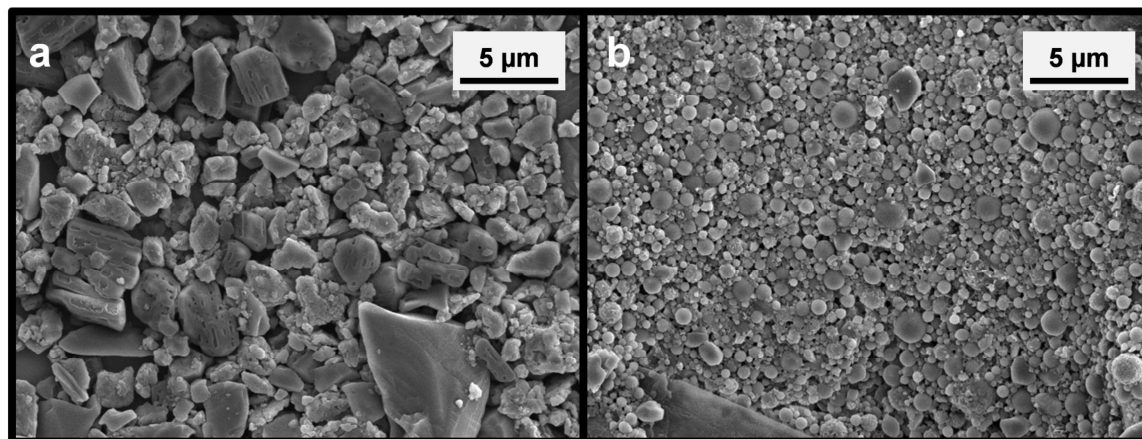


Figure 6.15: Electron micrographs of the black thermochromic concentrate (a) before and (b) after heating. By comparison, it can be clearly seen that the particles change their structures to form spherical particles.

6.4.2 Magenta thermochromic ink combined heat and transport experiment

The objective of the combined heat and transport experiment was to test the thermochromic concentrate temperature sensitivity during its flow through a porous medium.

The following sections will provide the details of the experimental setup and results.

6.4.2.1 Magenta thermochromic injection experimental method

The experimental apparatus used during the transport experiment of the magenta thermochromic sample can be seen in Figure 6.16. The apparatus consists of two water pumps, Dynamax (Model SD-200, head 50 WSS) and Cole-Parmer Masterflex (Model 7518-10), manometer, heating tape (BriskHeat), thermocouple and thermocouple signal conditioner (Digi-Sense, Model 92800-00), water vessel and glass column (Condenser, Liebig 24/40, No.2360-300). The glass condenser was used because it allows for visual observation of the color change under heat. Because this is a glass model, it is only applicable for testing thermochromic samples with reaction temperature of 80°C and below. Higher temperatures would boil the water under atmospheric pressure. Using back pressure to prevent boiling of water was not possible because the glass tube may not withstand high pressure. Glass beads (mesh 40-45, batch 1784 from Microbeads) were

packed inside the inner tube of the condenser. Water was heated using the heating tape in the water vessel and along the circulation loop. The hot water was circulated from the water vessel to the annulus of the condenser using the Cole-Parmer Masterflex pump. The temperature was measured in the annulus, within the glass beads at column outlet and at the water vessel. The temperature signal was read directly using the scanning thermocouple thermometer signal conditioner. The pressure difference between the inlet and outlet of the column was measured using a manometer.

Prior to the transport experiment, the column was saturated with testing fluid (i.e. pure water) by evacuating the column (using Welch vacuum pump) to a vacuum pressure of 50 millitorr for four hours. The pore volume and porosity was calculated using Equations 3.7-3.9. The column water permeability was determined using Equation 3.10. The physical properties of the column are summarized in Table 6.1. The inlet and outlet of the column was fitted with screen mesh (mesh 200) to prevent the glass beads from flowing out.

The thermochromic sample was injected through an injection loop using the Dynamax pump from the bottom of the column. The heated zone was about 5 cm from the inlet of the column (Figure 6.16b). The injection flow rate was kept constant at 1.0 cm³/min. The column was flushed with pure water for ten pore volumes prior to the thermochromic sample injection.

Table 6.1: Summary of the physical properties of the glass beads packed column^a

d (cm)	L (cm)	PV (cm ³)	Φ_{sat} (%)	k_w (darcy)
1.20	41.50	21.54	35.90	5.23

^a d and L are column diameter and length, respectively, Φ_{sat} is porosity by resaturation, k_w is the water permeability and PV is pore volume.

CHAPTER 6. POTENTIAL TEMPERATURE-SENSITIVE NANOSENSOR CANDIDATES

The thermochromic sample was diluted one to two parts of pure water and the volume injected was approximately 37% of the pore volume (8 cm^3). The particle suspension was thoroughly sonicated prior to the injection using a Branson 2510 Sonicator. One and half pore volumes of pure water were post injected and effluent samples were collected at volumes of 2.5 cm^3 . The temperature was held constant at 80°C (20°C above the rated temperature of the magenta sample) because the sample was expected to reach its full color density 20°C above the rated temperature. Although this temperature is lower than the temperature range in most geothermal reservoirs, the aim of this experiment was to verify the temperature functionality of the thermochromic sample while flowing through a porous medium.

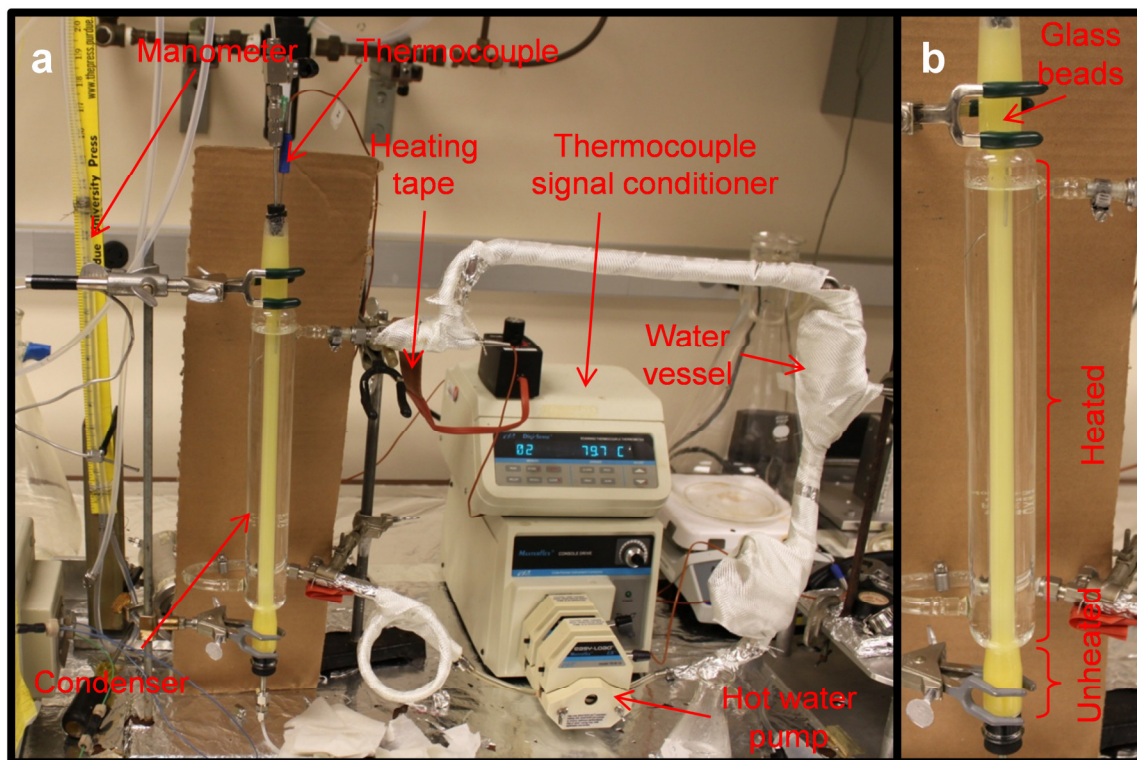


Figure 6.16: (a) Experimental apparatus used during the combined heat and transport experiment, and (b) condenser column packed with glass beads.

6.4.2.2 Results and discussion

Direct observation of the temperature sensitivity as a change in color of the thermochromic sample during its transport through a porous medium was the main focus of this experiment.

Visual observation (Figure 6.17) confirmed unambiguously the temperature sensitivity of the thermochromic sample during its transport through the glass beads. The sample switched color immediately from off-white to magenta at the entry of the heated zone of the column. The injected slug flowed with a clearly apparent sample front as it moved through the column.

The breakthrough of the particles occurred about 0.93 of the pore volume with a residence time of 20 minutes, slightly faster than the bulk fluid. The progression of the particle transport through the column at different time intervals can be seen in Figure 6.18. The bulk of the particles were flushed out of the column by the post-injection of about 1.5 pore volumes of pure water. It was observed that air started to evolve from the water at the entry of the column due to heating, which caused some particles to deposit at the air-water interface (AWI). Particles interact with the AWI in similar ways as they interact with solid surfaces (or grains). The AWI serves as a favorable attachment site for particles due to their hydrophobicity (Keller and Auset, 2007). Wan and Wilson (1994a, 1994b) reported that particles sorbed irreversibly at the AWI. They also observed that particle retention increased with increasing air saturation. The entrapment of the thermochromic particles at the AWI can be seen visually the snapshots (3-10) of Figure 6.18. Particles were deposited permanently and could not be remobilized by flushing at higher flow rates.

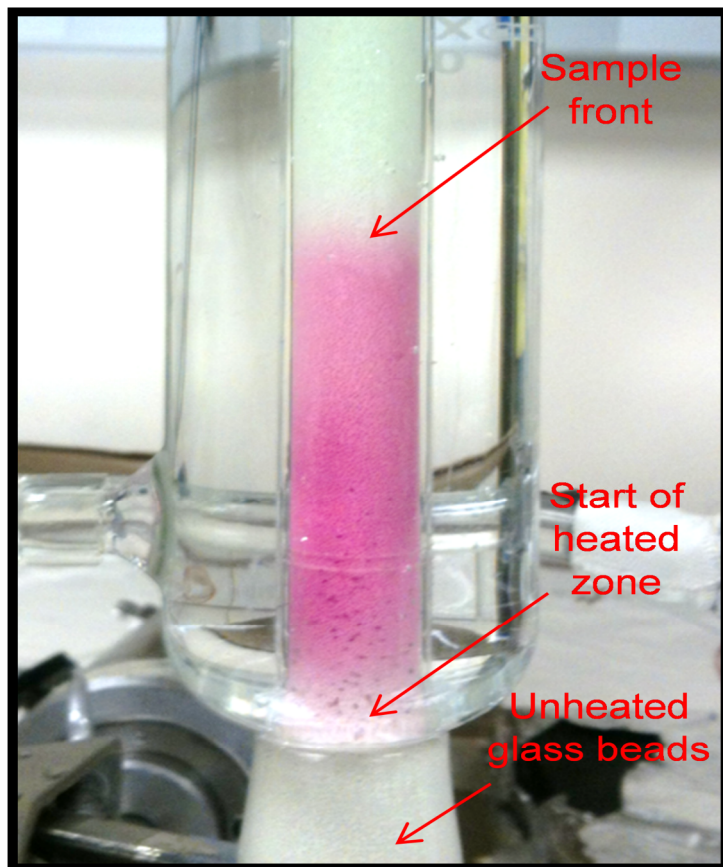


Figure 6.17: A snapshot of the thermochromic sample entering the heated zone of the glass beads column. The sample has changed its color immediately from off-white to magenta as a result of temperature. The change in color confirmed that the column temperature is at least 60°C.

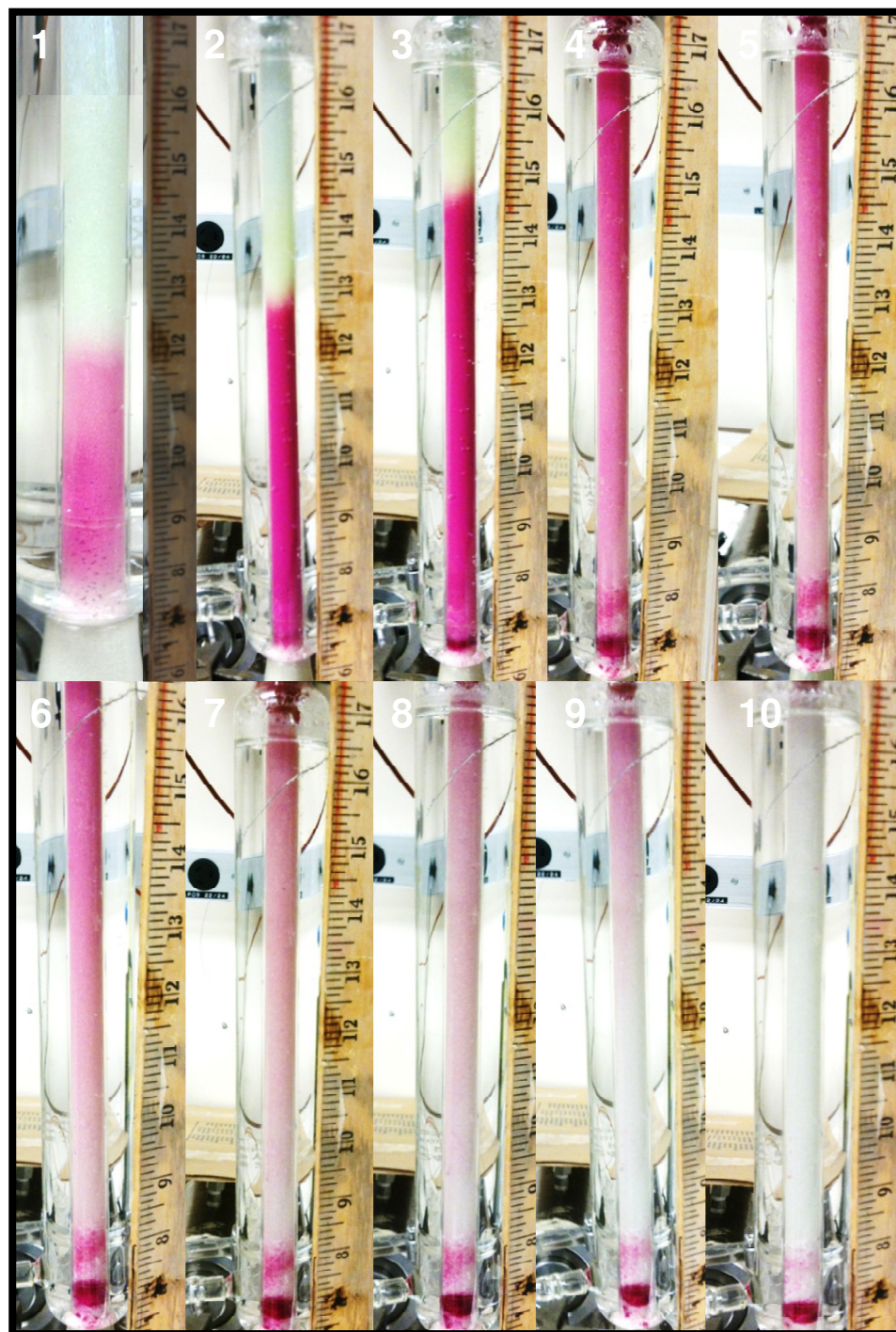


Figure 6.18: Snapshots of the thermochromic slug during its flow under heat through the glass bead column.

The intensity of the magenta color increased as the thermochromic particles remain under heat for longer time. This can be observed by comparing snapshots 1 and 3 in Figure 6.18. Particles in snapshot 3 were exposed to heat about 10 minutes longer than those in snapshot 1. Change in the color intensity as function of time could be particularly useful to determine the geolocation of the particles. The particles had also reshaped to spheres upon heating. Figure 6.19 shows a comparison between the heated and unheated thermochromic samples. The change in particle shape could be used as another characteristic of temperature measurement. As observed in this column experiment, the thermochromic sample changed its color instantly. So irregularly (rod-like) shaped particles (Figure 6.19a) may not impose constraint on the particle transport as they will transform to spheres, because the transport of spherically-shaped particles was facilitated; a conclusion based on the transport of silver nanowire and hematite nanorice through porous media. The details of those transport studies can be found in Chapter 3.

It was concluded that irreversible thermochromic material has the potential to be used as a temperature sensor to measure the temperature of subsurface reservoirs. However, surface characteristics of thermochromic particles and their interaction with constituents of reservoir rock, fluids and reservoir conditions of pressure, salinity are subjects for further investigations.

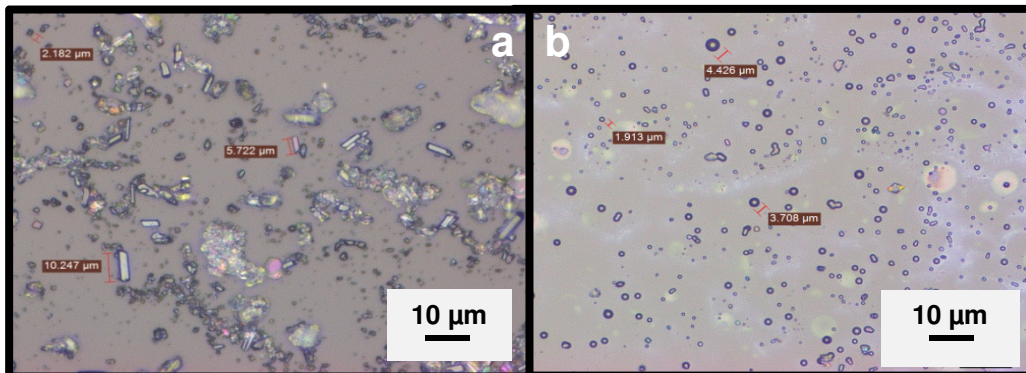


Figure 6.19: Optical images of the (a) unheated and (b) heated thermochromic sample. The particles change shape from crystalline to spherical solids.

6.5 Silica-encapsulated DNA nanoparticles

Deoxyribonucleic acid (DNA) is a nucleic acid that encodes the genetic organisms. Nucleic acids are known of their exceptional capability to store information, encryption and barcoding, allowing for wide range of industrial applications such as food and consumer goods labeling (Bancroft et al., 2001; Popping, 2002). Nucleic acids, however, degrade greatly when subjected to conditions beyond their biological origin. Paunescu et al. (2013) suggested a simple DNA encapsulation inside silica particles. The encapsulation was accomplished by surface modification of the silica particle with ammonium to give it a net positive charge. A negatively charged DNA was then adsorbed on the silica particle of opposite charge. After neutralizing the remaining negative charge of the DNA, a dense shell of silica was grown around the DNA using TEOS by polycondensation (Paunescu et al., 2013). The primary application of the silica-encapsulated DNA particles was barcoding for polymer labeling. The authors tested the protected DNA under conditions similar to those in an actual polymers manufacturing process of elevated temperatures and radical treatments. They reported that the DNA, after being heated to temperatures as high as 200°C, can still be detected and quantified using real-time polymerase chain reaction (qPCR) technique. The DNA concentration was decreasing to a distinct amount with increasing temperature. This behavior may be used as a sensing mechanism of temperature sensor.

The idea of using silica-encapsulated DNA particles as a temperature sensor was based on the fact that the concentration of the DNA changes with temperature. By using calibration curves, it may be possible to relate the DNA concentration to the reservoir temperature and exposure time at that temperature. Calibration curves can be constructed using laboratory controlled heat tests by heating the silica-protected DNA sample to a range of temperatures for different times.

6.5.1 Silica-DNA particles

The silica-protected DNA sample was received from Daniela Paunescu, Institute for Chemical and Bioengineering at Eidgenossische Technische Hochschule Zurich. The

particle size prior and after the encapsulation of the DNA was measured using SEM and TEM imaging. The particle size distribution was determined by counting at least 50 particles per sample. The mean particle size was found to be approximately 175 nm, of which 10-12.5 nm was the thickness of the silica layer (Paunescu et al., 2013).

The original sample concentration was 0.1 mg/ml (with 1.73 μg DNA per 1 mg SiO_2). One volume of the original sample was diluted with 6 volumes of pure water. The diluted sample of new concentration of 1.43×10^{-2} mg/ml, corresponding to 5.09×10^9 particle/ml, was used during testing.

6.5.2 Sample preparation and DNA quantification

A real-time polymerase chain reaction (qPCR), Applied Biosystems StepOnePlus Instrument, was used to quantify the DNA. Prior to the DNA amplification, the DNA was released by means of hydrofluoric acid chemistry as suggested by Paunescu et al. (2013).

Buffered hydrofluoric acid, commonly known as buffered oxide etch (BOE), was used to dissolve the silica layer. The BOE is a mixture of ammonium fluoride (NH_4F) and hydrofluoric acid (HF). The addition of NH_4F was to slow down and control the attack rate of HF on oxides. The BOE solution was prepared as follows. First, 40 g of NH_4F powder was mixed with 60 g of water to make 40% solution. The NH_4F /water solution was sonicated until the NH_4F was fully dissolved (15 minutes) and the mixture became clear. The solution was left to cool. Second, 0.5 ml of 49% HF acid was then added to the 40% NH_4F solution to make 200:1 BOE solution with HF concentration of 0.24%. The etching rate of this BOE was about 2.18 nm/min.

The DNA extraction was performed by adding four volumes (40 μl) of the BOE solution to one volume (10 μl) of the silica-encapsulated DNA particles sample (Paunescu et al., 2013). The time the BOE was allowed to react with the silica-protected DNA particles was calculated based on the BOE etching rate and the thickness of the silica shell (about 4.59-5.73 min).

CHAPTER 6. POTENTIAL TEMPERATURE-SENSITIVE NANOSENSOR CANDIDATES

The reaction was halted by separating the DNA from the BOE solution using GET clean DNA spin column kit, (catalog number 786-356/357) obtained from G-Biosciences Geno Technology Inc. The spin columns were supplied with binding buffer (Guanidine Hydrochloride), DNA wash (various salts) and TE buffer (Tris and Ethylenediaminetetraacetic acid solution). The separation process was conducted according to the following protocol suggested by the manufacturer of the spin tubes. First, the silica-protected DNA sample was mixed with the BOE solution (total volume was 50 μ l) and allowed to react for the specified time. 250 μ l of the binding buffer was added and mixed with the DNA sample. The mixture was transferred to the spin column and centrifuged to bind the DNA, using Eppendorf Microcentrifuge Model 5430, for one minute at 14,000g. The flow-through was discarded and the column was placed back into the same collection tube. 750 μ l of the DNA wash (cooled on ice before use) was added to the column and centrifuged for one minute at 14,000g. The flow-through was discarded and the column was centrifuged again one minute at 14,000g to ensure that the DNA wash was removed completely. The column was then placed in a clean collection tube (micro-tube). 50 μ l of TE buffer (preheated to 55°C) was added to the center of the column membrane and incubated at room temperature for one minute. The column was centrifuged for one minute at 14,000g. The DNA in collected sample was then amplified using qPCR.

PCR runs were conducted using the same primers, master mix and primer mix as outlined in Paunescu et al. (2013). Every sample was mixed with 10 μ l of qPCR master mix (SYBR Green I), 7 μ l of PCR grade water and 2 μ l of forward and reverse primer mix. Dilutions of standard amplicon of known concentrations (10^{-8} to 10^{-4} μ g/ μ l) were used to quantify qPCR. All samples were carried out in triplicate.

In order to test the nucleic acid (DNA) release protocol, a test qPCR run to quantify the (DNA) was carried out using the silica-encapsulated DNA sample at its original concentration. Based on the silica layer thickness and etching rate, the release of the DNA should occur approximately between 4.59-5.73 minutes. Six samples were allowed

to react with the BOE solution for specific time before separation using the spin columns. The shortest reaction time used during the qPCR test run was 3 minutes, with an increment of 1 minute for subsequent samples.

The DNA was detected and amplified for all samples. The amplification plot and standard curve for standards and samples can be seen in Figure 6.20 and 6.21, respectively. The cycle thresholds (C_t), defined as number of cycles required for fluorescent signal to exceed background fluorescent level, showed strong reaction ($C_t \leq 29$) indicating that there was an abundant amount of target DNA in all samples. There was variability in the amount of DNA among samples ranging from 0.006 to 0.739 pg/ml, with the majority around 0.357 pg/ml.

6.5.3 Silica-encapsulated DNA combined heat and transport experiment

6.5.3.1 Characterization of porous medium

A stainless steel (316L) tube packed with sand with inner diameter of 0.46 cm and length of 30.48 cm was used. The tube was packed with Ottawa sand with a density of 2.65g/cm^3 and grain size ranging from 150 to 180 μm . The sand was washed several times with pure water and dried prior to use. The porosity, pore volume and liquid permeability were measured as outlined in Section 3.3.2, and found to be approximately 36.19%, 2.0 cm^3 and 9.17 darcy.

6.5.3.2 Experimental setup and injection method

A schematic of the experimental apparatus used during the combined heat and flow test of the silica-encapsulated DNA particles can be seen in Figure 6.22. The apparatus consists of a water pump, Eldex (Model PN 597-Optos Pump 2SM, minimum and maximum flow rates of 0.01 and $10\text{ cm}^3/\text{min}$), air bath oven manufactured by Blue M (maximum temperature of 400°C), syringe (Monojet 3 ml), differential pressure transducer (Validyne Model DP15-56), thermocouple and thermocouple signal conditioner (Digi-Sense, Model 92800-00), balance (Mettler balance Model PE 300), water pocket and a back pressure regulator.

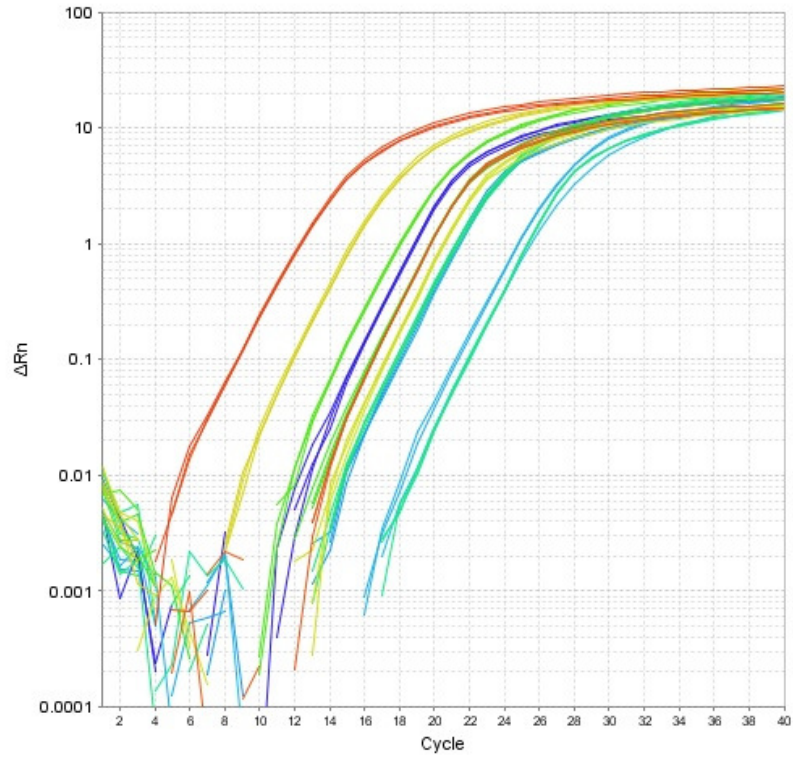


Figure 6.20: Amplification plot of standards and nucleic acid samples.

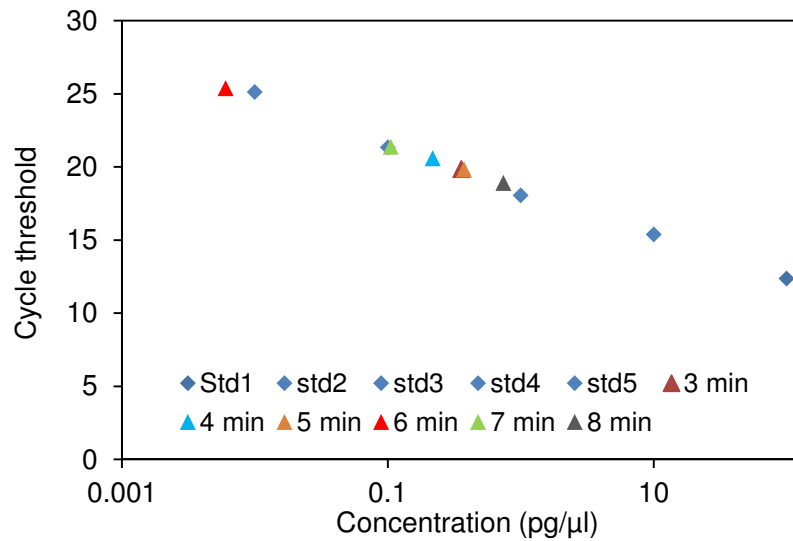


Figure 6.21: Standard curve of standards and samples showing the relation between the cycle threshold and concentration (picogram per microliter).

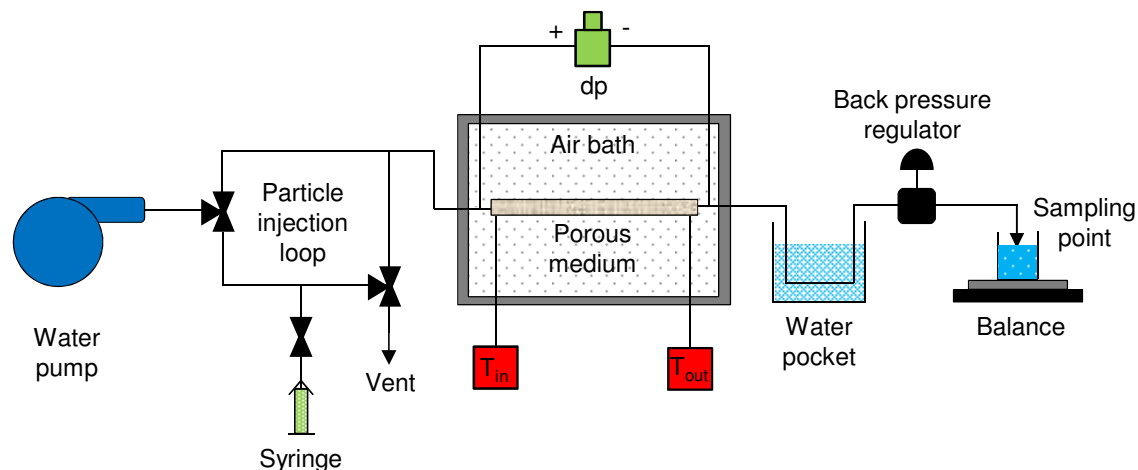


Figure 6.22: Schematic of the experimental apparatus for testing the silica-encapsulated DNA particles.

The syringe was used to place the particle suspension through the injection loop. The particle suspension was injected into the sand packed tube at flow rate of $1 \text{ cm}^3/\text{min}$ using the water pump. The pressure measurements were collected using a data acquisition card (National Instruments Model USB-6009). The temperature data was recorded directly from the thermocouple signal conditioner. The sand packed tube was placed inside the air bath to control the temperature at which each experiment was conducted. The silica-encapsulated DNA particles were injected at three different temperatures (120, 150 and 180°C). To prevent water boiling, a back pressure of 4, 7 and 12 atm was provided during the 120, 150 and 180°C injection experiments using the back pressure regulator. The outflow was cooled down to room temperature before reaching the back pressure regulator using a water jacket. The discharge flow rate was measured using the balance and stop watch to ensure constant steady-state conditions.

The injected volume of the particle suspension was 20% of the pore volume (2 cm^3). The system was flushed with several pore volumes of pure water before and after each injection. The particle suspension injection was carried as follow. First, the air bath oven temperature was raised to desired temperature. A continuous injection of particle-free water was introduced using the water pump. When the inlet and outlet temperatures

reached the preset temperature of the air bath, the particle suspension slug was flowed through the porous medium. Typically, four pore volumes of pure water were post-injected and effluent samples were collected at a volume of 0.70 cm³.

6.5.3.3 Silica-protected DNA injection results

The silica-protected DNA particles were injected into a porous medium to investigate their mobility under elevated temperatures. It was observed that the silica particles exhibited reduction in their size. Electron micrographs of the silica sample before and after injection can be seen in Figure 6.23 (a and b). As temperature increased from 25 to 150°C, the particle size was reduced by about a factor of four. Pierre (1998) attributed the decrease in particle size with increasing temperature to the high nucleation rate, because nucleation rate increases with increasing temperature.

Analysis of the effluent using electron microscopy showed that particles were aggregating when transported at high temperatures (Figure 6.23c). This was due to the increased solubility of silica particles and high collision between particles at high temperature (Brinker and Scherer, 1990). Rahman et al. (2007) reported similar observations during their investigation of an optimized sol-gel synthesis of stable silica particles. They observed reduction in the particle size and increased particle aggregation with increasing temperature.

The silica-protected DNA particles were transported through the sand-packed tube at room temperature as a control experiment. Neither particle size reduction nor aggregation was observed, as seen in the micrographs in Figure 6.23d, suggesting that the dissolution of silica particles was associated with higher temperature.

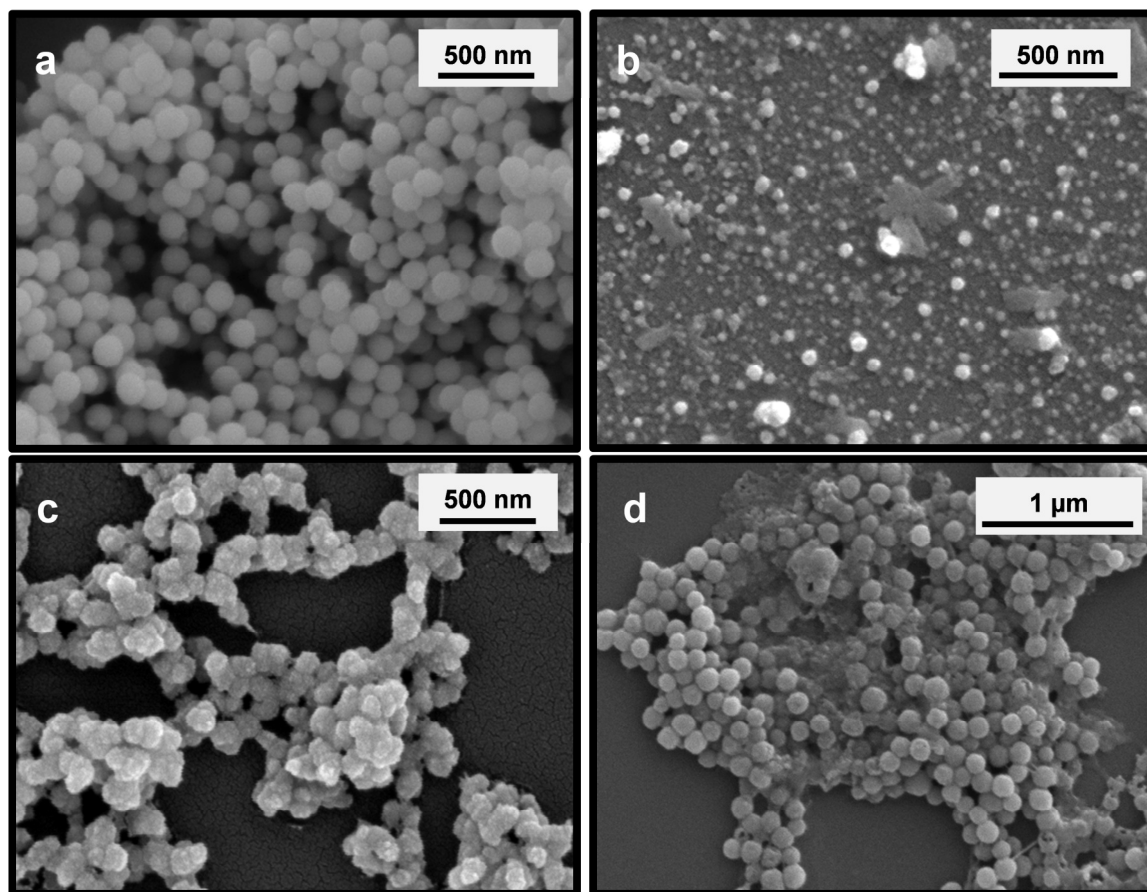


Figure 6.23: Electron micrograph of (a) influent, (b) and (c) effluent sample during particle injection at 150°C showing reduction in particle size and particle aggregation, respectively, (d) effluent sample collected during injection at room temperature where neither the particle size reduction nor aggregation of particles were observed.

6.6 Chapter summary

This chapter focuses on the investigation of the sensing mechanism of temperature-sensitive particles using bench heat and/or combined heat and flow tests. The tested temperature-sensitive particles included tin-bismuth, dye-attached silica, irreversible thermochromic and silica-encapsulated DNA particles.

The sensing scheme of melting and subsequent growth in size of the tin-bismuth particles was tested using a bench heating apparatus. The sample was heated to temperatures within the melting range. Electron microscopy confirmed the melting of the tin-bismuth

CHAPTER 6. POTENTIAL TEMPERATURE-SENSITIVE NANOSENSOR CANDIDATES

particles. Upon melting, fusion of particles occurred and therefore a growth in the average particle size. Despite the temperature sensitivity of the tin-bismuth particles, transport studies (Chapter 3) showed that the tin-bismuth particles have an affinity to the rock material and therefore tin-bismuth may not be suitable temperature nanosensor.

Temperature-sensitive silica particles were synthesized. Temperature sensitivity was achieved by modifying the surface of the silica particle and attaching a fluorescent dye through covalent bond. The sensing mechanism of the dye-attached silica particles rely on the breakage of the covalent bond at elevated temperatures, which would result in a detectable change in the fluorescent emission spectrum of the particles before and after heating. Bench heat test of the dye-attached silica particles was carried out. Fluorescent emission measurements showed an observable difference between the emission spectra of the silica particles before and after exposure to heat, confirming their sensitivity to heat. Because silica-based particles exhibited a good mobility through reservoir rocks and the fact fluorescent emission measurements are cheap and available, the dye-attached silica nanosensor is an attractive candidate for field application.

Irreversible thermochromic particles are organic compounds that change color when heated to their reaction temperature. Bench heat test of the thermochromic particles was conducted to verify their temperature sensitivity. The tested samples, when heated to their rated temperature, a change in their color was observed. The temperature sensitivity and mobility of the thermochromic particles were investigated simultaneously. The thermochromic particles were injected into a heated porous medium. The particles switched their color while getting transported through the porous medium. The thermochromic particles show promise because of the simplicity of their sensing scheme and they can be produced at mass quantities.

Silica-encapsulated DNA particles were provided by ETH Zurich, synthesized by the methods described in Paunescu et al. (2013). The main application of these particles was barcoding or labeling of consumer goods. The silica-encapsulated DNA particles were investigated as temperature nanosensor because of the behavior of DNA under heat. The

CHAPTER 6. POTENTIAL TEMPERATURE-SENSITIVE NANOSENSOR CANDIDATES

degradation of DNA concentration with increasing temperature is the sensing mechanism. Initial testing showed the compatibility of the DNA with the hydrofluoric acid chemistry. A detailed protocol on how to dissolve the silica layer using buffered oxide etchant without completely destroying the DNA was established. This was accomplished by allowing the etchant to react with the sample for specific time (based on the etching rate and the silica layer thickness), and then separate the DNA from the etchant using spin columns. Following the sample treatment with the buffered solution, the nucleic acid was detectable by means of quantitative qPCR analysis.

The silica-protected DNA particles were flowed through a porous medium at elevated temperatures. Direct observations using scanning electron microscopy of effluent samples showed that particles experienced reduction in their size at high temperature, presumably due to dissolution of the silica in the water. Also, electron micrographs showed that particles were aggregating. This was due to the dissolution and high collision between particles at high temperature. Size reduction and aggregation of the silica particles were not observed when particles were transported at room temperature.

CHAPTER 7

CONCLUSIONS AND RECOMMENDATIONS FOR FUTURE WORK

7.1 Conclusions

The main goal of this research study was to develop thermally-responsive particles to measure temperature far in the formation and use such measurements to infer other reservoir and fracture properties. This approach involved synthesizing temperature-sensitive particles and investigating their mobility through porous and fractured media. This research study has shown that temperature-sensitive particles undergo observable change as per their design and can be transported through a reservoir rock. The conclusions of this research work are presented here.

7.1.1 Potential temperature-sensitive particles

Several temperature-sensitive particles were investigated, each with different sensing scheme. These include irreversible thermochromic, dye-attached and silica-encapsulated DNA and tin-bismuth particles. These particles were shown to respond to temperature upon heating.

7.1.1.1 Irreversible thermochromic particles

The irreversible thermochromic particles change their color permanently due to change in temperature. These pigments are available with trigger temperatures as high as 200°C, and many subsurface reservoirs are within this range. The temperature sensitivity and transport of the irreversible thermochromic particles were tested simultaneously. The thermochromic particles were injected through a heated porous medium. The thermochromic sample changed color during its transport through the heated zone of the

porous medium. This confirmed that thermochromic particles can be used to measure the temperature subsurface reservoirs.

7.1.1.2 Silica-based temperature-sensitive particles

In this study, two temperature-sensitive silica particles were investigated; namely, dye-attached and silica-encapsulated DNA particles.

The dye was incorporated to the surface of the silica particle by surface modification and dye attachment. The silica particle surface was modified by attaching an amino group, and then the dye molecule was attached to the particle surface by covalent bond. Upon heating, the covalent bond breaks resulting in an observable change in the fluorescent dye emission spectrum. The difference in the fluorescent emission spectrum is the characteristic of the temperature measurement. A heating experiment was conducted on the dye-attached silica particles. It was observed that the fluorescent emission spectrum of the heated sample was very different than that before heating.

The sensing mechanism of the silica-encapsulated DNA particles is the degradation in the DNA concentration with increasing temperature. The DNA encapsulation was accomplished by functionalizing the surface of the silica particle to yield a positively charged particle. A negatively charged DNA was adsorbed on the positively charged particle. A dense silica layer surrounding the DNA was then deposited using TEOS. At this stage, the DNA is suspended between the core and shell of silica particle. The applicability of the silicate and hydrofluoric acid chemistry with nucleic acid analysis (qPCR) was verified.

The mobility of the silica-encapsulated DNA particles was investigated. Particle suspensions were transported through sand-packed tube at three different temperatures. Particle size was generally decreased with increasing temperature due to the high rate of dissolution. Also, particles were aggregating with increasing temperature. This was attributed to the increased dissolution and collision between particles at high temperature. On the other hand, reduction in particle size and aggregation were not observed during

the particles injection at room temperature. It was concluded that the silica-encased DNA particles should be synthesized with some kind of protective coating to yield particles that are less soluble at high temperature to prevent silica dissolution at these temperature conditions.

7.7.1.3 Tin-bismuth alloy particles

Tin-bismuth particles were investigated because of their temperature sensitivity. The sensing mechanism of the tin-bismuth particles was the melting of the particles at temperatures between 139°C and 271°C and subsequent growth in particle size. The temperature sensitivity by melting and growth in particle size was investigated using a bench heating apparatus. It was observed that there was an increase in the average particle size, which was indicative of particle fusion upon melting.

The mobility of a polydisperse tin-bismuth sample was explored by injecting the particles through a porous medium. Because particles would grow in size resulting in a range of particle sizes, the transport of the tin-bismuth particles was tested using a polydispersed sample. It was found that there was an optimum particle size for the transport of tin-bismuth particle through the sandstone. Therefore, the sensing scheme of growth in size of the tin-bismuth particles as a temperature measurement could result in significant particle deposition within the porous medium if the particle size is very different from the optimum particle size. The affinity of the tin-bismuth alloy to rock material was investigated by transporting the tin-bismuth particles through glass beads (in the absence of rock materials). The recovery of the tin-bismuth particles (of all sizes) was considerably higher than that during the sandstone injection. This result suggested that there may be an affinity of the tin-bismuth to the rock material and therefore tin-bismuth may not be a suitable temperature nanosensor.

Another sensing scheme is using the tin-bismuth alloy as shell material of core-shell particles. Upon heating to temperatures within the melting range, the shell (tin-bismuth) would undergo a phase change that would result in a detectable change in its optical properties. This sensing scheme was not tested during this work.

7. 2 Particle mobility in porous and fractured systems

The main function of the temperature-sensitive particles is to measure temperature at the interwell spaces between an injection and a producing well. The particles would accompany the injection fluid, infiltrate through the rock pore spaces, flow through the fractures, measure the temperature, and then be produced at the production wells. Thus, the particles need to be transported through the porous and/or fractured systems with the least deposition inside the flow medium. Therefore, the mobility of the particles through reservoir rocks was investigated. In this work, several particles of different sizes, shape, surface properties and materials were transported through various flow systems including porous and fractured rocks as well as slim tubes packed with sand or glass beads.

Temperature sensing based on changes of particle shape was investigated by transporting rod-like silver particles (nanowires) through a reservoir rock. Experimental results showed that rod-like particles experienced a complete deposition within the pore network. It was concluded that nonspherical particles may not be suitable as temperature nanosensors because due to the difficulty imposed by shape on their transport through the rock pore network.

Further investigation of the viability of transporting nonspherical particles was carried out by injecting hematite nanorice, an order of magnitude shorter than the silver nanowires. Hematite was also investigated because of its behavior under an applied magnetic field that would make it suitable core material of the core-shell temperature nanosensor concept. This involves the melting of the shell, hence change in the core surface characteristic including its surface charge. Therefore, the effect of surface-charge on the transport of hematite was explored by injecting hematite suspensions of different surface charge. It was found that the recovery of hematite nanorice was improved, primarily due to its surface charge. The highest recovery was observed during the injection of hematite of surface charge that was compatible with flow medium. It was concluded that hematite could potentially be used as a core material of a core-shell

CHAPTER 7. CONCLUSIONS AND RECOMMENDATIONS FOR FUTURE WORK

nanosensor; however, compatibility of surface charge shell material to rock constituents must be assessed prior to injection into the reservoir.

Because the primary application for the temperature sensors was fractured reservoir, particle transport through fractured reservoir rocks was studied using silica particles. Silica particles were used as precursor of the silica-based temperature-sensitive particles (dye-attached and silica-encapsulated DNA particles). The investigation focused on the effect of the particle size, suspension concentration and fluid velocity on particle transport through different reservoir rocks, greywacke and Berea sandstones. Generally, the experimental results showed that the recovery of particles was inversely proportional to particle size and directly proportional to the suspension concentration and fluid velocity. The existence of the fracture facilitated the particle transport. The rapid breakthrough of particles suggested that particles were mainly flowing through the fracture, which represents the large flow path, along the fast-moving streamlines. These results were consistent with visual observations during the particle injections into micromodels. With regard to the field application of the temperature sensors into fractured reservoirs, these results show promise as fractures would aid the mobility of the temperature-sensitive particles.

Controlling transport or deposition mechanisms of the silica particles were also identified. Among all, gravitational sedimentation, and straining based on the individual particle size or an aggregate of particles were the main particle deposition mechanisms. Settling of the silica particles was due to the density difference between the silica particles and suspension fluid. This suggests that the silica-based temperature sensors must be designed to have a density similar to the suspension fluid and/or the injection rate during field application should be engineered to offset gravitational forces.

Initial testing of using particles as a fracture caliper to estimate the fracture aperture was addressed in this study. The fracture caliper concept was demonstrated by injecting a polydispersed silica suspension through a fractured greywacke rock of predetermined hydraulic fracture aperture. Only particles of size smaller than the fracture aperture were

recovered. The size of largest recovered particle was comparable to the fracture aperture. These results were closely consistent with the micromodel results.

7.2 Recommendations for future work

Recent research had shown that temperature measurements carry useful information about the reservoir properties and structure. Temperature-sensitive particles could potentially provide temperature measurement far in the formation. Having such a detailed temperature distribution map would enhance the ability to infer other reservoir and fracture properties, which in turn, would inform a proper reservoir engineering decisions. The following recommendations for future work are suggested:

1. Besides temperature sensing, developing or synthesizing particles having the functional capability for sensing other reservoir properties or enhancing oil recovery may be feasible. These particles could be designed to record data such as pressure and register fluid type encountered within the reservoir. Labeled particles, such as silica-encapsulated DNA particles, could be used to provide information about connectivity between injection and production wells. Therefore, laboratory-scale experiment using silica-encapsulated DNA particles to study the interwell connectivity would be useful. Investigating paramagnetic particles for enhanced oil recovery applications would also be useful. Due to their behavior under magnetic field, paramagnetic particles could be used to control the injected fluid.
2. In this research study, the transport experiments were conducted under unfavorable attachment conditions (presence of energy barrier) to study the effect of hydrodynamic parameters on the mobility of particles. The influence of chemical interactions, including ionic strength and/or pH, has not been considered. Previous research (e.g. Li et al., 2004; Tufenkji and Elimelech, 2004; Saleh et al., 2008; French et al., 2009) has shown that increasing solution salinity (ionic strength) suppresses the electrostatic double layer (repulsive forces)

CHAPTER 7. CONCLUSIONS AND RECOMMENDATIONS FOR FUTURE WORK

between particles and/or between particles and surfaces. This could lead to particle aggregation and attachment to flow medium and thus increased particle deposition. Similarly, as the pH approaches the pH of the point of zero charge, the size of the particles aggregation increases while their mobility decreases (Guzman et al., 2006; Fang et al., 2009). At or near the pH of the zero charge point, the surface ionization of particles is decreased to zero, resulting in reduction in the magnitude of the electrostatic repulsive forces and therefore formation of particle aggregates. Investigating the influence of ionic strength and solution pH on the transport of the temperature-sensitive particles addressed in this study is highly encouraged. It is recommended to test the temperature sensors at typical reservoir conditions of salinity and pH levels.

3. A pore-scale modeling of particle transport in porous and fractured media would be beneficial. Such models should include not only the system hydrodynamics (fluid drag, gravity), but the electrostatic and chemical interactions. Models with geometry corresponding to that of the micromodels in Chapter 5 could be used. This is of particular interest because it allows experimental comparison.

APPENDIX A

MICROMODEL FABRICATION PROGRAM

Qing Chen

SUPRI-A, Stanford Petroleum Department

First work on 8/2/04

Version 1.1, last updated 10/26/06

Revised by: Amar J Alshehri and Bolivia Vega on June 2008

Revised by Mohammed Alaskar on July 2013

This document describes in details the micromodel fabrication procedures developed at Stanford Petroleum Department over the past 30 years. This procedure is a modified version of that found in Alshehri (2009), and used during the fabrication of the micromodels used in this study.

Note that this procedure was written with reference to processes and equipment in Stanford Nanofabrication Facility (SNF).

Reference

Alshehri, A. J. (2009). Low tension methods for fractured resources. Master thesis, Stanford University, CA.

Process Overview

Materials:

- 4” Si wafer, K Prime, 4P <100> B S42565. The Si wafers can be obtained from the SNF stockroom.
- Borofloat 4” diameter X 0.043” thick, standard transparent finish 80/50 – 60/40 scratch/dig, flat to 3-4 waves/inch (Valley Design Corp.).

Micromodel fabrication processes are listed in order below as:

- Wafer precleaning.
- Photolithography.
 - Coating.
 - Exposing.
 - Developing.
- Deep etching.
- Resist removing and cleaning.
- Anodic bonding.

Photolithography

Photoresist Coating

Equipment: SVG photoresist spin coater (svgcoat).

Person to contact: Uli Thumser (uthumser@stanford.edu).

Operating Procedures/parameters:

1. YES Oven for 30 minutes (HMDS vapor prime).
2. Prime program: off.
3. Coat program #8: 1-1.6 μm (for a 50 μm deep etching, consult Uli Thumser or Nancy Latta for deeper etching).
4. Prebake program #2.

APPENDIX A. MICROMODEL FABRICATION PROGRAM

Exposure

Equipment: Karl Suss MA-6 contact mask aligner (karlsuss).

Persons to contact: Mahnaz Mansourpour (mahnaz@stanford.edu) and Uli Thumser (uthumser@stanford.edu).

Operating Procedures/parameters:

1. Initiate the system.
2. Select program. For our case, soft contact mode is a good option. The other modes are vacuum, vacuum hard, and hard contact
3. Edit parameters for current program.
 - 3.1. Time = 2.6 sec.
 - 3.2. Gap width = 40 μm .
4. Change mask.
5. Load wafer.
6. Focus mask.
7. Expose.
8. Unload/change wafer.
9. Unload/change mask.

Developing

Equipment: SVG developer (svgdev).

Person to contact: Uli Thumser (uthumser@stanford.edu).

Operating Procedures/parameters:

1. Develop Program #4.
2. Post Bake.
3. Oven bake #2.

Deep dry etching

Equipment: STS multiplex ICP Deep Reactive Ion etcher (stsetch).

Person to contact: Nancy Latta (nlatta@stanford.edu).

Operating Procedures/Parameters

Etch recipe: DEEP

- Select a desired recipe and set it as current by clicking recipe field.
- Pre check: 400 Hz.
 - During process: P and Q are about 10 and 3, respectively, they should not fluctuate wildly.
- Check and modify settings of the current recipe. Press RECIPE button in the window of Press control-ICP. In the popped-out recipe window, check the settings with the parameters from the STSetch logbook. For those standard recipes, such as DEEP, the only parameter that can be changed is the etching time. With assumption that etching rate is constant, the desired etching time can be easily determined from the desired etching depth. Remember to save recipe before exiting the recipe menu if any setting is changed.
- Unload wafer if necessary.
- Load new wafer.
- Start etching process by pressing PROCESS button.
- Read parameters of machine conditions and write them down on the logbook. Those parameters include:
 - He pressure and flow which can be read from the low small window on the left side of the machine.
 - Chamber pressure (passivation and etch) which can be read from the right lower part of the machine view window.
- Unload wafer when etching is done.

Etching depth measurement tools

Equipment: Tencor P2 Profilometer.

Person to contact: Uli Thumser (uthumser@stanford.edu).

The P2 has a stylus that physically touches the etched and the non-etched surface and calculates the difference.

Equipment: Zygo 3D Surface Profiler.

Person to contact: Uli Thumser (uthumser@stanford.edu).

The Zygo relies on the reflectivity of different elevated surfaces.

Photoresist removal and wafer (Si and glass) cleaning

Equipment: Wet bench silicide (wbsilicide).

Person to contact: Uli Thumser (uthumser@stanford.edu).

Silicon and glass wafers must be cleaned before bonding as follow:

- Wafers are submerged in Sulfuric/Peroxide Piranha (9:1 H₂SO₄:H₂O₂) bath at 120 °C, for 20 min followed by 6-cycle deionized water rinse and spinning dry. It is recommended to change the mixture (Sulfuric/Peroxide) before starting the cleaning process to avoid contaminations from previous users.

Anodic Bonding

Equipment: Power supply, high voltage supply unit and hotplate.

The bonding can be conducted outside the SNF facility.

Operation Procedure:

- Place a cleaned wafer on a hotplate preheated to 350°C, with its etched side facing up. The wafer is left on the plate for around 45 minutes, by which a very thin SiO₂ film is formed on the wafer surface and the wafer, initially non-wetting, becomes water wetting.

APPENDIX A. MICROMODEL FABRICATION PROGRAM

- Inspect the wafer surface for any dust that might deposit during preheating period. Blow off any visible dust from the surface with compressed clean air.
- Place a cleaned glass wafer right on the top of the wafer, and align as desired. Allow the wafers to heat for at least 1 minute.
- Preset the voltage of the power supply between 900 and 1200 volts. Turn the power supply to standby mode, and allow it to warm up for 2 minutes. The anode of the power supply is connected to the hotplate and the other electrode (cathode) is connected to an aluminum plate wrapped by a copper mesh. Place the aluminum plate on the top of the glass wafer gently and then turn on the power supply to apply the high voltage.
- After 50 minutes, bonding should be achieved.
- Turn off the electricity, remove the micromodel from the hotplate using tweezers, and allow it to cool to room temperature. Do not leave the micromodel on the hotplate for cooling, because it was occasionally found that the glass got cracked during cooling on the hotplate.

APPENDIX B

PRESSURE TRANSDUCER AND MASS FLOW METER CALIBRATION

B.1 Pressure transducer calibration procedure

1. Schematic of pressure transducer calibration process diagram can be seen in Figure B.1.
2. Basically the system consists of the gas (nitrogen) source, pressure regulator, standard pressure gauge and the pressure transducer. The transducer is controlled by demodulator (Celesco or Validyne models, 10 VDC full range) and the signal displayed using voltmeter. Instead, the demodular can be connected to data acquisition card where signal can be read from LabView software.
3. Both the standard pressure gauge and pressure transducer must be connected in parallel as shown in the process diagram.
4. The maximum pressure that can be measured using the pressure transducer depends on the diaphragm used. To change the diaphragm, refer to the installation procedure provide by the manufacturer of the pressure transducer. It is recommended that the measured pressure should fall within the midrange of selected diaphragm.
5. The demodulator is adjusted through the zero and span knobs.
6. First, the system is kept at zero pressure (confirmed by the standard gauge). If the volt reading is not zero, the zero knob is adjusted to zero out the signal reading.
7. The system is then pressurized to full range (maximum pressure). If the volt reading does not display 10 volts, then the span knob is adjusted to read 10 volts.
8. Repeat steps 6 and 7 at least three times to make sure it has been done correctly.

APPENDIX B. PRESSURE TRANSDUCER AND MASS FLOW METER CALIBRATION

9. Finally, divide the full range into five different points and plot the measured data and use linear regression to fit the data.

Notes:

- After introducing the desired pressure to the transducer/standard gauge, make sure to put valve # 1 in close position.
- The demodulator should be turned on for at least 30 minutes before use to stabilize.
- The demodulator may be left on for a longer period of time (perhaps a few weeks or a month) if planned to be used more frequently.

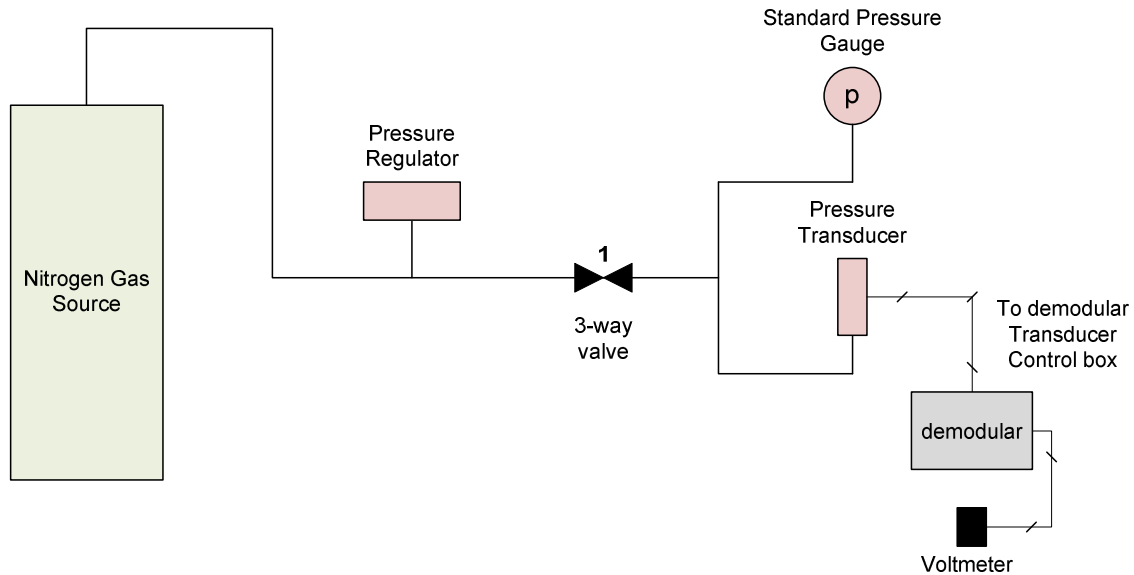


Figure B.1: Schematic of the pressure transducer calibration process diagram.

B.2 Mass flow meter calibration procedure

This procedure was used to calibrate Matheson mass flow transducers Models 8172-0422 and 8272-0423.

1. Experimental setup schematic can be seen in Figure B.2.
2. Connect the gas source to the pressure gauge and the needle valve. The needle valve is used to control the upstream pressure and therefore the volumetric flow rate.
3. The flow can be directed to either transducer using the 3-way valve.
4. Each transducer is connected to different mass flow controller system. Namely, transducer model 8172-0422 is connected to controller system model 8170. The second transducer model 8272-0423 is connected to controller system model 8270. The latter has the capability to monitor and control the flow through an integrated valve.
5. The mass flow meter is calibrated using a graduated cylinder and stop watch (Standard method).
6. Adjust the flow rate of the gas using the needle valve. Record the flow rate as measured by the mass flow meter (displayed in the controller unit). Record the time and the displaced volume of water in the graduated cylinder (the displaced volume divided by the time is the volumetric flow rate). This is one data point.
7. Repeat step 6 few times at different flow rates. Use bench vacuum to raise the water column back in the graduated cylinder. To do that, keep the main bench vacuum valve open. Turn on the two-way valve to raise the water level up.
8. The relation between flow rates obtained by standard method and flow meter is then plotted and fitted using linear regression.

APPENDIX B. PRESSURE TRANSDUCER AND MASS FLOW METER CALIBRATION

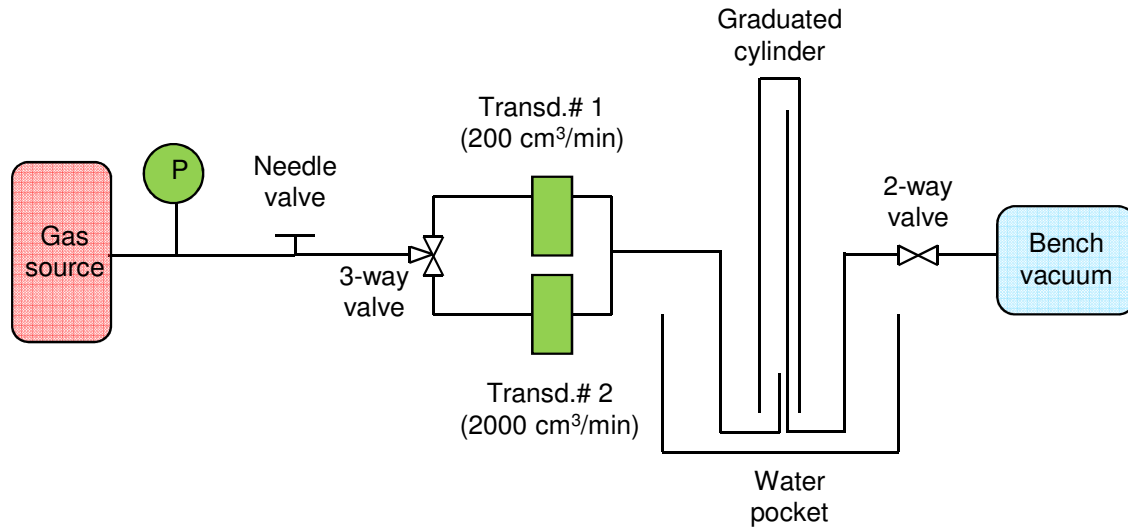


Figure B.2: Schematic of the experimental setup used during the mass flow meter calibrations.

APPENDIX C

IRREVERSIBLE THERMOCHROMIC DATA

C.1 Material safety data sheet

Page 1 of 3
MSDS004 Revision 2
Revision Date 2/8/2010

1. PRODUCT AND COMPANY IDENTIFICATION

Product name	Irreversible ThermoChromic Ink - NH
Description	Ranges: Black K170-NH, Black K115-NH, BlackK90-NH, Black K75-NH, Black K60-NH, MB50Y-NH, MB60-NH, Magenta K65-NH, Magenta K75-NH, Magenta K90-NH, Magenta K100-NH, Magenta K120-NH, Magenta K200-NH, Blue K150-NH, Turquoise K150-NH.
Company	LCR Hallcrest 1911 Pickwick Lane Glenview IL 60026
Telephone	+1 847 998 8580
Fax	+1 847 998 6866
Emergency telephone number	+1 847 998 8580

2. HAZARDOUS IDENTIFICATION.

Statement of Hazard

Properties	Color	Off white.
	Odor	Characteristic.
	State	Liquid.

3. COMPOSITION / INFORMATION ON INGREDIENTS.

Hazardous ingredients

	Conc.	CAS
Isopropanol (2-Propanol)	2.5-25%	67-63-0
Heterocyclic Organic Dye - Only Black Chromax Ranges	2.5-25%	
Further information	Only inks contain isopropanol.	

4. FIRST AID MEASURES

Skin contact	May cause irritation to skin. Wash off immediately with plenty of soap and water. Remove contaminated clothing. Seek medical attention if irritation or symptoms persist.
Eye contact	May cause irritation to eyes. Rinse immediately with plenty of water for 15 minutes holding the eyelids open. Seek medical attention if irritation or symptoms persist.
Inhalation	May cause irritation to mucous membranes. Move the exposed person to fresh air.
Ingestion	May cause irritation to mucous membranes. DO NOT INDUCE VOMITING. Seek medical attention if irritation or symptoms persist.

5. FIRE FIGHTING MEASURES

Extinguishing media	Use extinguishing media appropriate to the surrounding fire conditions.
Fire hazards	Burning produces irritating, toxic and obnoxious fumes.
Protective equipment	Wear suitable respiratory equipment when necessary.

6. ACCIDENTAL RELEASE MEASURES

Personal precautions	Ensure adequate ventilation of the working area.
Environmental precautions	Do not allow product to enter drains. Prevent further spillage if safe.
Clean up methods	Absorb with inert, absorbent material. Sweep up. Transfer to suitable, labeled containers for disposal. Clean spillage area thoroughly with plenty of water.

7. HANDLING AND STORAGE

Handling	Avoid contact with eyes and skin. Ensure adequate ventilation of the working area. Adopt best Manual Handling considerations when handling, carrying and dispensing.
Storage	Keep in a cool, dry, well ventilated area. Keep containers tightly closed. Store in correctly labeled containers.

8. EXPOSURE CONTROLS / PERSONAL PROTECTION

Exposure limits		
Isopropanol (2-Propanol)	ACGIH TLV TWA: 200 ppm Notations: A4 OSHA PEL 8hr TWA mg m3: 980	ACGIH TLV STEL: 400 ppm OSHA PEL 8hr TWA ppm: 400 Skin Designation: -
Engineering measures	Ensure adequate ventilation of the working area.	
Hand protection	Chemical resistant gloves (PVC)	
Eye protection	In case of splashing, wear: Approved safety goggles.	
Protective equipment	Wear protective clothing.	

APPENDIX C. IRREVERSIBLE THERMOCHROMIC DATA

Page 3 of 3
 MSDS004 Revision 2
 Revision Date 2/8/2010

9. PHYSICAL AND CHEMICAL PROPERTIES

Description	Liquid.
Color	Off white.
Odor	Characteristic
pH	5 – 7.5
Boiling point	100°C
Flammability limits	n/a
Relative density	1.0 – 1.1
Water solubility	Miscible in water.

10. STABILITY AND REACTIVITY

Stability	Stable under normal conditions.
------------------	---------------------------------

11. TOXICOLOGICAL INFORMATION

12. ECOLOGICAL INFORMATION

13. DISPOSAL CONSIDERATIONS

General information	Dispose of in compliance with all local and national regulations.
----------------------------	---

14. TRANSPORT INFORMATION

Further information	The product is not classified as dangerous for carriage.
----------------------------	--

15. REGULATORY INFORMATION

Inventories	TSCA	MA	SARA313	CALPROP65	CWA307	CAA112	CWA311	SARA302	SARA303
Ingredient									
Propan-2-ol	Y	N	Y 1.0	N	N	N	N	N	N

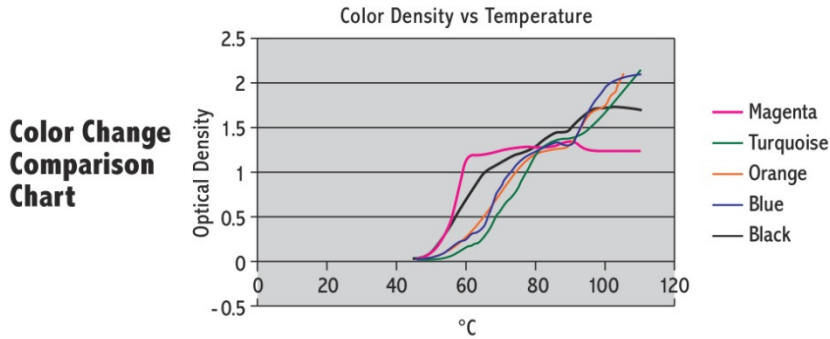
16. OTHER INFORMATION

Statement of Hazard	
Further information	The information supplied in this Safety Data Sheet is designed only as guidance for the safe use, storage and handling of the product. This information is correct to the best of our knowledge and belief at the date of publication however no guarantee is made to its accuracy. This information relates only to the specific material designated and may not be valid for such material used in combination with any other materials or in any other process.
TSCA	All components are TSCA compliant.
HMIS LABELLING	HEALTH 0, FLAMMABILITY 0, PHYSICAL HAZARD 0.

C.2 Product color comparison chart



High Temperature Activated, Irreversible, White-to-Color Change Ink



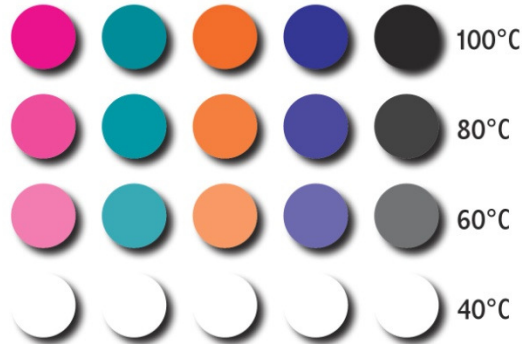
Test prints of various Hallcrest Permanent Change ThermoChromic Inks were heated for 3 minutes and measured for color density.

Magenta, closely followed by Black reached the strongest color point at 60°C of the colors measured. **The color change for magenta and black is sharp.**

Turquoise, Orange and Blue need a higher temperature point to reach a comparable density and have a more gradual color change profile.

NOTE: Magenta is best for lower temperature activation; at 60°C it shows good color

This information is for illustration only; it has been developed under strict laboratory conditions. The user should test and verify that the ink works for their particular application.



As Temperature Increases, Color Density Increases

Please contact us to see how we might bring your idea to life!

C.3 Product specification sheet



Permanent Change ThermoChromic Ink SPECIFICATIONS

Permanent Change ThermoChromic Ink is supplied in two kinds of formats:

CONCENTRATE

Concentrates are primarily intended for use in the formulation of inks using water based resins or binders.

INKS

Printing methods including Screen and Flexographic onto print receptive plastics and absorbent surfaces such as paper.

SPECIFICATION DETAILS

Pigment Concentrates

Solids: 48% \pm 2%
Pigment Concentration: 39% \pm 2%
Particle Size: 95% < 15 μ m
pH: 6-8 depending on range
Light Fastness: 1-3 (BWS) depending on color

Water Based Inks

Solids: 44% \pm 2%
Pigment Concentration Flexo: 26% \pm 2%
Screen: 29% \pm 2%
Particle Size: 95% < 15 μ m
pH: 6-8 depending on range
Light Fastness: 1-3 (BWS) depending on color

TEMPERATURE RANGE

60 to 200°C

STORAGE

A shelf life of 1 year is guaranteed provided that the containers are not opened and are stored in an ambient temperature of 16 to 22°C with no exposure to UV (Sun) light. Concentrates may be subject to settlement on standing and should be stirred well before use.

A full product information and material safety data sheets (PI & MSDS) are available for concentrate and/or ink and is available upon request.

*Please contact us to see how
we might bring your idea to life!*

C.4 Product technical data sheet

TECHNICAL DATA SHEET

1. IDENTIFICATION OF SUBSTANCE

KROMAGEN THERMAL INKS AND CONCENTRATES

Use:	Thermal Ink
Manufacturer / Supplier:	Thermographic Measurements Ltd Riverside Buildings, Dock Road, Connah's Quay, Flintshire, CH5 4DS
Telephone:	+ 44 (0) 1244 818348
Fax:	+ 44 (0) 1244 818502

2. DETAILS

Kromagen inks are an irreversible colour change water based ink. They are supplied at approximately 44% solids with a viscosity between 45 and 60 seconds on a B4 Cup @ 25C for flexo and 2000-3000cps for screen inks. The pH of the ink is slightly alkaline and at start of printing will be 7-8 pH.

Pigment concentrates are dispersions of the reactive pigments in an acrylic solution having good compatibility with many typical water based varnishes or ink systems. Pigment content is approximately 39 – 41% solids.

The SG of inks and concentrates is between 1.0 and 1.1.

Demineralised water may be used to thin the ink and clean up. A 50 / 50 mix of water and isopropyl alcohol can also be used for thinning.

On no account should other solvents be used. Exposure to organic solvents may cause an irreversible colour change. Dry prints will also be damaged by solvent exposure.

The ink is suitable for use on paper and print receptive plastics. For screen printing a water proof stencil should be used. Mesh size from 77T to 125 / 150T may be used depending on final colour strength required.

Colour formation is from off white to named colour. A faint colour change starts to occur at approximately 10 -30°C below the rated temperature (depending on type). A distinct colour change is seen at the rated temperature and full shade is seen between 10-20°C above the rating (depending on type). Prints exposed to less than 90C may show a fading of the developed colour on standing. Individual colour change plots against temperature may be available.

This type of ink produces a strong colour change which intensifies when removed from heat. The ink is best suited to short periods of temperature exposure. Prolonged exposure to elevated temperature will eventually cause the colour development to fade.

Compatible water based varnishes may be used to give good scratch resistance as abrasion can mark the Kromagen by causing colour development.

The information on this Data Sheet is based on our experience and is correct to the best of our knowledge at the date of publication. The company do not accept any liability for any loss, damage or injury resulting from its use (except as required by law).

8/10/2006

1820 Pickwick Lane, Glenview Ill 60026

BIBLIOGRAPHY

- Adams, M. C., Benoit, W. R., Doughty, C., Bodvarsson, G. S., and Moore, J. N. (1989). The Dixie Valley, Nevada, Tracer Test. *Geothermal Resources Council Transactions*, 13, 215–220.
- Adams, M. C., and Davis, J. (1991). Kinetics of Fluorescein Decay and its Application as a Geothermal Tracer. *Geothermics*, 20, No.1/2, 53.
- Aguilera, R., and Poolen, H. K. (1977). Current Status on the Study of Naturally Fractured Reservoirs. *The Log Analyst*.
- Alaskar, M., Ames, M., Connor, S., Liu, C., Cui, Y., Li, K., and Horne, R. (2012). Nanoparticle and Microparticle Flow in Porous and Fractured Media- an Experimental Study. *SPEJ*, 17, 1160-1171.
- Alaskar, M., Ames, M., Liu, C., Connor, C., Horne, R.N., Li, K., and Cui, Y. (2011). Smart Nanosensors for In-situ Temperature Measurement in Fractured Geothermal Reservoir. *Annual Meeting of the Geothermal Resources Council, San Diego, California*, 35.
- Alkafef, S. F., Gochin, R. J., and Smith, A. L. (1999). Measurement of the Electrokinetic Potential at Reservoir Rock Surfaces Avoiding the Effect of Surface Conductivity. *Colloids Surf., A* 159 (2–3), 263–270. [http://dx.doi.org/10.1016/S0927-7757\(99\)00263-0](http://dx.doi.org/10.1016/S0927-7757(99)00263-0).
- Alonso, U., Missana, T., Patelli, A., et al. (2007). Colloid Diffusion in Crystalline Rock: an Experimental Methodology to Measure Diffusion Coefficients and Evaluate Colloid Size Dependence. *Earth and Planetary Science Letters*, 259, 372-383.

BIBLIOGRAPHY

- Alonso, U., Missana, T., Patelli, A., et al. (2009). Quantification of Au Nanoparticles Retention on a Heterogeneous Rock Surface. *Colloid and Surfaces A. Physicochemical and Engineering Aspects*, 347, 230-238.
- Ames, M. F. (2011). Nanosensors as Reservoir Engineering Tools to Map In-Situ Temperature Distributions in Geothermal Reservoirs. MS thesis, Stanford University
- Amyx, J. W., Bass, D. M. Jr., and Whiting, R. L. (1960). *Petroleum Reservoir Engineering, Physical Properties*. McGraw-Hill Book Co.
- Auset M, and Keller, A. A. (2004). Pore-Scale Processes That Control Dispersion of Bioparticles in Saturated Porous Media. *Water Resour Res.*, 40 (3), W03503. doi:10.1029/2003WR002800.
- Auset M, and Keller A. A. (2006). Pore-Scale Visualization of Colloid Straining and Filtration in Saturated Porous Media Using Micromodels. *Water Resour Res.*, 42 (3): W12S02. doi:10.1029/2005WR004639.
- Axelsson, G. O. Flovenz, G., Hauksdottir, S., Hjartarson, A., and Liu, J. (2001). Analysis of Tracer Test Data, and Injection-induced Cooling, in the Laugaland Geothermal Field, N-Iceland. *Geothermics*, 30, 697-725.
- Bales, R. C., Gerba, C. P., Grondin, G. H., and Jensen, S. L. (1989). Bacteriophage Transport in Sandy Soil and Fractured Tuff. *Appl. Environ. Microbiol.*, 55, 2061-2067.
- Bamfield, P. (2001). *Chromic Phenomena - Technological Applications of Colour Chemistry*. Cambridge: The Royal Society of Chemistry.
- Bancroft, C., Bowler, T., Bloom, B., and Clelland, C. T. (2001). Long-Term Storage of Information in DNA. *Science*, 293, 1763-1765.

BIBLIOGRAPHY

- Baumann T., and Werth C. J. (2004). Visualization and Modeling of Polystyrol Particle Transport in a Silicon Micromodel. *Vadose Zone J.*, 3, 434–43.
- Bayouhd, S., Othmane, A., Mora, L., et al. (2009). Assessing Bacteria Adhesion Using DLVO and XDLVO Theories and the Jet Impingement Technique. *Colloids and Surfaces Biointerfaces*, 73, 1-9.
- Bear, J. (1972). *Dynamics of Fluids in Porous Media*. Dover. Mineola, NY: Dover Publications, Inc.
- Becker, M. W., Metge, D. W., Collins, S. A., Shapiro, A. M., and Harvy, R. W. (2003). Bacterial Transport Experiments in Fractured Crystalline Bedrock. *Ground Water*, 41, 682-689.
- Becker, M. W., Reimus, P. W., and Vilks, P. (1999). Transport and Attenuation of Carboxylate-Modified Latex Microspheres in Fractured Rock Laboratory and Field Test. *Ground Water*, 37, 387-395.
- Becker, M. W. and Shapiro, A. M. (2003). Interpreting Tracer Breakthrough Tailing from Different Forced Gradient Tracer Experiment Configuration in Fractured Bedrock. *Water Resour. Res.*, 39 (1), 1024. doi:10.1029/2001WR001190.
- Bergendahl, J., and Grasso, D. (1999). Prediction of Particle Detachment in a Model Porous Media: Thermodynamics. *AIChE J.*, 45 (3), 475-484.
- Bergendahl, J., and Grasso, D. (2000). Prediction of Particle Detachment in a Model Porous Media: Hydrodynamics. *Chem. Eng. Sci.*, 55, 1523-1532.
- Bogush, G. H., Tracy, M. A., and Zukoski, C. F. (1988). Preparation of Monodisperse Silica Particles: Control of Size and Mass Fraction. *Non-Cryst. Solids*, 104, 95.
- Bradford, S. A., and Bettahar, M. (2005). Straining, Attachment, and Detachment of *Cryptosporidium* Oocysts in Saturated Porous Media. *J. Environ. Qual.*, 34, 469-478.

BIBLIOGRAPHY

- Bradford, S. A., and Bettahar, M. (2006). Concentration Dependent Transport of Colloids in Saturated Porous Media. *J. of Contaminant Hydrology*, (82), 99-117.
- Bradford, S. A., Simunek, J., Bettahar, M., van Genuchten, M. T., and Yates, S. R. (2003). Modeling Colloid Attachment, Straining, and Exclusion in Saturated Porous Media. *Environ. Sci. Technol.*, 37, 2242-2250.
- Bradford, S. A., Simunek, J., Bettahar, M., van Genuchten, M. T., and Yates, S. R. (2006). Significance of Straining in Particle Deposition: Evidence and Implications. *Water Resour. Res.*, 42, W12S15. doi:10.1029/2005 WR004791.
- Bradford, S. A., and Torkzaban, S. (2008). Colloid Transport and Retention on in Unsaturated Porous Media: a Review of Interface-, Collector-, and Pore-Scale Processes and Models. *Vadose Zone J.*, 7, 667-681.
- Bradford, S. A., S. Torkzaban, and S. L. Walker (2007), Coupling of Physical and Chemical Mechanisms of Particle Straining in Saturated Porous Media, *Water Res.*, 41, 3012–3024.
- Bradford, S. A., Yates, S. R., Bettahar, M., and Simunek, J. (2002). Physical Factors Affecting the Transport and Fate of Particles in Saturated Porous Media. *Water Resour. Res.*, 38, 1327 (12).
- Brant, J. A., and Childress, A. E. (2002) Assessing Short-Range Membrane-Colloid Interactions Using Surface Energetics. *Journal of Membrane Science*, 203, 257-273.
- Brigham, W. E., and Ahbaszadeh-Dehghani, M. (1987). Tracer Testing for Reservoir Description. *J. Pet.Tech.*, 519-527.
- Brinker, C. J., and Scherer, G. W. (1990). *Sol–Gel Science: The Physics and Chemistry of Sol–Gel Processing*. San Diego: Academic Press Inc.

BIBLIOGRAPHY

- Buckley, J. S. (1991). Multiphase Displacements in Micromodels: Interfacial Phenomena in Petroleum Recovery. Morrow, N.R. (ed.), Marcel Dekker Inc., New York, NY, 157-189.
- Cantrell, D. L., and Hagerty, R. M. (1999). Microporosity in Arab Formation Carbonates, Saudi Arabia. *Geo Arabia*, 4 (2), 129-154.
- Champ, D. R., and Schroeter, J. (1988). Bacterial Transport in Fractured Rock-A Field-Scale Tracer Test at the Chalk River Nuclear Laboratories. *Water Sci. Technol.*, 20, 81-87.
- Characterization of Fractured Reservoirs, Reliable, Predictive Model to Optimize Carbonate Reservoir Performance. No Date. Schlumberger Market Analysis, (2008). Retrieved on September 30, 2009 from http://www.slb.com/media/services/solutions/reservoir/char_fract_reservoirs.pdf
- Chen J. Y., Klemic, J. F., and Elimelech, M. (2002). Micropatterning Microscopic Charge Heterogeneity on Flat Surfaces for Studying the Interaction Between Colloidal Particles and Heterogeneously Charged Surfaces. *Nano Letter*, 2 (4), 393-6.
- Chen, H., Li, Z., and Wu, Z. (2005). A Novel Route to Prepare and Characterize Sn-Bi Nanoparticles. *J. Alloys Compd.*, 394 (1-2), 282-285. <http://dx.doi.org/10.1016/j.jallcom.2004.10.044>.
- Chilkoti, A., Dreher, M. R., Meyer, D. E., and Raucher, D. (2002). Targeted Drug Delivery by Thermally Responsive Polymers. *Adv. Drug Delivery Rev.*, 54, 613-630
- Chinju, H., Kuno, Y., Nagasaki, S., and Tanaka, S. (2001). Deposition Behavior of Polystyrene Latex Particles on Solid Surfaces During Migration Through an Artificial Fracture in a Granite Rock Sample. *J. Nucl. Sci. Technol.*, 38, 439-443.
- Churcher, P. L., French, P. R., Shaw, J. C., and Schramm, L. L. (1991). Rock Properties of Berea Sandstone, Baker Dolomite, and Indiana Limestone. Published in

BIBLIOGRAPHY

- Proceedings from the SPE International Symposium on Oilfield Chemistry, Anaheim, California. SPE Paper No. 21044.
- Clarke, A. R. (2002). *Microscopy Techniques for Material Science*. Boca Raton: CRC Press LLC.
- Cumbie, D. H., and McKay, L. D. (1999). Influence of Diameter on Particle Transport in a Fractured Shale Saprolite. *J. Contam. Hydrol.*, 37 (1-2): 139-157.
- Derjaguin, B. V., and Landau, L. D. (1941). Theory of the Stability of Strongly Charged Lyophobic Sols and the Adhesion of Strongly Charged Particles in Solutions of Electrolytes. *Acta Physicochim URSS*, 14, 633-662.
- Detwiler, R. L., Rajaram, H., and Glass, R. J. (2000). Solute Transport in Variable-Aperture Fractures: an Investigation of the Relative Importance of Taylor Dispersion and Macrodispersion. *Water Resour. Res.*, 36, 1611-1625.
- Digital image. *Phase Diagrams & Computational Thermodynamics*. The National Institute of Standards and Technology. Web. 7 July 2010.
<<http://www.metallurgy.nist.gov/phase/solder/bisn.html>>.
- Diomampo, G. P. (2001). *Relative Permeability Through Fractures*. MS thesis, Stanford University.
- Dong, H., Onstott, T. C., Ko, C. H., Hollingsworth, A. D., Brown, D. G., and Mailloux, B. J. (2002). Theoretical Prediction of Collision Efficiency Between Adhesion-Deficient Bacteria and Sediment Grain Surface. *Particle Surf. Biointerfaces*, 24, 229-245.
- Dongjo Kim, Sunho, J., and Moon, J. (2006). Synthesis of Silver Nanoparticles Using the Polyol Process and the Influence of Precursor Injection. *Nanotechnology*, 17 (16), 4019-4024. <http://dx.doi.org/10.1088/0957-4484/17/16/004>.

BIBLIOGRAPHY

- Egerton, R. F. (2005). *Physical Principles of Electron Microscopy: an Introduction to TEM, SEM, and AEM*. Springer, 202.
- Elimelech, M., Gregory, J., Jia, X., and Williams. R. A. (1995). *Particle Deposition and Aggregation-Measurement, Modelling and Simulation*. Elsevier.
- Energy Information Administration. 2006. *System for the Analysis of Global Energy Markets*. Appendix I of *International Energy Outlook*. Report: DOE/EIA-0484(2006).
- Fang, J., Shan, X. Q., Wen, B., Lin, J. M., and Owens, G. (2009). Stability of Titania Nanoparticles in Soil Suspensions and Transport in Saturated Homogeneous Soil Columns. *Environmental Pollution*, 157 (4), 1101-1109.
- French, R. A., Jacobson, A. R., Kim, B., Isley, S. L., Penn, R. L., and Baveye, P. C. (2009). Influence of Ionic Strength, pH and Cation Valence on Aggregation Kinetics of Titanium Dioxide Nanoparticles. *Environmental Science & Technology*, 43 (5), 1354-1359.
- Grabbe, A., and Horn, R. G. (1993). Double-Layer and Hydration Forces Measured between Silica Sheets Subjected to Various Surface Treatments. *J. Colloid Interface Sci.*, 157 (2), 375–383. <http://dx.doi.org/10.1006/jcis.1993.1199>.
- Gregory, J. (1981). Approximate Expressions for Retarded van der Waals Interactionn. *J. Colloid Interface Sci.*, 83 (1): 138-145. [http://dx.doi.org/10.1016/0021-9797\(81\)90018-7](http://dx.doi.org/10.1016/0021-9797(81)90018-7).
- Gunderson, R., Parini, M., and Sirad-Azwar, L. (2002). Fluorescein and Naphthalene Sulfonate Liquid Tracer Results at the Awibengkok Geothermal Field, West Java, Indonesia. *Proceedings, 27th Workshop on Geothermal Reservoir Engineering*, Stanford, Cal, Jan 28-30, 53-58.

BIBLIOGRAPHY

- Guzman, K. A. D., Finnegan, M. P., and Banfield, J. F. (2006). Influence of Surface Potential on Aggregation and Transport of Titania Nanoparticles. *Environmental Science & Technology*, 40 (24), 7688-7693.
- Hagedorn C., McCoy, E. L., and Rahe, T. M. (1981). The Potential for Groundwater Contamination from Septic Effluents. *J. Environ Qual.*, 10 (1), 1-8.
- Hahn, M. W., Abadzic, D., and O'Melia, C.R. (2004). Aquasols: On the Role of the Secondary Minima. *Environmental Science & Technology*, 38 (22), 5915-5924.
- Happel, J. (1958). Viscous Flow in Multiparticle Systems: Slow Motion of Fluids Relative to Beds of Spherical Particles. *AIChE J.*, 4, 197-201.
- Happel, J., and Brenner, H. (1965). *Low Reynolds Number Hydrodynamics*. Englewood Cliffs, NJ: Prentice Hall.
- Harter T., Wagner, S., and Atwill, E. R. (2000). Bioparticle Transport and Filtration of *Cryptosporidium Parvum* in Sandy Soils and Aquifer Sediments. *Environ. Sci. Technol.*, 34 (1), 62-70.
- Harton, A. D. (1996). Influence of Flow Rate on Transport of Bacteriophage in a Column of Highly Weathered and Fractured Shale. MS Thesis, University of Tennessee, Knoxville.
- Harvey, R. W., Kinner, N. E., Bunn, A., MacDonald, D., and Metge, D. W. (1995). Transport Behavior of Groundwater Protozoa and Protozoan-Sized Microspheres in Sandy Aquifer Sediments. *Appl. Environ. Microbiol.*, 61 (1), 209-17.
- Harvey, R. W., Kinner, N. E., MacDonald, D., Metge, D. W., and Bunn, A. (1993). Role of Physical Heterogeneity in the Interpretation of Small-Scale Laboratory and Field Observations of Bacteria, Microbial-Sized Microsphere, and Bromide Transport Through Aquifer Sediments. *Water Resour. Res.*, 29, 2713-2721.

BIBLIOGRAPHY

- Herzig, J. P., Leclerc, D. M, and Leggof, P. (1970). Flow of Suspensions Through Porous Media Applications to Deep Filtration. *Ind. Eng. Chem.*, 62, 8-35.
- Hinsby, K., McKay, L. D., Jorgensen, P., Lenczewski, M., and Gerba, C. P. (1996). Fracture Aperture Measurements and Migration of Solutes, Viruses, and Immiscible Creosote in a Column of Clay-Rich Till. *Ground Water*, 34 (6), 1065-1075.
- Hoek, E. M. V., and Agarwal, G. K. (2006). Extended DLVO Interactions Between Spherical Particles and Rough Surfaces. *Journal of Colloid and Interface Science*, 298, 50-58.
- Hogg, R., Healy, T. W., and Fuerstenau, D. W. (1966). Mutual Coagulation of Colloidal Dispersions. *Trans. Faraday Soc.*, 62, 1638-1651.
- Hornbrook J. (1991). Visualization of Foam/Oil Interactions in a New, High Resolution Sandstone Replica Micromodel. Master thesis, Stanford University.
- Introduction to Polarized Light Microscopy. No Date. Nikon Microscopy U, the source for microscopy education. Retrieved on September 4, 2009 from <http://www.microscopyu.com/articles/polarized/polarizedintro.html>
- Inwood, S. (2008). High-Resolution Microvisual Study of High Mobility Ratio, Immiscible Displacements. Master thesis, Stanford University.
- Israelachvili, J. N. (1992). *Intermolecular and Surface Forces*. 2nd ed. London: Academic Press.
- Jackson, S. A. (2005). *Innovation and Human Capital: Energy Security and the Quiet Crisis*. American Petroleum Institute.
- James, S. C., and Chrysikopoulos, V. C. (1999). Transport of Polydisperse Colloid Suspensions in a Single Fracture. *Water Resources Research*, 35(3), 707-718.

BIBLIOGRAPHY

- Jillavenkatesa, A., Dapkunas, S. J. and Lum, L. H. (2001). Particle Size Characterization. Materials Science and Engineering Laboratory, National Institute of Standards and Technology, Washington, Special Publication 960-1.
- Johnson, P. R., and Elimelech, M. (1995). Dynamics of Particle Deposition in Porous Media: Blocking Based on Random Sequential Adsorption. *Langmuir*, 11, 801-812.
- Kanj, M., Funk, J., and Al-Yousif, Z. (2009). Nanofluid Coreflood Experiments in the Arab-D. Published in Proceedings from the SPE Saudi Arabia Technical Symposium and Exhibition, Alkhobar, Saudi Arabia. SPE paper No. 126161.
- Keller, A. A., and Auset, M. A. (2007). Review of Visualization Techniques of Biocolloid Transport Processes at the Pore Scale Under Saturated and Unsaturated Conditions. *Advanced Water Resour.*, 30, 1392-1407.
doi:10.1016/j.advwatres.2006.05.013.
- Keller, A. A., Sirivithayapakorn, S., and Chrysikopoulos, C. (2004). Early Breakthrough of Particles and Bacteriophage Ms2 in a Water-Saturated Sand Column, *Water Resour. Res.*, 40, W08304. doi:10.1029/2003WR002676.
- Knapp, R. B., Chiarapa, M. L., and Durham, W. B. (2000). An Experimental Exploration of the Transport and Capture of Abiotic Colloids in a Single Fracture. *Water Resour. Res.*, 36, 3139-3149.
- Kretzschmar, R., Barmettler, K., Grolimun, D., Yan, Y. D., Borkovec, M., and Sticher, H. (1997). Experimental Determination of Particle Deposition Rates and Collision Efficiencies in Natural Porous Media. *Water Resour. Res.*, 33 (5), 1129-1137.
- Kretzschmar, R., Borkovec, M., Grolimund, D., et al. (1999), Mobile Subsurface Colloids and Their Role in Contaminant Transport. *Advances in Agronomy*, 66, 121-193.
- Kreuter, J. (1994). Nanoparticles. In Kreuter, J. (Ed.), *Colloidal Drug Delivery Systems*, (pp. 219-342). Marcel Dekker. New York: NY, CRC press.

BIBLIOGRAPHY

- Lanning, L. M., and Ford, R. M. (2002). Glass Micromodel Study of Bacterial Dispersion in Spatially Periodic Porous Networks. *Biotechnol. Bioeng.*, 78, 556-66.
- Li, X., Scheibe, T. D., and Johnson, W. P. (2004). Apparent Decreases in Colloid Deposition Rate Coefficient with Distance of Transport Under Unfavorable Deposition Conditions: a General Phenomenon. *Environ. Sci. Technol.*, 38, 5616-5625.
- Liu, D., Johnson, P. R., and Elimelech, M. (1995). Colloid Deposition Dynamics in Flow-Through Porous Media: Role of Electrolyte Concentration. *Environ. Sci. Technol.*, 29 (12), 2963-2973.
- Lu, Y., Yin, Y., Mayers, B. T., and Xia, Y. (2002). Modifying the Surface Properties of Superparamagnetic Iron Oxide Nanoparticles through a Sol-Gel Approach. *Nano Letters*, 2, 182-186.
- Matthess, G., and Pekdeger, A. (1985). Survival and Transport of Pathogenic Bacteria and Viruses in Ground Water. In Ward, C. H., Giger, W., and McCarty, P. (Ed.), *Ground Water Quality* (pp. 472-482). Hoboken, NJ: John Wiley.
- McCarthy, J. F., McKay, L. D., and Bruner, D. D. (2002). Influence of Ionic Strength and Cation Charge on Transport of Colloidal Particles in Fractured Shale Saprolite. *Environ. Sci. Technol.*, 36, 3735- 3743.
- McDowell-Boyer, L. M., Hunt, J. R., and Sitar, N. (1986). Particle-Transport Through Porous Media. *Water Resour. Res.*, 22, 1901-1921.
- McKay, L. D., Cherry, J. A., and Gilliam, R. W. (1993a). Field Experiment in a Fractured Clay Till: 1. Hydraulic Conductivity and Fracture Aperture. *Water Resour. Res.*, 29, 1149-1162.

BIBLIOGRAPHY

- McKay, L. D., Gillham, R. W., and Cherry, J. A. (1993b). Field Experiments in a Fractured Clay Till: 2. Solute and Colloid Transport. *Water Resour. Res.*, 29, 3879-3890.
- McKay, L. D., Sanford, W. E., and Strong, J. M. (2000). Field Scale Migration of Colloidal Tracers in a Fractured Shale Saprolite. *Ground Water*, 38, 139-147.
- McKay, L. D., Sanford, W. E., Strong-Gunderson, J. M., and De Enriquez, V. (1995). Microbial Tracer Experiments in a Fractured Weathered Shale Near Oak Ridge, Tennessee. Published in Intl. Assoc. Hydrogeologists Congress, Edmonton, Alberta, Canada.
- Micromeritics Autopore IV 9500, Operator's Manual V. 1.09, Part No. 950-42801-01, April 2008.
- Moghimi, S. M., Hunter, A. C., and Murray, J. C. (2001). Long-Circulating and Target-Specific Nanoparticles: Theory to Practice. *Pharmacol. Rev.*, 53, 283-318.
- Mondal, P. K., and Sleep, B. E. (2012). Colloid Transport in Dolomite Rock Fractures: Effects of Fracture Characteristics, Specific Discharge, and Ionic Strength. *Environmental Science & Technology*, 46, 9987-9994.
- Mori, A., Alexander, W. R., Geckeis, H., Hauser, W., Schafer, T., Eikenberg, J., Fierz, T., Degueldre, C., and Missana, T. (2003). The Colloid and Radionuclide Retardation Experiment at the Grimsel Test Site: Influence of Bentonite Colloids on Radionuclide Migration in a Fractured Rock. *Colloids Surf. A.*, 217 (1-3), 33-47.
- Oswald, J. G., and Ibaraki, M. (2001). Migration of Colloids in Discretely Fractured Porous Media: Effect of Colloidal Matrix Diffusion. *Journal of Contaminant Hydrology*, 52, 213-244.

BIBLIOGRAPHY

- Ozaki, M., Kratochvil, S., and Matijević, E. (1984). Formation of Monodispersed Spindle-Type Hematite Particles. *J. Colloid Interface Sci.*, 102 (1), 146-151.
[http://dx.doi.org/10.1016/0021-9797\(84\)90208-x](http://dx.doi.org/10.1016/0021-9797(84)90208-x).
- Panyam, J., and Labhasetwar, V. (2003). Biodegradable Nanoparticles for Drug and Gene Delivery to Cells and Tissue. *Adv. Drug Del. Rev.*, 55, 329-347.
- Panyam, J., Sahoo, S. K., Prabha, S., Bargar, T., and Labhasetwar, V. (2003). Fluorescence and Electron Microscopy Probes for Cellular and Tissue Uptake of poly(D,L-lactide-co-glycolide) Nanoparticles. *Int. J. Pharm.*, 262, 1-11.
- Paunescu, D., Fuhrer, R., and Grass, R. (2013). Protection and Deprotection of DNA - High-Temperature Stability of Nucleic Acid Barcodes for Polymer Labeling. *Angew. Chem. Int. Ed.*, 52, 4269-4272.
- Pierre, A. C. (1998). *Introduction to Sol–Gel Processing*. Boston: Kluwer Academic Publishers.
- Popping, B. (2002). The Application of Biotechnological Methods in Authenticity Testing. *J. Biotechnol.*, 98, 107-112.
- Poulton, S. W., and Raiswell, R. (2005). Chemical and Physical Characteristics of Iron Oxides in Riverine and Glacial Meltwater Sediments. *Chem. Geol.*, 218 (3-4), 203-221. <http://dx.doi.org/10.1016/j.chemgeo.2005.01.007>.
- Prieve, D. C., and Ruckenstein, E. (1976). Rates of Deposition of Brownian Particles Calculated by Lumping Interaction Forces into a Boundary Condition. *J. Particle Interface Sci.*, 57(3), 547-550.
- Rahman, I. A., Vejayakumaran, P., Sipaut, C. S., Ismail, J. (2007). An optimized Sol-gel Synthesis of Stable Primary Equivalent Silica Particles. *Colloids and Surfaces A: Physicochem. Eng. Aspects*, 294, 102-110.

BIBLIOGRAPHY

- Rajagopalan, R., and Tien, C. (1976). Trajectory Analysis of Deep-Bed Filtration with the Sphere-In-Cell Porous-Media Model, *AICHE J.*, 22, 523-533.
- Rajagopalan, R., Tien, C., Pfeffer, R., and Tardos, G. (1982). Letter to the editor, *AICHE J.*, 28, 871-872.
- Rangel-Germán, E. (2002). Water Infiltration in Fractured Porous Media: In-Situ Imaging, Analytical Model, and Numerical Study. PhD thesis, Stanford University.
- Redden, G., Stone, M., Wright, K. E., Mattson, E., Palmer, C. D., Rollins, H., Harrup, M., and Hull, L. C. (2010). Tracers For Characterizing Enhanced Geothermal Systems. Proceedings of Thirty-Fifth Workshop on Geothermal Reservoir Engineering, Stanford University, Stanford, CA.
- Redman, J. A., Grant, S. B., Olson, T. M., and Estes, M. K. (2001). Pathogen Filtration, Heterogeneity, and the Potable Reuse of Wastewater. *Environ. Sci. Technol.*, 35 (9), 1798-1805.
- Reich, M., Utsunomiya, S., Kesler, S. E., Wang, L., Ewing, R. C., and Becker, U. (2006). Thermal Behavior of Metal Nanoparticles in Geologic Materials. *Geol. Soc. Am.* 34.
- Reimus, P. W. (1995). The Use of Synthetic Colloids in Tracer Transport Experiments in Saturated Rock Fractures. PhD Thesis, University of New Mexico, Albuquerque, New Mexico.
- Reimus, P. W. (1995). The Use Synthetic Particles in Tracer Transport Experiments in Saturated Rock Fractures. LA-13004-T, Los Alamos National Laboratory, Los Alamos, NM.
- Rose, P., Riassetto, D., Siy, J., Bartl, M., Reimus, P., Mella, M., Leecaster, K., and Petty, S. (2011). Quantum Dots as Tracers in Geothermal and EGS Reservoirs. Proceedings of Thirty-Sixth Workshop on Geothermal Reservoir Engineering, Stanford University, Stanford, CA.

BIBLIOGRAPHY

- Ruckenstein, E., and Prieve, D. C. (1976). Adsorption and Desorption of Particles and Their Chromatographic Separation. *AIChE. J.*, 22 (2), 276-283.
- Russel, W. B., Saville, D. A., and Schowalter, W. R. (1989). *Particle Dispersion*. Cambridge: Univ. Press.
- Ryan, J. N., and Elimelech, M. (1996). Particle Mobilization and Transport in Groundwater, *Particle Surf. A: Physicochem. Eng. Aspects*, 107, 1-56.
- Sakthivadivel, R. (1969). Clogging of a Granular Porous Medium by Sediment, Rep. HEL 15-7, 106 pp., Hydraul. Eng. Lab., Univ. of Calif., Berkeley.
- Sakthivadivel, R. (1966). Theory and Mechanism of Filtration of Non-Particle Fines Through a Porous Medium, Rep. HEL 15-5, 110 pp., Hydraul. Eng. Lab., Univ. of Calif., Berkeley.
- Saleh, N., Kim, H. J., Phenrat, T., Matyjaszewski, K., Tilton, R. D., and Lowry, G. V. (2008). Ionic strength and composition affect the mobility of surface-modified FeO nanoparticles in water saturated sand columns. *Environmental Science & Technology*, 42 (9), 3349-3355.
- Saleh, S. M., Muller, R., Mader, H. S., Duerkop, A., and Wolfbeis, O. S. (2010). Novel Multicolor Fluorescently Labeled Silica Nanoparticles for Interface Fluorescence Resonance Energy Transfer to and from Labeled Avidin. *Anal. Bioanal. Chem.*, 398, 1615-1623.
- Schmitz, K. S. (1990). *An Introduction to Dynamic Light Scattering by Macromolecules*. San Diego, CA: Academic Press. Inc.
- Seeboth, A., Klukowska, A., Ruhmann, R., and Lotzsch, D. (2007). Thermochromic Polymer Materials. *Chin. J. Polym. Sci.*, 25(2), 123-135.

BIBLIOGRAPHY

- Shaw, J. C., Churcher, P. L., and Hawkins, B. F. (1989). The Effects of Firing on Berea Sandstone. Published in Proceedings from the SPE International Symposium on Oilfield Chemistry, Houston, Texas. SPE Paper No. 18463.
- Srivithayapakorn, S., and Keller, A. A. (2003). Transport of Particles in Saturated Porous Media: a Pore-Scale Observation of the Size Exclusion Effect and Particle Acceleration. *Water Resour. Res.*, 39 (4), 1109. doi:10.1029/2002WR001583.
- Smith, M. S., Thomas, G. W., White, R. E., and Ritonga, D. (1985). Transport of Escherichia Coli Through Intact and Disturbed Soil Columns. *Journal of Environmental Quality*, 14 (1), 87-91.
- Smith, P.A., and Degueldre, C. (1993). Colloid-Facilitated Transport of Radionuclides Through Fractured Media. *Journal of Contaminant Hydrology*, 13, 143-166.
- Snow, D. T. (1968). Rock Fracture Spacings, Openings and Porosities. *J. Soil Mech. Found. Div. Am. Soc. Civ. Eng.*, 94, 73-91.
- Sun, Y., Yin, Y., Mayers, B. T., Herricks, T., and Xia, Y. (2002). Uniform Silver Nanowires Synthesis by Reducing AgNO₃ with Ethylene Glycol in the Presence of Seeds and Poly (Vinyl Pyrrolidone). American Chemical Society.
- Sutera, S. P., and Skalak, R. (1993). The History of Poiseuille's Law. *Annual Review of Fluid Mechanics*, 25 (1), 1-20.
- Sutton, D., Nasongkla, N., Blanco, E., and Gao, J. (2007). Functionalized Micellar Systems for Cancer Targeted Drug Delivery. *Pharmaceutical Research*, 24.(6), 1029-1046.
- Swanton, S. W. (1995). Modelling Colloid Transport in Groundwater; the Prediction of Colloid Stability and Retention Behaviour. *Advances in Colloid and Interface Science*, 54, 129-208.

BIBLIOGRAPHY

- Syndansk, R. D. (1980). Discussion of the Effect of Temperature and Confining Pressure on Single-Phase Flow in Consolidated Rocks. *JPT*, August, 1329-1330.
- Tan, Y., Gannon, J. T., Baveye, P., and Alexander, M. (1994). Transport of Bacteria in an Aquifer Sand: Experiments and Model Simulations. *Water Resour. Res.*, 30 (12), 3243- 3252.
- Tang, X. Y., and Weisbrod, N. (2009). Colloid-Facilitated Transport of Lead in Natural Discrete Fractures. *Environmental Pollution*, 157, 2266-2274.
- Tang, X.Y., and Weisbrod, N. (2010). Dissolved and Colloidal Transport of Cesium in Natural Discrete Fractures. *Journal of Environmental Quality*, 39, 1066-1076.
- Tester, J. W., Blackwell, D. D., Petty, S., Moore, M. C., Anderson, B. J., Livesay, B., DiPippo, R., Nichols, K., Veatch, R. W., Drake, E. M., Toksoz, M. N., Batchelor, A. S., Garnish, J., Baria, R., Augustine, C., Murphy, E., Negraru, P., and Richards, M. (2006). *The Future of Geothermal Energy: The Future of Impact of Enhanced Geothermal Systems (EGS) on the United States in the 21st Century*. Tech. Massachusetts Institute of Technology.
- Tipping, E. (1981). The Adsorption of Aquatic Humic Substances by Iron Oxides. *Geochim. Cosmochim. Acta*, 45 (2), 191-199. [http://dx.doi.org/10.1016/0016-7037\(81\)90162-9](http://dx.doi.org/10.1016/0016-7037(81)90162-9).
- Tipping, E., and Cooke, D. (1982). The Effects of Adsorbed Humic Substances on the Surface Charge of Goethite (α -FeOOH) in Freshwaters. *Geochim. Cosmochim. Acta* 46 (1), 75-80. [http://dx.doi.org/10.1016/0016-7037\(82\)90292-7](http://dx.doi.org/10.1016/0016-7037(82)90292-7).
- Tufenkji, N., and Elimelech, M. (2004). Correlation Equation for Predicting Single-Collector Efficiency in Physiochemical Filtration in Saturated Porous Media. *Environ. Sci. Technol.*, 38, 529-536.

BIBLIOGRAPHY

- Van Golf-Racht (1982). *Fundamentals of Fractured Reservoir Engineering*. New York, NY: Elsevier.
- Van Oss, C.J. (1993). Acid-Base Interfacial Interactions in Aqueous Media. *Colloids and Surfaces A*, 78, 1.
- Verwey, E. J. W., and Overbeek, J. T. G. (1948). *Theory of Stability of Lyophobic Particles*. New York, NY: Elsevier.
- Vilks, P., and Bachinski, D. B. (1996). Particle and Suspended Particle Migration Experiments in a Granite Fracture. *Journal of Contaminant Hydrology*, 21, 269-279.
- Vilks, P., Frost, L. H., and Bachinski, D. B. (1997). Field Scale Particle Migration Experiments in a Granite Fracture. *Journal of Contaminant Hydrology*, 26, 203-214.
- Vilks, P., and Miller, N. H. (2009). Bentonite and Latex Colloid Migration Experiments in a Granite Fracture on a Metre Scale to Evaluate Effects of Particle Size and Flow Velocity. Published by Atomic Energy of Canada Limited. Report No.: NWMO TR-2009-26.
- Vilks, P., Miller, N. H., and Vorauer, A. (2008). Laboratory Bentonite Colloid Migration Experiments to Support the Äspö Colloid Project. *Physics and Chemistry of the Earth*, 33, 1035-1041.
- Wan, J. M., and Wilson, J. L. (1994a). Of the Role of the Gas-Water Interface on the Fate and Transport of Biocolloids in Porous-Media. *Water Resources Res.*, 30, 11-23.
- Wan, J. M., and Wilson, J. L. (1994b). Colloid Transport in Unsaturated Porous Media. *Water Resources Res.*, 30, 857-64.
- Wang, H., Brandl, D., Le, F., Nordlander, P., and Halas, N. (2006). Nanorice: A Hybrid Plasmonic Nanostructure. *Nano Letters*, 6 (4), 827-32.

BIBLIOGRAPHY

- Wei, Z., Xiangyu, T., Weisbrod, N., and Zhuo, G. (2012). Review of colloid transport in fractured rocks. *Journal of Material Science*, 9, 770-787.
- Weisbrod, N, Dahan, O., and Adar, E. A. (2002). Particle Transport in Unsaturated Fractured Chalk Under Arid Conditions. *Journal of Contaminant Hydrology*, 56, 117-136.
- White, M. A. and LeBlanc, M. (1999). Thermochromism in Commercial Products. *J. of Chem. Education*, 76 (9).
- Willis, M. S., and Tosun, I. (1980). A Rigorous Cake Filtration Theory. *Chem. Eng. Sci.*, 35, 2427-2438.
- Wittung, P., Kajanus, J., Kubista, M., and Malmström, Bo. G. (1994). Absorption Flattening in the Optical Spectra of Liposome-Entrapped Substances. *FEBS Letter*, 352, 37-40.
- Wu, E. C., Park, J. H., Park, J., Segal, E., Cunin, F., and Sailor, M. J. (2008). Oxidation-Triggered Release of Fluorescent Molecules or Drugs Form Mesoporous Si Microparticles. *ACS Nano*, 2 (11), 2401-2409.
- Xu, S., Gao, B., and Saiers, J. E. (2006). Straining of Colloidal Particles in Saturated Porous Media, *Water Resour., Res.*, 42, W12S08. doi:10.1029/2006WR004948.
- Yao, K., Habibian, M. T., and O'Melia, C. R. (1971). Water and Wastewater Filtration: Concepts and Applications. *Environ. Sci. Technol.*, 5, 1105-1112.
- Zvikelsky, O., Weisbord, N., and Dody, A. (2008). A Comparison of Clay Colloid and Artificial Microsphere Transport in Natural Discrete Fractures. *Journal of Colloid and Interface Science*, 323, 286-292.
- Zvikelsky, O., and Weisbrod, N. (2006). Impact of Particle Size on Colloid Transport in Discrete Fractures. *Water Resour. Res.*, 42, W12S08. doi:10.1029/2006WR004873.